

Finite Element simulation of Viscoelastic Flow: Effect of the Rheological Model and the Mesh

by

Alexandros Dionysios Gotsis

Dissertation submitted to the Faculty of the
Virginia Polytechnic Institute and State University
in partial fulfillment of the requirements for the degree of
Doctor of Philosophy
in
Chemical Engineering

APPROVED:

D.G. Baird, chairman

K. Kontad

J.M. Reddy

D.P. Telonis

G.L. Wilkes

September 23, 1986

Blacksburg, Virginia

Finite Element simulation of Viscoelastic Flow: Effect of the Rheological Model and the Mesh

by

Alexandros Dionysios Gotsis

D.G. Baird, chairman

Chemical Engineering

(ABSTRACT)

The numerical simulation of viscoelastic flows was studied in this work. In particular the effect of mesh refinement on the quality and the convergence of the finite element method was examined, as well as the differences that may be found by using several rheological models to describe the behaviour of the non-Newtonian fluids.

The finite element simulation of viscoelastic fluid flows results in non-linear simultaneous equation systems that have to be solved iteratively. The iterations for all the viscoelastic models and most flow geometries have been found to diverge when the stress level or the elasticity of the flow increases above some certain level. The limit of convergence depends both on the mesh used for the discretization of the flow domain and on the rheological model. The limit usually decreases with mesh refinement.

The effect of the mesh refinement on the convergence and the accuracy of the solution was studied here in two flow geometries: flow into an abrupt contraction (4/1 contraction ratio) and slit flow over a transverse slot. The penalty formulation of the finite element method (FEM) was used to numerically calculate the stress and the velocity fields in the flow domain using a number of coarse and fine meshes. Several rheological models were used, with their parameters chosen so that they would best fit a certain polystyrene melt. The solutions obtained were compared to results of flow birefringence measurements and streamline photographs of the same material flowing under the same conditions that were simulated. The range of conditions that were covered by the calculations was shear stress at the die wall of 0-43 kPa, flow rates of 0-17 (mm^3/sec mm -width) and elasticity of 0-11 Deborah number.

Even though oscillations in all numerical solutions were observed around the corners of the flow domain, it was found that the overall agreement of the numerical results with the experimental data was reasonable. The coarse meshes showed lower oscillations near the corners, but the accuracy of their predictions were poor. The limit of convergence for such meshes was the highest.

Finer meshes on the other hand, showed higher oscillations near the corners and lower limit of convergence, but more accurate results away from the corner. It seems that the optimum mesh for an engineering calculation is an intermediate fine mesh that will give relatively high limits and reasonable accuracy.

On the effect of the rheological model, it was found that the lower limit of convergence was given by the upper convected Maxwell model (UCM). The Leonov-like model also gave low limits. The Phan-Thien Tanner (P-T T) and the White-Metzner (W-M) models, on the other hand, showed quite higher limits in terms of the maximum stress levels and flow rates that they could handle. In terms of the quality of the solution inside the convergence range of each model, there is very little difference between the results of the models. In general, the Phan-Thien Tanner and the White-Metzner models show slightly better solutions. A possible reason for the better behaviour of these two models is believed to be the shear thinning viscosity and primary normal stress difference coefficient that these models are able to predict in simple flows.

A few other characteristics of the two flows that were studied included the hole pressure, the entrance pressure loss and the presence of extensional fields around the contraction. It was found that the numerical method gave lower results for the hole pressure than the experimental data. Two models (W-M and UCM) gave a maximum in the entrance pressure loss and then a decrease towards negative values as the wall shear stress in the die increased. The P-T T and the Leonov-like models predicted a monotonic increase with the wall shear stress. Finally, there are two areas with strong elongational flow field in the contraction flow. One extends along the centerline of the die and the other lies along a line that starts from the reentrant corner and extends towards the upstream wall at an angle of around 45° (but depending on the flow rate). It is believed that this area is related to the *natural entry* angle, at which the viscoelastic fluid enters the contraction.

Original Contributions

The author considers the following as his original contributions in the study of the numerical simulation of the viscoelastic flow:

1. The development of a finite element computer code that can solve flow problems utilizing eight rheological models: Newtonian, generalized Newtonian model with two empirical viscosity functions (Carreau, and power-law) and five codeformational models (upper convected Maxwell, White-Metzner, Johnson-Segalman, Phan-Thien Tanner and Leonov-like).
2. The comparison of the results of the numerical calculations of the viscoelastic flow with the experimental data for the stress field and the streamlines under the same conditions, which showed that the FEM will give reasonable results up to some stress level and can be used for engineering calculations. The comparison was done on the basis of true values for the coefficients of the rheological models, so that they would represent the viscoelastic material that was used in the experimental measurements, rather than using fictitious values.
3. The study of the effect of the mesh on the convergence and the accuracy of the iterative solution of the viscoelastic flow.
4. The study of the differences found in the predictions of several rheological models for complex flows of the same polymeric material.
5. The calculation of values of the hole pressure and the entrance pressure loss as predicted by the several models for a real material.
6. The calculation of values of the stress and the velocity in the slit flow over a transverse slot and the flow into a contraction. These values may be used for further study of the hole pressure theory and the analysis of the behaviour of the viscoelastic fluids in the entry region of dies or molds.

Acknowledgements

The author wishes to express his deep appreciation to his advisor Dr. Donald G. Baird, for his suggestions, criticism and advise during the course of the calculations of this work. It is doubtful whether this work would have been finished without his help and support. The author also wishes to express his thanks to Dr. J.N. Reddy for his advice in the area of the FEM and especially for the supply of his model FEM computer code, on which the code developed in this work was based. Not less, thanks should go to the members of the advisory committee, Drs. G.L. Wilkes, D.P. Telionis and K. Konrad for their interest and suggestions.

Sincere thanks also go to Scott White and Syi-Pang Chang, whose interest on the same flows as in this work was the stimulant for many suggestions and criticisms and who also supplied the experimental results, quite often under strong time pressure. Not less to Dr. Mike Read for his collaboration on the development of the computer program and the discussions on the flow over the hole.

Finally the author would like to express his gratitude to Mark Blizard, who did many of the graphs in this work and to his collaborators in the laboratory Lori Luxemburg, Din-Shon Done, Carl Reed and Kent Blizard for their help and understanding.

Table of Contents

1.0	Introduction	1
2.0	Literature Review	7
2.1	The Finite Element Method	7
2.1.1	Outline of the Method	7
2.1.2	Discretization of the domain	9
2.1.3	Formulation of the Element Equations	10
2.1.4	Assembly of the Elements and Incorporation of the Boundary Conditions	13
2.1.5	Solution of the Global System	14
2.2	The Finite Element Method in Flow Problems	15
2.2.1	General	15
2.2.2	Non-Newtonian Fluids. The Convergence Problem	17
2.3	Constitutive Equations for Viscoelastic Fluids	25
2.3.1	Leonov's Model	25
2.3.1.1	Description	25
2.3.1.2	Predictions of the Model and Evaluation of the Parameters	28
2.3.2	The Phan-Thien Tanner Model	30
2.3.2.1	Description	30
2.3.2.2	Predictions and Parameters of the P-T T model	32
2.3.3	Other Rheological Models	36
2.3.3.1	Upper Convected Maxwell Model	36
2.3.3.2	White Metzner Model	37
2.3.3.3	Giesekus Model	37
2.3.3.4	Johnson Segalman Model	38
2.4	Entry Flow	39
2.5	Flow Over a Hole	46
3.0	Calculations	51
3.1	Equations of Motion Using the Penalty Method	51
3.2	Galerkin Weak Form of the Constitutive Equations	53
3.2.1	Upper Convected Maxwell Model	54
3.2.2	White Metzner Model	55
3.2.3	Leonov-Like and Giesekus Models	56
3.2.4	Phan-Thien Tanner and Johnson Segalman Models	57
3.3	Shape Functions and Types of Elements	58
3.4	Boundary Conditions	60
3.4.1	Natural and Essential Boundary Conditions	60
3.4.2	Calculation of the Velocity Profiles in the Inlet and Outlet Planes	62
3.5	Further Considerations for a Computer Program to Solve Flow Problems by the FEM	63
3.5.1	Assembly of the Elements and Solution of the System	63
3.5.2	The Iterative Scheme	64

3.5.3	Post Processing Calculations	65
3.6	The Structure of the Program NONEWT.FEM	67
3.6.1	Pre-Processor	67
3.6.2	Processor	69
3.6.3	Post-Processor	69
3.6.4	Stream Function Calculation	70
3.6.5	Description of the Subroutines of NONEWT	70
3.6.6	Auxiliary Programs Used in the Calculations	73
4.0	Evaluation of the Parameters of the Models, Domain Dimensions and Meshes Used ...	74
4.1	Fit of the Models to the Rheological Properties of STYRON 678	74
4.1.1	Simple Shear Rheological Properties	74
4.1.2	Extensional Flow Properties	80
4.1.3	Transient Stress Growth Predictions	83
4.2	Meshes Used for the Two Flows	89
4.2.1	Slit Flow Over a Transverse Hole	89
4.2.2	Flow Into an Abrupt Planar Contraction	94
5.0	Results and Discussion	98
5.1	Limits of Convergence as a Function of Constitutive Equation	98
5.2	Comparison of the Results of the Hole Flow with the Experimental Data	107
5.2.1	The Stresses in the Flow Over a Hole	108
5.2.2	Streamlines for Flow over a Slot	125
5.2.3	Pressure Effects in Flow over a Slot	131
5.3	Results of Flow into a Contraction	138
5.3.1	Stress Field for Flow into a Contraction	138
5.3.2	Velocity Field for Flow into a Contraction	154
5.3.3	Entrance Pressure Loss	164
5.4	Behaviour of Solution at Limit of Convergence	164
6.0	Conclusions and Recommendations	173
6.1.1	The Numerical Method	173
6.1.2	Flow Over a Transverse Hole	175
6.1.3	Flow into a Contraction	176
6.2	Recommendations	176
References	180
Appendix A.	Listing of NONEWT.FEM	184
Appendix B.	Guide to the Program NONEWT.FEM	212

List of Illustrations

Figure 1. Domain for a general problem with natural and essential boundary conditions. . .	11
Figure 2. Global error during iterations for several Deborah numbers [27]	20
Figure 3. Possible variation of a solution χ with Deborah number	22
Figure 4. A two-dimensional network for the theory of Phan-Thien and Tanner	31
Figure 5. Extensional viscosity vs. extension rate of the Phan-Thien Tanner model	35
Figure 6. Entrance Pressure loss vs. the elasticity parameter We for three rheological models (from ref. [32])	45
Figure 7. Streamline over the mouth of the hole in a slit die.	47
Figure 8. Flow chart of the program NONEWT.FEM	68
Figure 9. Viscosity vs shear rate for polystyrene at 190° C	75
Figure 10. Normal force vs shear rate for polystyrene at 190° C	76
Figure 11. Extensional viscosity of polystyrene at 190° C	81
Figure 12. Effect of ϵ on the predictions of the P-T T model for the extensional viscosity. . .	82
Figure 13. Reduced transient viscosity for STYRON 678 at 190° C	85
Figure 14. Reduced transient primary normal stress difference ($N_1/2\eta\lambda\dot{\gamma}^2$) for STYRON 678 at 190° C.	86
Figure 15. Reduced transient extensional viscosity for STYRON 678 at 190° C	87
Figure 16. Schematic of the simulated flows	90
Figure 17. Meshes used for the P1 configuration of the hole flow	91
Figure 18. Meshes used for the P2 and the P3 configurations of the hole flow	92
Figure 19. Meshes used for the entry flow	95
Figure 20. Values of We ($We = N_1/2\tau_{12}$) as predicted by several models	100

Figure 21. Isochromatics as predicted for the flow over the hole by P-T T in three meshes at 15.35 kPa wall shear stress	110
Figure 22. Isochromatics as predicted for the flow over the hole by three models at 15.35 kPa wall shear stress	111
Figure 23. Isochromatics as predicted for the flow over the hole at 12.7 kPa wall shear stress.	112
Figure 24. Superposition of the experimental and the predicted isochromatic fringes around the hole at 15.35 kPa wall shear stress	113
Figure 25. Lines in the domain for the hole flow, along which the stresses are plotted in the subsequent figures	115
Figure 26. Dimensionless shear stress as predicted by PTT along the mouth of the hole ...	116
Figure 27. Dimensionless shear stress as predicted by PTT along the line $y = 0.2H$ for the flow over a hole	117
Figure 28. Dimensionless primary normal stress difference as predicted by PTT at the mouth of the hole	119
Figure 29. Dimensionless primary normal stress difference as predicted by PTT along a line $h = 0.2H$ for the flow over a hole	120
Figure 30. Comparison of the predictions of four models for the stresses at the mouth of the hole	121
Figure 31. Comparison of the stresses along the centerline of the hole as predicted by the PTT model	122
Figure 32. Comparison of the stresses along the centerline of the hole as predicted by three models	123
Figure 33. Streamlines for the flow over the hole P1 predicted by the PTT model for $Q/W = 1.4 \text{ mm}^2/\text{sec}$	126
Figure 34. Streamlines for the flow over the hole P1 predicted by three models for $Q/W = 1.4 \text{ mm}^2/\text{sec}$	127
Figure 35. Streamlines for the flow over the hole P2 predicted by three models for $Q/W = 2.8 \text{ mm}^2/\text{sec}$	128
Figure 36. Streamlines for the flow over the hole P3 predicted by three models for $Q/W = 2.8 \text{ mm}^2/\text{sec}$	129
Figure 37. Stresses along the wall opposite the hole for the P2 and the P3 slot geometries at 12.7 kPa wall shear stress	132
Figure 38. Hole pressure across the hole as predicted by the several rheological models at 8.23 kPa wall shear stress	134
Figure 39. Hole pressure as a function of the wall shear stress for the P1 geometry	135
Figure 40. Hole pressure across the hole as predicted by the several rheological models for P2 and P3 slot geometries	136

Figure 41. Isochromatic fringes at 16 kPa wall shear stress as predicted by the P-T T model in three meshes for the entry flow	139
Figure 42. Isochromatic fringes at 16 kPa wall shear stress as predicted by three models in MESH2 for the entry flow	140
Figure 43. Lines in the domain of the flow into a contraction, along which the birefringence was plotted in the following graphs	142
Figure 44. Fringe order along x as predicted by P-T T for three meshes in the flow into a contraction	143
Figure 45. Fringe order along y as predicted by P-T T for three meshes in the flow into a contraction	144
Figure 46. Fringe order along x as predicted by four models in the flow into a contraction at 16 kPa wall shear stress using MESH3	148
Figure 47. Fringe order along y as predicted by four models in the flow into a contraction at 16 kPa wall shear stress using MESH3	149
Figure 48. Fringe order downstream from the contraction for 16 kPa wall shear stress using MESH3.	150
Figure 49. Normal stress difference along the centerline at 16 kPa wall shear stress for the flow into a contraction	155
Figure 50. Streamlines in the entry flow as predicted by P-T T in four meshes at 16 kPa wall shear stress.	157
Figure 51. Streamlines in the entry flow as predicted by three models in MESH3 at 16 kPa wall shear stress.	158
Figure 52. Streamlines in the entry flow as predicted by four models in MESH3 at $Q/W = 1.90 \text{ mm}^2/\text{sec}$	159
Figure 53. Velocity at centerline for 16 kPa wall shear stress in the flow into a contraction .	161
Figure 54. Contour plot of the extension rate for the contraction flow at 16 kPa wall shear stress	163
Figure 55. Entrance pressure loss in a 4/1 contraction as predicted by four models	165
Figure 56. Fringe order along the line $y = 0$ for several wall shear stress levels around the limit of convergence in the entry flow	167
Figure 57. Velocity along the centerline at several wall shear stress values around the limit of convergence.	168
Figure 58. Fringe order along the line $y = -0.30h$ at a wall shear stress of 26 kPa beyond the limit of convergence	169

List of Tables

1.	References on the Numerical Simulation of Planar Entry Flow	40
2.	References on the Hole Pressure Problem	48
3.	Coefficients of the Models	78
4.	Dimensions of the Dies (and the Meshes) for the Two Flow Geometries	92
5.	Characteristics of the Meshes Used for the Numerical Simulation	95
6.	Limits of Convergence for the Entry Flow	105
7.	Limits of Convergence for the Flow over a Hole	106
8.	Values of $\Delta P/L$ (kPa) for 12.7 kPa Wall Shear Stress Predicted by Four Models	140
9.	Maximum Extension Rates that Can Be Predicted by Five Models in the Flow into a Contraction	199

1.0 Introduction

A major portion of all the polymer processing operations involves either the isothermal or, most often, the non-isothermal flow of polymer melts or solutions through complex geometries. The study of the rheology of such systems is, therefore, of greatly useful to the plastics processing industry. The science of theoretical polymer rheology includes two parts: The first is the development of theories that describe realistically the stress (σ) - rate of strain ($\dot{\gamma}$) relationship of polymeric materials and the second is the application of these theories to simple or complex flow situations.

Rheologists have realized very early that polymeric fluids in flow do not show the simple linear Newtonian relation between stress and rate of strain : ($\tau = \eta\dot{\gamma}$). Not only is their viscosity a function of the shear rate, in contrast to the low molecular weight fluids for which it is constant, but they also show normal components of stresses in shear flow, not predicted by Newton's law of viscosity. Polymeric fluids also exhibit different behaviour in flows under different time scales (memory effects). There are many more phenomena that can not be explained by Newton's law of viscosity but are common among polymeric fluids. Some good examples are given in the fundamental book by Bird et al. [1]. All the above phenomena encouraged the rheologists to seek more complicated theories to describe the flow behaviour of non-Newtonian fluids.

The first approach to correct Newton's law of viscosity for polymeric fluids was the generalized Newtonian fluid models. In these empirical models the Newtonian relation between stress and rate of strain was kept but the viscosity, η , was taken as a function of the invariants of the shear rate or the stress. Models for this viscosity function include the power-law fluid, the Carreau model and others [1]. The generalized Newtonian fluid does not predict any normal stresses in simple shear flow or any elasticity or memory effects. Another approach was the linear viscoelastic fluid models, where the combination of basic elements like springs and dash-pots might give the mechanical an-

analogue of the flow behaviour of polymeric fluids. Even though these models are empirical and do not have any molecular basis, they are more successful in predicting some memory effects but they do not predict normal stresses in simple shear flow. They are also not "objective" (not coordinate frame invariant) [1].

The linear viscoelastic theories, however, were used to present some molecular theories and became the basis to develop the corotational and the codeformational models. Many molecular theories exist today, which try to simulate the motion of the macromolecules during flow of the polymer, from the simple dumbbell model [2] to the more complicated non-affine network theories [3]. The corotational and the codeformational models are similar to the viscoelastic models but they are corrected to give objectivity. The non-linear time derivatives lead to the prediction of normal stresses, but the same time-dependence as the linear viscoelastic models. So the predictions of these theories fit the experimental results much better. But still there is no universal model that will describe the behaviour of all polymeric fluids under all conditions. Also the more general the theory is, the more parameters there are to be measured (or assumed) and the more difficult it is to be applied.

The simulation of specific flows depends very much on the success of the constitutive relation used. There is a standard way to set up a flow problem. The equations that are used in such a problem are the equations of the conservation of mass (continuity), of momentum and of energy (if the flow problem is non-isothermal) and the appropriate constitutive equations. The equations of conservation are the same for Newtonian and non-Newtonian fluids and the boundary conditions depend only on the geometry of the particular flow problem. The constitutive relation, then, will dictate the differences in flow behaviour, that will be predicted for polymeric and low molecular weight fluids. This is the reason for the grave importance of the choice of the constitutive equation.

There are basically two ways that constitutive equations are expressed. These are the differential form and the integral form [1]. In the first formulation the constitutive relation consists of differential equations relating the stress tensor and its derivatives to the rate of deformation tensor and its derivatives. In general, in this case there is no explicit form of the stress tensor as a function of $\dot{\gamma}$ and its derivatives and the constitutive equations have to be solved simultaneously with the equations of motion. The velocities, the stresses and the pressure are the unknown variables. The integral models on the other hand, give the stress tensor explicitly as an integral (or sum of integrals) of some functions of the deformation of the fluid for all past times along the path-lines of the fluid

particles. In order to solve the flow problem, then, one must know (or guess) these path-lines. In reality an iteration procedure is used [4]. The predictions of the integral models are, in general, better than the differential models. They are, however, more difficult to use and result to more expensive computer codes. In this work, the main interest lies in the differential models and very little reference to the integral models will be made.

Even though the basic equations of motion have been known for a long time, problems of flow in even moderately complex geometries even for Newtonian fluids have only (relatively) recently been attempted. The reason for this is that analytical solutions exist only for very simple flow problems. In most of the cases numerical techniques and digital computers have to be used. The amount of the calculations and the computer time needed increase very rapidly with the complexity of the flow geometry and even more rapidly with the complexity of the constitutive relation used. For some models there are no analytical solutions for any flow more complicated than simple shear. It is evident, then, that successful solutions of flows of polymeric fluids in complicated geometries, like the ones that may be of interest to plastics manufacturing, will necessarily employ computer techniques and (possibly) long computer times and large storage requirements.

One of the most successful numerical techniques to solve ordinary or partial differential equations in 1,2 or 3 dimensions is the finite element method (FEM). In this method the actual continuum (domain) is represented as an assemblage of subdivisions, called finite elements, considered to be interconnected at specified joints, called "nodes". The field variables inside each element are approximated by simple functions (usually polynomials), which are defined in terms of the values of the field variables at the nodes. When the field equations for the whole domain are written and the boundary conditions are incorporated, a system of simultaneous equations is produced with the values of the field variables at the nodes as unknowns. After this system is solved, the global approximation of the solution of the initial differential equation can be computed at any point in the domain with the help of the approximating functions in each element.

The finite element method, as it was outlined above, will give results only as long as the differential equations are linear with respect to the dependent variables. If the differential equations are not linear, an iterative technique is needed, in which the FEM is used for a linearized problem at each iteration, then the variables are updated and another iteration follows until the solution converges. A Newton-Raphson iteration scheme may also be used.

As it was mentioned in the previous paragraphs, in solving flow problems the equations of motion and a constitutive equation is needed. The conservation of momentum equations include non-linear terms (the "inertial terms"). For slow flows the inertial terms can be neglected. For problems of slow flow of a Newtonian fluid then, the differential equations become linear and direct finite element techniques can be (and have extensively been) used. However, the constitutive equations for non-Newtonian fluids also include non-linear terms. The non-linearities of non-Newtonian constitutive equations can not be neglected. Iterative techniques are always necessary for non-Newtonian fluids.

The necessity of employing an iterative technique in solving non-Newtonian flow problems, however, brings the problem of the convergence of such techniques. The solution of several flow problems for some non-Newtonian models have been attempted [22-46]. However, most of their success was limited to flows, where the elastic or non-Newtonian nature of the flow was not very pronounced. The main parameters, which characterize where the elastic effects in a constitutive equation becomes comparable to viscous effects, is the Deborah number (De), defined as the ratio of a characteristic fluid relaxation time, λ , to a characteristic time scale for the flow and the Weissenberg number (We) usually defined as the ratio of the normal force over twice the shear stress at some point. Most of the reports on numerical simulation of viscoelastic fluids until now show a failure of the iterative method to converge at a Deborah number of below 10. This limit may be too low for the simulation of some processes and there is a great effort either to eliminate it or at least to increase it.

Some possible reasons for the inability for convergence of the methods at high elasticity levels are given by Mendelson et al. [55]. According to that article, non-convergence may be introduced by either excessive approximation error or by the loss or the multiplicity of the solution of the flow field that may be predicted by the model or the numerical method above some elasticity level. By approximation error it was meant both the inability of the method of weighted residuals to give correct results and the problems connected with the need of having a mesh with finite distances instead of a continuum. Sometimes a finer mesh may improve the convergence of certain codes by reducing the approximation error but in general the convergence limit decreases with the mesh refinement.

The multiplicity or non-existence of the solution is a far more severe problem inherent to the constitutive relations. The non-linearities of these relations for polymeric fluids are responsible for

this problem. Many of the flow simulations that have been reported used the upper convected Maxwell model or the second order fluid as constitutive relations. These models, however, show a constant (non-shear rate dependent) shear viscosity, a primary normal stress difference that increases as the square of the shear rate and an extensional viscosity that rises to infinity at an extensional rate that would correspond to a Deborah number of 0.5. The problems that were tried to be solved with these models (and especially the ones, where the convergence limits were the strictest) included flow around sharp corners or abrupt contractions (entry flow etc.), where high extensional rates were very possible at certain points. At these points (nodes) then, the predicted value of the extensional viscosity and the corresponding normal stresses could become unbounded. The existence, therefore, of nodes with infinite values of the field variables in the mesh (singular points) may be responsible for the divergence of the finite element method. That is, the divergence of the methods may be due to the choice of the above constitutive equations, which can only handle very low elasticity levels. It is suggested then that constitutive equations which do not show such unbounded values of the extensional properties may show better convergence behaviour than the above models. Further, relations that will fit simple shear (viscometric) and extensional properties of the fluids more accurately, may also give more accurate results in complex flows.

A finite element computer code was developed in this work that uses some specific rheological models which have the above properties (bounded values of the extensional viscosity everywhere and a shear thinning viscosity) to study whether the convergence properties and the accuracy of the values of the calculated stresses are improved. Two such models were chosen: a model derived from a continuum mechanics approach by Leonov et al. [6,7] and another derived from a molecular network theory by Phan-Thien and Tanner [8,9]. The choice of these two models is made because, even though they are differential models (and, therefore, easier to work with in a numerical simulation code), existent viscosity and primary normal stress difference data were fit well by these models and they do not show any infinite values of the extensional viscosity.

The determination of the effect of the constitutive equation is only one part of solving the problem of the divergence and the limited accuracy of the numerical simulation. The other part of this problem, the one arising by the approximation error, will also be studied in this work. This error may be affected by refining the mesh, choosing higher order approximation functions, where it is possible, using special boundary conditions such as slip on the wall near the corners and implementing special (singular) elements near singularities.

Finally the results of a new numerical simulation technique can not be used until the reliability of the technique has been established. For this reason the results of the numerical calculations are compared to experimental data of stresses and velocity profiles. Further this comparison can be done both when the numerical method converges and just when it diverges. In this way one may get some more insight into the nature (and perhaps the cause) of the divergence and see whether it is preceded by abnormal behaviour of the solution and increasingly erroneous values of the variables. More specifically, shear and normal stresses have been measured in flow over a hole [11] and in entry flow [86] using the flow birefringence technique. The study of these two flows is the main goal of this work.

This thesis is organized in six chapters. Following the introduction, in chapter 2 the finite element method (FEM) is reviewed, as well as how it is applied to flow problems of viscoelastic fluids. The reports on the numerical simulation of the flow into a contraction and the flow over a transverse slot are also reviewed there. In chapter 3 the implementation of the FEM for the specific rheological equations presented in the literature review is described, together with the structure of the computer code that was developed to simulate the viscoelastic flow. In chapter 4 are given the characteristics of the material on which the calculations were based. Viscosity and normal force curves for polystyrene (STYRON 678) are shown, as well as the parameters of the models that best fit the data. Predictions of the models for stress growth experiments are included there. In the same chapter are also shown the meshes that were used for the calculations. The fifth chapter contains the comparison between the experimental data and the results of the numerical simulation using several rheological models and different meshes. The limits of convergence that are given by the different combinations of the models and the meshes are also discussed in that chapter, as well as the behaviour of the numerical solution as these limits are approached. In the last section (ch. 6) the major conclusions that can be drawn from the numerical results and the comparisons with the experimental data are summarized. A few recommendations for further investigation of the problem of viscoelastic flow are also given there. The listing of the computer code is in the appendix. Finally in the same section is given a small guide for the use of this code.

2.0 Literature Review

2.1 *The Finite Element Method*

The finite element method (FEM) is a numerical method that can be used for the solution of differential equations in complex engineering problems. The method was first developed in 1956 [13] and in 1960 [14,15] and at first it was used mainly for structural problems. Over the years the finite element method has been expanded and it is by now so well established that it is considered to be one of the best methods for solving a wide variety of problems [16], including flow problems of Newtonian or non-Newtonian fluids. In this chapter the basic concepts of this numerical technique will be outlined and the advantages of using the FEM instead the Finite Difference technique will be discussed. Then the several steps that are required for the formulation and the solution of this method will be briefly described.

2.1.1 Outline of the Method

The basic idea of the finite element method is to find an approximate solution of a complicated problem by replacing it by a simpler one. In this method the continuum domain of the problem is taken as an assemblage of subdivisions called "finite elements". These elements are considered to be interconnected at specified joints called "nodes", which usually lie on the boundaries of the elements. Inside each element the field variables are approximated by simple functions (usually polynomials). The approximating (or interpolation) functions are defined in terms of the values of the field variables at the nodes, they have finite values only within the element and are zero every-

where else. When the field equations are written for each element using the interpolating functions, a system of equations is produced for each element with the nodal values of the field variables and the right hand side vector as unknowns. By assembling the equations that are obtained from all the finite elements in the domain and incorporating the boundary conditions, a "global" system of simultaneous equations is produced, where only the nodal values of the field variables are unknown. This system can then be solved either directly, if it is linear, or by iterative techniques if it is non-linear. The continuous global solution at all other points can then be found using the interpolating functions.

The finite element method is superior to the finite difference technique in handling very complicated problems, especially where irregular geometries are involved as it will be shown in the following. In the finite difference approximation the derivatives in the equations are replaced by finite differences, involving the values of the solution at discrete points on a mesh. After imposing the boundary condition the resulting discrete equations are solved for the values of the solution at the mesh points. The solution, therefore, can be found only on discrete points (non-continuous solution) and the derivatives that can be calculated from this approximate solution are very inaccurate. Also the problems of accurately representing and imposing boundary conditions on irregular boundaries and the inability to employ non-uniform or non-rectangular meshes make the use of the finite difference method limited to rather simple problems and regular domains. On the contrary, in the finite element method, geometrically complex domains are represented as a collection of simple (triangular or quadrilateral) finite elements. Also the solution that is obtained (and its derivatives, depending on the degree of the interpolation polynomials) is continuous. The derivatives of the solution can be calculated from the interpolating polynomials at each element. Finally, by using this technique, one has to write the numerical code only once and then use it in several similar problems by simply changing the input (geometry and boundary conditions).

The various steps that are followed in order to develop a routine to solve a problem by the finite element technique are the following (5):

1. Discretization of the given domain into a collection of preselected finite elements (ch. 2.1.2).

This step includes the construction of the finite element mesh, the numbering of the nodes and elements and the generation of the x and y coordinates.

2. Derivation of the element equations for all typical elements in the mesh (ch. 2.1.3)

This step includes the choice of the interpolation polynomials, their application in the field equations of the problem and the calculation of the "element stiffness matrices".

3. Assembly of the element equations to obtain the global equations (ch. 2.1.4)

This step includes relating the element node numbers to the global nodes, identification of the "equilibrium" conditions between secondary variables (eg. forces) and assembly of the element equations by superposition of the elements.

4. Imposition of the boundary conditions (ch.2.1.4).

Impose the specified values of the primary and secondary global degrees of freedom.

5. Solution of the assembled equations (ch. 2.1.5)

Direct solution if the problem is linear or iterative techniques if it is non-linear.

6. Post processing of the results (ch. 2.1.5).

Compute gradients etc. if needed and print the results.

2.1.2 Discretization of the domain

The discretization of the domain into finite elements is the first step in the finite element method. This step consists of replacing the whole solution region with an assemblage of elements with some preselected shapes. The shapes, sizes and number of the elements have to be chosen so that they simulate closely the original domain.

The most popular element shapes in two dimensions are the triangular and the quadrilateral. The number of the nodes in each element can also be chosen but they depend on the degree of the interpolation polynomials. The boundaries of the elements can be straight (linear elements) or curved (higher order elements), in which case mid-side nodes are necessary. Also irregularly shaped elements can be transformed into regular (eg. square) elements through transformation of the local

axes, thus making the calculation of the element stiffness matrices simpler. If the same interpolation functions that are used to transform the axes also define the field variables in an element, the elements are called isoparametric. In this way the calculations of the element equations are done in a simple square element (for an original quadrilateral isoparametric element) with boundaries at -1 and 1 for both axes and they are then transformed back to the original element shape in the finite element mesh.

The number and the size of the elements influence the convergence and the accuracy of the solution. If the size of the elements is small, the final solution is expected to be more accurate, but the computation time will increase. Also above a certain number of elements, the improvement of the solution with more elements will be insignificant [17]. Therefore, there will be an optimum number of elements for a specific problem.

The location of the nodes in the mesh will also influence the convergence and the accuracy of the solution. More nodes in areas, where high gradients of the field variables are expected, will improve the solution. In most cases, crowding a large number of nodes in such areas and keeping the nodes sparse in areas without much change will improve the solution accuracy and convergence without extensively increasing the computation time and storage requirements [17].

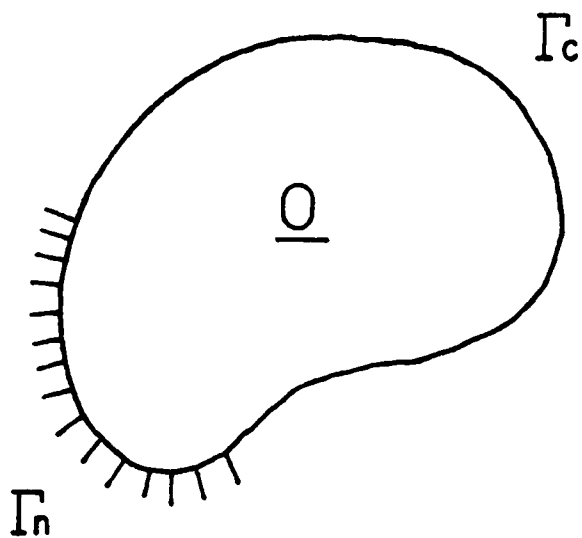
Finally, another factor that influences computation time is the way the numbering of the nodes is done in the mesh because it affects the "bandwidth" of the matrix of the final system of simultaneous equations. In general, numbering the nodes first across the shortest (in the number of nodes) dimension of the mesh will result in minimizing the bandwidth of the matrix and, therefore, in minimum computer storage requirements.

2.1.3 Formulation of the Element Equations

The following general problem is considered to be solved by the finite element method:

$$L\vec{U} = \vec{f} \quad (2.1)$$

where L is a differential operator and \vec{U} is the vector field variable in two dimensions. The domain Ω is shown in figure 1, where Γ_e is a boundary with "essential" boundary conditions $\vec{U} = \vec{U}_0$ and Γ_n is a boundary with "natural" boundary conditions $\partial\vec{U}/\partial\vec{x} = \vec{F}$.



$$L\vec{U} = \vec{f} \quad \text{in } \Omega$$

$$\vec{U} = \vec{U}_0 \quad \text{at } \Gamma_c$$

$$\frac{\partial \vec{U}}{\partial \vec{x}} = \vec{F}_0 \quad \text{at } \Gamma_n$$

Figure 1. Domain for a general problem with natural and essential boundary conditions.

The first step in the formulation of the element equations for this problem is the approximation of the field variables inside each element by a vector function \vec{U}^e :

$$\vec{U}^e(\vec{x}) = \sum_{i=1}^n \varphi_i(\vec{x}) \cdot \vec{U}_i^e \quad (2.2)$$

where n in the summation is the number of the nodes in the element and \vec{U}_i^e are the nodal values of \vec{U} . In this approximation $\varphi_i(\vec{x})$ are the shape functions and have the property of $\varphi_i = 1$ at node i . The shape functions may be different for each component of \vec{U} .

There are two approaches to formulate the finite element algorithm in order to solve the above problem. One is the variational approach and the second is the weighted residuals method. The variational approach is described in a number of books as for example in [16] and [17] and no description will be given in this work. The weighted residual method tries to minimize the residual of eq. 2.1 \vec{R} , which is defined by:

$$\vec{R} = L\vec{U} - \vec{f} \quad (2.3)$$

over the element in a weighted way:

$$\int_{\Omega^e} \omega_i g(\vec{R}) d\Omega^e = 0 \quad i = 1, \dots, n \quad (2.4)$$

By choosing the weighting factors ω_i and the function g , several methods are obtained [17]. A method that has been found to give accurate results and is rather easy to formulate in complicated problems is the Galerkin formulation. This is a weighted residual method with ω_i chosen to be the same interpolation functions that describe the field variables in each element and $g(\vec{R}) = \vec{R}$. If the operator L is linear it can be shown that this formulation gives the same results as the variational formulation [16]. Using the Galerkin method then at each element with φ_i the interpolation polynomials, the problem reduces to:

$$\int_{\Omega^e} \varphi_i (L\vec{U} - \vec{f}) d\Omega^e = 0 \quad i = 1, \dots, n \quad (2.5)$$

Setting $\vec{U} = \sum \varphi_j \vec{U}_j^e$, where φ_j need not be the same for all the components of \vec{U} , and \vec{U}_j^e are the values of the vector at node j of the element e , the above equation becomes:

$$\int_{\Omega^e} \varphi_i (L'(\varphi_j)) d\Omega^e \vec{U}_j^e = \int_{\Omega^e} \varphi_i \vec{f} d\Omega^e \quad (2.6)$$

After this step the description of the method depends on the particular problem and it will be shown in ch 2.2.1. In general, the next step employs the application of the divergence theorem to reduce the order of the differential equations. Finally the system (2.5) becomes:

$$[K^e]_k \{U^e\}_k = \{F_1^e\}_k + \{F_2^e\}_k \quad (2.7)$$

(no summation over k), where k denotes each component of the field variable vector (the velocities, the stresses etc.). The matrix $[K^e]$ is called element stiffness matrix. As it will be shown in ch. 2.2 this method can be extended to cases where the operator L is not linear, as it is the case of non-Newtonian fluids. The system is now ready for the assembly and the incorporation of the boundary conditions.

2.1.4 Assembly of the Elements and Incorporation of the Boundary Conditions

As it was shown in ch.2.1.3 the characteristic equation of the elements are calculated in terms of the nodal values of the field variables that are numbered in the local numbering system. During the assembly of the elements this local numbering has to be translated to the global numbering system of the nodes in the total mesh. This is done with the help of the "connectivity matrix", a matrix that relates the numbers of the nodes in each element with their numbers in the mesh.

The incorporation of the boundary conditions depends on whether they are "natural" or "essential". In the first case the values of the right hand vector at these boundary nodes are defined. In the second case the values of the field variables at the boundary nodes are known (constrained). There are two ways to treat such constrained values of the variables. One is to eliminate the equations that correspond to these variables and update the right hand vector of the remaining system. The second method is to replace these equations by trivial equations of the form $\vec{U}_i = \vec{U}_i^0$ or to penalize them by multiplying the diagonal term as well as the corresponding term in the right hand side vector by a large number. The last method is the easiest to handle but the first offers some decrease in the size of the global matrix with the corresponding economy in computer time and storage.

During the assembly and after the incorporation of the boundary condition the problem of the (unknown in general) right hand side vector of eq. (2.6) is also resolved. Due to the nature of the integrals, this vector is cancelled on the inter-boundaries between adjacent elements. Thus the only components that are left are the ones lying on the boundaries of the total domain. However, those that are on boundary points on Γ_n are also known (from the natural boundary conditions). On Γ_c , where the values of the field variables are known, the equations that include the unknown components of the right hand side vector are excluded from the system of the simultaneous equations but can be used in the post-processing step to calculate these components if needed.

Therefore after the assembly the (linear) global system becomes:

$$[K]\{U\} = \{F_1\} + \{F_2\} \quad (2.8)$$

where $[K]$ is the "global stiffness matrix" and it may be solved:

$$\{U\} = [K]^{-1}(\{F_1\} + \{F_2\}) \quad (2.9)$$

2.1.5 Solution of the Global System

The solution of the final system of the simultaneous equations (2.8) can be done with any of the available methods, like the Gauss elimination or lower-upper decomposition techniques etc. Caution should be taken that no zeros exist on the diagonal of the matrix because zeros will create problems for the computer due to the way these methods work. Also the global matrices that are typically obtained from finite element calculations are "banded", that is they include elements only in a zone along the diagonal. This zone is defined by a maximum bandwidth. The fact of having only a small portion of the elements in the global matrix with a non zero value is very important because it reduces the storage requirements and the computation time. The half bandwidth depends on the way the global numbering of the nodes is made, as it was stated in ch 2.1.2 and care should be taken to keep its value lowest. Inside this band, however, there are still plenty of zero elements. A technique has been developed that considers only the elements that are under the "skyline", which is defined as the curved line inside the band, above which all elements are zero [18]. This technique has been found to decrease the storage and time requirements even further [18].

The banded matrix may be symmetrical for some problems (it is unsymmetrical in general). The inversion of a symmetrical matrix reduces significantly the time and storage needed. Therefore, efforts should be made to formulate the problem so that the global matrix become symmetric if it is possible.

When the nodal values of the field variables are found, the continuous solution can be computed with the help of the interpolation polynomials in each element. Also the derivatives of the solution can then be calculated at each element by the following formula:

$$\frac{\partial \vec{U}}{\partial \vec{x}} = \sum \frac{\partial \phi_i}{\partial \vec{x}} \vec{U}_i \quad (2.10)$$

Finally, the pressure can be calculated, as well as several quantities like streamlines, potential functions etc. depending on the specific problem.

2.2 The Finite Element Method in Flow Problems

2.2.1 General

A general flow problem consists of solving the following equations [1] along with the appropriate boundary conditions:

$$\text{Conservation of mass (continuity equation): } \frac{\partial \rho}{\partial t} = - \nabla \cdot \rho \vec{u} \quad (2.11)$$

$$\text{Conservation of momentum: } \frac{\partial (\rho \vec{u})}{\partial t} = - [\nabla \cdot \rho \vec{u} \vec{u}] - [\nabla \cdot \underline{\sigma}] - \rho \vec{g} \quad (2.12)$$

$$\text{Conservation of energy: } \frac{\partial (\rho U)}{\partial t} = - [\nabla \cdot \rho U \vec{u}] - [\nabla \cdot \vec{q}] - [\underline{\sigma} : \nabla \vec{u}] \quad (2.13)$$

$$\text{Constitutive equation: } h(\underline{\sigma}, \dot{\underline{\gamma}}, \dots) = 0 \quad (2.14)$$

where h is a differential or integral operator acting on the total stress tensor, $\underline{\sigma}$, the rate of deformation tensor, $\dot{\underline{\gamma}}$, and the velocity vector, \vec{u} , and the other symbols are the material density, (ρ), the body force, \vec{g} , the internal energy, U , and the heat flux, \vec{q} .

It can be seen that all the above equations are interrelated and have to be solved simultaneously to determine the unknown stresses $\sigma_{\alpha\beta}$, the velocities u_p and the temperature T . In the case of the steady state isothermal flow at low Reynolds numbers of an incompressible fluid, as it is the case of interest in this work, the above equations in component form reduce to:¹

¹ The summation convention is followed in this work: Whenever the same Greek subscript occurs repeated in a term, it is understood to represent summation over the range 1,2 or 1,2,3 for 2-D or 3-D problems respectively. Latin subscripts represent summation over the range 1,...N with N the number of nodes per element in the FEM.

$$u_{\alpha, \alpha} = 0 \quad \text{continuity} \quad (2.15)$$

$$\tau_{\alpha\beta, \beta} - P_{, \alpha} = 0 \quad \text{motion} \quad (2.16)$$

$$h(\tau_{\alpha\beta}, \dot{\gamma}_{\alpha\beta}, u_{\alpha}) = 0 \quad \text{constitutive} \quad (2.17)$$

with $\tau_{\alpha\beta} = \sigma_{\alpha\beta} - P\delta_{\alpha\beta}$ the extra stress tensor and h an operator acting on the stresses and the velocities and their derivatives. These equations are then solved with the velocity, the pressure, and the extra stress tensor as unknowns in the "mixed" finite element formulation.

Replacing the field variables with their approximations inside each elements one gets:

$$p^e = \psi_i P_i \quad (2.18)$$

$$\vec{u}^e = \varphi_i \vec{u}_i^e \quad (2.19)$$

$$\tau^e = \pi_i \tau_i^e \quad (2.20)$$

The Galerkin weak form of equations 2.5 to 2.7 then becomes:

$$\int_{\Omega^e} \psi_j u_{\alpha, \alpha} d\Omega^e = 0 \quad (2.21)$$

$$\int_{\Omega^e} \varphi_j (\tau_{\alpha\beta, \beta} + P_{, \alpha}) d\Omega^e = 0 \quad (2.22)$$

$$\int_{\Omega^e} \pi_j h d\Omega^e = 0 \quad (2.23)$$

where ψ_j , φ_j and π_j are the interpolation functions and the integration is done over the element domain Ω^e .

For the mixed formulation it was found [19] that the shape functions for the velocities and the stresses have to be one degree higher than for the pressure in order to have non-singular stiffness matrices. Usually then $\pi_i = \varphi_i$ are second order polynomials and ψ_i are first order.

Setting $\varphi_i = \pi_i$, substituting the field variables with their approximations (eq. 2.18, 2.19 and 2.20) and applying the divergence theorem on equations (2.21) and (2.22) then, yields the element equations that correspond to the equations of continuity and motion.

$$\int_{\Omega^e} \psi_{i, \alpha} \psi_j u_{\alpha j}^e d\Omega^e = \int_{\Gamma^e} \psi_i u_{\alpha} n_{\alpha} d\Gamma^e \quad (2.24)$$

$$\int_{\Omega^e} (\varphi_{i, \beta} \varphi_j \tau_{\alpha\beta}^e + \varphi_{i, \alpha} \varphi_j P_j^e) d\Omega^e = \int_{\Gamma^e} \varphi_i (\tau_{\alpha\beta} n_{\beta} + P n_{\alpha}) d\Gamma^e \quad (2.25)$$

where the integration at the left hand side of the equation is done along the element boundary Γ^e and n_j are the components of the normal vector of the boundary.

(The equation that results from the constitutive equation is dependent on the particular form of the constitutive equation and it will be derived in a following chapter.)

An alternative (approximate method) to the mixed formulation is the "penalty" method. In this method one of the equations is taken as a "constraint" to the rest of the equations. It is then incorporated into another as an extra term multiplied by a large number, the "penalty parameter" (γ_p). The result of using this method is the elimination of the constraint equation and of one of the variables with the corresponding reduction in the size of the stiffness matrix. In the case of flow problems the equation that is treated in the above way is the continuity equation. It can be shown [20,22] that this formulation also leads to the replacement in the remaining equations of the pressure as a variable with the following expression:

$$P = -\gamma_p \mu_{\alpha, \alpha} \quad (2.26)$$

Thus the pressure is eliminated in equation (2.16) and the system reduces to eq. (2.17) and (2.18) with unknowns only the velocities and the extra stresses. Another advantage of this method is that it eliminates the need to use quadratic interpolation functions for the velocities or the stresses since the pressure is eliminated. Finally the pressure can be calculated after the velocities are found.

One should note here that the penalty formulation is an approximation and becomes exact only as the penalty parameter goes to infinity. In reality, numerical codes with extremely high values of γ_p do not give accurate results because of truncation errors. Also, due to the same source of error, reduced integration in the calculation of the element matrices has to be performed for the components that are obtained from the penalty terms in order to have non-trivial solutions. Further the values of the pressure that are obtained by eq (2.26) may in general be not accurate enough, because they require the calculation of the derivatives of the velocities. Therefore, if pressure is the desired variable the penalty method may not be sufficient.

2.2.2 Non-Newtonian Fluids. The Convergence Problem

As it was mentioned already, the application of the Finite Element Method in engineering problems is straightforward when the problems are linear. In the case of non-Newtonian fluids,

however, where non-linearities exist due to the complex constitutive equations, iterative techniques are required to linearize the problem and implement the method. The iterative techniques that have mostly been used for this purpose are the Newton Raphson technique and the direct (Picard) iteration method. In this chapter a few of the problems that have been encountered in the implementation of the FEM for non-Newtonian flows will be summarized with emphasis on the failure of the methods to converge at high elasticity levels.

The first attempt to formulate a FEM code to solve a flow of an upper convected Maxwell fluid was reported by Kawahara and Takeuchi [22]. The authors used the mixed FEM formulation, a Newton Raphson iterative technique to solve the equations of the steady state flow and a perturbation technique for the unsteady flow. It was stated in that article that six-noded triangular elements were used with second order interpolation polynomials for the velocities and first order for the stresses and the pressure. However, according to Crochet and Walters [23], this choice of interpolation polynomials would lead to singular stiffness matrices and it is more possible that second order polynomials were used even for the stresses. The viscoelastic flow problems that they studied were flow in a straight two dimensional channel and flow through a bending channel with variable section at low Reynolds numbers. No comparison with experiments and no study of the convergence behaviour was made. That report demonstrated, however, that the application of the finite element method in viscoelastic flow calculation was possible.

Since then, numerical simulations of viscoelastic flows using the FEM and several constitutive models were developed for the following (among other) cases: planar entry flow [5,24-33], axisymmetric entry flow [4,30,34-36] tapered entry flow [31,33,37], planar die swell [38-41], axisymmetric die swell [24,39], cavity flow (top plane driven) [5,42], Poiseuille driven cavity flow [43,44], slit flow over a hole [26,44,45] and flow between eccentric cylinders (journal bearing problem) [47]. The models that were used were the generalized Newtonian fluid models, the upper convected Maxwell (UCM), the White-Metzner (W-M), the second order fluid (SOF), the Oldroyd-B, the Phan-Thien Tanner (P-T T) the Leonov model and others in their differential or their integral form. Almost all of these reports showed the problem of the failure of the method at high elasticity levels. This problem will be discussed in this chapter. An extensive review of the numerical studies of viscoelastic flows is given in reference [23].

Except the mixed formulation and the penalty method, stream function methods were also used [26]. A fourth approach was made by Chang et al. [24,38], who did not define nodal stresses

but used a Picard iterative scheme, where the velocity vector \vec{u} was calculated in terms of the values of the stresses in the previous steps in a weighted way. The stresses were also explicitly computed from previous steps, so that they did not come into the finite element scheme as unknown nodal values. The success of this technique was limited to low elasticity levels.

One of the most popular models in FEM calculations of viscoelastic flows is the upper convected Maxwell model:

$$\tau_{\alpha\beta} + \lambda\tau_{\alpha\beta(1)} = \eta\dot{\gamma}_{\alpha\beta} \quad (2.27)$$

with $\tau_{\alpha\beta(1)}$ the upper convected time derivative (see chapter 2.4). Also most of the codeformational models that were used have this basic form with constant or variable coefficients η and λ (as eg. the White Metzner model) and (perhaps) extra terms. So another way to formulate the problem is to substitute $\tau_{\alpha\beta}$ from eq. (2.27) into the equations of motion (2.16):

$$-P_{,\alpha} + \eta(\dot{\gamma}_{\alpha\beta})_{,\beta} - \lambda(\tau_{\alpha\beta(1)})_{,\beta} = 0 \quad (2.28)$$

Equations (2.28) are then solved instead of (2.16) together with the equation of continuity (2.15) and the constitutive equation (2.17). This formulation was applied in [5] and [39] and it was found that the appearance of a viscous term in the momentum equation, smoothed the results at low elasticity levels. The same favorable results were also found in the addition to the stress of a retardation (purely viscous) term. This term will describe the infinite shear rate plateau (if any) in a simple shear flow. Even though its value is rather small, it has been found to have a rather strong effect in stabilizing the solution [23]. In general, then, the presence of velocity derivatives in the equations of motion through either of the above methods may lead to a better behaving solution. A good comparison between all the above techniques, however, is still missing.

Several studies have been carried out about the behaviour of the numerical solutions [5,30,46-51,etc.]. In general, as the elasticity of the flow (or the stress levels) increases, oscillations start to appear, especially around singular points like corners, boundary discontinuities or stagnation points and the solution deteriorates. At even higher elasticity levels the oscillations increase and the method ceases to converge. The general picture of the behaviour of the global error during iterations is presented in Fig. 2 from [27]. The limit of De or We (as indicators of the elasticity of the flow), above which no convergence could be achieved, depended on the type of the flow, the

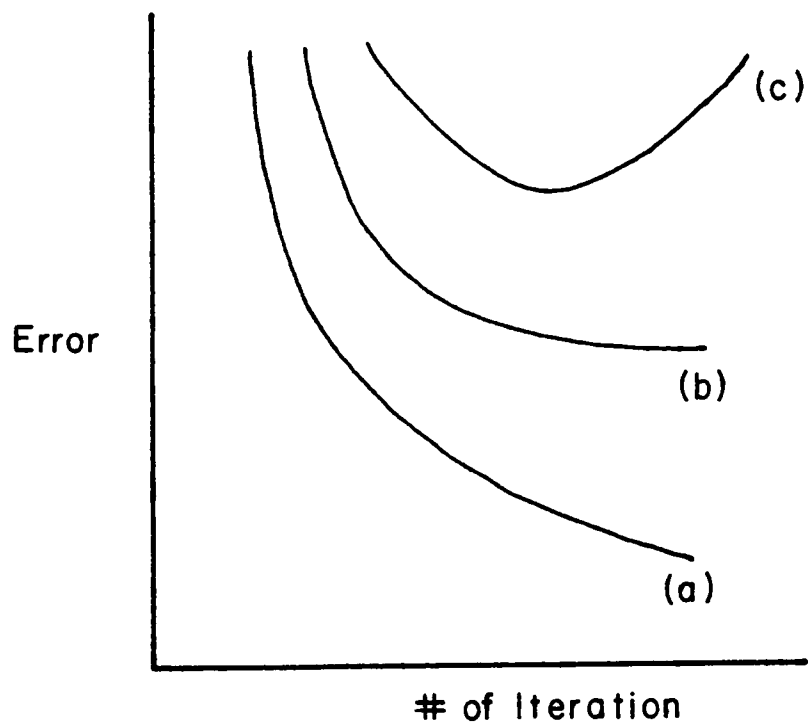


Figure 2. Global error during iterations for several Deborah numbers [27]: (a) $De < De_L$, (b) $De = De_L$, (c) $De > De_L$, where De_L is the limit of convergence.

rheological model and the mesh that was used. Most disturbingly, the limits for convergence decreased as the mesh was refined.

From the reports concerned with this problem, Mendelson et al. [5] divided the possible causes for the failure of the convergence into two categories: approximation error and multiplicity or loss of the solution. By approximation error it was meant either the inability of the weighted residuals method to approximate the differential equations and the boundary conditions of the problem or the inability of the mesh to describe the local behaviour of the field variables (eg. steep gradients approximated by low order polynomials). The multiplicity or the loss of the solution may be caused by the full set of the differential equations or by the discretized algebraic form of these equations [48]. There are three possibilities for the behaviour of the flow field: regular, bifurcation and limit point (Fig. 3).

At regular points (Fig.3a) the solution is (at least locally) unique. The numerical techniques are expected to converge here. At bifurcation points the solution becomes multivalued and the numerical method may diverge because the method cannot discriminate between the multiple solutions, or it may choose a physically unrealistic solution and the correct solution is lost (Fig.3b). The limit points occur when the solution turns upon itself at a certain point (Fig.3c). Beyond that point no solution exists and the method naturally cannot produce any results [5].

The existence of bifurcation or limit points was not found in the calculations made by Mendelson et al. [5] for planar entry flow and wall-driven cavity flow. The loss of the convergence in these problems was preceded by oscillations of the stresses and it was attributed to accumulation of approximation error. In more recent articles, however, Yeh et al. [35], Keunings [71] and Debaut et al. [78] found such bifurcation and limit points for an UCM [35], a Leonov-like [71] and a P-T T model [78]. In the cases of the works reported in references [71] and [78], however, the limit points were dependent on the mesh and were also considered a result of approximation error. Such bifurcation points were also found by Josse et al. [79] even in fully developed flow. It is believed now that these points are simply artifacts due to the discretization of the problem. However, true bifurcation points were found experimentally in the axisymmetric contraction flow by Lawler et al. [80] that may reflect anomalous points also to be found in the numerical calculations. Finally the change of the type of the equations from elliptic to hyperbolic was also found by Joseph et al. [79] near (before) the failure of the convergence for some systems, something that may also be a possible

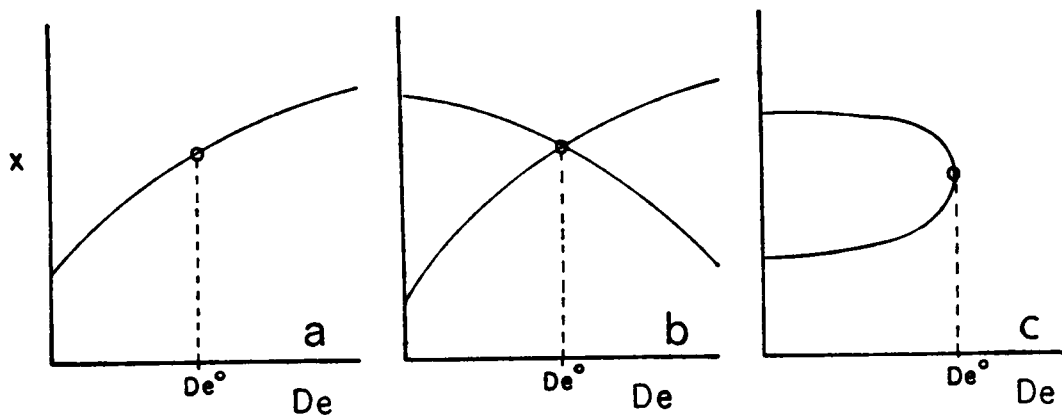


Figure 3. Possible variation of a solution χ with Deborah number: De^0 is a: (a) regular point, (b) bifurcation point, (c) limit point [5].

reason for this failure, as the numerical methods that are commonly used can not easily handle hyperbolic problems [84].

The problem of whether the loss of convergence is caused by steep gradients due to the constitutive equations rather than to specific geometric or boundary characteristics of the test flows, was studied by Beris et al. [46]. Perturbation analysis was used to study the flow between two rotating eccentric cylinders (journal bearing flow). This flow was chosen as the test problem because of its lack of any corners (singular points) and because the boundary conditions are simple and beyond any controversy: no slip at the walls. They found that steep stress gradients did develop even in this flow at Deborah numbers as low as 4 for the upper convected Maxwell, the CEF and the White-Metzner model.

The numerical calculations of the same flow [47] also demonstrated that the existence of steep stress gradients may be independent of the geometry and inherent to the viscoelastic models. The loss of the solution and the severe oscillations in the journal bearing flow began at higher values of We (~ 10) than in the entry flow. It is possible, however, that a singularity (in the stress gradient this time) may not be avoided even in this flow. The need of graded meshes (with more nodes in places with faster changes) was also demonstrated for accurate results [47].

Tanner [49] also studied the problem of non-convergence of the finite difference method in a simplified, one dimensional case and in a plane creeping flow using a Fourier series analysis. It was predicted that in the case of a Maxwell fluid, instabilities would occur when $\lambda V/h \geq 1$, where $\lambda V/h$ is the Weissenberg number based on a characteristic average velocity V and h is the characteristic mesh size. That is, instabilities and, therefore, divergence of the numerical technique, were inherent to that method (at least for that simple treatment). Further, by increasing the number of the elements, or decreasing the size h , the limit of convergence would decrease even more! A Newton Raphson technique would probably eliminate some of the problems of the numerical method and it would somewhat stabilize the method [49] but it certainly would not eliminate the problem of divergence.

Davies [48] was also concerned with these instabilities. He also used finite differences and Fourier analysis and proposed a system of "filtering functions", that would dampen to some degree the non-Newtonian effects in the governing equations at high elasticity levels and attain numerical stability even for very high Deborah numbers. This analysis could be extended to finite element

discretizations but the achievement of convergence at high De was accompanied by some loss of non-Newtonian information in the filtering process.

In another article, Lee and Finlayson [50] considered the fully developed flow of an UC Maxwell fluid in a tube (axisymmetric flow with approximation in both the radial and the axial direction) and they found that the convergence behaviour depended on whether Galerkin or Petrov-Galerkin finite element method was used. The Petrov Galerkin method is also a weighted residuals method, where the weighting functions (ω_j) are not the same as the shape functions ψ_j as in the case of simple Galerkin method but are given by [51]:

$$\omega_j = \psi_j + \frac{h}{\sqrt{u^2 + v^2}} \left[u \frac{\partial \psi_j}{\partial x} + v \frac{\partial \psi_j}{\partial y} \right] \quad (2.29)$$

with u and v the x - and y - components of the velocity vector and h the size of the element.

Lee and Finlayson found that convergence was possible up to $We = 4.0$ when Petrov Galerkin method was used but the convergence limit reduced to 0.8 with simple Galerkin. However, when the element size was decreased, the convergence limit also decreased in agreement to reference [49] above. Also, even though there was no physical change in the z -direction, the methods were sensitive to the number of elements along z and oscillations appeared also in that direction. Apparently gradients did develop in the axial direction due to the iterative scheme [50]. This result, together with the influence on the convergence of the type of the elements and the shape functions that were used for each of the field variables [78,82] indicates that even the implementation of the Galerkin finite element method as it stands today may also be the subject of improvement.

There are a few reports about improvement of the solution with the refining of the mesh. Davies et al. reported that a finer mesh decreased the oscillations and secondary vortices in planar entry flow of a Maxwell fluid, even though the convergence limit decreased. Also Mitsoulis et al. [27] reported that the refinement of the mesh lead to an increase of the convergence limit for a CEF fluid. The authors also incorporated a shear thinning viscosity in the CEF model, but the limit in convergence for this case was not reported.

In summary, it is evident that the reasons for the divergence of the numerical simulation of viscoelastic flows are not yet clearly understood. It seems that singular points in the domain play a very important role and that the divergence is influenced by the specific constitutive model and the numerical technique that is used. There is also a possibility of bifurcation or limit points oc-

curing at some elasticity level due to either the constitutive equation or the numerical technique or both. Further, an improvement of the mesh may not bring improvement to the convergence, but it may decrease to some degree the oscillations of the solution when convergence occurs. Finally the effect of the constitutive model on the convergence is still an open question. For this reason, some constitutive equations used in the numerical studies of the viscoelastic flow will be outlined in the following chapter.

2.3 Constitutive Equations for Viscoelastic Fluids

The importance of the constitutive equation used in the numerical simulation of viscoelastic flows was strongly stressed in the previous chapter, as well as its possible influence on the convergence behaviour of the iterations. In this work, a number of such rheological models were used for comparison of the numerical results and their effect on the convergence of the finite element method. In this chapter an outline is given of two models that are used in the numerical simulation and may be promising because of their predictions in simple flows. These models are the Phan-Thien Tanner and the Leonov models. A few more models are also listed in this chapter for reference purposes because they have been extensively used in simulations and are also used here for comparison.

2.3.1 Leonov's Model

Leonov [6] proposed a model based on irreversible thermodynamics and extended the rubber elasticity theory to viscoelastic media. A brief description of the results of that derivation are presented in this chapter. A complete derivation can be found in ref. [6,7].

2.3.1.1 Description

Before proceeding an introduction is given to the several tensors that describe the state of a continuum:

$$\begin{array}{ll}
 \text{Linear strain tensor} & \varepsilon_{\alpha\beta} = \left(\frac{\partial p_\beta}{\partial x_\alpha} + \frac{\partial p_\alpha}{\partial x_\beta} \right) \\
 \text{Finger Strain Tensor} & \underline{\underline{C}} = (\underline{\underline{\delta}} - \underline{\underline{\varepsilon}}) \\
 \text{Rate of Deformation Tensor} & \underline{\underline{\dot{\gamma}}} = (\nabla \vec{u} + (\nabla \vec{u})^t)
 \end{array}$$

$$\text{Vorticity Tensor} \quad \omega = (\nabla \vec{u} - (\nabla \vec{u})')$$

with \vec{p} the deformation and \vec{u} the velocity vector.

The relations between the above quantities for incompressible materials are [6]:

$$\underline{\varepsilon}_{(1)} + \underline{\varepsilon} \cdot \dot{\underline{\gamma}} + \dot{\underline{\gamma}} \cdot \underline{\varepsilon} = \underline{0} \quad (2.30)$$

$$\underline{C}_{(1)} = 0 \quad (2.31)$$

$$\det \underline{C} = 1 \quad (2.32)$$

where the upper convected derivative $\underline{a}_{(1)}$ of a tensor \underline{a} is :

$$\underline{a}_{(1)} = \frac{\partial \underline{a}}{\partial t} + \vec{u} \cdot \nabla \underline{a} - ((\nabla \vec{u})' \cdot \underline{a} + \underline{a} \cdot \nabla \vec{u}) \quad (2.33)$$

Also if $W(I_1, I_2, T)$ is an elastic potential with I_1 and I_2 the traces of the tensors \underline{C} and \underline{C}^{-1} , it can be shown [6] that:

$$\underline{\sigma} = -P\underline{\delta} + 2 \frac{\partial W}{\partial I_1} \underline{C} - 2 \frac{\partial W}{\partial I_2} \underline{C}^{-1} \quad (2.34)$$

with $\partial W / \partial I_i > 0$.

For the non-equilibrium state, Leonov assumed that the tensors that describe the viscoelastic material and correspond to the above tensors include an elastic (reversible) and an irreversible portion:

$$\underline{C} = \underline{C}_e + \underline{C}_p, \quad \underline{\sigma} = \underline{\sigma}_e + \underline{\sigma}_p, \quad \dot{\underline{\gamma}} = \dot{\underline{\gamma}}_e + \dot{\underline{\gamma}}_p$$

where subscript e denotes the elastic and subscript p the dissipative portion of the tensors.

Leonov assumed that the relations (2.30 to 2.32) remain valid for the elastic part of these quantities:

$$\underline{C}_{(1)e} + \underline{C}_e \cdot \dot{\underline{\gamma}}_p + \dot{\underline{\gamma}}_p \cdot \underline{C}_e = 0 \quad (2.35)$$

$$\det \underline{C}_e = 1 \quad (2.36)$$

$$\underline{\sigma}_e = -P\underline{\delta} + 2 \frac{\partial W}{\partial I_1} \underline{C}_e - 2 \frac{\partial W}{\partial I_2} \underline{C}_e^{-1} \quad (2.37)$$

with $I_1 = \text{tr}(\underline{C}_e)$ and $I_2 = \text{tr}(\underline{C}_e^{-1})$

In order to relate $\dot{\gamma}_p$ to \underline{C}_e , Leonov used a "non-linear Maxwellian" model with a dissipative term:

$$\dot{\gamma}_p = C_1(C_e - \frac{1}{3}\delta I_1) - C_2(C_e^{-1} - \frac{1}{3}\delta I_2) \quad (2.38)$$

$$\underline{\sigma}_p = s\eta\dot{\gamma} \quad (2.39)$$

where C_1 and C_2 are scalar functions of I_1 and I_2 and $s = \eta_\infty/\eta_0$. For the viscosity η the following form is given by Leonov:

$$\eta = \eta_0 \exp\left(\frac{\beta\lambda}{\eta_0} W_s\right)$$

with $2W_s = W(I_1, I_2) + W(I_2, I_1)$.

Further Leonov generalized the model by including several non-intersecting relaxation modes. Thus the equations that describe the model proposed by Leonov can be written:

$$\underline{\sigma} + P\underline{\delta} = s\eta_0 \exp\left(-\frac{\beta\lambda}{\eta_1} W_s\right) \dot{\gamma} + 2 \sum_{k=1}^n \left[C_e^k \frac{\partial W^k}{\partial I_1^k} - (C_e^k)^{-1} \frac{\partial W^k}{\partial I_2^k} \right] \quad (2.40)$$

$$C_{e(1)}^k + C_e^k \dot{\gamma}_p + \dot{\gamma}_p \cdot C_e^k = 0 \quad (2.41)$$

$$\det C_e^k = 1 \quad (2.42)$$

$$\dot{\gamma}_p = \frac{2}{\eta_1} \exp\left(-\frac{\beta\lambda}{\eta_1} W_s\right) \left[(C_e^k - \frac{1}{3}\delta I_1^k) \frac{\partial W_s^k}{\partial I_1^k} - ((C_e^k)^{-1} - \frac{1}{3}\delta I_2^k) \frac{\partial W_s^k}{\partial I_2^k} \right] \quad (2.43)$$

where β in eq. (2.43) was set to zero for all relaxation modes except the first (longest relaxation time).

For the elastic potential Leonov used the potential of the network theory of elasticity [52]:

$$W^k = \frac{\eta_k}{2\lambda_k} (I_1^k - 3) \quad (2.44)$$

In subsequent papers Leonov et al. [7] also used the Mooney Rivlin strain energy function and even Tschoegl's n-measure of strain.

With the potential in eq. (2.44), the equations of the model become:

$$\underline{\sigma} = -P\underline{\delta} + s\eta_0 \exp\left[\frac{\beta}{4}(I_1 + I_2 - 6)\right] + \sum_{k=1}^n \frac{\eta_k}{\lambda_k} C_e^k \quad (2.45)$$

$$\det C_e^k = 1 \quad (2.46)$$

$$(C_e^k)^{-1} + \sum_{k=1}^n \frac{1}{2\lambda_k} \left[C_e^k \cdot C_e^k - \delta + \frac{1}{3} (I_2^k - I_1^k) C_e^k \right] = 0 \quad (2.47)$$

This model can be considered as a non-linear form of the generalized Maxwell model with n relaxation modes and a viscous retardation element. For example, in simple shear flow and with only one relaxation time, it can be shown [53] that the above relations reduce to :

$$\underline{\tau} + \lambda \underline{\tau}_{(1)} + \frac{\lambda}{2\eta} \underline{\tau} \cdot \underline{\tau} = \eta \dot{\gamma} \quad (2.48)$$

$$\text{where } \underline{\tau} = \underline{\sigma} - \frac{\eta}{\lambda} \delta \quad (2.49)$$

Eq. 2.48 will be referred to as the Leonov-like model in the following chapters.

In the case of only one relaxation time and for $s=0$ the equations of the model can be written so that only the stress tensor and not the tensor C_e will appear. In this case eq. 2.45 becomes:

$$\underline{\tau} = \underline{\sigma} + P\delta = \frac{\eta}{\lambda} C_e \quad (2.50)$$

Then one can substitute C_e from eq. 2.46 into 2.49:

$$\lambda \underline{\tau}_{(1)} + \frac{\lambda}{2\eta} \underline{\tau} \cdot \underline{\tau} - \frac{\eta}{2\lambda} \delta + \frac{1}{3} \left(\frac{\eta}{\lambda} tr(\underline{\tau}^{-1}) - \frac{\lambda}{\eta} tr(\underline{\tau}) \right) \underline{\tau} = \eta \dot{\gamma} \quad (2.51)$$

This equation has the same form with eq. 2.48 but its application is not restricted to simple shearing flows.

2.3.1.2 Predictions of the Model and Evaluation of the Parameters

In simple shear flow (and for $\beta = 0$), Leonov's model has an analytical solution [7]. The viscosity and the first normal stress difference are then given by the following formulas:

$$\eta = \eta_0 \left(1 + \sum_{k=1}^n 2 \frac{\eta_k}{1 + x_k} \right) \quad (2.52)$$

$$N_1 = \sum_{k=1}^n \sqrt{2} \frac{\eta_k}{\lambda_k} \frac{x_k - 1}{1 + x_k} \quad (2.53)$$

$$\text{with } x_k = \sqrt{1 + 4\lambda_k^2 \dot{\gamma}^2}$$

In small amplitude oscillatory flow the storage and the loss modulus are [10,33]:

$$G' = \sum_{k=1}^n \frac{\eta_k \lambda_k \omega^2}{1 + \lambda_k^2 \omega^2} \quad (2.54)$$

$$G'' = s\eta_0 + \sum_{k=1}^n \frac{\eta_k \omega}{1 + \lambda_k^2 \omega^2} \quad (2.55)$$

The asymptotic behaviour of these rheological properties is as follows:

At low $\dot{\gamma}$ (ω)

$$\eta \rightarrow \eta_0$$

$$N_1 \propto \dot{\gamma}^2$$

$$G' \cong 1/2N_1$$

At high $\dot{\gamma}$ (ω)

$$\eta \rightarrow \eta_\infty$$

$$N_1 \propto \dot{\gamma}^{1/2}$$

$$G' \rightarrow \sum \frac{\eta_k}{\lambda_k}$$

$$G'' \propto \omega$$

At high $\dot{\gamma}$ (ω) and $s=0$

$$\eta \propto \dot{\gamma}^{-1}$$

G'' has a maximum and then decreases with ω

From the set of equations (2.52) to (2.55) one can evaluate the relaxation parameters η_k and λ_k by fitting either the viscosity, the normal force, the storage or the loss modulus. By evaluating the parameters with one set of data and predicting the other it has been shown that the model gives good predictions for simple shear flows and fits well the viscometric data [54].

The shear stress growth and relaxation predictions of the model have been studied by Upadhyay [33] and Upadhyay et al. [54,55]. The model was found to predict both shear and normal stress overshoot in start up of flow and the comparison with birefringence data was excellent [33] for a variety of polymeric fluids with 3 to 4 relaxation modes.

In elongational flow, it was found [33] that the predictions of the model depends on the value of β . For $\beta = 0$ there is a steady state elongational viscosity, which rises monotonically from $3\eta_0$ at low elongational rates to $6\eta_0$ at higher. No overshoot was observed for the stress growth in this case. For $\beta \neq 0$, it was found that there exists a critical value (β_{cr}) of β , above which the viscosity rises to infinity and the steady state ceases to exist. In general the elongational viscosity increased with β when there was a steady state. Also β_{cr} depended on the extension rate [33]. Nevertheless, the ability of the method to predict strain hardening makes it attractive for materials that show such effects and indicates that the parameter β should be evaluated from elongational measurements.

2.3.2 The Phan-Thien Tanner Model

While the model that was proposed by Leonov and was described in the previous chapter was derived from continuum mechanics and thermodynamics arguments, the Phan-Thien Tanner model was derived from molecular considerations. More specifically, this model was based on the ideas of the non-affine network theories. A brief description of this model follows.

2.3.2.1 Description

Consider the temporary network of Fig. 4 made by the molecules of the polymer melt. If r_1 and r_2 are the position vectors of two junctions in this network and \vec{p} is the vector that connects them, the rate of change of \vec{p} with stretching will be:

$$\frac{\partial \vec{p}(t)}{\partial t} = \nabla \vec{u} \cdot \vec{p} + \frac{\partial \vec{a}}{\partial \vec{r}} \cdot \vec{p} \quad (2.56)$$

where \vec{a} is a "slip vector". It can be shown then [8] that a general form of the derivative of \vec{a} is:

$$\frac{\partial \vec{a}}{\partial \vec{r}} = \beta_1 + \beta_2 \dot{\gamma} + \beta_3 \dot{\gamma}^2 \quad (2.57)$$

Substituting into eq. 2.56 and keeping only the linear terms, Phan-Thien and Tanner arrived to the following expression:

$$\dot{\vec{p}} = \nabla \vec{u} \cdot \vec{p} - k\vec{p} - \xi \dot{\gamma} \cdot \vec{p} \quad (2.58)$$

with k and ξ constants.

With these assumptions and using the theory of the Gaussian network, the authors arrived at the following constitutive equation:

$$\lambda \underline{\tau}_{(1)\dot{\gamma}} + H(t\tau) \underline{\tau} = \eta \dot{\gamma} \quad (2.59)$$

where $\underline{\tau}_{(1)\dot{\gamma}}$ is a convective time derivative based on an effective velocity gradient \underline{D} :

$$\underline{D} = \nabla \vec{u} - \frac{\xi}{2} \dot{\gamma} \quad (2.60)$$

$$\underline{\tau}_{(1)\dot{\gamma}} = \frac{\partial \underline{\tau}}{\partial t} + \vec{u} \cdot \nabla \underline{\tau} - \underline{D} \cdot \underline{\tau} - \underline{\tau} \cdot \underline{D}^t = \frac{\partial \underline{\tau}}{\partial t} + \vec{u} \cdot \nabla \underline{\tau} - (\nabla \vec{u})^t \cdot \underline{\tau} - \underline{\tau} \cdot \nabla \vec{u} + \frac{\xi}{2} (\dot{\gamma} \cdot \underline{\tau} + \underline{\tau} \cdot \dot{\gamma}) \quad (2.61)$$

and $H(t\tau)$ is a function that represents the rate of destruction of the network junction points. The parameter ξ on the other hand is a measure of the slippage in the non-affine network.

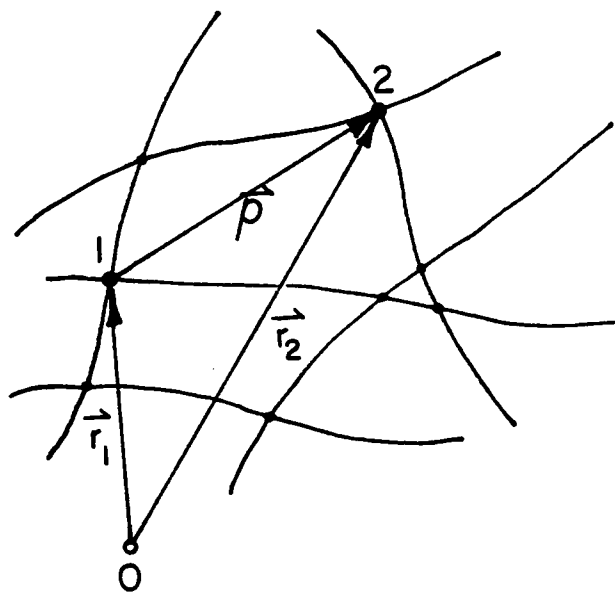


Figure 4. A two-dimensional network for the theory of Phan-Thien and Tanner: The vector between junctions 1 and 2 is \vec{p}

If one takes into consideration the whole spectrum of the relaxation times, the equation above is replaced by a cluster of equations:

$$\underline{\tau} = \sum_i \underline{\tau}^i \quad (2.62)$$

$$\lambda_i \underline{\tau}_{(1)}^i + H(t\tau) = \eta_i \dot{\gamma} \quad i = 1, \dots, n \quad (2.63)$$

For the function $H(t\tau)$, Phan-Thien and Tanner proposed two forms. In an earlier article [8] they proposed a linear formula:

$$H(t\tau^i) = 1 + \frac{\varepsilon_i \lambda_i}{\eta_i} t\tau^i \quad (2.64)$$

In a subsequent article [9], the authors proposed an exponential formula:

$$H(t\tau^i) = \exp\left[\frac{\varepsilon_i \lambda_i}{\eta_i} t\tau^i\right] \quad (2.65)$$

When ε is zero, the model presented above reduces to the one proposed by Johnson and Segalman [3]. When both ξ and ε are zero, the model is the same as the upper convected Maxwell model. It should be noted here that the effect of the function $(t\tau)$ is more pronounced in the predictions of the elongational viscosity as it will be described in the following chapter.

The Phan-Thien Tanner model is used also with a retardation term. This will correspond to adding an infinite shear rate viscosity plateau. With this addition and in the case of one relaxation mode, the extra stress tensor $\underline{\tau}$ can be separated into a viscoelastic component ($\underline{\tau}^1$) which will be described by eq. (2.63), and a purely viscous component ($\underline{\tau}^2$). For this case, then, after using the definition of $\underline{\tau}_{(1)}$, (eq. 2.60), the P-T T model becomes:

$$\underline{\tau} = \underline{\tau}^1 + \underline{\tau}^2 \quad (2.66)$$

$$\eta = \eta_1 + \eta_2 \quad (2.67)$$

$$H(t\tau^1) \underline{\tau}^1 + \lambda_{\tau(1)} + \frac{\lambda \xi}{2} (\dot{\gamma} \cdot \underline{\tau}^1 + \underline{\tau}^1 \cdot \dot{\gamma}) = \eta^1 \dot{\gamma} \quad (2.68)$$

$$\underline{\tau}^2 = \eta_2 \dot{\gamma} \quad (2.69)$$

2.3.2.2 Predictions and Parameters of the P-T T model

In small amplitude oscillatory flow the effect of the value of ε on the predictions of the Phan-Thien Tanner (P-T T) model is very small, as long as ξ is not zero, because in such weak flow

the micro-structure is not deformed very much. Therefore setting ε equal to zero is a good approximation and one can get an analytical solution for such flow:

$$G' = \sum_{k=1}^n \frac{\omega^2 \eta_k \lambda_k}{1 + (\omega \lambda_k)^2} + O(\varepsilon) \quad (2.70)$$

$$G'' = \sum_{k=1}^n \frac{\omega \eta_k \lambda_k}{1 + (\omega \lambda_k)^2} + O(\varepsilon) \quad (2.71)$$

$$\eta' = \sum_{k=1}^n \frac{\eta_k}{1 + (\omega \lambda_k)^2} + O(\varepsilon) \quad (2.72)$$

In simple flow and using the same approximation the model yields the following expressions for the shear viscosity and the normal forces:

$$\eta = \sum_{k=1}^n \frac{\eta_k}{1 + \xi(2 - \xi)(\lambda_k \dot{\gamma})^2} + O(\varepsilon) \quad (2.73)$$

$$N_1 = 2 \sum_{k=1}^n \frac{\eta_k \lambda_k \dot{\gamma}^2}{1 + \xi(2 - \xi)(\lambda_k \dot{\gamma})^2} + O(\varepsilon) \quad (2.74)$$

$$N_2 = -\frac{\xi}{2} N_1 \quad (2.75)$$

Comparing eq. (2.72) and (2.73) it can be seen that:

$$\eta'(x) = \eta \left[\frac{x}{\sqrt{\xi(2 - \xi)}} \right] \quad (2.76)$$

which can be used to evaluate ξ

The asymptotic behaviour of the above equations is:

At low $\dot{\gamma}$ (ω)	$\eta \rightarrow \eta_0$
	$N_1 \propto \dot{\gamma}^2$
	$G' \cong 1/2 N_1$
	$G'' \propto \omega$
	$\eta' \cong \eta$
At high $\dot{\gamma}$ (ω)	$\eta \propto \dot{\gamma}^2$
	$N_1 \rightarrow \text{const.}$
	$G' \rightarrow \text{const.}$
	$G'' \propto \omega^{-1}$ (has a maximum and then decreases with ω)

It is obvious that the change of η with $\dot{\gamma}$ at high shear rates is unrealistic when the retardation viscosity is zero and will create problems for calculations carried out at high $\dot{\gamma}$. A plot of shear stress

vs. shear rate for this model will show a maximum and the stress will decrease above a certain $\dot{\gamma}$. This behaviour can be avoided by adding a non-zero retardation viscosity (η_2) [26,32]. The choice of η_2 has, however, some limits. Crochet [26] found that, in order to have increasing stress (with $\dot{\gamma}$) at any shear rate, η_1 and η_2 should be related by the following inequality:

$$\eta_1 \leq 8\eta_2 \quad (2.77)$$

That is, the lowest value that the shear viscosity can take at high shear rates is 1/9 of the zero shear viscosity, the same ratio as for the Jeffrey's corotational model [56]. This value of η_2 may be not low enough for some materials.

In elongational flows the predictions of the model depend on the form of the function $H(tr\tau)$ and the value of the parameter ε . For $\varepsilon = 0$, the model is the same as the Johnson Segalman model [3] and predicts that the elongational viscosity rises to infinity at a value of elongational rate:

$$\dot{\varepsilon}_c = \frac{1}{2\lambda(1-\xi)} \quad (2.78)$$

If $H(tr\tau)$ has a linear form (eq. 2.64), the behaviour of the elongational viscosity $\bar{\eta}$ vs. the extension rate $\dot{\varepsilon}$ is shown in Fig. 5a. Then $\bar{\eta}$ rises with $\dot{\varepsilon}$ and finally it levels off. In the case of the exponential form of $H(tr\tau)$, a maximum in $\bar{\eta}$ is observed and then the elongational viscosity decreases (Fig. 5b). However, it was found [32, also by the present author] that there exist multiple real values for the steady elongational viscosity for a given elongational rate. For the case of linear $H(tr\tau)$ three branches of elongational viscosity were found (calculated analytically in ref. [32]). In the case of the exponential form of H at least two branches of η were found (numerically in ref [32] and by the author), one of which was negative and its magnitude decreased with elongation rate. Only one of all the branches is physically admissible but the existence of the others may create problems in the convergence of iteration in the numerical simulations of such fluids.

Comparisons with experimental shear and elongational data were done by Phan-Thien and Tanner [9] and excellent agreement was found. The transient shear behaviour was also studied and compared to data in the same article. Even though oscillations were created by the model at the start up of flow, the overall agreement with the traces of the growing stresses was good. Phan-Thien and Tanner stated that the oscillations could be eliminated with a small modification of the form of the equations (2.62) [9].

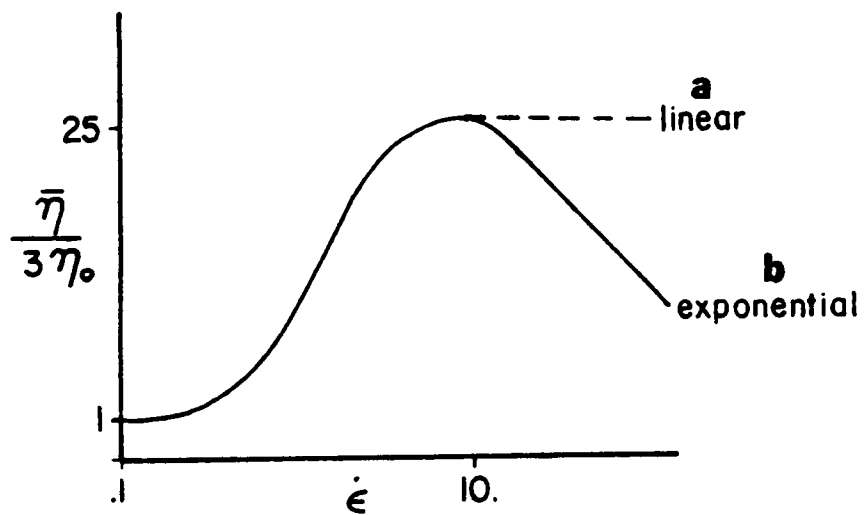


Figure 5. Extensional viscosity vs. extension rate of the Phan-Thien Tanner model: (a) Using the exponential form of $H(t\tau)$, (b) Using the linear form of $H(t\tau)$.

While Leonov's model did not have any extra parameters but the relaxation viscosities and times, the P-T T model requires the evaluation of two extra parameters: the "non-affinity" parameter ξ and the elongational parameter ε . The relaxation parameters can be calculated from the relaxation spectrum or by fitting viscometric data (equations 2.70 to 2.74). The parameter ξ can be evaluated by a horizontal shift of the curves of the shear and the dynamic viscosities vs. $\dot{\gamma}$ or ω according to eq. 2.76. Another way to evaluate ξ is to compare the values of N_1 and N_2 (if there are data for N_2 available):

$$\xi = - \frac{2N_2}{N_1} \quad (2.79)$$

Typical values of ξ is 0.15 to 0.25 for polymeric melts. It may be possible that ξ is also a function of $\dot{\gamma}$ [9].

The value of the parameter ε has to be found by fitting the elongational data. In general, for polymer melts and for the exponential form of H, ε takes a value of 0.01 to 0.015 [9].

2.3.3 Other Rheological Models

Four other rheological models are listed in the following: The Upper Convected Maxwell, the White Metzner, the Giesekus and the Johnson Segalman models. Of these four, the Upper Convected Maxwell (UCM) model [1] has been used most extensively because of its simplicity. The White Metzner (W-M) model [1] is an empirical modification of UCM and fits the simple shear data much better. The Giesekus model [69,70] is a general model and can be reduced to several others by a proper choice of its constants. Finally the Johnson Segalman [3] is similar to the Phan-Thien Tanner model, predicting the same shear behaviour but it shows different extensional viscosity.

2.3.3.1 Upper Convected Maxwell Model

The so called upper convected Maxwell model is the transcription into the codeformational formalism of the simple linear viscoelastic model proposed by Maxwell in 1867 [74]. Its equations are:

$$\underline{\underline{\tau}} + \lambda \underline{\underline{\tau}}_{(1)} = \eta_0 \dot{\underline{\underline{\gamma}}} \quad (2.80)$$

where $\underline{\tau}_{(1)}$ is the upper convected derivative given in eq. (2.53). The predictions of this model in simple shear and extensional flows are:

$$\eta = \eta_0 \quad (\text{constant}) \quad (2.81)$$

$$N_1 = 2\eta_0\lambda\dot{\gamma}^2 \quad (2.82)$$

$\bar{\eta}$ becomes unbounded at $\dot{\epsilon} = \frac{1}{2\lambda}$

2.3.3.2 *White Metzner Model*

The White Metzner model is an empirical modification of the upper convected Maxwell model, in which the relaxation time and the viscosity coefficients are functions of the second invariant of the shear rate:

$$\underline{\tau} + \lambda(II_{\dot{\gamma}}) \underline{\tau}_{(1)} = \eta(II_{\dot{\gamma}}) \dot{\underline{\gamma}} \quad (2.83)$$

The functions $\lambda(II_{\dot{\gamma}})$ and $\eta(II_{\dot{\gamma}})$ can take any form that will fit the experimental data, including the forms used for the shear thinning viscosity of the generalized Newtonian fluid (power-law, Carreau etc.) and their value decreases with $\dot{\gamma}$. The parameters of the models are evaluated by fitting the viscosity (for $\eta(\dot{\gamma})$) and the normal force (for $\lambda(\dot{\gamma})$) in simple shear flow experiments. In this way the viscosity and the normal force are perfectly fitted. The extensional viscosity, however, will eventually go to infinity above a certain extensional rate, which is higher than for the UCM model with parameters evaluated with the same set of data.

The shear viscosity and the normal force predictions of the model are given in the following:

$$\eta = \eta(II_{\dot{\gamma}}) \quad (2.84)$$

$$N_1 = 2\eta(II_{\dot{\gamma}})\lambda(II_{\dot{\gamma}})\dot{\gamma}^2 \quad (2.85)$$

2.3.3.3 *Giesekus Model*

The model proposed by Giesekus [69,70] was derived from continuum principles, but it can also be based on the network theories. In its final form [70], it is a general model that can include a retardation term and it reduces to other models with a proper choice of the coefficients. The equations that describe the model are:

$$\underline{\tau} = \underline{\tau}^1 + \underline{\tau}^2 \quad (2.86)$$

$$\underline{\tau}^1 + \lambda_1 \underline{\tau}_{(1)}^1 + \alpha \frac{\lambda_1}{\eta_1} \{\underline{\tau}^1 \cdot \underline{\tau}^1\} = \eta_1 \dot{\underline{\gamma}} \quad (2.87)$$

$$\underline{\tau}^2 = \eta_2 \dot{\underline{\gamma}} \quad (2.88)$$

with α the "mobility" parameter taking values between 0 and 1. For $\alpha = 0$ one has the UCM model. With $\alpha = \frac{1}{2}$ one has the Leonov-like model that was described in chapter 2.3.1.

The two equations above can be combined into one:

$$\underline{\tau} + \lambda_1 \underline{\tau}_{(1)} + a \frac{\lambda_1}{\eta_0} \{\underline{\tau} \cdot \underline{\tau}\} - a \lambda_2 \{\dot{\underline{\gamma}} \cdot \underline{\tau} + \underline{\tau} \cdot \dot{\underline{\gamma}}\} = \eta_0 \left[\dot{\underline{\gamma}} + \lambda_2 \dot{\underline{\gamma}}_{(1)} - a \frac{\lambda_2^2}{\lambda_1} \{\dot{\underline{\gamma}} \cdot \dot{\underline{\gamma}}\} \right] \quad (2.89)$$

with :

$$a = \frac{\alpha}{1 - \frac{\lambda_2}{\lambda_1}}, \quad \lambda_2 = \frac{\lambda_1 \eta_2}{\eta_0} \quad \text{and} \quad \eta_0 = \eta_1 + \eta_2$$

2.3.3.4 Johnson Segalman Model

Johnson and Segalman approached the problem of the rheological model from a continuum viewpoint. The model they proposed is very similar to the Phan Thien Tanner model in that it describes a "non-affine" network. It does not include the function $H(tr\underline{\tau})$, which describes the rate of destruction of the network junctions in eq. 2.59. The equations of this model coincide with equations 2.66 to 2.69 with $H(tr\underline{\tau})$ set equal to 1 or $\varepsilon = 0$.

Following the above similarity, the predictions of the Johnson Segalman model in shear flow are almost identical with the predictions of the PTT model. Equations 2.70 to 2.75 will describe the viscosity, the normal force and the dynamic properties of the model. This similarity is in general true only for weak flows like the simple shear flow. In strong flows as in extensional flow, the effect of the value of ε becomes more pronounced and the predictions of the two models are different. The J-S model does not show a bounded extensional viscosity. Instead, $\bar{\eta}$ grows exponentially to infinity much like the UCM model at some critical value of the extension ratio:

$$\dot{\varepsilon}_{crit} = \frac{1}{2\lambda(1 - \xi)}$$

It is at that point that the assumption of the constant rate of the destruction of the junctions in the network breaks down and the PTT model may be able to describe better the behaviour of the fluid.

2.4 Entry Flow

The problem of flow through a contraction (entry flow) has been studied quite extensively both numerically and experimentally. The main reason for the importance of this specific flow is the problem of the entrance pressure loss that has been observed in the flow into slit dies and capillaries [55]. Another reason for the importance of the entry flow of viscoelastic fluids is the appearance (under certain conditions) of vortices at the blind corners in the upstream region of the contraction. There has been a certain degree of controversy over the results of the above studies. In this chapter some reports on numerical and experimental studies of the entry flow will be summarized. Especially the constitutive models that have been used, the limits of the convergence of the numerical methods that have been encountered, the vortices that have or have not been observed and problems related to difficulties of the computations will be addressed.

Some of the references about finite element calculations of entry flows with differential models are given in Table 1. They are classified there by the model that was used. The maximum Deborah number (De) (or any other measure of the elasticity of the flows) for which convergence was achieved, as well as the predictions about vortices are also shown in the same Table. In the following paragraphs these reports will be summarized.

From Table 1. one can immediately see that in the recent years, the limits of convergence that were described in chapter 2.2.2 for this flow problem have been raised significantly, reaching values of De of 8 or 9 in some cases [84]. However, the existence of the corner vortex depends on the model and, in general, the convergence deteriorates with the refining of the mesh. There are, however, a few exceptions. Using an empirical non-Newtonian model, Mitsoulis and Vlachopoulos [80] reported no limit in the Deborah number and a limit of 4.5 for another (also empirical) model. These models were simple power law type models that described the stresses as "corrected" Newtonian stresses e.g. $\tau_{xx} = \eta \dot{\gamma}_{xx} + \Psi(\dot{\gamma}) \dot{\gamma}_{xy}^2$, where the second term was an empirical power-law type correction to the Newtonian first term and did not satisfy the laws of objectivity. So the models are not viscoelastic models even though they will predict normal stresses in simple shear flow.

Table 1. References on the Numerical Simulation of Planar Entry Flow

Model	Contraction Ratio	Elasticity Limit (De)	Vortices	References
Upper Convected Maxwell	2/1	?	yes	22
		0.9	yes(?)	26
	4/1	1.2	?	25
		0.11-0.87 depending on the mesh	no	30,75
Oldroyd-4	4/1	2.4	?	30
		0.5-1.75 depending on the mesh	yes(?)	32
		1.9-6.57 depending on shape functions and mesh	yes	82
White-Metzner	4/1	1.2	no	30
Phan-Thien Tanner	2/1	0.9	yes	26
	4/1	0.5-1.75 depending on the mesh	yes	32
		1.2-7.8 depending on mesh and shape functions	yes	78
Leonov	6.8/1	only at 0.66	yes	76
	4/1	??	?	77
Leonov-like	4/1	0.41-4.55 depending on the mesh	yes	75,76
CEF and modified GNF	4/1	4.5 and ∞ depending on the model	depended on the model	27,28,29

The second notable exception among the results of the numerical simulations of the entry flow is the report by Keunings and Crochet [32], where the limit in convergence increased from $De = 0.7$ to 1.75 when the size of the corner element was decreased by a factor of 5. Keunings and Crochet used the Phan-Thien Tanner model (P-T T) with a linear function $H(trt)$ (see eq. 2.68 and 2.64) and a retardation (purely viscous) term to correct for the unrealistically rapid decrease of the viscosity with $\dot{\gamma}$ that this model predicts in simple shear flow. The improvement of convergence with a finer mesh was opposite to the observations of previous studies. This improvement might be due to the different model (Phan-Thien Tanner) that was used by Keunings and Crochet or the retardation term that seems to stabilize the solution. The improvement of the convergence with the P-T T model might also be due to the fact that this model, in contrast to the UCM and the White Metzner (W-M) models, predicts an everywhere bounded elongational viscosity, as well as a shear thinning viscosity.

The hopes, however, that a very fine mesh might solve the problem of non-convergence, were shattered by Keunings in a recent article [75]. In that paper, the author calculated the contraction flow using the upper convected Maxwell and the Leonov-like models in a series of increasingly finer meshes (the finest had 40974 degrees of freedom!) and found that, despite an initial increase of the limit of convergence (in agreement with [32]), the limit decreased sharply for both models for the finer meshes. (A maximum of $We = 4.54$ was found for the Leonov-like model and an intermediate mesh and a critical value of $We = 0.61$ for the finest mesh and the same model). In light of this, it seems now that the few previous reports about better behaviour of the solutions in finer meshes [30,27,28,32], simply described this initial improvement with mesh refinement before the rapid deterioration of the solution at very fine meshes. But this fact may also indicate that there exist meshes with a moderate degree of refinement that may give the best compromise of a high convergence limit and solutions with less oscillations.

Severe oscillations are also found around the corner, even before the failure of the convergence at higher Deborah numbers. These oscillations occur between the nodes of the mesh, are purely a numerical artifact and contribute to the subsequent loss of convergence [5]. The cause of the oscillations is thought to be the large gradients of the stresses generated at the corner (singular point).

Lipscomb et al. [76] showed that a singularity in the stresses exists in the neighborhood of the entry corner for a Second Order Fluid and calculated its order. This singularity results in very large values of the stresses and in a decrease of the critical value of the Weissenberg number with mesh refinement, as the finer mesh will decrease the smoothing effect of the discretization. It was also speculated that the UCM model (and all the viscoelastic models) would again have a singularity at the corner, but its order is not known and, therefore, the use of singular elements to overcome it is not possible at this time. In order to avoid the physically inadmissible high values of the stress that develop in the neighborhood of the singularity, it is concluded in that article that the no-slip condition should be relaxed there. However, a boundary condition that would permit slip along the wall is difficult to implement without allowing flow through the boundary wall at the corner. An attempt to use such a slip boundary condition was made by Yeh [35] and led to a decrease of the oscillations of the stresses, but it also decreased the limit of convergence. Obviously, the way that the slip condition was implemented did not eliminate the singularity [35]. A rounded corner was also tried [5,32], but the improvement was rather small because the singularity was again not avoided. Finally by abandoning the viscoelastic nature of the fluid at the element near the corner, that is, by setting the relaxation time of the model equal to zero in the neighborhood of the corner only, the limit of convergence can be dramatically increased, without affecting the solution away from the corner [76].

In summary, it seems that a major reason for the divergence of the numerical methods for the simulation of the entry flow of viscoelastic fluids is the singularity of the stresses at the entry corner, which is responsible for non-integrable stresses at the corner and the propagation of the error that causes the method to fail. The cure of this problem is not known yet, as the order of the singularity has not been found. There are two major directions that may lead to finding such a cure. One is the study of the implementation of special boundary conditions that will allow slip at the wall near the corner and (perhaps) the relaxation of the viscoelastic nature of the fluid at this point. In the same direction, the study of the singularity in an attempt to find its order and implement special (singular) elements at the corner, may also be suggested. Finally a different approach might be the study of the smoothing effect that a coarser mesh will have on this singularity, so that the results

of the simulation, at least far from the corner, will be accurate (from an engineering point of view) and higher elasticity limits of convergence will be obtained.

Comparison of the results of the numerical simulations with experimental data was done by Isayev and Upadhyay [77,88]. The Leonov model with 3 relaxation times was used, which described the simple shear data of the test material (poly-isobutylene) rather well. The model shows a maximum in We vs $\dot{\gamma}$ at quite high shear rates, at a point which sets the limit of the usefulness of the model. Although no limit of convergence was reported (the authors were careful enough to do all their comparisons at elasticity levels much lower than the maximum in We), the reasonable agreement between birefringence measurements and theoretical predictions is an indication of both the usefulness of the Leonov model and the success of the numerical scheme. On the other hand, the existence of a vortex in the flow was not clear in that article. The authors indicated only the existence of a region of "secondary flow" at the corners without showing any streamlines. A vortex was, however, calculated by Upadhyay [76] and by Upadhyay and Isayev in a more recent article [88] using the same model.

The predictions about the existence of the vortices based on the calculations in which other models were used, has been the topic of some controversy. Most numerical simulations have shown (at least one) vortices at the corner in the upstream of the contraction [5,26,30,32]. However, both Mendelson [5] for the case of the SOF and Davies [30] for an UCM and an Oldroyd-B models showed that this vortex growth for the planar contraction was merely a numerical artifact, as the vortices could be eliminated with finer meshes. For the W-M model, Davies [30] could not find such a vortex. For the axisymmetric case and the UCM model the vortex was considered real. It is believed now [39,40] that the planar entry flow of a Maxwell, a Second Order or an Oldroyd-B fluid does not generate recirculating corner vortices (at least when the customary mixed method is used that involves quadratic shape functions for the stresses and the velocities and linear shape functions for the pressure). On the other hand, it was found [32,78] that the use of a Johnson - Segalman (J-S) or a P-T T model leads to a non-trivial recirculating vortex. The size of the vortex was found in ref. [32] to increase monotonically with the elasticity of the fluid up to the convergence limits but it was found to show a maximum at a value of $We = 4$ in ref. [78]. The vortex was not affected

by refining the mesh and, therefore, it was considered "real". The same vortex was found by Mitsoulis et al. [29] for their simple rheological models. No mesh refinement was made in that article to examine its effect on vortex size and some uncertainty may exist. However, because of the simplicity of their models, the vortex growth in their calculations seems to be real. Finally Marchal [82] showed that the Oldroyd-B model may show vortices in a 4/1 circular contraction flow, something that agrees with the experimental observation that vortices are more often found in axisymmetric than in planar flows.

The entrance pressure loss correction is another important feature of entry flow that has been extensively studied. Again most of the studies show some dependence of ΔP_{ent} on the elasticity and the flow rate but there is also a degree of controversy. Before finishing this section, a small summary of the results of these studies will be given.

Mitsoulis et al. [28] found (with their non-elastic models) that, depending on the elongational viscosity behaviour of the model, the entrance pressure loss may either decrease or increase with the flow rate. If the elongational viscosity decreases with deformation rate, ΔP_{ent} also decreases. If the elongational viscosity is constant ($\bar{\eta} = 3\eta_e$), ΔP_{ent} increases with the flow rate. The P-T T and the Johnson Segalman fluids also show a strong dependence of ΔP_{ent} on the elasticity and the flow rate (Fig. 6) [31,32]. The entrance pressure loss initially decreases up to a Weissenberg number of 0.2 and then it increases with We . The same (qualitatively) behaviour is shown also by the White Metzner model [32]. Available numerical results with the Maxwell and the Oldroyd-B models have shown that the entrance pressure loss decreases with the flow rate, a fact which is opposite to the experimental results [59]. It is possible however that these results just show the initial part of Fig. 6 where even in the case of the P-T T model the entrance pressure loss initially decreases. Results at higher flow rates (not available at this point because of the failure of the numerical techniques) are needed to completely study the behaviour of the entrance pressure loss for these fluids.

There is a great volume of reports on experimental results for the flow into a sudden contraction. References [33,60-63 and 88-89] are some examples giving the shape of the streamlines and values of the stresses measured by means of flow birefringence. In general, the experimental measurements show an increase of the entrance pressure loss with the flow rate and the elasticity of the fluid. The existence and growth of the corner vortex, however, was not a uniform characteristic of

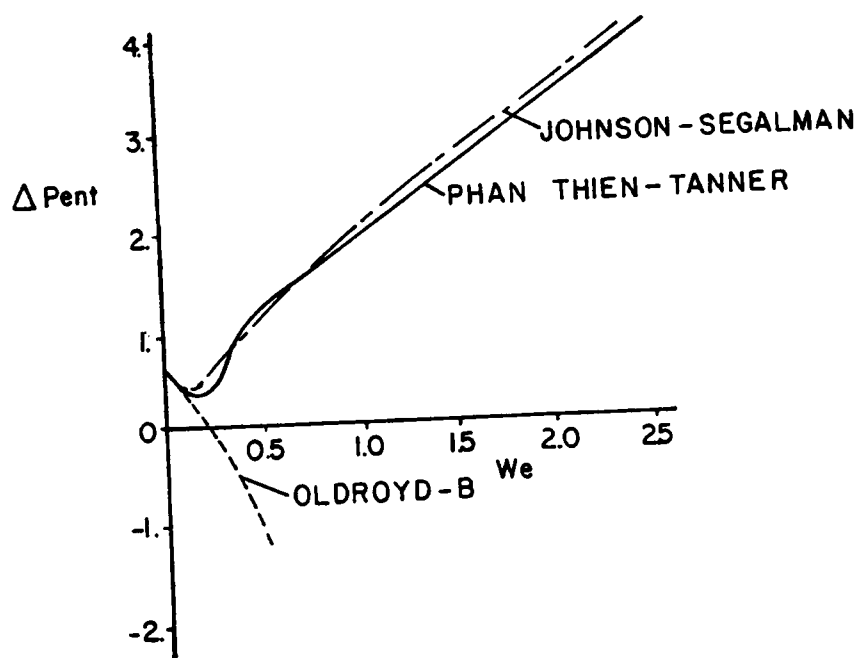


Figure 6. Entrance Pressure loss vs. the elasticity parameter We for three rheological models (from ref. [32])

the polymers that were studied in the above reports. As an example, LDPE and PS may show vortices under conditions that HDPE, PB and the iso-polypropylene (i-PP) do not show any. It seems that the corner vortex formation may be related to the elongational behaviour of the material [64] and especially the stress-strain relation during extensional stress growth [89].

2.5 Flow Over a Hole

When a polymeric fluid flows over a depression in the conduit wall, the pressure on the wall in the depression (P_2) is not the same as the pressure on the opposite wall (P_1) [17]. For many polymeric fluids $(-P + \tau_{yy})_2$ is lower than $(-P + \tau_{yy})_1$ even for very small holes and for slow flows.² The difference in these quantities is the hole pressure error:

$$\Delta P_H = (-P + \tau_{yy})_1 - (-P + \tau_{yy})_2 \quad (2.90)$$

Some reports on the numerical simulation and the experimental studies of this particular flow problem will be discussed in this chapter.

The hole pressure error can be explained by the presence of elasticity in the fluid. Considering a streamline over the mouth of the hole in a slit die that has a transverse slot (Fig. 7), there is some deformation and stretching due to the hole. Because of the elasticity of the fluid, there is a force acting on the fluid elements along the deformed streamline, pulling the fluid upwards. The result is that the pressure that will be sensed by a pressure transducer at the bottom of the hole (point 2) is less than the pressure at point 1 exactly opposite on the upper wall of the slit die.

The existence of the hole pressure error has a great importance in the polymer processing for two reasons. The first reason is that it introduces an error in the measurements of the pressure, which has to be corrected, especially because many measurements have been done without flush mounted transducers. The second is the possibility to use the measurements of the hole pressure error to evaluate the primary normal stress difference.

Higashitani and Pritchard [65], Baird [66,67] and Pike [11] have studied the relation of the hole pressure and N_1 both theoretically and experimentally. It has been shown that it is possible to evaluate N_1 from ΔP_H with a reasonable accuracy from a simple relation: $N_1 = (1/c)\Delta P_H$ where c

² In the present work a tensile stress e.g. τ_{xx} is considered to be positive and a compressive to be negative.

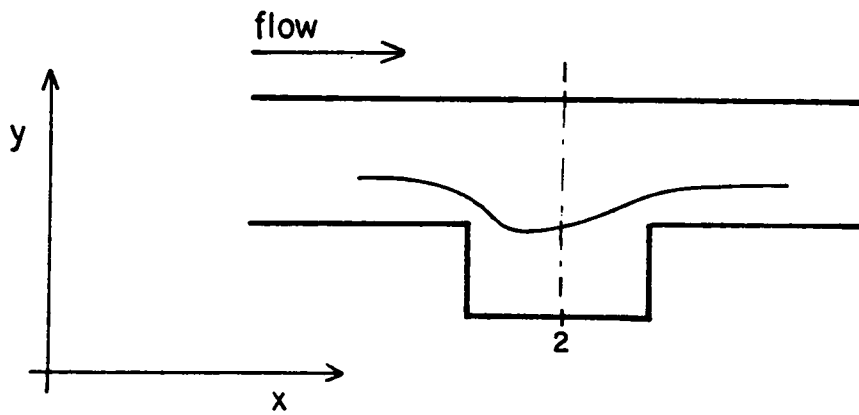


Figure 7. Streamline over the mouth of the hole in a slit die.

Table 2. References on the Hole Pressure Problem

Model	Elasticity Limit	References
Upper Convected Maxwell	0.8 1	45,90 98
Oldroyd-3	0.8	44
Second Order Fluid	1.0	12
Johnson Segalman	(0.6)	26,97

is a constant of the order of 0.25. However, even though experimental quantitative results were in rather good agreement with the theoretical predictions, several assumptions that were made concerning the nature of the flow, as for example the symmetry of the stress field around the slot centerline, proved to be incorrect [11]. The streamlines have been found to be asymmetric both for a Newtonian and viscoelastic fluids. For a Newtonian fluid, the asymmetry exists because of the fluid inertia and the maximum deflection of the streamlines occurs near the exit plane of the slot [68]. For a viscoelastic fluid at low Reynolds numbers on the other hand, the asymmetry is caused by the elasticity of the fluid and the maximum deflection of the streamlines occurs near the entry plane of the slot [11]. Further, Malkus [90] showed theoretically (and Pike [11] experimentally, using flow birefringence measurements) that there exists a pole in the values of $(\tau_{11} - \tau_{22})/2\tau_{12}$ making the integration of this quantity impossible along the centerline of the hole, an integration that is used in the theory of Higashitani and Pritchard [65]. This also raised strong doubts about the validity of that theory. To clear these controversies, the numerical modeling of this flow will offer some more insight because values of the stresses and the stream function can be calculated at each point in the flow domain.

Rheologically this flow appears to be "weaker" than the entry flow, because the hole does not disturb the shear flow in the die to a very large degree. Therefore, one expects less severe problems with the corners and the divergence than in the case of the entry flow. However, the magnitude of the hole pressure is rather small relatively to the stresses in the die and high accuracy is needed.

Some numerical simulations of the problem of the planar flow over a transverse hole are listed in Table 2. It can be seen there that this flow problem has been given less attention than the entry flow as a test problem for numerical methods. The parameter that was usually compared in these studies was the value of the hole pressure ΔP_H .

Jackson and Finlayson [44] found good agreement between the calculated values of the hole pressure and experimental data by Baird [67] at low Weissenberg numbers (0.06 to 0.14). At higher elasticity levels (We 0.3 to 0.8) the comparison was poor. An Oldroyd model was used with variable relaxation time and viscosity. Results were reported up to $We = 0.8$ but it was not stated whether that value was the limit for the convergence of their finite element method.

Crochet and Bezy [26] used a Maxwell fluid and the finite element method and found that the dimensionless hole pressure $\Delta P_H/(\tau_{xx} - \tau_{yy})_w$ was of the order of 0.25 in agreement with ref. [65].

This value decreased when the Reynolds number increased. The limit for convergence was not mentioned in that article.

Richards and Townsend [45] also studied the same flow with a corotational and a codeformational Maxwell fluid. In their comparisons the hole pressure due to the viscous effects was separated from the hole pressure due to purely elastic effects in order to eliminate the effect of the Reynolds number. Their values for the (elastic part of the) dimensionless hole pressure was less than 0.25 and decreased with the Deborah number and the Reynolds number. Also the assumption of symmetry (around the centerline of the hole) was found to be incorrect. However, the asymmetry produced by the high Reynolds number tended to cancel the asymmetry introduced by the elasticity of the fluid.

Experimental studies of the flow over a transverse slot were made by Pike [11] using the technique of flow birefringence to measure the stresses directly. He also found that the stress field was asymmetric. The interest of the present author in that work, however, lies on the fact that it includes data of the stresses at several points in the domain of the flow, with which direct comparisons with numerical calculations may be done.

In conclusion, most numerical and experimental studies show a positive value of $\Delta P_H/N_{1w}$ which decreases with increasing Reynolds number from (around) 0.25 at zero Reynolds number. The elasticity levels that have been tested in the numerical techniques were rather low and no problem of convergence arose. Therefore, results at higher Deborah numbers are needed to complete the comparisons.

3.0 Calculations

It was shown in the previous chapter that the equations that have to be solved for an isothermal flow problem, are the equations of motion, the continuity equation and the constitutive equation. The Galerkin weak form of the mixed formulation of these equations (except for the constitutive equations) was given in the same chapter. The penalty method, an alternative method to the mixed formulation was also outlined in chapter 2.3. In the present section the calculations that are made to apply that method in flow problems of viscoelastic fluids, as well as the Galerkin weak form of the several constitutive equations used in this work will be outlined.

In the following, first the weak form of the equation of motion will be shown (ch. 3.1). Then the weak form of the equations of the upper convected Maxwell model, the White Metzner, the Phan-Thien Tanner and the Leonov-like models will be given (ch. 3.2). In chapter 3.3 the form of the elements and the shape functions that were used in this work will be presented. The implementation of the boundary conditions will be described in ch. 3.4. Finally the structure of a computer program to implement the FEM for the solution of viscoelastic flows will be outlined in chapters 3.5 and 3.6

3.1 *Equations of Motion Using the Penalty Method*

The "penalty" method is an approximate method to formulate a flow problem, in which the equation of continuity is taken as a "constraint" to the equations of motion. To do so, it can be

³ The Continuum Mechanics convention is used here with regard to the signs of $\sigma_{\alpha\beta}$, P , and $\tau_{\alpha\beta}$. That is, both P and $\tau_{\alpha\beta}$ are negative in compression (positive in tension). Therefore, $\sigma_{\alpha\beta} = -\delta_{\alpha\beta}P + \tau_{\alpha\beta}$.

shown [20,22] that the equation of continuity is eliminated from the system and the pressure as a variable is replaced in the equation of motion by the expression of eq. 2.26:

$$P = -\gamma_p u_{\alpha, \alpha}$$

Then the equations of motion (eq. 2.16) become³:

$$\tau_{\alpha\beta, \beta} + \gamma_p (u_{\beta, \beta})_{, \alpha} = 0 \quad (3.01)$$

The system of the equations that have to be solved, then, consists of only eq. 3.01 and the constitutive equation. The continuity constraint is also approximately satisfied, as long as the penalty parameter γ_p is sufficiently large, that is, several orders of magnitude larger than the stresses.

It was mentioned in chapter 2.3.1 that the PTT model requires a retardation term in order to predict an ever increasing (with $\dot{\gamma}$) shear stress. The Giesekus model also includes such a term. The presence of a retardation term has been found to increase the stability of the finite element method. It is advisable then, to include this term even into models that do not require it by choosing an appropriate low infinite shear rate viscosity η_2 .

A retardation term can be incorporated into a model by separating the stress tensor into two terms: a viscoelastic term and a purely viscous term (eq. 2.66 to 2.69):

$$\underline{\tau} = \underline{\tau}^1 + \underline{\tau}^2 ,$$

with $\underline{\tau}^2 = \eta_2 \dot{\underline{\gamma}}$ and $\underline{\tau}^1$ the viscoelastic term defined by the specific rheological equation. Then the stress can be replaced in the equation of motion by the above two terms. Finally dropping the superscript 1 from $\underline{\tau}^1$, eq. 3.01 becomes:

$$\tau_{\alpha\beta, \beta} + \eta_2 \dot{\gamma}_{\alpha\beta, \beta} + \gamma_p (u_{\beta, \beta})_{, \alpha} = 0 \quad (3.02)$$

where $\tau_{\alpha\beta}$ is now the viscoelastic part of the stress tensor (that is $\tau_{\alpha\beta}^1$ in the previous notation).

Galerkin's weak form of 3.02 after the application of the divergence theorem becomes:

$$\begin{aligned} \int_{\Omega^e} [\varphi_{i, \beta} \tau_{\alpha\beta}^e + \eta_2 \varphi_{i, \beta} (\varphi_{j, \beta} u_{\alpha j}^e + \varphi_{j, \alpha} u_{\beta j}^e) + \gamma_p \varphi_{i, \alpha} \varphi_{j, \beta} u_{\beta j}^e] d\Omega^e \\ = \int_{\Gamma_e} \varphi_j ((\tau_{\alpha\beta} + \eta_2 \dot{\gamma}_{\alpha\beta}) n_{\beta} + P n_{\alpha}) d\Gamma^e \end{aligned} \quad (3.03)$$

As previously, the subscripts α, β take the values 1,2 or 1,2,3 for 2-D or 3-D problems respectively and the subscripts i, j take the values of 1,...,N with N the number of the nodes in the element.

In the 2-D case the components of eq. 3.03 are:

$$[\gamma_p[S11] + \eta_2[S22]]\{u^e\} + \gamma_p[S12]\{v^e\} + [S1]'\{\tau_{11}^e\} + [S2]'\{\tau_{12}^e\} = \{F_1^e\} \quad (3.04)$$

$$\gamma_p[S12]'\{u^e\} + [\gamma_p[S22] + \eta_2[S11]]\{v^e\} + [S1]'\{\tau_{12}^e\} + [S2]'\{\tau_{22}^e\} = \{F_2^e\} \quad (3.05)$$

with the matrices S11, S22 etc. representing the Galerkin integrals over the element:

$$S11_{ij} = \iint_{\Omega_e} \frac{\partial \varphi_i}{\partial x} \frac{\partial \varphi_j}{\partial x} dx dy \quad (3.06)$$

$$S12_{ij} = \iint_{\Omega_e} \frac{\partial \varphi_i}{\partial x} \frac{\partial \varphi_j}{\partial y} dx dy \quad (3.07)$$

$$S22_{ij} = \iint_{\Omega_e} \frac{\partial \varphi_i}{\partial y} \frac{\partial \varphi_j}{\partial y} dx dy \quad (3.08)$$

$$S1_{ij} = \iint_{\Omega_e} \varphi_i \frac{\partial \varphi_j}{\partial x} dx dy \quad (3.09)$$

$$S2_{ij} = \iint_{\Omega_e} \varphi_i \frac{\partial \varphi_j}{\partial y} dx dy \quad (3.10)$$

$$F_{1i}^e = \int_{\Gamma_e} \varphi_i (\sigma_{11} n_x + \sigma_{12} n_y) d\Gamma^e \quad (3.11)$$

$$F_{2i}^e = \int_{\Gamma_e} \varphi_i (\sigma_{12} n_x + \sigma_{22} n_y) d\Gamma^e \quad (3.12)$$

and the vectors $\{u^e\}, \{v^e\}, \{\tau_{11}^e\}, \{\tau_{12}^e\}$ and $\{\tau_{22}^e\}$ representing the values of the velocities and the stresses at the N nodes of the element. Equations 3.04 and 3.05 are used in place of the equations of motion in the subsequent chapters for the numerical simulation of the viscoelastic flows. In the assembly process they contribute to the global stiffness matrix 2N linear equations and 5N unknowns (the nodal values of the five field variables). The 3N equations that are still needed for the solution of the system, come from the constitutive equation. Finally, in the above equations, in order to include or not the retardation term, η_2 should take either a finite value or zero.

3.2 Galerkin Weak Form of the Constitutive Equations

The Galerkin weak form of the several constitutive equations is outlined in this chapter. Only basic considerations are presented here and all the intermediate steps are omitted. For more details, the reader should look at the book by Crochet et al [19] or others. Also in this chapter, only the viscoelastic part of the stress tensor is regarded, because the retardation term participates only in the equation of motion when the formulation presented here is used.

3.2.1 Upper Convected Maxwell Model

The equations of the UCM model were given in ch. 2.3.3.1:

$$\underline{\tau} + \lambda \underline{\tau}_{(1)} = \eta_1 \dot{\underline{\gamma}} \quad (2.80)$$

Replacing the upper convected derivative in this equation, the upper convected Maxwell model becomes:

$$\underline{\tau} + \lambda \left[\frac{\partial \underline{\tau}}{\partial t} + \vec{u} \cdot \nabla \underline{\tau} - ((\nabla \vec{u})^t \cdot \underline{\tau} + \underline{\tau} \cdot \nabla \vec{u}) \right] - \eta_1 \dot{\underline{\gamma}} = 0 \quad (3.13)$$

This equation is not linear and cannot be expressed in the same form as equations 3.04 and 3.05. To solve this nonlinear problem an iterative technique is used. At each iteration the velocities and their derivatives in the nonlinear terms are replaced with their values from the previous iteration. So at each iteration the system becomes linear and can be solved. The iterations continue until the change between two successive iterative solutions is less than a specified amount.

To implement this technique on eq. 3.13, one writes the weak form without replacing u and v or their derivatives in the non-linear terms with their approximations. Since there are only first order derivatives in this equation, the divergence theorem is not needed. Then, Galerkin's weak form of equation 3.13 finally becomes:

$$-2\eta_1[S1]\{u^e\} + [S] + \lambda[S1U] + [S2V] - 2[SU1]\{\tau_{11}^e\} - 2\lambda[SU2]\{\tau_{12}^e\} = 0 \quad (3.14)$$

$$-\eta_1[S2]\{u^e\} - \eta_1[S1]\{v^e\} - \lambda[SV1]\{\tau_{11}^e\} + [S] + \lambda[S1U] + [S2V]\{\tau_{12}^e\} - \lambda[SU2]\{\tau_{22}^e\} = 0 \quad (3.15)$$

$$-2\eta_1[S2]\{v^e\} - 2\lambda[SV1]\{\tau_{12}^e\} + [S] + \lambda[S1U] + [S2V] - 2[SV2]\{\tau_{22}^e\} = 0 \quad (3.16)$$

with the matrices S, S1U, S2V etc. defined as:

$$S_{ij} = \iint_{\Omega_e} \varphi_i \varphi_j \, dx \, dy \quad (3.17)$$

$$S1U_{ij} = \iint_{\Omega_e} \varphi_i \frac{\partial \varphi_j}{\partial x} u_{pr} \, dx \, dy \quad (3.18)$$

$$S2U_{ij} = \iint_{\Omega_e} \varphi_i \frac{\partial \varphi_j}{\partial y} u_{pr} \, dx \, dy \quad (3.19)$$

$$S1V_{ij} = \iint_{\Omega_e} \varphi_i \frac{\partial \varphi_j}{\partial x} v_{pr} \, dx \, dy \quad (3.20)$$

$$S2V_{ij} = \iint_{\Omega_e} \varphi_i \frac{\partial \varphi_j}{\partial y} v_{pr} \, dx \, dy \quad (3.21)$$

$$SU1_{ij} = \iint_{\Omega_e} \varphi_i \varphi_j \left(\frac{\partial u}{\partial x} \right)_{pr} dx dy \quad (3.22)$$

$$SU2_{ij} = \iint_{\Omega_e} \varphi_i \varphi_j \left(\frac{\partial u}{\partial y} \right)_{pr} dx dy \quad (3.23)$$

$$SV1_{ij} = \iint_{\Omega_e} \varphi_i \varphi_j \left(\frac{\partial v}{\partial x} \right)_{pr} dx dy \quad (3.24)$$

$$SV2_{ij} = \iint_{\Omega_e} \varphi_i \varphi_j \left(\frac{\partial v}{\partial y} \right)_{pr} dx dy \quad (3.25)$$

where the subscript *pr* denotes that the terms are evaluated from the results of the previous iteration. The other matrices are defined in eq. 3.06 - 3.10.

3.2.2 White Metzner Model

As it was stated in ch. 2.3.3.2, the White Metzner model is an empirical modification of the upper convected Maxwell model with variable viscosity and relaxation time coefficients. In this work a Carreau model:

$$\eta(\dot{\gamma}) = \eta_0 \left(1 + (m\dot{\gamma})^2 \right)^{\frac{n-1}{2}} \quad (3.26)$$

was adopted for the viscosity coefficient. For the relaxation time, a polynomial of $\log(\dot{\gamma})$ was adopted:

$$\lambda(\dot{\gamma}) = a + b \log(\dot{\gamma}) + c (\log \dot{\gamma})^2 \quad (3.27)$$

All the constants of the two functions were evaluated by curve fitting data of polymeric melts, as it will be described in chapter 4.1.

The magnitude of the rate of deformation tensor, which is the argument of the functions of the viscosity and the relaxation time coefficients, is based on the second invariant $II_{\dot{\gamma}}$ of this tensor, which is given as:

$$II_{\dot{\gamma}} = \sum \dot{\gamma}_{\alpha\beta} \dot{\gamma}_{\alpha\beta} \quad (3.28)$$

where $\dot{\gamma}_{\alpha\beta}$ are the components of $\dot{\gamma}$ and involve the derivatives of the velocity with respect to space.

In 2-D, the argument $\dot{\gamma}$ of the functions $\eta_1(\dot{\gamma})$ and $\lambda(\dot{\gamma})$ is:

$$\dot{\gamma} = \sqrt{\frac{1}{2} II \dot{\gamma}} = \sqrt{2\left(\frac{\partial u}{\partial x}\right)^2 + 2\left(\frac{\partial v}{\partial y}\right)^2 + \left(\frac{\partial u}{\partial y} + \frac{\partial v}{\partial x}\right)^2} \quad (3.29)$$

The final equations of the White Metzner model, therefore, include all the linear and non-linear terms that were found in the UCM model with the addition of the functions in equations 3.26 and 3.27 instead of the constants η_1 and λ . These functions introduce more non-linearity in the equations, which are dealt with in the same manner as the non-linearities introduced by the convected derivative. Namely, the derivatives of the velocities in equation 3.28 are calculated from the values of the variables at the previous iteration and from them the values of the viscosity and the relaxation time are found and replaced in equations 3.14 to 3.16.

3.2.3 Leonov-Like and Giesekus Models

The Leonov-like equation may be seen as a special case of the Giesekus model (eq. 2.87) or as an extension of the upper convected Maxwell model (eq. 2.80) with the addition of a quadratic term in the stress:

$$\underline{\tau} + \lambda \underline{\tau}_{(1)} + \frac{\lambda}{2\eta_1} \{\underline{\tau} \cdot \underline{\tau}\} = \eta_1 \dot{\underline{\gamma}} \quad (3.30)$$

From this equation it can be seen that, in addition to the non-linear terms due to the convective derivative, there is a new type of non-linearity introduced. This non-linearity now involves terms that include only stresses. In order to linearize the problem to solve the system of equations one has to calculate not only the values of the velocities from the previous iteration, but also the values of the stresses. So in the place of such a quadratic term there will be a coefficient matrix and the vector of the nodal values as in equations 3.14 to 3.16, but the integrals in the coefficients are now calculated not only from the values of the velocities but also from the stresses at the previous step.

The Giesekus model has an adjustable parameter α instead of the 1/2 at the coefficient of the quadratic term of eq. 3.30, which depends on the material. This model then is:

$$\underline{\tau} + \lambda \underline{\tau}_{(1)} + \alpha \frac{\lambda}{\eta_1} \{\underline{\tau} \cdot \underline{\tau}\} = \eta_1 \dot{\underline{\gamma}} \quad (3.31)$$

Following the steps described above, the Galerkin weak form of the the equations of Giesekus or the Leonov-like (with $\alpha = 1/2$) model, in the case of two dimensions becomes:

$$\begin{aligned}
-2\eta_1[S1]\{u^e\} + \left[[S] + \lambda[S1U] + [S2V] - 2[SU1] \right] + \alpha \frac{\lambda}{\eta_1}[ST11] \left\{ \tau_{11}^e \right\} \\
- \left[2\lambda[SU2] - \alpha \frac{\lambda}{\eta_1}[ST12] \right] \left\{ \tau_{12}^e \right\} = 0
\end{aligned} \tag{3.32}$$

$$\begin{aligned}
-\eta_1[S2]\{u^e\} - \eta_1[S1]\{v^e\} - \left[\lambda[SU2] - \alpha \frac{\lambda}{\eta_1}[ST12] \right] \left\{ \tau_{11}^e \right\} + \left[[S] + \lambda[S1U] + [S2V] \right] \left\{ \tau_{12}^e \right\} \\
- \left[\lambda[SU2] - \alpha \frac{\lambda}{\eta_1}[ST12] \right] \left\{ \tau_{22}^e \right\} = 0
\end{aligned} \tag{3.33}$$

$$\begin{aligned}
-2\eta_1[S2]\{v^e\} - \left[2\lambda[SV1] - \alpha \frac{\lambda}{\eta_1}[ST12] \right] \left\{ \tau_{12}^e \right\} + \\
\left[[S] + \lambda[S1U] + [S2V] - 2[SV2] \right] + \alpha \frac{\lambda}{\eta_1}[ST22] \left\{ \tau_{22}^e \right\} = 0
\end{aligned} \tag{3.34}$$

with the matrices ST11, ST12, ST22 defined as:

$$ST11 = \iint_{\Omega_e} \varphi_i \varphi_j \tau_{11pr} dx dy \tag{3.35}$$

$$ST12 = \iint_{\Omega_e} \varphi_i \varphi_j \tau_{12pr} dx dy \tag{3.36}$$

$$ST22 = \iint_{\Omega_e} \varphi_i \varphi_j \tau_{22pr} dx dy \tag{3.37}$$

and the other matrices as defined previously.

3.2.4 Phan-Thien Tanner and Johnson Segalman Models

The equations that describe the PTT model were given in ch. 2.3.2. For one relaxation mode this equation in its expanded form becomes:

$$\exp\left(\frac{\varepsilon \lambda}{\eta_1} t r \underline{\tau}\right) \underline{\tau} + \lambda \underline{\tau}_{(1)} + \frac{\lambda \xi}{2} (\dot{\underline{\gamma}} \cdot \underline{\tau} + \underline{\tau} \cdot \dot{\underline{\gamma}}) = \eta_1 \dot{\underline{\gamma}} \tag{3.38}$$

where the exponential form (eq. 2.64) of the function $H(tr\underline{\tau})$ was adopted. The exponential term that is included in this equation introduces again some non-linearity, which is dealt with in the same manner as the quadratic terms in the stress in the Leonov-like model. Here the term $\exp(tr\underline{\tau})$ is calculated from the previous iteration before the calculation of the Galerkin integrals. Other non-linear terms in this model include the $\dot{\underline{\gamma}} \cdot \underline{\tau}$ and $\underline{\tau} \cdot \dot{\underline{\gamma}}$ terms. It was chosen here to evaluate the components of $\dot{\underline{\gamma}}$ from the previous iteration and keep the stresses as nodal unknown values much the same as for the convected derivative terms. So the Galerkin weak form of the PTT model in 2-D becomes:

$$-2\eta_1[S1]\{u^e\} + [[SX] + \lambda[S1U] + [S2V] - 2(1 - \xi)[SU1]]\{\tau_{11}^e\} - \lambda [(2 - \xi)[SU2] - \xi[SV1]]\{\tau_{12}^e\} = 0 \quad (3.39)$$

$$-\eta_1[S2]\{u^e\} - \eta_1[S1]\{v^e\} - \frac{\lambda}{2}[(2 - \xi)[SV1] - \xi[SU2]]\{\tau_{11}^e\} + [[SX] + \lambda[S1U] + [S2V]]\{\tau_{12}^e\} - \frac{\lambda}{2}[(2 - \xi)[SU2] - \xi[SV1]]\{\tau_{22}^e\} = 0 \quad (3.40)$$

$$-2\eta_1[S2]\{v^e\} - 2\lambda[(2 - \xi)[SV1] - \xi[SU2]]\{\tau_{12}^e\} + [[SX] + \lambda[S1U] + [S2V] - 2(1 - \xi)[SV2]]\{\tau_{22}^e\} = 0 \quad (3.41)$$

with the matrices described as before and:

$$SX_{ij} = \iint_{\Omega_e} \varphi_i \varphi_j \exp\left[\frac{\varepsilon\lambda}{\eta_1} (\tau_{11pr} + \tau_{22pr})\right] dx dy \quad (3.42)$$

With $\varepsilon = 0$ (in which case $SX_{ij} = S_{ij}$) the above equations reduce to the Galerkin weak form of the equations of the Johnson Segalman model.

3.3 Shape Functions and Types of Elements

When choosing shape functions to approximate the field variables, one has to satisfy the "completeness" and the "conformity" requirements [16], in order to make sure that the approximate solution of the linear problem approaches the exact solution at very fine meshes (the convergence of the non-linear problem is of course another story). For a differential equation of order $2m$, the completeness requirement states that the derivatives of the field functions up to m th order should remain bounded as the size of the element goes to zero. For conformity, it is required that the $(m-1)$ th derivative remain continuous across the boundaries of the elements.

In the case of the flow problems that are described in this work, the maximum order ($2m$) of the derivatives of the velocities gives $m = 1$, while for the stresses and the pressure $m = 1/2$. Therefore, linear shape functions for all variables will satisfy both requirements. However, it was found [19] that in the mixed formulation of problems of viscoelastic flow, the same order of approximation polynomials for both the velocity and the pressure leads to unstable solutions for the pressure. In fact most of the elements that have been used successfully in such formulation had shape functions one order higher for the velocities (quadratic) than for the pressure (linear) [19].

The above problem is easily bypassed when one uses the penalty formulation. Here the pressure is not explicitly a variable and the choice for the approximation functions for all the field variables (the components of the velocity and the stress) is greater. Indeed in this case, linear

interpolation polynomials can be used for all five field variables, as well as quadratic etc. In this work either linear or quadratic shape functions were used to approximate all the variables in the FEM-penalty formulation.

For the discretization of the domain, either triangular or quadrilateral elements can be used. There is no certain advantage of using one type of elements or the other. In this work only quadrilateral elements were used: 4-node bi-linear quadrilateral elements with the nodes at the four corners or 8-node bi-quadratic serendipity elements with nodes 5 to 8 at the midsides.

In order to facilitate the calculations of the element stiffness matrices and make the program more flexible, isoparametric elements were used. By this method all the elements are transformed to square parent elements with dimensions from -1 to 1. Then all the calculations could be done in this simple parent element and then transformed back to the original by the following transformation:

$$x = \sum \pi_i(\xi, \eta) x_i \quad (3.43)$$

$$y = \sum \pi_i(\xi, \eta) y_i \quad (3.44)$$

$$U_\alpha = \sum \pi_i(\xi, \eta) U_{\alpha i} \quad (3.45)$$

where x_i, y_i are the global nodal coordinates, the shape functions π_i are now expressed only in the local variables ξ and η ($\xi, \eta \in [-1, 1]$), and U_α represents the field variables (i.e. $u, v, \tau_{11}, \tau_{12}$ and τ_{22}).

For bi-linear isoparametric elements, the shape functions are:

$$\pi_i = (1 + \xi \xi_i)(1 + \eta \eta_i) \quad \text{no summation over } i \quad (3.46)$$

with ξ_i and η_i the local coordinates of the nodes of the parent element:

$$\begin{array}{ll} \xi_1 = -1 & \eta_1 = -1 \\ \xi_2 = +1 & \eta_2 = -1 \\ \xi_3 = +1 & \eta_3 = +1 \\ \xi_4 = -1 & \eta_4 = +1 \end{array}$$

For the serendipity element, the shape functions are:

$$\psi_i = \frac{1}{4}(1 + \xi \xi_i)(1 + \eta \eta_i)(\xi \xi_i + \eta \eta_i - 1) \quad \text{for nodes 1 to 4 (no summation over } i) \quad (3.47)$$

$$\psi_i = \frac{1}{2}(1 - \xi^2)(1 + \eta \eta_i) \quad \text{for nodes 5 and 7} \quad (3.48)$$

$$\psi_i = \frac{1}{2}(1 - \eta^2)(1 + \xi \xi_i) \quad \text{for nodes 6 and 8} \quad (3.49)$$

with ξ_i, η_i ($i = 5, \dots, 8$) the local coordinates of the midsides of the parent element:

$$\begin{array}{ll}
\xi_5 = 0 & \eta_5 = -1 \\
\xi_6 = 1 & \eta_6 = 0 \\
\xi_7 = 0 & \eta_7 = 1 \\
\xi_8 = -1 & \eta_8 = 0
\end{array}$$

Following the transformation of the coordinates, the derivatives and the integrals must also be transformed. The calculation of the derivatives of φ_i with respect to x and y make use of the Jacobian of the transformation:

$$J = \begin{bmatrix} \frac{\partial x}{\partial \xi} & \frac{\partial y}{\partial \xi} \\ \frac{\partial x}{\partial \eta} & \frac{\partial y}{\partial \eta} \end{bmatrix} = \begin{bmatrix} \sum \frac{\partial \pi_i}{\partial \xi} x_i & \sum \frac{\partial \pi_i}{\partial \xi} y_i \\ \sum \frac{\partial \pi_i}{\partial \eta} x_i & \sum \frac{\partial \pi_i}{\partial \eta} y_i \end{bmatrix} \quad (3.49)$$

$$\text{Then } \begin{bmatrix} \frac{\partial}{\partial x} \\ \frac{\partial}{\partial y} \end{bmatrix} = [J]^{-1} \begin{bmatrix} \frac{\partial}{\partial \xi} \\ \frac{\partial}{\partial \eta} \end{bmatrix} \quad (3.51)$$

Also the differential $dA = dxdy$ is transformed in the same way:

$$dxdy = |J| d\xi d\eta \quad (3.52)$$

Now the limits of the integration for the integrals in equations 3.04 to 3.41 become -1 and 1 for both independent variables. However, with the substitution of φ_i and their derivatives with π_i, ψ_i etc. from equations 3.42 to 3.52, the functions under the integrals become quite complicated and analytical integration may not be possible. For this reason numerical integration is performed. Four point Gauss quadrature was used for the linear elements and nine point quadrature for the quadratic elements for all the integrals except the ones that came from the penalty terms, where reduced integration is required for non-trivial solutions according to what was said in ch. 2.2.1. For these terms, the numerical integration was carried out at one order lower (1 point for the linear elements and 4 points for the quadratic) than the other terms.

3.4 Boundary Conditions

3.4.1 Natural and Essential Boundary Conditions

There are two types of boundary conditions in the problems that are described in this work and each has a different way to be treated in the finite element method. These are the "natural" and

the "essential" boundary conditions. In this chapter, it will be described how each of them is implemented in the calculations of the viscoelastic flows.

The "natural" boundary conditions will give the value of the global vectors \vec{F}_1 and \vec{F}_2 as boundary forces acting on the fluid. As such, they can be incorporated in the right hand side vector of the global system of equations to be solved for the unknown nodal values. (The vectors \vec{F}_1 and \vec{F}_2 cancel on the inter-element boundaries because of their opposite signs between adjacent elements. However, on the sides of the elements that lie on a boundary, these vectors do not cancel)

The second type of boundary conditions are the "essential" boundary conditions (the most common), where the values of the field variables are given at some points (nodes) on the boundary. Since some degrees of freedom at these nodes are specified, the equations that correspond to these nodes can be drawn out of the system or replaced by the trivial equation $U^i = U^i_{spec}$. In this way one also overcomes the problem of defining the non zero effective global force vector at these points. The value of this vector can be calculated from the original equation when all the field variables are known.

Using the penalty method, the two dimensional flow problem has five unknown field variables: two components of the velocity and three components of the stress tensor. The differential equations are second order for the velocities and first order for the stresses. It is necessary, then, to define boundary conditions for the velocities at all the boundaries of the domain and for the stresses at only one point. There were three different types of boundaries in the flows that were studied here: inlet and outlet surfaces, wall boundaries and flow centerlines (planes of flow symmetry).

Since all the flows that were studied in this work included inlet and outlet flow conditions, a fully developed velocity profile was assumed as the boundary condition at points far away from any disturbance such as the hole or the contraction etc. This assumption implies the knowledge of the previous flow history of the viscoelastic fluid element and it is necessary because the fluid has "memory". The assumption holds, however, only if the distance between the inlet or outlet surface and the disturbance is infinite. Of course, infinite meshes cannot be implemented in a numerical scheme and the condition of a "far enough" undisturbed region has to be assumed. A discussion of how far this undisturbed region should be, is given in [72]. The entry and the exit planes in the present work were placed at a distance of twice the die height or larger. The calculation of the flow profile in the inlet/outlet conditions was not a trivial task for the viscoelastic fluids and it will be

described in the following section. The values of both velocity components were specified at both the upstream and the downstream ends of the mesh.

For the walls, the no slip condition was assumed. The velocities of the fluid were given there the same value as the velocity of the wall (if any). At the centerline, symmetry conditions were used. One component of the velocity and the force vector of the other were set to zero there. Finally, values of the stress tensor were specified at the inlet surface.

3.4.2 Calculation of the Velocity Profiles in the Inlet and Outlet Planes

The velocity and the stress profiles at the inlet and outlet of the flow domain were calculated as a separate one dimensional problem of pressure driven flow between two infinite plates. An analytical solution for such flow exists for the upper convected Maxwell fluid (identical velocity profile as the Newtonian fluid) and could be used in that case. For all the other models the analytical solution was not possible and a numerical method was used. For such a flow ($u = u(y)$, $v = 0$), assuming that the pressure changes linearly along the flow direction (x) and the stresses depend only on y , the equation of motion gives:

$$\tau_{xy} = - \frac{\Delta P}{L} y \quad (3.53)$$

Assuming that the equations, which give the viscosity for simple shear flow, are still valid for the flow in question and treating the fluid as a Generalized Newtonian Fluid with these equations as the non-newtonian viscosity functions, the shear rate can be calculated by solving the following equation (in general numerically) as a function of y :

$$\tau_{12} = \eta(\dot{\gamma})\dot{\gamma} \quad (\dot{\gamma} = \frac{du}{dy}) \quad (3.54)$$

The velocity profile can then be found by (numerically) integrating the shear rate:

$$u = \int_0^y \dot{\gamma}(y) dy \quad (3.55)$$

The normal stresses can be finally calculated from the shear rate $\dot{\gamma}$ by expressions similar to the equations (2.51), (2.52) etc.:

For the UCM model the normal stresses become:

$$\tau_{11} = 2\eta_1 \lambda \dot{\gamma}^2 \quad (3.56)$$

$$\tau_{22} = 0 \quad (3.57)$$

For the White Metzner model they are:

$$\tau_{11} = 2\eta_1(\dot{\gamma})\lambda(\dot{\gamma})\dot{\gamma}^2 \quad (3.58)$$

$$\tau_{22} = 0 \quad (3.59)$$

For the PTT model one has:

$$\tau_{11} = \frac{\eta_1\lambda(2 - \xi)\dot{\gamma}^2}{1 + \xi(2 - \xi)\lambda^2\dot{\gamma}^2} \quad (3.60)$$

$$\tau_{22} = \frac{-\eta_1\lambda\xi\dot{\gamma}^2}{1 + \xi(2 - \xi)\lambda^2\dot{\gamma}^2} \quad (3.61)$$

Finally, the Leonov-like model gives:

$$\tau_{11} = \frac{\eta_1}{\lambda} \left(\frac{\sqrt{2} x_k}{\sqrt{1 + x_k}} - 1 \right) \quad (3.62)$$

$$\tau_{22} = \frac{\eta_1}{\lambda} \left(\frac{\sqrt{2}}{\sqrt{1 + x_k}} - 1 \right) \quad (3.63)$$

$$\text{with } x_k = \sqrt{1 + 4\lambda^2\dot{\gamma}^2}$$

3.5 Further Considerations for a Computer Program to Solve Flow Problems by the FEM

In the previous chapters were described the forms of the element stiffness matrices, the specific types of the elements and shape functions and the boundary conditions that were used in this work. In the following, a few details about the assembly of the elements, the solving of the system and the post-processing calculations that were done will be mentioned.

3.5.1 Assembly of the Elements and Solution of the System

The assembly of the elements takes place after the calculation of each element stiffness matrix and before the implementation of the boundary conditions. In this step the corresponding entries in the global stiffness matrix and the right hand side vector are updated by the addition of the components of the element stiffness matrix and the force vector. In this way the element stiffness matrices did not have to be stored, with the corresponding economy of computer space.

The resulting global stiffness matrix was banded and asymmetric and was stored in an array with dimensions of the total number of equations by the bandwidth of the matrix. To further fa-

cilitate the transfer of the data in the arrays, the right hand side vector was stored as the last column of this array. To invert the stiffness matrix stored in such a manner, a routine was developed that uses the Gaussian elimination. The solution vector was in turn stored as the last column of the array that used to carry the global stiffness matrix before the inversion.

3.5.2 The Iterative Scheme

It was mentioned in ch. 3.2.1 that an iterative technique was used to deal with the non-linearities in the equations of the system introduced by the non-linear constitutive models. In this chapter this iterative technique will be described.

The non-linear terms in the equations of the problem may have one of the forms: $\mu_{\alpha}\tau_{\beta\gamma}$ or $\mu_{\alpha,\beta}\tau_{\gamma\delta}$ or $\tau_{\alpha\beta}\tau_{\gamma\delta}$ or they may also have the form $\exp(\tau_{11} + \tau_{22})\tau_{\alpha\beta}$. There are also the non-linear terms from the viscosity and the relaxation time function of the White Metzner or the GNF models. There are, therefore, a few choices of how to linearize the non-linear problem. So, it was chosen here to express the viscosity and the relaxation time functions, as well as the exponential function above, in terms of the values of the variables that were calculated at a previous iteration. In the first cases above, it was chosen that μ_{α} and $\mu_{\alpha,\beta}$ were expressed in terms of the results of the previous iterative step. Finally, in the case of the quadratic in stresses term or the exponential term, there is no choice but to express one of the stresses in terms of the results of the previous step. After all these substitutions were made, the system became linear and could be solved. When the next solution was calculated, the results were compared with the previous solution vector. If the method had not converged yet, new substitutions would take place and another iteration would start until the method converged to the final solution.

The linearization of the non-linear terms in the way described above constitutes the so called "simple" or Picard iteration scheme. In order to accelerate the convergence of such technique the following formula may be used for the evaluation of the variables in iteration $i + 1$ from the previous iterations:

$$U^{i+1} = \beta U^i + (1 - \beta)U^{i-1} \quad (3.64)$$

In this equation β is the "acceleration" parameter ($0 < \beta \leq 1$), the value of which should be chosen so that it optimizes the rate of convergence. Values for β used in this work were 0.8 and 1. In order

to start the iterations, the Newtonian model was used, for which the problem is linear. The results of the Newtonian iteration and $\beta = 1$ were used as first guess ($i = 1$) for the above formula.

3.5.3 Post Processing Calculations

When the iterations of the method converge, the calculations for the nodal values of the field variables will have been finished. Then, there takes place the post processing step. In this step the two parts of the stresses (the viscoelastic part $\tau_{\alpha\beta}^1$ and the retardation term $\tau_{\alpha\beta}^2$ of eq. 2.76) are added together to calculate the values of the total extra stress tensor. The pressure is also calculated in this step. Then the results of the calculations can be printed. Finally the stream function and the values of the birefringence are calculated and can be plotted as contour plots.

In the formulation that was given in the previous chapters, the variable stresses that were calculated by the FEM are only the $\tau_{\alpha\beta}^1$ terms in equation 2.72 (the superscript 1 was not shown in the previous part of this chapter but it has to be shown again in this part to avoid confusion). In order to calculate the total extra stress ($\tau_{\alpha\beta} = \tau_{\alpha\beta}^1 + \tau_{\alpha\beta}^2$), the retardation terms ($\tau_{\alpha\beta}^2 = \eta_2 \dot{\gamma}_{\alpha\beta}$) are calculated from the approximation functions at each node of each element and then added to the nodal value of $\tau_{\alpha\beta}^1$.

Because of the penalty formulation, the pressure is not a primitive unknown in the FEM calculations. It is, therefore, calculated in the post-processing step. Since the velocity field is now known, the pressure can be calculated from equation 2.26:

$$P = -\gamma_p \left(\frac{\partial u}{\partial x} + \frac{\partial v}{\partial y} \right)$$

In a 2-D flow domain, the birefringence is related to the shear and the normal stresses by the following expression [11]:

$$\bar{N} = \frac{\lambda'}{WC} \sqrt{(\tau_{11} - \tau_{22})^2 + 4\tau_{12}^2} \quad (3.65)$$

where λ' is the wavelength of the laser beam passed through the flow domain along the third dimension, C is the stress optical coefficient and W is the thickness of the domain in the direction of the beam (Details about the theory from which this equation is derived should be looked in ref. [87]).

Finally the calculation of the stream function is done by solving the following equation [19]:

$$\frac{\partial^2 \Psi}{\partial x^2} + \frac{\partial^2 \Psi}{\partial y^2} = \frac{\partial u}{\partial y} - \frac{\partial v}{\partial x} \quad (3.66)$$

where $\Psi(x,y)$ is the stream function. The vorticity at the right hand side of this equation is evaluated from the known (calculated in the processing step) velocity field. The Galerkin weak form of equation 3.66, that is used in the FEM calculation is:

$$\iint_{\Omega_e} \left[\frac{\partial \phi_i}{\partial x} \frac{\partial \phi_j}{\partial x} + \frac{\partial \phi_i}{\partial y} \frac{\partial \phi_j}{\partial y} \right] dx dy \Psi_j^e = - \iint_{\Omega_e} \phi_i \left(\frac{\partial u}{\partial y} - \frac{\partial v}{\partial x} \right) dx dy + \int_{\Gamma_e} \phi_i \left[\frac{\partial \Psi}{\partial x} n_x + \frac{\partial \Psi}{\partial y} n_y \right] d\Gamma \quad (3.67)$$

Rewriting this equation in matrix notation it becomes:

$$[S11] + [S22](\Psi^e) = \{F_3^e\} + \{F_4^e\} \quad (3.68)$$

The matrices S11 and S22 are given in eq. 3.06 and 3.07. The vectors \vec{F}_3^e and \vec{F}_4^e are given in the following:

$$F_{3i}^e = - \iint_{\Omega_e} \phi_i \left(\frac{\partial u}{\partial y} - \frac{\partial v}{\partial x} \right) dx dy \quad (3.69)$$

$$F_{4i}^e = \int_{\Gamma_e} \phi_i \left(\frac{\partial \Psi}{\partial x} n_x + \frac{\partial \Psi}{\partial y} n_y \right) d\Gamma \quad (3.70)$$

This differential equation is solved using the same FEM algorithm that was used for the solution of the linearized problem with the necessary changes of the values of the internal parameters of the method. The boundary conditions for this calculation may, in principle be calculated from the results of the velocities and stresses calculation, if the value of Ψ is given at one point. However, in order to have more accurate results and make the program general and able to handle a greater variety of flow problems, it was chosen here to input the appropriate boundary conditions into the program, rather than have the program calculate them. These boundary conditions consist of the inlet and outlet plane conditions, where the value of Ψ is specified, the centerline, where $\Psi = \text{constant}$ and the walls, along which the stream function is also constant (Ψ is arbitrarily set equal to zero at one of the walls). To calculate the value of Ψ at the inlet or outlet planes, the following equation (coming directly from the definition of the stream function) is used:

$$\Psi = \Psi_0 + \int_0^s (u n_x - v n_y) ds' \quad (3.71)$$

Since the velocity profile is calculated for the inlet/outlet boundary conditions of the main calculations, the stream function can also be calculated at that step and be read into the program with the other boundary conditions.

3.6 The Structure of the Program *NONEWT.FEM*

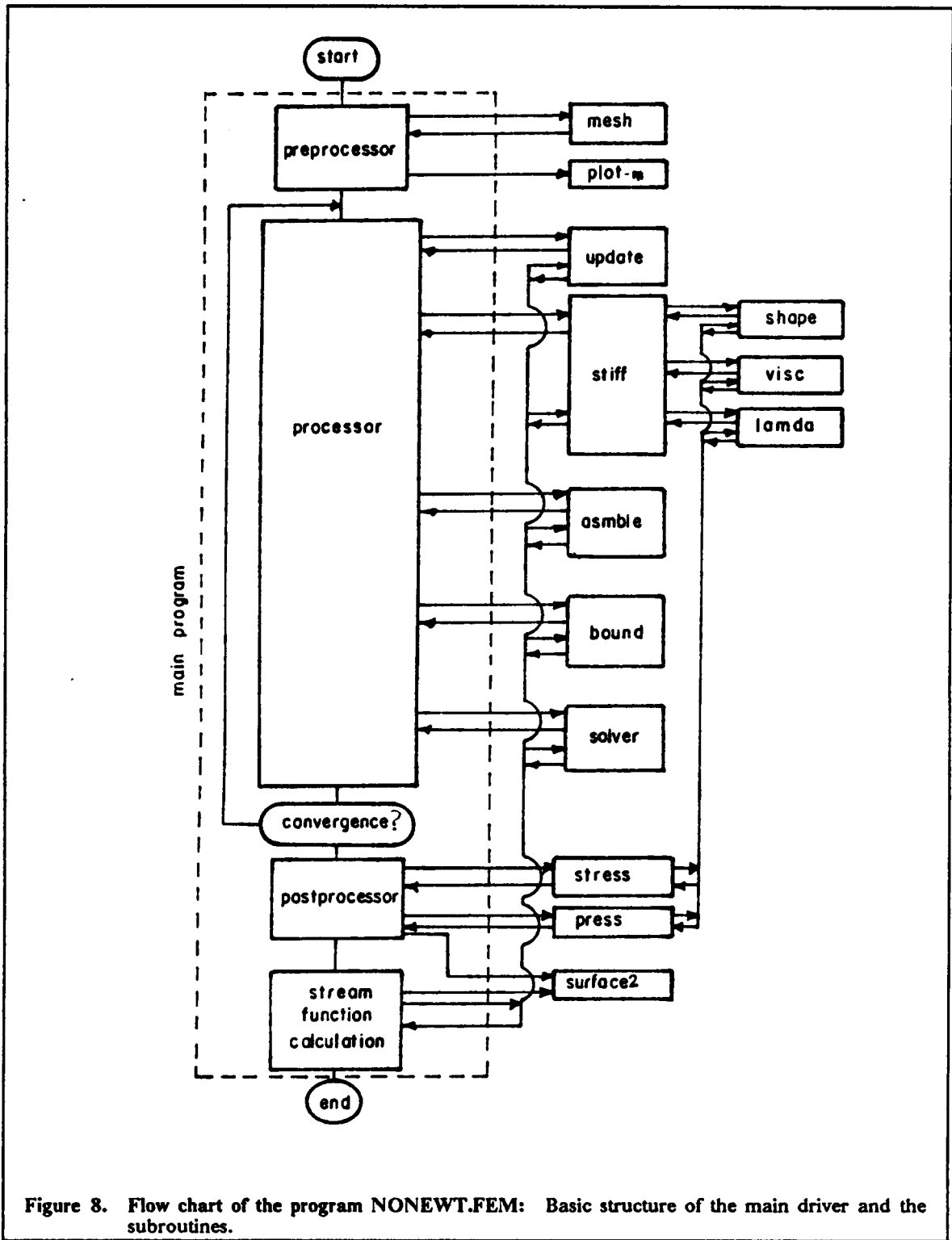
Following all that was described in the previous parts of this chapter, a FORTRAN computer program was developed to implement the finite element method to solve viscoelastic flow problems. The listing of the code is located in the appendix. In the appendix is also located a small guide for the use of the program. In the following, the basic structure of the program will be outlined.

NONEWT is a finite element code for the solution of two dimensional flow problems that can use a number of constitutive equations. The present computer algorithm is based on a model finite element program *FEM2D* developed by Reddy [17] for the solution of two-dimensional Newtonian flow problems. That program was altered for the inclusion of the five primitive field variables, which the viscoelastic finite element calculations require, and individual subroutines were added for the viscosity and relaxation time functions (for the White Metzner model). The subroutines that calculate the element matrices were also altered to accommodate the several rheological models and the extra variables and a routine to calculate the stream function and the birefringence was added to the main program.

The structure of the program consists of a main driver program that reads the data, initializes the variables and calls the several subroutines to do the calculations (Fig. 8). The main driver consists of four parts: The pre-processor, the processor, the post-processor and the stream function calculation. In the following, these four parts are described. In the final part of this chapter is given a brief description of the subroutines that the program uses.

3.6.1 Pre-Processor

The pre-processor is logically located at the beginning of the code. It reads and checks the data, initializes the arrays, calculates a few preliminary parameters such as the bandwidth of the global stiffness matrix, prints the echo of part of the input and plots the mesh by calling the subroutine *MPLLOT*. It also sets the internal variables that are needed to distinguish between the different constitutive models in the subsequent calculations.



In terms of the construction of the mesh, the program gives two options. Either the program generates a rectangular mesh from a minimum amount of input data (by calling the subroutine MESH) or the user inputs the data for the mesh. These data consist of the connectivity array and the coordinates of the nodes. The connectivity array NOD(N,I) is used to relate the local with the global node numbers. The value of NOD(N,I) gives the global number of the local node I of the element N (the range for the values of I is 1 to 4 for the linear and 1 to 8 for the quadratic elements). This is a very important array and is used in many subsequent steps to relate local (element level) to global quantities.

3.6.2 Processor

The role of the processor unit is to linearize the problem, calculate all the element stiffness matrices, assemble them, implement the boundary conditions and solve the linear system (for the velocities and the stresses). It includes a loop over all the elements, in each step of which it calls the subroutine UPDATE to update the vector of the solution with the results from the previous iteration, then it calls STIFF to calculate the element stiffness matrix of the current element and the subroutine ASMBLE to incorporate the components of this matrix into the appropriate positions of the global stiffness matrix. When the loop over the elements is over, the boundary conditions are incorporated in subroutine BOUND and the linear system is solved in subroutine SOLVER.

3.6.3 Post-Processor

When the linear system has been solved, the post-processor will check the relative change between the previous and the current solution and compare this change to the specified tolerance. This relative change is specified here as follows:

$$\frac{\sum(U^i - U^{i-1})^2}{\sum(U^i)^2} < (TOL)^2 \quad (3.71)$$

The parameter TOL is read with the data. Values of TOL between 0.1 and 0.01 give acceptable results.

If the criterion in eq. 3.71 is not met, execution is transferred to the beginning of the processor unit for the next iteration. When the tolerance is satisfied, the unit calculates and adds the retarda-

tion terms in the subroutine STRESS, calculates the pressure and the birefringence and prints the results in two parts: First it prints the nodal values of the velocities and the stresses and then it prints the pressure, velocity gradients, the viscosity, the vorticity etc in the element level. The program will stop there if no boundary conditions for the stream function have been entered, giving an error message. Otherwise it will go to the next step, which is the stream function calculation.

3.6.4 Stream Function Calculation

This final part of the code is a scaled down version of the processor because the stream function calculation uses the same finite element method, but with only one variable and a simpler element stiffness matrix (eq. 3.67). The number of the degrees of freedom is, therefore, changed, the bandwidth is decreased and a different element stiffness matrix is calculated. The problem now is linear and no iterations are needed. The last part of the code, therefore, does these changes of the parameters needed by the subroutines and calls again the subroutines UPDATE, STIFF, and ASMBLE for each element and BOUND and SOLVER for the solution of the global system in the same way as in the processor. Then it prints the values of the stream function for each node. When all the calculations have been finished, the program will link to the commercial routine SURFACE2 [91] to plot the contour of the birefringence (as fringes with whole order) and the streamlines.

3.6.5 Description of the Subroutines of NONEWT

There are 10 subroutines with different functions in the program NONEWT. Each of them is described in the following.

MESH is a subroutine that will construct a mesh. In the current version of NONEWT, subroutine MESH will construct meshes for rectangular domains only. It may use linear or quadratic elements. It will number the nodes along the 'x' direction and return both the connectivity array and the coordinates of the nodes. For most cases, when the domain is not rectangular, this subroutine cannot be used and the mesh data have to be input with the other data of the problem.

MPLOT is a subroutine that will plot the mesh using the VERSATEC or the CALCOMP plotter [93]. It will also print the global node number at each node on the plot.

STIFF This subroutine calculates the element stiffness matrix. Depending on the value of the parameter ISTR, it is used on either the calculation of the velocities and the stresses (ISTR=0) or in the calculation of the stream function (ISTR=1) (at the post-processing step). In the first case, depending on the value of the parameter MODEL, it will return the stiffness matrix of the current element using one of the six rheological models or the Newtonian model. For the calculations it uses the appropriate equations from the set of eq. 3.06 to 3.42. It calls the subroutine SHAPE to calculate the shape functions at each one of the Gauss points. In the case of the White Metzner model or the Generalized Newtonian Fluid it also calls the subroutines VISC and LAMDA to calculate the variable viscosity and relaxation time from the shear rate.

SHAPE is a subroutine that calculates the shape functions (eq. 3.46 to 3.49) and their derivatives for an isoparametric quadrilateral element at a given point (ξ, η) . It will return the derivatives transformed back to the original space (x,y) , as well as the Jacobian of the transformation. It has the options of using either bi-linear or bi-quadratic (serendipity) elements.

VISC calculates the viscosity η_1 as a function of the magnitude of the rate of the deformation tensor for the GNF or the White Metzner models. In the current version it uses a power law or a Carreau model.

LAMDA calculates the value of the relaxation time λ as a function of the magnitude of the rate of deformation tensor for the White Metzner model. The form of the function of $\lambda(\dot{\gamma})$ depends on the material and must be given by the user.

UPDATE updates the non-linear terms by saving the solution of the previous iteration and transferring it to the next (look at ch. 3.5.2 for details).

ASMBLE This subroutine is called directly after the calculation of every element stiffness matrix. It adds the components of this matrix to the appropriate components of the global stiffness matrix. To do so it uses the connectivity array $NODE(N,I)$. It returns the global stiffness matrix as a $NEQ \times NBW$ array, where NEQ is the total number of equations in the system and NBW is the bandwidth of the banded global stiffness matrix. The last column of the array contains the right hand side vector of the global system.

BOUND incorporates the boundary conditions according to ch. 3.4. It does not eliminate the equations that correspond to the specified degrees of freedom but rather it replaces them by the trivial equations $U^i = U^i_{spec}$. It also updates the right hand side vector for the natural boundary conditions in the last column of the array that contains the global stiffness matrix.

SOLVER solves the global linear system. It uses Gaussian elimination. It has, therefore, to check for zeros in the diagonal. If a zero is encountered, the program is stopped and an error message is issued. It uses a banded asymmetrical matrix and returns the solution vector as the last column of the original array.

PRESS is used in the post processor to calculate the pressure in the center of the quadrilateral using the penalty parameter. It calls **SHAPE** to calculate the derivatives of the shape functions. It also calculates other quantities at the center of the elements as the shear rate, the viscosity the relaxation time and the extension rate.

STRESS is also used in the post processor. It calculates the retardation terms and adds them to components of the stresses. It calls **SHAPE** for the calculation of the shape functions and **VISC** and **LAMDA** (if needed) for the calculation of the viscosity and the relaxation time.

A few system subroutines are also called in the course of the program, to estimate time consumption and plot the mesh. These are **:TIMEON**, and **TIMECK**, which calculate elapsing time and **PLOTS**, **PLOT**, **LINE**, **FACTOR**, **SCALE** and **SYMBOL**, which instruct the plotter. Details

for these subroutines should be looked at the manuals of the IBM computer and the VERSATEC/CALCOMP plotters.

3.6.6 Auxiliary Programs Used in the Calculations

Two other programs were used in the course of the numerical calculations in this work. One was developed by the author to integrate the 1-D problem of eq. 3.53-3.55 (flow in a slit die) for the calculation of the boundary conditions of the 2-D FEM problem. The other was developed by D. Pelletier [93] and was used to construct 2-D irregular meshes from a minimum amount of input data.

The first program (INIT) is a FORTRAN routine that integrates eq. 3.54, 3.55 and 3.71 for the five models and calculates the viscosity, the shear stress, the two normal stresses and the value of the stream function as a function of the distance from the centerline of the slit die. It uses a simple Simpson rule for the integration and 200 points equally spaced along y . GEN2D constructs an irregular mesh with linear or higher order elements. The user inputs the rough outline of the flow domain in the form of 8-nodded quadratic super elements that cover the whole domain. The spacing of the nodes may be made non-uniformly. The code returns the Boolean matrix-NOD(I,J), as well as the coordinates of the nodes in the generated mesh. Further details for this routine can be found in the GEN2D manual [93].

4.0 Evaluation of the Parameters of the Models, Domain Dimensions and Meshes Used

The material that was used in the experimental verification of the results of the numerical simulation is described in this chapter. The viscometric properties of the material and the evaluation of the parameters of the rheological models to fit these properties is summarized here. The predictions of the models for the stress growth behaviour of the material is also described. The flow geometries simulated in this work and the meshes that were used to discretize them are also outlined in this chapter.

4.1 *Fit of the Models to the Rheological Properties of STYRON 678*

4.1.1 Simple Shear Rheological Properties

The principal polymer material, for which all the calculations were done, was polystyrene melt (PS) of a molecular weight (\bar{M}_w) of around 255000 (trade name STYRON 678 made by DOW Chemicals). This polystyrene melt exhibited excellent thermal, oxidative and mechanical stability and for these reasons it was a preferable material to be used for the testing of the results of the numerical simulation of this work. The rheological properties of this material were measured at 190° C. The shear properties (η and N_1) were measured in a Rheometrics Mechanical Spectrometer (RMS 605) using the cone-and-plate fixture. The viscosity as a function of the shear rate ($\eta(\dot{\gamma})$) is shown in Fig. 9. The primary normal stress difference ($N_1(\dot{\gamma})$) is shown in fig 10.

The practical limit of the shear rates for the cone-and-plate device in the steady state mode was around 20 sec⁻¹ for this melt at 190° C, which corresponded to a shear stress of 40 kPa. Above

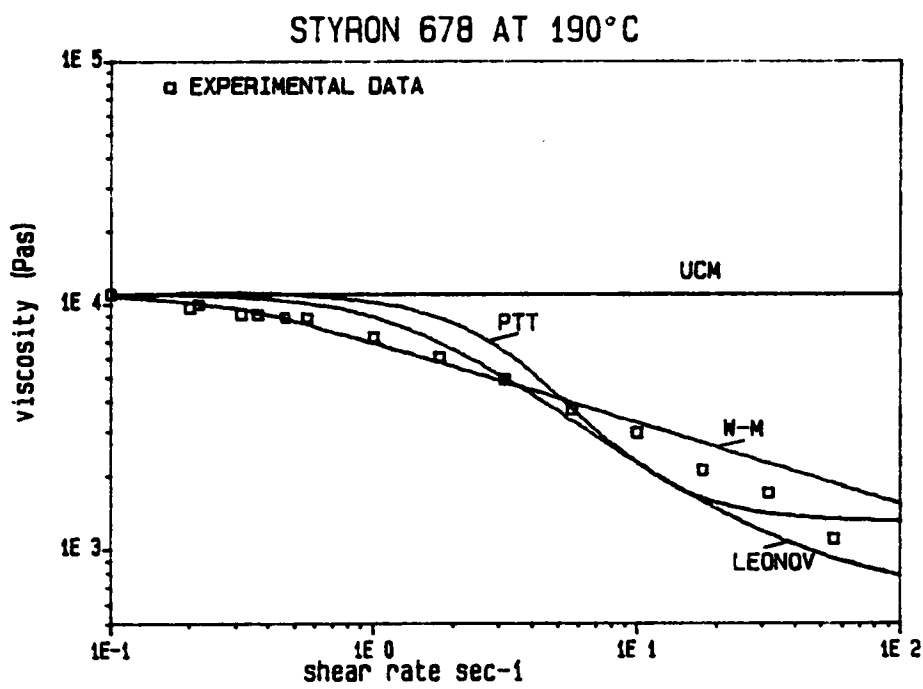


Figure 9. Viscosity vs shear rate for polystyrene at 190° C: Symbols: experimental data. Solid lines: model predictions.

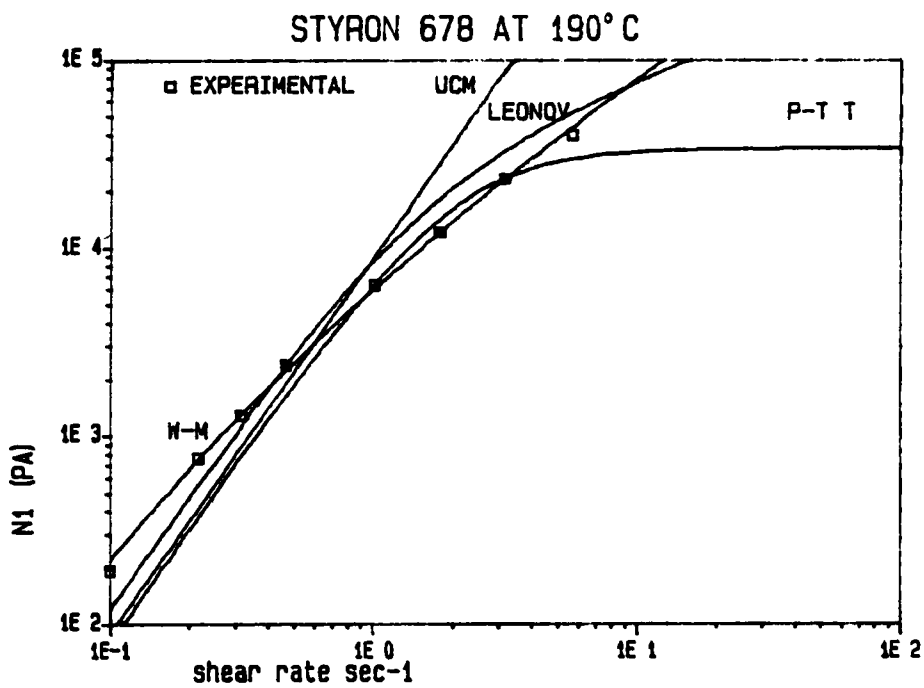


Figure 10. Normal force vs shear rate for polystyrene at 190°C: Symbols: experimental data. Solid lines: model predictions.

that limit sample loss and edge fracture decreased the accuracy of the measurements. The values of the viscosity above this value of the shear rate were taken from dynamic measurements, using the Cox-Mertz rule. For even higher values of the viscosity an INSTRON capillary viscometer was used. For the higher shear rates the value of half the storage modulus was used for an approximation of the normal force.

The way the viscosity and the normal force experimental data was fitted depended on the rheological model. For the upper convected Maxwell model both η and N_1 were needed to calculate the viscosity and the relaxation time coefficients. For the Leonov-like, the Johnson-Segalman and the Phan-Thien Tanner models, only the values of η were used and the values of N_1 were referenced only to check the accuracy of the predictions of these models in simple shear flow. In the following, the fit of η (and N_1) for the several models will be discussed. The values of the calculated coefficients for each model are given in table 3.

The UCM model predicts a constant viscosity ($\eta = \eta_1$). This of course does not agree with the experimental measurements in Fig. 9, which shows a shear thinning viscosity. It was chosen here to pick the value of the zero shear rate viscosity for the coefficient η_1 , so that the predictions of the model become exact at $\dot{\gamma} \rightarrow 0$. The relaxation time was evaluated from N_1 data. According to ch. 2.3.3.1, the UCM model predicts a quadratic increase of N_1 with $\dot{\gamma}$. The experimentally measured normal force for this PS melt increased with $\dot{\gamma}$ with a rate that was less than quadratic. To evaluate the relaxation time then, the fit was done using a simple least squares approximation. The values of the constants η_1 and λ that were calculated for this model are given in table 3. The plot of η and N_1 vs $\dot{\gamma}$ evaluated both from the measurements and the predictions are shown in figures 8 and 9.

A non-linear least squares technique was used to fit the viscosity data of PS to the Carreau model (eq. 3.26) for the evaluation of the viscosity function of the White-Metzner model. For this purpose, the subroutine LMDIF of the commercial package MINPACK (non-linear equation solver) [95] was used. The relaxation time was calculated from the following equation that comes directly from eq. 2.85:

$$\lambda(\dot{\gamma}) = \frac{N_1(\dot{\gamma})}{2\eta_1(\dot{\gamma})\dot{\gamma}^2} \quad (4.1)$$

Table 3. Coefficients of the Models

Model	Value of the Coefficient
Phan-Thien Tanner or Johnson Segalman	$\eta_1 = 9660 \text{ Pa.s}$ $\eta_2 = 1288 \text{ Pa.s}$ $\lambda = 0.5 \text{ sec}$ $\xi = 0.2$ $\varepsilon = 0.015 \text{ (PTT only)}$
White Metzner	$\eta_1 = \eta_0(1 + (m\dot{\gamma})^2)^{\frac{n-1}{2}}$ $\eta_2 = 0$ $\eta_0 = 11100 \text{ Pa.s}$ $m = 4.0 \text{ sec}$ $n = 0.67$ $\lambda = 0.43504 - 0.45297 \log_{10}\dot{\gamma} + 0.1388(\log_{10}\dot{\gamma})^2$
Upper Convected Maxwell	$\eta_1 = 11100 \text{ Pa.s}$ $\lambda = 0.6 \text{ sec}$
Leonov like	$\eta_1 = 10400 \text{ Pa.s}$ $\eta_2 = 624 \text{ Pa.s}$ $\lambda = 0.6 \text{ sec}$

Since at each experimental data point both N_1 and η were measured, the value of λ for the White-Metzner model could be calculated at that point. The data points thus obtained were fit by the function in eq. 3.27 by the least squares method using the same routine as above (LMDIF). Finally the form of the function of $\lambda(\dot{\gamma})$ for polystyrene at 190° C becomes:

$$\dot{\gamma} < 0.2 \quad \lambda = 2.0$$

$$\dot{\gamma} > 0.2 \quad \lambda = 0.43504 - 0.45297 \log_{10} \dot{\gamma} + 0.138 (\log_{10} \dot{\gamma})^2 \quad (4.2)$$

(Note that this relation will give acceptable results up to a shear rate of around 60 sec⁻¹)

The Phan-Thien Tanner and the Johnson Segalman models predict almost identical functions for the simple shear properties η and N_1 (eq. 2.69, 2.70). For these models $\eta_1 + \eta_2 = \eta_0$ (η_0 is the zero shear rate viscosity). Also the ratio η_1/η_2 should not be greater than 8 to avoid a maximum in the stress in shear flow. The data, however, did not show any indication of infinite shear rate plateau, which is in disagreement with the model. So the value of $\eta_1/\eta_2 = 7.5$ was chosen here for the calculations with the understanding that the model will not describe the experimental data at high shear rates. When this ratio is thus fixed, the value of η_1 becomes $\eta_1 = 0.8824\eta_0$ (the zero shear rate viscosity η_0 can be found by extrapolating the viscosity data to zero shear rate) and $\eta_2 = 0.1177\eta_0$. The value of the constant ξ may be calculated from a horizontal shift between the steady shear and the dynamic viscosity curves (eq. 2.72) and averaged over $\dot{\gamma}$. The value of $\xi = 0.2$ was found, which is a good estimate for polymer melts according to the results in ref. [9]. With this constant fixed, the relaxation time could be evaluated by fitting the viscosity data by eq. 2.69. The last constant that has to be found for the P-T T model, the parameter ϵ , may be evaluated from the extensional viscosity data as it will be described in the following chapter. The values of η_1 , η_2 , ξ and λ that were calculated for the PS melt are given in Table 3. When all these constants were known, N_1 could be calculated and the results compared with the experimental data of the normal force (Fig. 10) for an evaluation of the predictions of the model in simple shear flow. It is obvious, then, that the fit of N_1 is rather good at the region where experimental data exist.

For the Leonov-like model without a retardation term, the viscosity coefficient has the value of the zero shear rate viscosity. The relaxation time can then be directly calculated from a non-linear regression of the viscosity data with eq. 2.52. The results are presented in Table 3. The predicted curves of η_1 and N_1 are given in figures 9 and 10. The fit of the N_1 data with this model is re-

markably good for a model with only two parameters, but the shear thinning of the viscosity is too fast with only one relaxation mode.

When the Leonov-like model has a retardation term (η_2), the evaluation of the two viscosity coefficients is done in the same manner as for the Phan-Thien Tanner model above. In this case, however, the choice for the value of the ratio of η_1/η_2 is greater because this model does not show a maximum in the stress. The results for the retardation term that best fitted the data are also shown in table 3.

4.1.2 Extensional Flow Properties

Uniaxial extensional flow is another simple flow that gives important information about the behaviour of the fluid in complex flows. White and Baird [64] have found that the extensional behaviour of the fluid may be connected to the existence of vortices in the blind corners upstream of the flow in an abrupt contraction. Because of this importance, the elongational flow of polystyrene was also studied in this work, together with the predictions for this flow of the several rheological models that were used in the numerical simulation.

Measurements of the extensional viscosity of PS (STYRON 678) were done at 190° C in a Rheometrics Extensional Rheometer (RER 9000). The useful range of extension rates of the instrument for this melt is up to 0.7 sec⁻¹. Up to this point the values of $\bar{\eta}$ are approximately $3\eta_0$ (the Newtonian value). The behaviour of the extensional viscosity above this extension rate is not known. As a result, the predictions of all models agree well with the existing experimental data, because all the models show a Newtonian extensional viscosity at low extension rates. Comparisons between the predictions of the models and the data are, therefore, meaningless. The only meaningful comparisons are between the predictions of the several models (Fig. 11).

The predictions of the extensional viscosity of the several models that were used in this work are also shown in Fig. 11. In this figure the extensional viscosity was calculated using the parameters that were evaluated in the previous chapter. The parameter ϵ of the P-T T model is the only parameter that has to be evaluated from the experimental data of $\bar{\eta}$. The influence of the value of ϵ on the prediction of the extensional viscosity for this model is shown in Fig. 12. Since the experimental data for PS cover only the lower plateau that is common for all the curves of Fig. 12, the evaluation of ϵ is not possible from the data. The value of $\epsilon = 0.015$ was used instead as it was

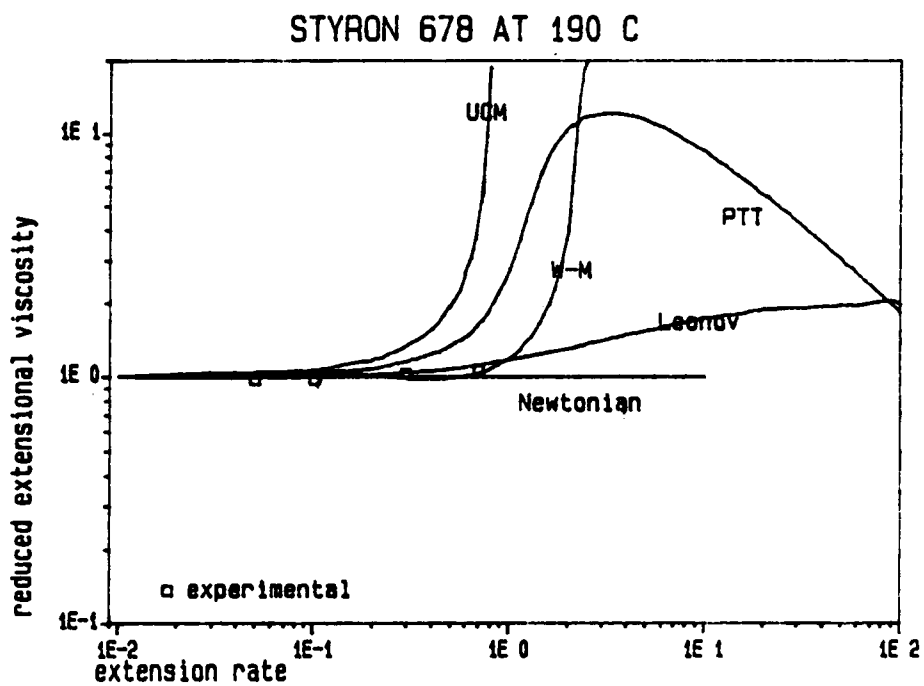
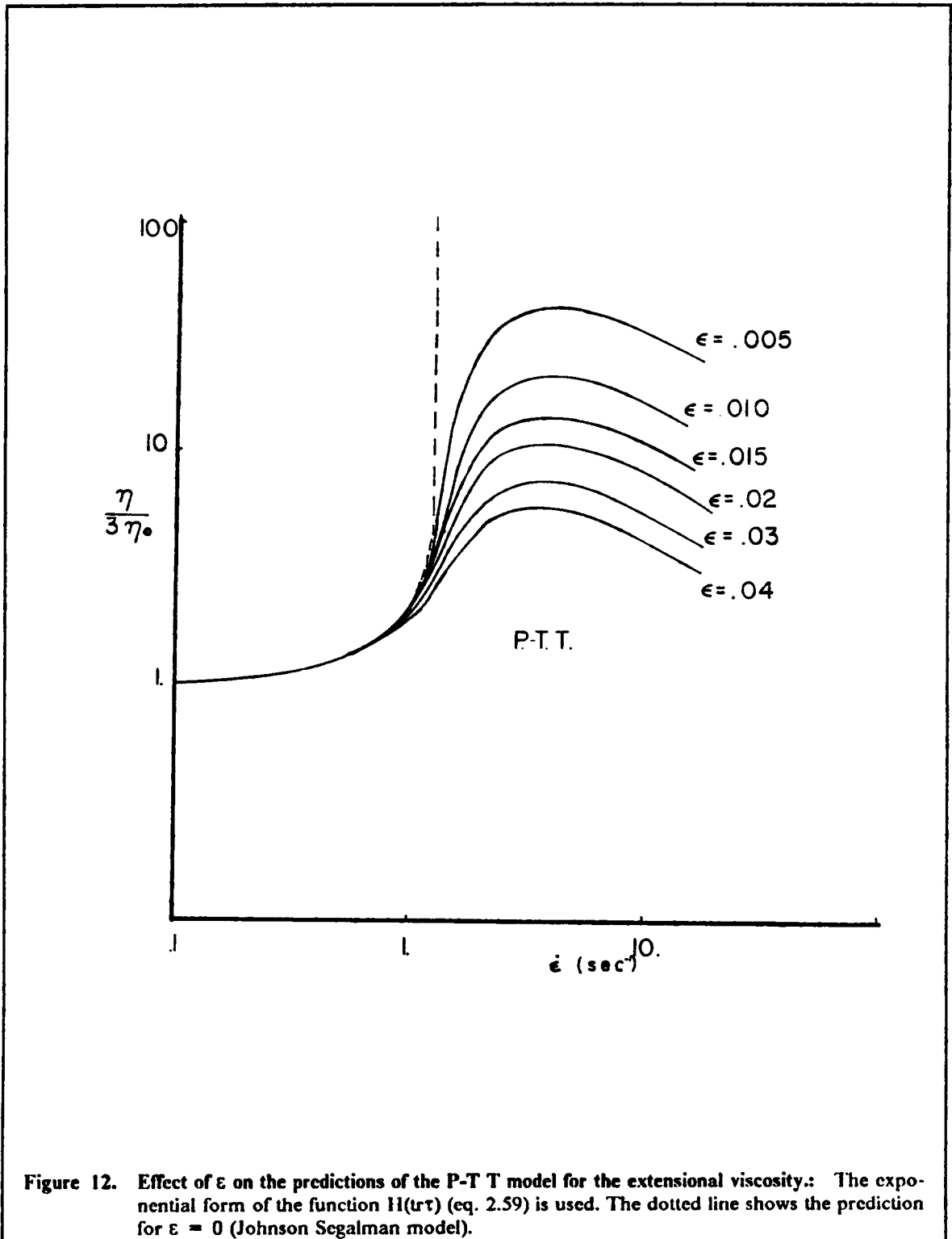


Figure 11. Extensional viscosity of polystyrene at 190° C: Symbols: experimental data. Solid lines: predictions of the models.



suggested by Phan-Thien and Tanner [9] to be a good estimate for melts. This value was also used in Fig. 11.

In terms of comparisons between the predictions of the several models, it may be seen from Fig. 11 that, while the UCM, the W-M and the J-S models predict an asymptotic increase of the extensional viscosity to infinity at a certain critical value of the extension rate, the P-T T model shows instead a maximum in $\bar{\eta}$, after which the extensional viscosity decreases toward $3\eta_2$ (where it levels off at very high extension rates). The Leonov model on the other hand, shows only a gradual increase of the extensional viscosity with extension rate from $3\eta_0$ to $6\eta_0$. Comparing the critical extension rates of the first three models, it may be seen in Fig. 11 that as the extension rate increases, the extensional viscosity of the UCM model will become unbounded first, then the J-S model and finally the W-M model, for which the increase of $\bar{\eta}$ and the subsequent unbounded values will come later than the others.

4.1.3 Transient Stress Growth Predictions

Even though the flows that were studied in this thesis are steady state flows in terms of the values of the velocity and the stress field at each point (that is in the Eulerian description of the problem, where the coordinates of the system are stationary), they include regions of acceleration, where the state of a fluid particle changes rapidly along its path. An example is the region near the contraction corners in the entry flow problem, where fluid elements not only change the direction of their motion but they also go through a strong acceleration field. The flow, therefore, may not be in steady state in the Lagrangian description, where the coordinate system is embedded in the fluid elements. Further, the fluid elements in this region may never attain their high steady state values for the stress because the time they spend inside the rapidly accelerating flow region may be less than their response (relaxation) times. Since the viscoelastic fluids have distinct time dependent flow characteristics, their transient behaviour in simple time dependent flows may also influence their behaviour in complex flows like the flow into a contraction. Consequently, the predictions of the rheological models for these transient simple flows may also influence the quality and the convergence of the solutions that are obtained from the numerical calculations using these models.

In a stress growth experiment the fluid is presumed to be at rest for $t < 0$. At $t \geq 0$ a constant shear rate $\dot{\gamma}_0$ is imposed. The transient viscosity (η^+) and primary normal stress difference coefficient (N_1^+) describe the growth of the stresses responding to this change in the flow state of the fluid. The

transient extensional viscosity ($\bar{\eta}^+$) will describe the stress growth in the start up of uniaxial extensional flow. From the models that were studied, only the upper convected Maxwell and the White Metzner show an analytical solution for η^+ , N_1^+ and $\bar{\eta}^+$ for a given $\dot{\gamma}_0$ or $\dot{\epsilon}$:

$$\eta^+ = \eta_1(1 - e^{-t/\lambda}) \quad (4.3)$$

$$N_1^+ = 2\eta_1\lambda\dot{\gamma}_0^2(1 - (1 + \frac{t}{\lambda})e^{-t/\lambda}) \quad (4.4)$$

$$\bar{\eta}^+ = \eta_1 \left[\frac{2(1 - e^{-(1-2\lambda\dot{\epsilon})t/\lambda})}{1 - 2\lambda\dot{\epsilon}} + \frac{1 - e^{-(1+\lambda\dot{\epsilon})t/\lambda}}{1 + \lambda\dot{\epsilon}} \right] \quad (4.5)$$

In these relations η_1 and λ are constants for the UCM model. For the W-M model they are functions of $\dot{\gamma}_0$ or $\dot{\epsilon}$. Figures 13 to 15 show these quantities vs time for shear rates of 1.0 and 10. sec^{-1} and for extension rates of 0.4 and 0.8 sec^{-1} . The values of the viscosity in fig. 11 were non-dimensionalized by dividing η^+ by η_1 . The normal force was non-dimensionalized by dividing N_1^+ by $2\eta_1\lambda\dot{\gamma}_0^2$. The transient extensional viscosity was divided by $3\eta_0$. In that way the viscosity and the extensional viscosity were normalized with respect to the Newtonian viscosity and the normal force was normalized with respect to the steady state value predicted by the UCM model. The same figures also show the values of the transient functions for the other models.

The calculation of the transient functions for the other models has to be done numerically. For the shear stress growth experiment the constitutive equations (eq 2.68) for the viscoelastic terms of the P-T T model reduce to the following ordinary differential equations (where the superscript 1 is omitted from these terms for clarity, as in ch. 3):

$$\lambda \frac{d\tau_{11}}{dt} - \lambda(2 - \xi)\dot{\gamma}_0\tau_{12} + \tau_{11} \exp\left[\frac{\epsilon\lambda}{\eta}(\tau_{11} + \tau_{22})\right] = 0 \quad (4.6)$$

$$\lambda \frac{d\tau_{12}}{dt} - \lambda\dot{\gamma}_0\tau_{12} + \frac{\lambda\xi}{2}\dot{\gamma}_0(\tau_{11}\tau_{22}) - \eta\dot{\gamma}_0 + \tau_{12} \exp\left[\frac{\epsilon\lambda}{\eta}(\tau_{11}\tau_{22})\right] = 0 \quad (4.7)$$

$$\lambda \frac{d\tau_{22}}{dt} - \lambda\xi\dot{\gamma}_0\tau_{12} + \tau_{22} \exp\left[\frac{\epsilon\lambda}{\eta}(\tau_{11}\tau_{22})\right] = 0 \quad (4.8)$$

These coupled ODE's could be integrated by a numerical method with initial conditions of $\tau_{\alpha\beta} = 0$ at $t = 0$. The IMSL routine DGEAR was used for this. When the values of $\tau_{\alpha\beta}(t)$ were found the retardation term was added. Finally the transient viscosity is given by the following equation:

$$\eta^+ = \frac{\tau_{12}(t)}{\dot{\gamma}_0} + \eta_2 \quad (4.9)$$

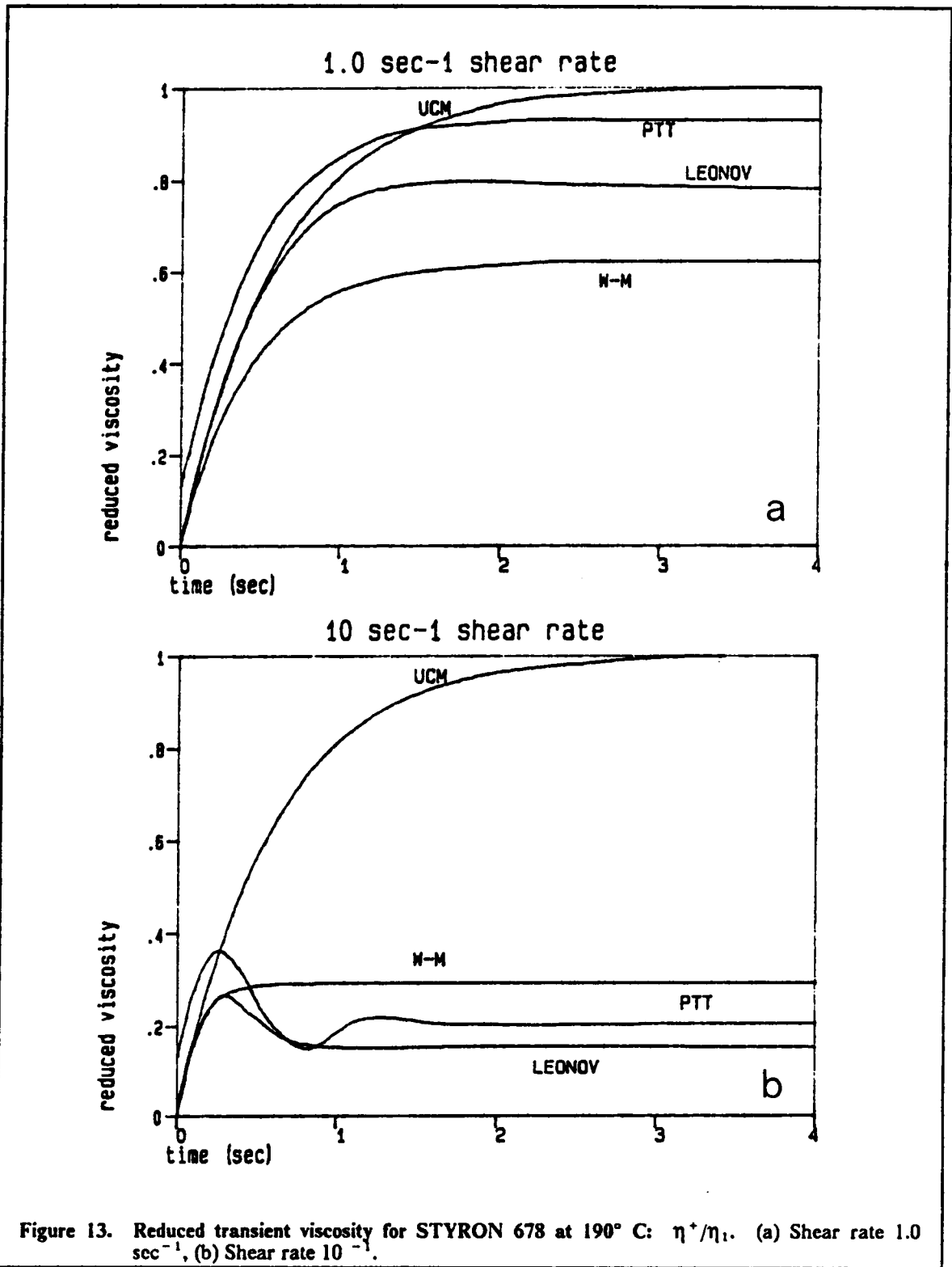


Figure 13. Reduced transient viscosity for STYRON 678 at 190° C: η^+/η_1 . (a) Shear rate 1.0 sec^{-1} , (b) Shear rate 10 sec^{-1} .

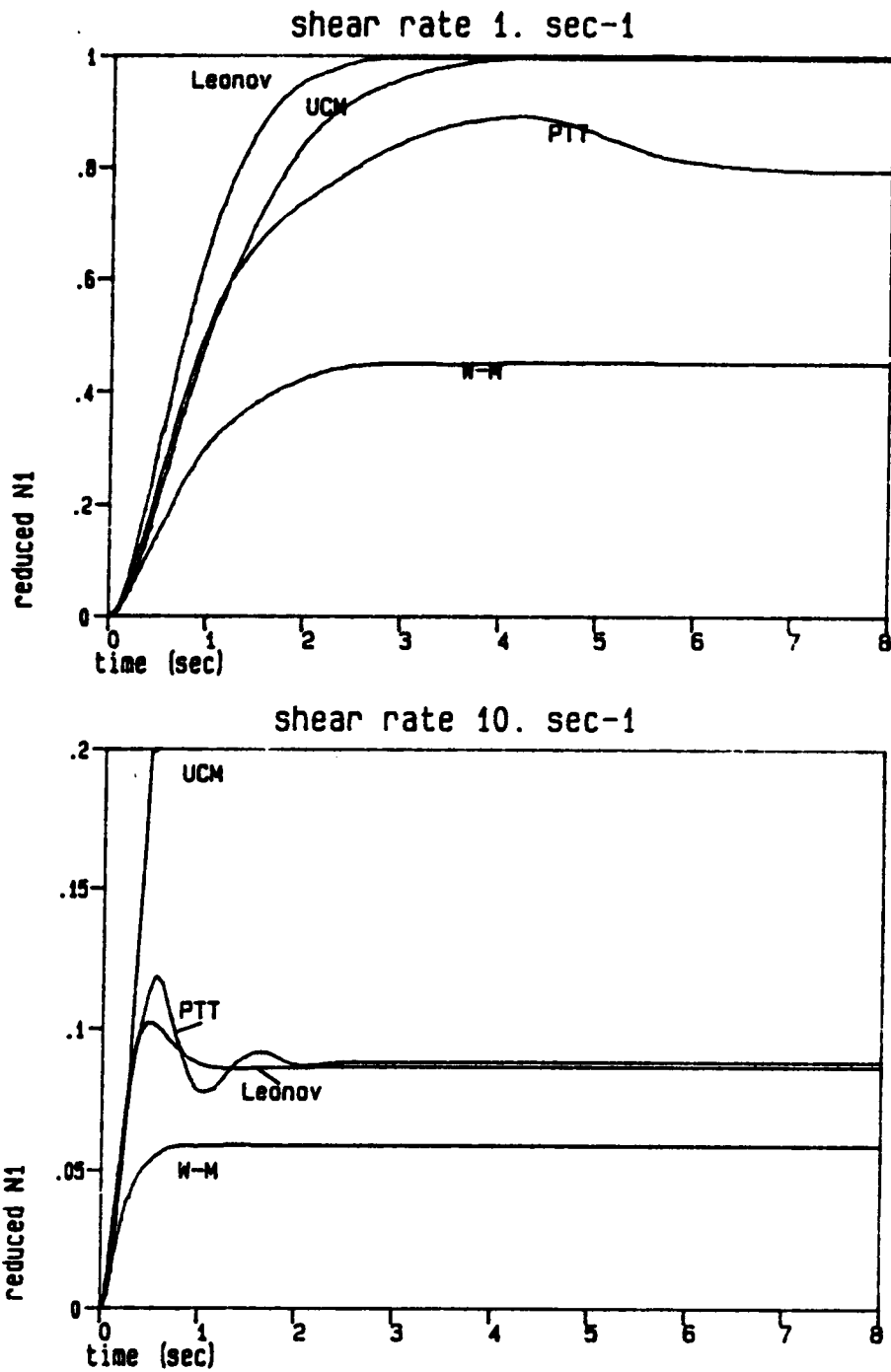
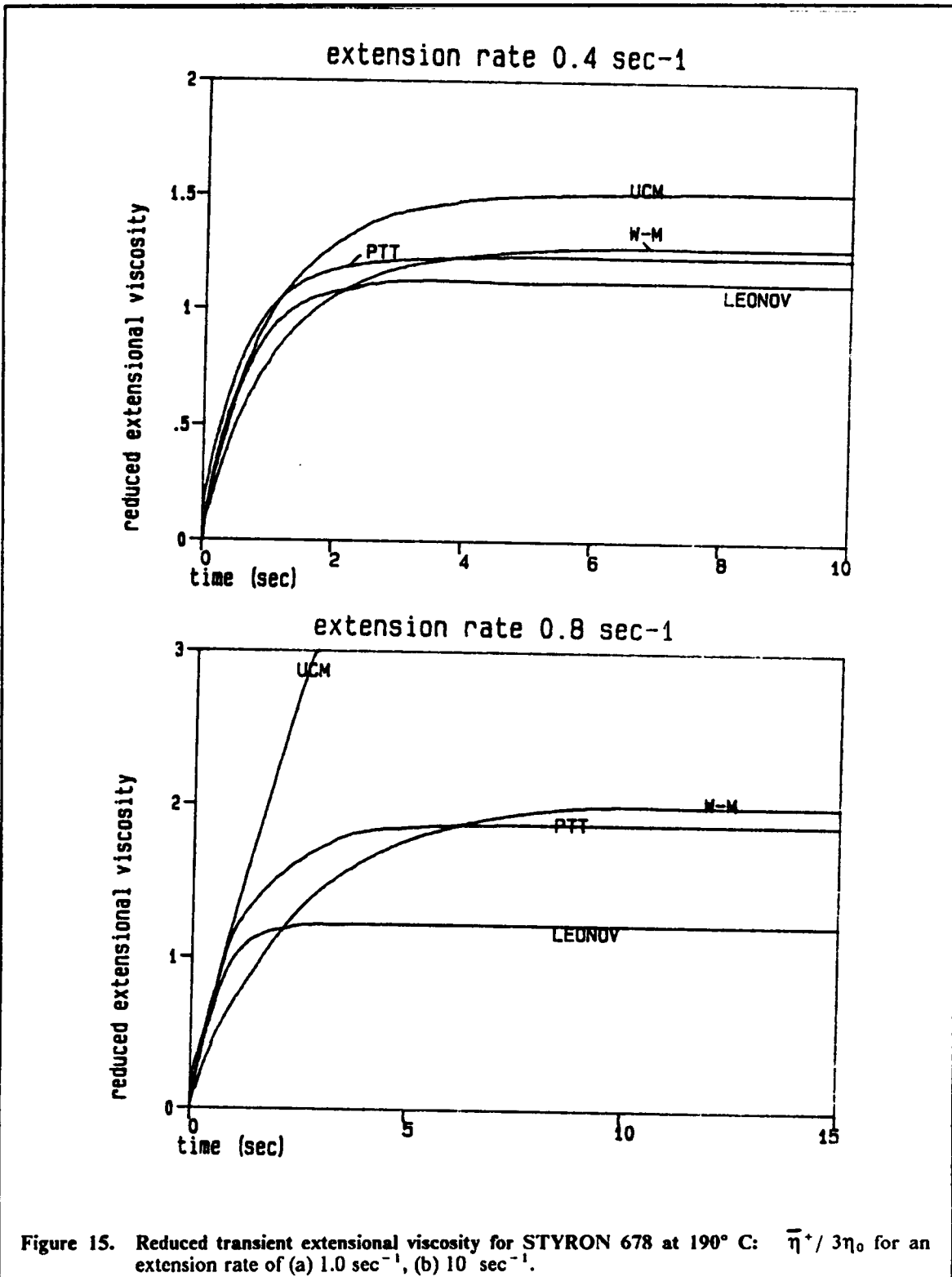


Figure 14. Reduced transient primary normal stress difference ($N_1/2\eta\lambda\dot{\gamma}^2$) for STYRON 678 at 190°C.: (a) Shear rate 1.0 sec^{-1} , (b) Shear rate 10 sec^{-1}



For the extensional stress growth the stresses were calculated from the following equations that result from the constitutive equations 2.68:

$$\lambda \frac{d\tau_{11}}{dt} - 2\lambda\dot{\epsilon}(1 - \xi)\tau_{11} + \exp\left[\frac{\epsilon\lambda}{\eta_1}(\tau_{11} + 2\tau_{22})\right]\tau_{12} = 2\eta_1\dot{\epsilon} \quad (4.10)$$

$$\lambda \frac{d\tau_{22}}{dt} + \lambda\dot{\epsilon}\tau_{22} + \exp\left[\frac{\epsilon\lambda}{dt}(\tau_{11} + 2\tau_{22})\right]\tau_{22} = -\eta_1\dot{\epsilon} \quad (4.11)$$

$$\tau_{33} = \tau_{22} \quad (4.12)$$

The same routine (DGEAR) was used for the integration of these differential equations also. The transient extensional viscosity with the addition of the retardation term then becomes:

$$\bar{\eta}^+ = \frac{\tau_{11} - \tau_{22}}{\dot{\epsilon}} + 3\eta_2 \quad (4.13)$$

For the Leonov model the ODE' s that have to be solved for the shear stress growth are:

$$\frac{d\tau_{11}}{dt} = 2\dot{\gamma}_0 C_{12} - (C_{11}^2 + C_{12}^2 - 1)\frac{1}{2\lambda} \quad (4.14)$$

$$\frac{d\tau_{12}}{dt} = \dot{\gamma}_0 C_{22} - \frac{1}{2\lambda}(C_{11} + C_{22})C_{12} \quad (4.15)$$

$$C_{22} = \frac{1 + C_{12}^2}{C_{11}} \quad (4.16)$$

From the tensor $C_{\alpha\beta}$ the stresses and the transient viscosity (η^+) can be calculated according to ch. 2.3.1:

$$\tau_{11} = \frac{\eta}{\lambda}C_{11} \quad \tau_{12} = \frac{\eta}{\lambda}C_{12} \quad \tau_{22} = \frac{\eta}{\lambda}C_{22} \quad \eta^+ = \frac{\eta C_{12}}{\lambda}\dot{\gamma}_0$$

Similarly for the extensional flow the initial value problem becomes:

$$-6\lambda\dot{\epsilon}C_{11}\frac{dC_{11}}{dt} = C_{11}^4 + C_{11}^3 + 6\dot{\epsilon}\lambda C_{11}^2 - C_{11} - 1 \quad (4.17)$$

$$C_{22} = C_{11}^{-2} \quad (4.18)$$

$$C_{33} = C_{22} \quad (4.19)$$

The transient extensional viscosity for this model then becomes:

$$\bar{\eta}^+ = \frac{\eta}{\dot{\epsilon}\lambda}(C_{11} - C_{22})$$

The results of these calculations are shown in figures 13-15. It can be seen in Fig. 13 that at low shear rates only the Leonov model gives a very low overshoot ($\cong 2\%$) for the viscosity growth. At a higher shear rate there are two oscillations apparent in P-T T. The initial overshoot for this model is about twice the steady state value at this rate. No oscillations are predicted by the Leonov

model. The overshoot for this model is also about twice the steady state value. The UCM and the W-M models show only a monotonic increase in the stresses to their steady state values. The curves for all the models except the UCM model reach different value long times because of their different shear thinning behaviour.

For the normal force growth at low $\dot{\gamma}_0$ (Fig. 14), the P-T T model is the only one that shows an overshoot. At higher rates, N_1^+ for the P-T T model oscillates showing an initial overshoot of 1.5 times the steady state value. Leonov's model does not show oscillations but it shows an overshoot. The normal stress for the UCM model increases much more slowly than the other models to its steady state value.

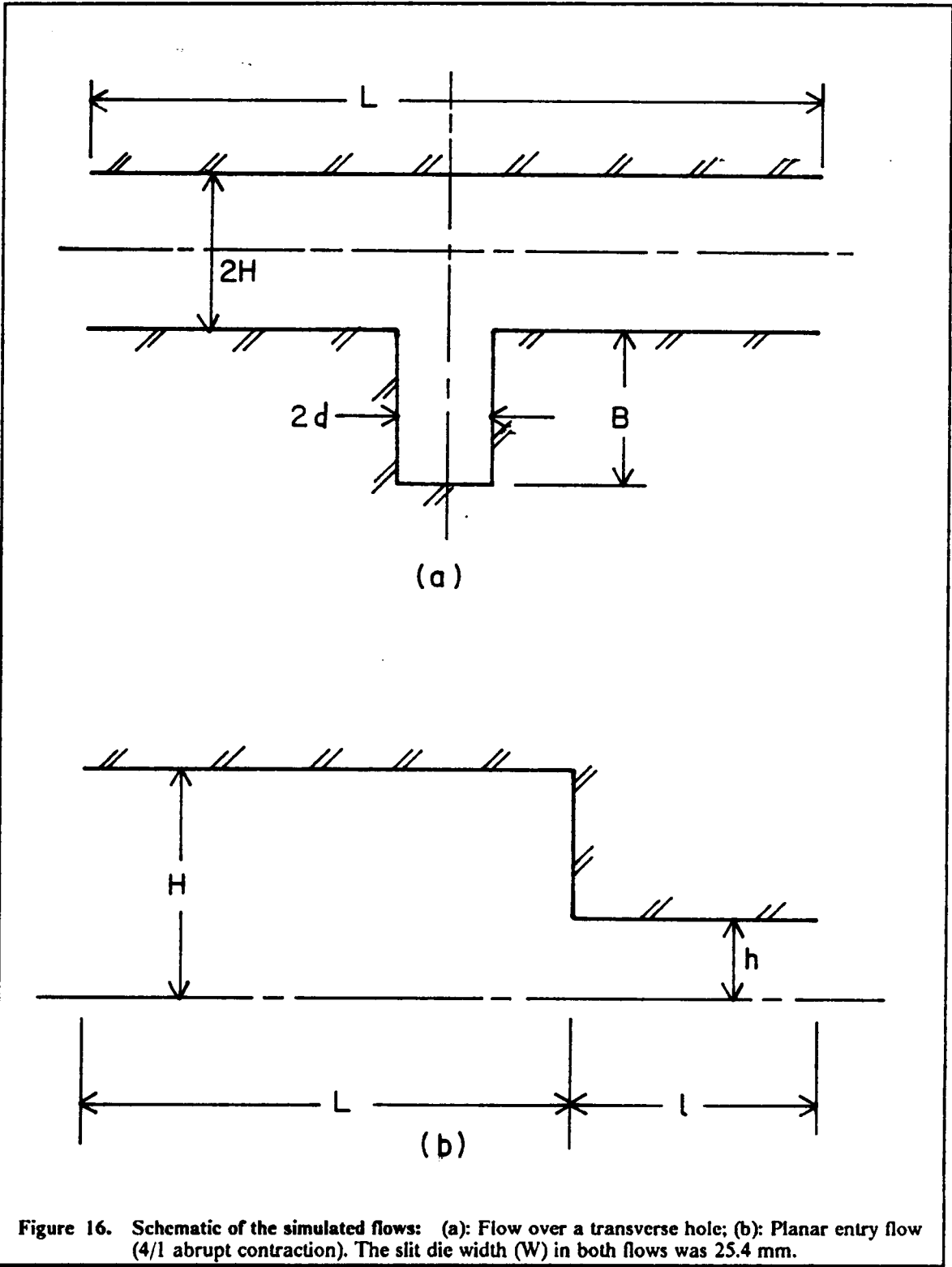
The extensional stress growth is seen in Fig. 15. Here no overshoot is predicted by any model at either shear rate (0.4 or 0.8 sec^{-1}). Both the P-T T and the Leonov models attain their steady state value much faster than the W-M model. The extension rate of 0.8 sec^{-1} is close to the critical extension rate for the UCM model. For this reason the steady state value of the extensional viscosity for this model is much higher than the other models. At this extension rate the UCM model needs around 60 sec to reach its steady state value for $\bar{\eta}^+$.

4.2 Meshes Used for the Two Flows

4.2.1 Slit Flow Over a Transverse Hole

Three geometries were used for the study of the flow over a hole referred here as P1, P2 and P3. The schematic of this flow is shown in Fig. 16a and the dimensions of each specific configuration are given in table 4. Configuration P1 had sharp corners and the width of the hole was less than the height of the slit die. Configuration P2 also had sharp corners, but the width of the hole was larger than the slit height. Configuration P3 has the same dimensions as P2 but the corners around the hole were rounded.

These three geometries were used both for the experimental measurements [11,86] and as the basis for the domain of the numerical simulations of the flow over a transverse hole. Values of the stresses measured at several points of the domain using the technique of flow birefringence are given in ref. [11] for several flow conditions. Photographs of the fringes are also given there. Flow streamlines are given in [86].



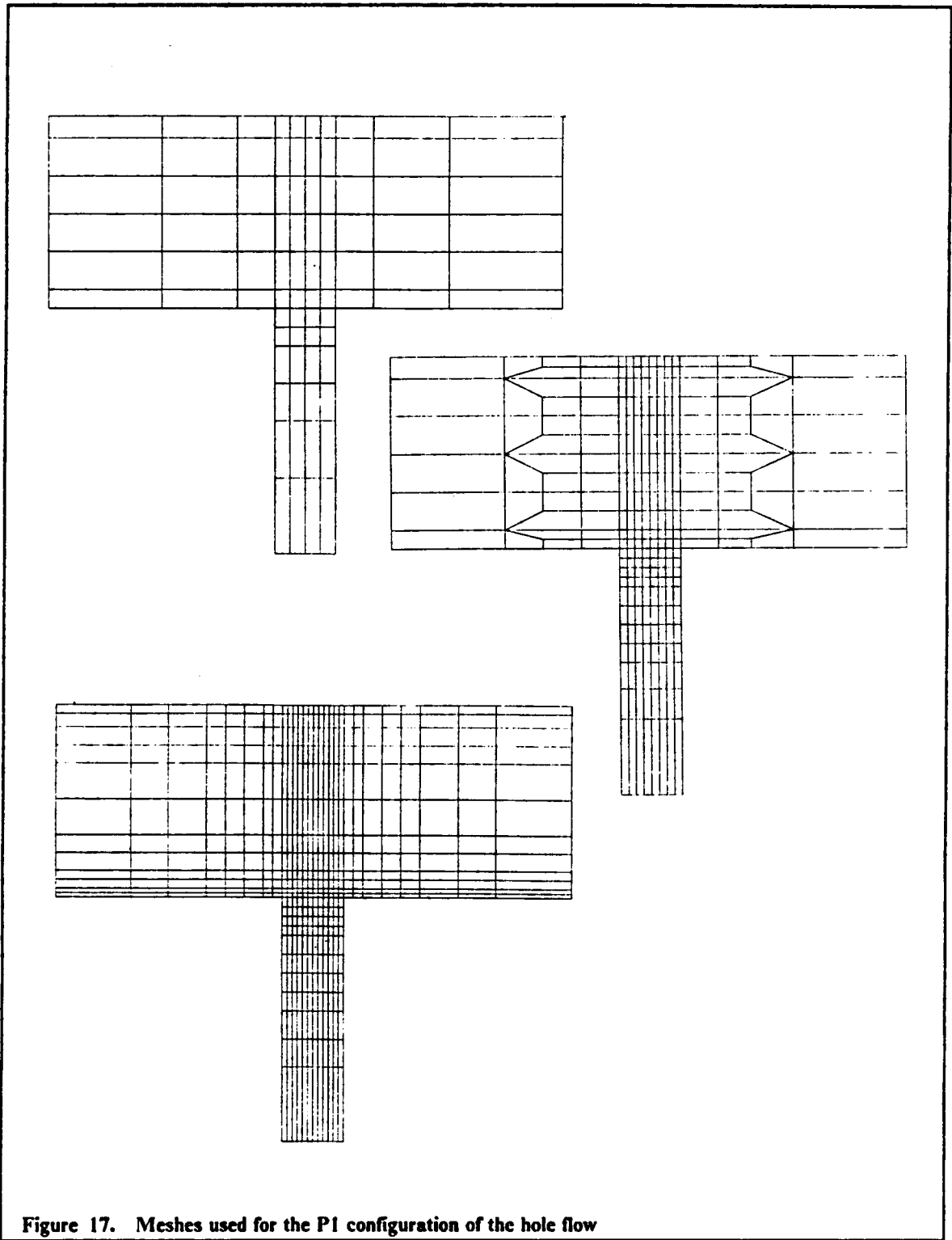


Figure 17. Meshes used for the P1 configuration of the hole flow

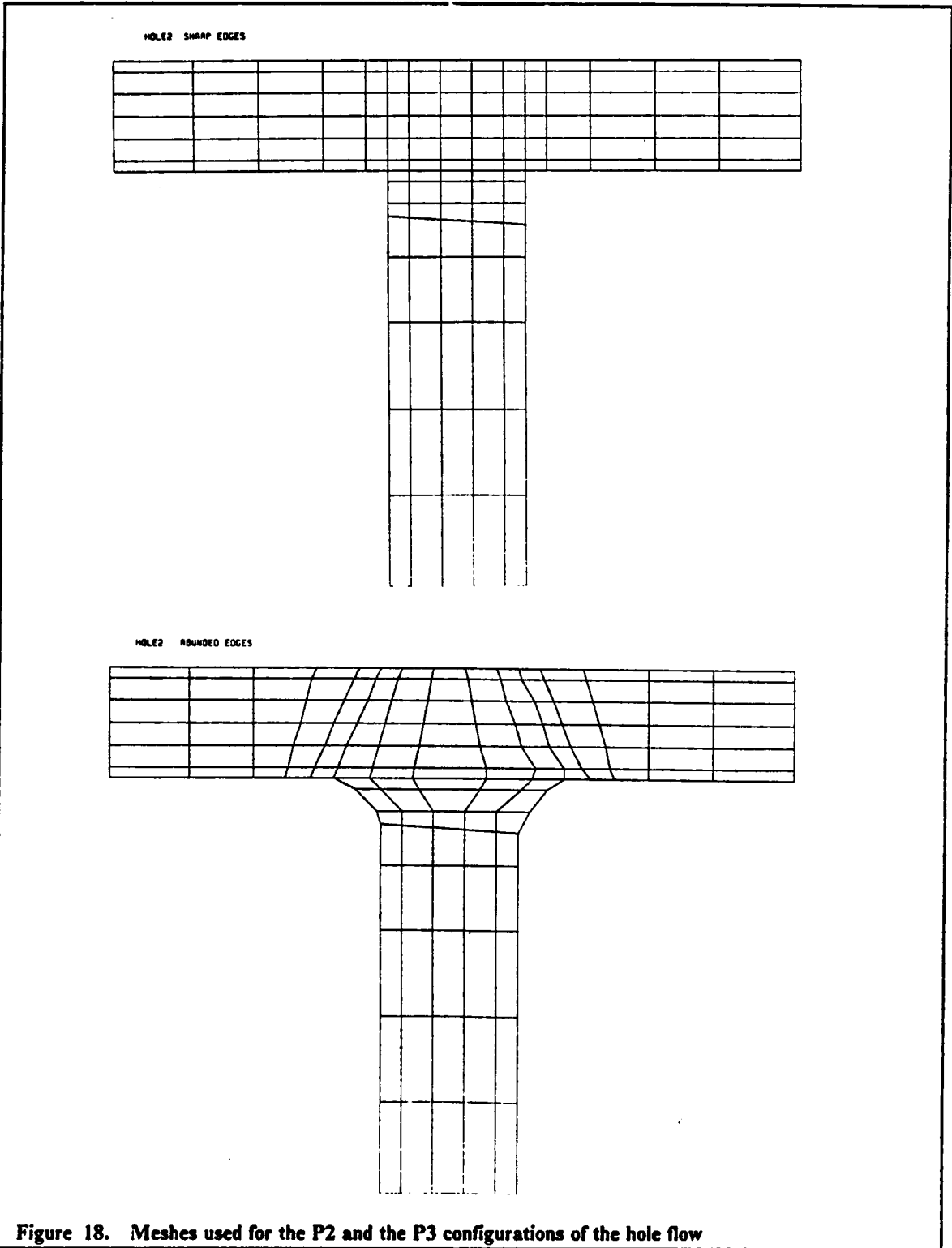


Table 4. Dimensions of the Dies (and the Meshes) for the Flow Geometries in Figure 13

Flow Geometry	Dimensions
Hole-1 (configuration P1)	$2H = 2.54 \text{ mm}$ $2d = 0.81 \text{ mm}$ $B = 3.25 \text{ mm}$ $L = 6.81 \text{ mm}$
Hole2 (configuration P1 or P2)	$2H = 2.54 \text{ mm}$ $2d = 3.18 \text{ mm}$ $B = 9.60 \text{ mm}$ $L = 15.90 \text{ mm}$
Entry	$H = 5.08 \text{ mm}$ $h = 1.27 \text{ mm}$ $L = 10.0 \text{ mm}$ $l = 5.0 \text{ mm}$
<p>The width of the dies in all cases above was 25.4 mm</p>	

To discretize the geometry P1, three meshes were used (Fig. 17). All three meshes employed linear quadrilateral elements. The numbers of elements and nodes of each mesh are given in table 5. For the discretization of P2 only one mesh was used consisting again of linear quadrilateral elements. In order to facilitate comparisons with P3, the same number of elements was used for the discretization of P3 and approximately the same arrangement of the nodes. The only differences between MESH-P2 and MESH-P3 exist around the corners, where the position of the nodes had to be shifted to accommodate the rounded edges of P3 (Fig. 18)

The dimensions of the flow domains for the simulation were determined by the dimensions of the experimental apparatus. Only the length of the die, that is the position of the inlet and outlet planes, where the fully developed velocity profiles were assumed had to be determined independently. These planes were then set at a distance of $\pm 6d$ (with $2d$ the width of the hole), a distance that was considered long enough for the disturbance to have been absorbed.

4.2.2 Flow Into an Abrupt Planar Contraction

A contraction ratio of 4/1 was used to analyze the flow into an abrupt contraction. This geometry was investigated experimentally and the results were compared with the results of the numerical simulation as in the previous case of the flow over a transverse slot. Values of the stresses were also measured by means of flow birefringence at points covering the entire flow domain and are given in [85]. Streamlines of that flow are given in [11]. To discretize this domain, four meshes were used. Three of them employed linear quadrilateral elements and the fourth used quadratic serendipity elements. The number of the elements increased from MESH1 to MESH3 and the mesh with quadratic elements had approximately the same number of nodes as MESH2. These four meshes are shown in Fig. 19. The number of the elements and the nodes for each mesh are given in table 5. The length of the upstream and the downstream channels was set at $-4H$ and $+6h$ respectively with $2H$ the height of the channel before the contraction and $2h$ the height of the downstream channel. Only one half of the domain was used for the numerical simulation as symmetry conditions were assumed for the other half beyond the centerline.

An IBM 3090 main-frame computer was used for the numerical computations. Since the code used an in core simultaneous equations solver, the full global stiffness had to be stored in core (in a banded form). The storage requirements for this matrix ranged from 1200 kilobytes for the

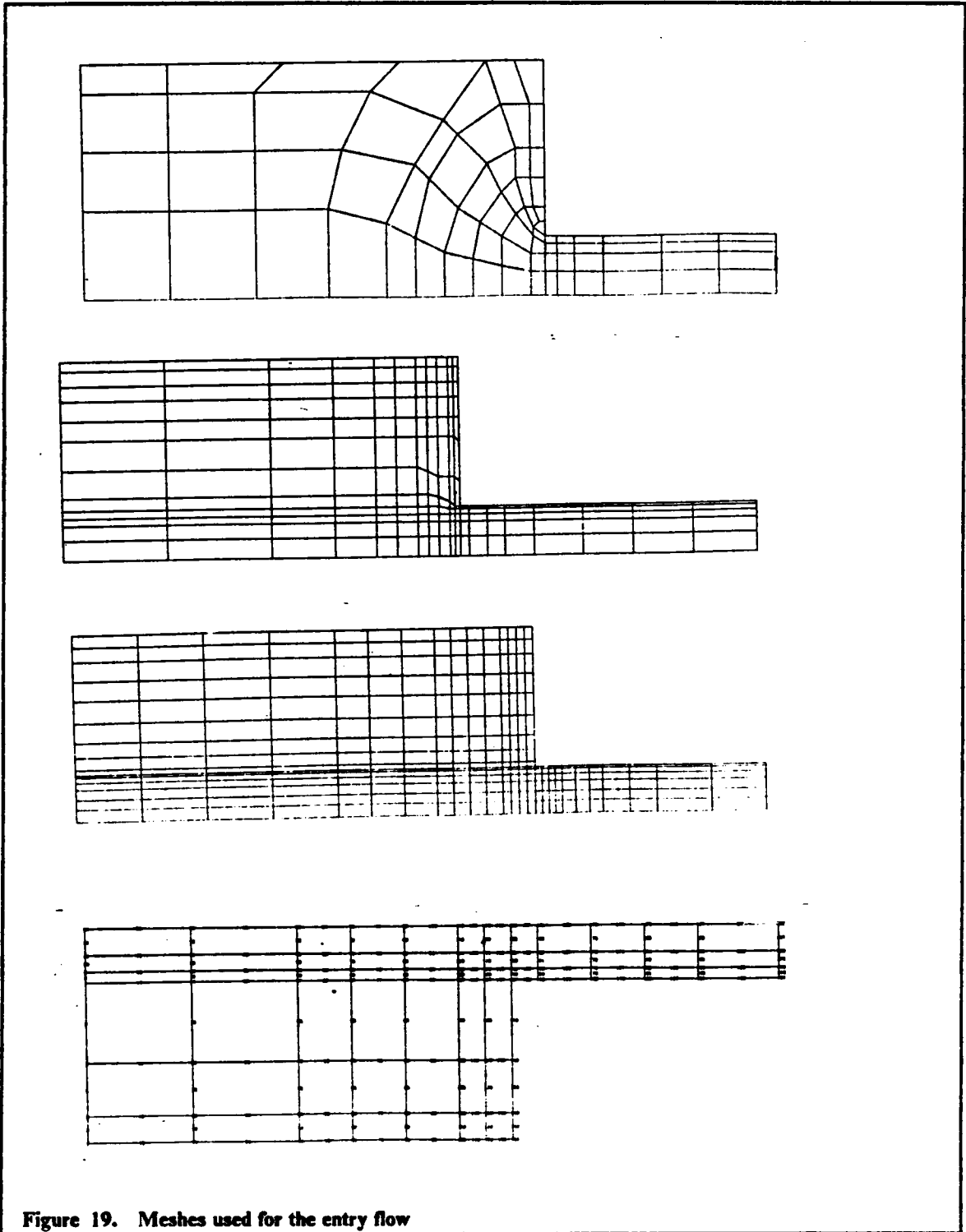


Figure 19. Meshes used for the entry flow

Table 5. Characteristics of the Meshes Used for the Numerical Simulation

Mesh	Elements	Nodes	DOF*	HBW*	CPU seconds per iteration
Hole1 (Geometry P1)					
MESH1	84	107	535	160	1.62
MESH2	256	290	1450	320	15.2
MESH3	468	520	2600	390	98.7
Hole2 (Geometry P2 and P3)					
MESH1	130	160	800	230	6.75
MESH2	130	160	800	230	6.75
Entry					
MESH1	75	97	485	90	0.72
MESH2	172	204	1020	150	5.0
MESH3	291	333	1665	180	11.4
MESH4**	57	208	1040	230	11.0
<p>* DOF : Number of Degrees of Freedom in the Problem NBW : Half Bandwidth of the Global Stiffness Matrix</p> <p>** All the meshes above had linear elements except Mesh4 for the entry flow, which had quadratic elements.</p>					

coarsest mesh to more than 5500 kilobytes for MESH3 of the hole flow problem (1.014×10^6 elements of the array containing the global stiffness matrix in double precision). The approximate CPU times for each mesh without using the vectorization capability of the computer were between 0.6 sec to 100 sec per iteration and are given also in table 5.

5.0 Results and Discussion

Chapter 5 includes the results of the numerical computations and the comparisons with the flow birefringence data from Pike [11] and White [85], as well as the streamlines from [87]. In the first section of this chapter the limits for the convergence of the several models and the different meshes for both flows are presented and discussed. The basis for comparing numerical results of viscoelastic flows are also discussed here. In the second section direct comparisons of the numerical predictions with experimental data are made for the flow over a transverse slot. These include comparisons between five constitutive models and a number of different meshes. The three geometries of the hole (P1, P2 and P3) are also examined here. In section 5.3 the same comparisons are made for the flow into an abrupt contraction. Finally in chapter 5.4 the behaviour of the numerical solution around the limit for the convergence of the iterations is discussed.

5.1 Limits of Convergence as a Function of Constitutive Equation

It was described in ch. 2.2.2 that in almost all reports concerned with the numerical simulation of the viscoelastic flows, it has been found that the iterations fail to converge at high elasticity levels. These limits of convergence were found to depend on the rheological model that was used and on the mesh used to discretize the flow domain. The limit usually decreased for finer meshes. In the present study the same eventual divergence of the Galerkin-FEM method was found for both flows that were studied. The approximate convergence limits for all the models and the meshes that were used are shown in Tables 6 and 7. In general the global error during the iterations of the numerical method in the present work showed the same behaviour as in Fig. 2 (in chapter 2). The limits in tables 6 and 7 correspond to the case (b) of that figure, for which the error stops decreasing, re-

maintaining approximately constant at a value higher than the tolerance and no further improvement of the solution can be achieved with any more iterations. It is interesting to note here, that the change from behaviour (a) to (b) and (c) was rather abrupt. The solution converged rather fast (within 3-6 iterations) until suddenly the rate of convergence decreased and soon no convergence could be achieved, a change that took place within a relatively small increase of the level of the stress in the flow.

From Tables 6 and 7, it may be seen that the limits of convergence differ widely between the several models. But before examining these differences, the problem of the basis of the comparison has to be mentioned. In most reports, where comparisons between models were given, the basis for these comparisons was the level of the elasticity of the flow, as it was given by the Deborah number (De) or the Weissenberg number (We). The main advantage for this choice was the fact that these two numbers show the extent of the difference between the viscoelastic nature of the flow in question and the Newtonian flow. Another reason for this choice is that De or We may in some cases be used directly into the equations as dimensionless parameters and no specific choices for viscosity, relaxation time and stress levels have to be made. However, this choice is not sufficient for comparing different rheological models, as the same elasticity level will result in different flow fields when different models are used. The reason for this uncertainty is that each model will only approximately describe the properties of the materials of interest here. From Figure 9 (in ch. 4), which shows the viscosity that each model predicts as a function of the shear rate, it can be inferred that the stresses in the flow in a die as predicted by the UCM model will be higher than the stresses of the Leonov model with the same relaxation time and the same Deborah number (defined as $De = \lambda\dot{\gamma}$). This is because the viscosity function that the Leonov model predicts is shear thinning, while the viscosity predicted by the UCM model is not.

There is another reason why an elasticity parameter should not be used as an absolute criterion for the comparison between rheological models. Figure 20 shows the predictions of $We (= N_1/2\tau_{12})$ in simple shear flow for the models that were used in this work, with their coefficients evaluated to fit the same polystyrene melt. It can be seen from this figure that the predictions of the models for the same material and the same simple flow are different from each other, especially at high shear rates. Further the experimental data in the same figure indicate that We may actually level off at high shear rates. No model can describe exactly this behaviour, except perhaps the White Metzner model (at low shear rates), whose parameters were determined from experimental data

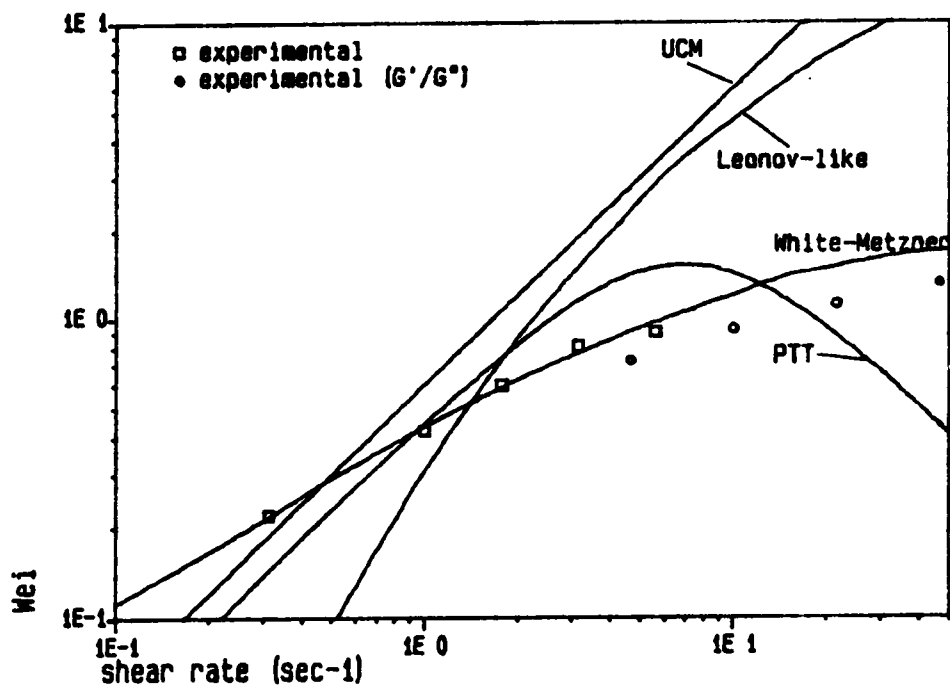


Figure 20. Values of We ($We = N_1/2\tau_{1,2}$) as predicted by several models: The symbols represent experimental results measured in a cone and plate fixture of a rotary rheometer (\square) and values of G'/G'' measured on the same device (\circ).

Table 6. Limits of Convergence for the Entry Flow

Mesh	Model	τ_{12w} * (kPa)	Q/W * mm ² /sec	De *	We *
1	P-T T	34	17.54	11.41	1.55
	J-S	33	16.44	10.95	1.59
	W-M	43.5	14.05	1.42	1.42
	Leonov-like	24	8.21	7.49	1.79
	UCM	32	3.29	1.84	1.84
2	P-T T	27	9.32	7.98	1.90
	J-S	27	9.32	7.98	1.90
	W-M	34	9.93	1.23	1.23
	Leonov-like	22	6.37	5.85	1.68
	UCM	24	2.32	1.30	1.30
3	P-T T	24	5.71	6.17	2.08
	J-S	24	5.71	6.17	2.08
	W-M	20	4.42	0.92	0.92
	Leonov-like	17.5	3.49	3.01	1.32
	UCM	19	1.84	1.03	1.03
4 (quadr.)	P-T T	25	6.90	6.82	2.03
	J-S	25	6.90	6.82	2.03
	W-M	27	8.56	1.17	1.17
	Leonov-like	18	3.59	3.11	2.33
	UCM	20	1.94	1.08	1.08
<p>* τ_{12w} : Wall shear stress at a point far down stream from the contraction Q/W : Flow rate per unit width De = $\lambda\dot{\gamma}_w$ We = $(N_1/2\tau_{12})_w$</p>					

Table 7. Limits of Convergence for the Flow over a Hole

Mesh	Model	τ_{12w} * (kPa)	Q/W * mm ² /sec	De *	We *
1	P-T T	24.2	5.86	6.26	2.08
	J-S	24.2	5.86	6.26	2.08
	W-M	22.5	7.40	1.13	1.13
	Leonov-like	17.8	3.48	2.99	1.31
	UCM	16.5	1.60	0.89	0.89
2	P-T T	22.7	4.35	5.26	2.11
	J-S	22.7	4.35	5.26	2.11
	W-M	19	5.47	1.01	1.01
	Leonov-like	16.5	2.90	2.36	1.18
	UCM	15.4	1.48	0.82	0.82
3	P-T T	21.6	3.12	3.70	2.16
	J-S	21.4	3.08	3.61	2.12
	W-M	15.3	3.78	0.87	0.87
	Leonov-like	14	2.02	1.48	0.92
	UCM	14	1.35	0.75	0.75
hole2 sharp corners	P-T T	22.9	4.39	5.30	2.13
	J-S	22.9	4.39	5.30	2.13
	W-M	21.6	6.73	1.09	1.09
	Leonov-like	17.8	3.48	2.99	1.31
	UCM	21.6	2.09	1.17	1.17
hole2 rounded corners	P-T T	25.4	7.39	7.07	2.00
	J-S	25.4	7.39	7.07	2.00
	W-M	22.9	7.40	1.13	1.13
	Leonov-like	15.2	2.41	1.91	1.04
	UCM	22.9	2.21	1.24	1.24

* τ_{12w} : Wall shear stress away from the hole

Q/W : FLOW rate per unit width

$$De = \lambda \dot{\gamma}_w$$

$$We = (N_1/2\tau_{12})_w$$

using both the shear stress and the primary normal stress difference. On the contrary, the Weissenberg number for the PTT and the Johnson Segalman models shows a maximum and then it decreases with increasing shear rate, whereas the Leonov-like model climbs to much higher values of We (even though it levels off at very high shear rates). The slope of the curve that corresponds to the upper convected Maxwell model is approximately double the slope of the experimental data. In any case, if the experimental We tends to level off at a value of 1.5 or 2.0, it may not make sense to compare it with numerical results that show values of $We = 6$ or even $We = 9$.

The need for another basis of comparison is then obvious. The importance of the elasticity numbers remains, but additional criteria have to be used. Because the same material and the same flow conditions are considered in all comparisons, it is suggested in tables 6 and 7 that the values of the stress at some characteristic point may also be used for such comparisons. The flow rate is another important quantity that can be used, especially from an industrial point of view. In the tables both elasticity numbers are included, as well as the shear stress. All three of these parameters were evaluated at the wall at a point far from the hole for the case of the flow over a slot or at the downstream wall in entry flow. The limiting value of the flow rate (in mm^3 per sec per mm of die width) is also listed in Tables 6 and 7.

The problems described above regarding the basis of the comparisons become obvious in Tables 6 and 7. Therefore, in the following, the limits of convergence for the several models will be compared in terms of either the highest stress levels that can be reached by each model, or in terms of the highest flow rate through the die for which the method converges, or in terms of the elasticity of the flow that the model can handle (the values of De and We). All of these comparisons are done for each mesh that was used and between the meshes with linear and quadratic elements. These limits will be discussed first for entry flow and then for the flow over the hole.

In terms of the maximum wall shear stress, it can be seen from Table 6 that the White-Metzner model shows the best results in entry flow. In fact it can handle a much higher shear stress level than the next model, which is the Phan-Thien Tanner. The P-T T and the Johnson Segalman models show the same stress limits for convergence. The upper convected Maxwell model also shows a surprisingly high limit, at least for the most coarse mesh. The Leonov-like model is found to give the lowest limits of convergence in terms of the shear stress level.

When the comparison is done in terms of the maximum flow rates, then the picture is somewhat changed. For MESH1, the P-T T and the J-S model will exhibit higher limits for the flow

rates than the W-M model. For the other two meshes, the latter will handle higher flow rates than the two former ones. This peculiar behaviour can be explained by the shape of the viscosity curves of the three models (Fig.9 in ch. 4). At low shear rates (lower than 0.8 sec^{-1}) the viscosity of the P-T T model is higher than the viscosity predicted at the same rate by the W-M model. At high shear rates, however, this is reversed and the W-M model will predict higher values for viscosity. For slow flows then, the P-T T and the J-S models will predict lower shear rates than the W-M at the same shear stress level. The flow rates then are lower for the two former models than the latter at these stress levels. At the higher stress levels, however, up to where convergence is possible for MESH1, the higher viscosity near the wall (where the shear rate is higher than 0.8 sec^{-1}) of the W-M model will result in a lower flow rate than the other two models. The same behaviour is also observed for the Leonov-like and the UCM models. The former model shows a higher limiting flow rate at a lower shear stress than the latter, also because the former model has a shear thinning viscosity, while the UCM model shows a constant viscosity.

In terms of the Weissenberg number, direct conclusions concerning limits of convergence can not be made because the values of We_L for both the P-T T and the J-S models fall in the decreasing branch of the corresponding curve in Fig. 20. The comparison of the values of De_L , however, shows that these two models show the highest elasticity limits. The Leonov-like model is next in handling high elasticity levels. The W-M model shows the lowest elasticity limit of convergence because the value of its relaxation time, λ , decreases with the shear rate in the same way as the experimental data dictate.

Comparing the results between the different meshes, it is seen that all the limits decrease for each model with the refinement of the mesh. The decrease of these limits from MESH1 to MESH2, which has about double the number of nodes of the former is around 20 to 25 % and from MESH2 to MESH3 (the latter has about 1.5 times the number of nodes of the former) there is another 20 % average decrease for all the models. The Leonov-like model shows the lowest decrease in the limits of convergence with the mesh refinement, but it remains constantly lower than the other models. On the other hand, the mesh refinement has the maximum effect on the W-M model, the limits of which decrease from MESH1 to MESH3 to such a degree that at the finest mesh this model shows lower limits for convergence than the P-T T model in terms of stress. The other three models lie in between.

Comparing the mesh with quadratic elements with the one with linear elements and the same number of nodes, it can be seen that higher limits of convergence are achieved by the mesh with the linear elements. All the models seem to be affected in the same way by the quadratic mesh and approximately to the same degree. Achieving higher limits of convergence with a mesh employing linear elements than one with quadratic is quite surprising. Yeh et al [35] and Debaut and Crochet [78] have reported that a higher order of interpolation polynomials would be more likely to show higher limits, in contrast to the results in this work. It is possible that this apparent contradiction is due to the mixed FEM formulation (velocities, stresses and pressure as field variables) that the above authors used instead of the penalty/FEM formulation that was used in the present work.

Comparison between the limits of the numerical computations of the present work and the literature can not be done directly in terms of the stress levels or the flow rates because most of the results that have been reported are in dimensionless form. For the comparison in terms of the Deborah number, it should be noted that its definition varies. For the P-T T model, Keunings and Crochet [32] and Debaut and Crochet [78] defined the Deborah number as $De = \sqrt{\xi(2 - \xi)} \lambda \dot{\gamma}$. With this definition the limits of De for convergence become 6.8, 4.8 and 2.64 for MESH1, 2 and 3 respectively, which are in the same level as the results in [32] and [78]. The limits of the Leonov-like model compare well with those reported by Keunings [75] for meshes with a comparable number of nodes, even though the elements that were used there were not linear. The limits of the UCM model are lower in the present work than the ones found in the same flow and comparable meshes by Davies [30] and Crochet [78,82]. The dependence of the convergence on the specific mesh, however, makes a quantitative comparison between the results of this work and the literature very difficult. Comparisons are more meaningful, therefore, between theoretical results and experimental data obtained for the same material under the same flow conditions and between numerical solutions obtained in the same mesh.

After examining the limits of convergence for the entry flow, the convergence limits for the flows over the transverse slot have to be studied next. From Table 7, it can be seen that the same differences between the limits of the several models and the meshes, as in the entry flow, can also be found in these flows. There are some differences, however, between the three hole configurations P1, P2 and P3 of figures 11 and 12 in ch. 4. The highest limits of convergence in terms of the stress level in the flow over a hole is found for the P-T T and the J-S models. No difference could be found between these two models. For P1, the W-M model showed the next highest limit of con-

vergence, followed by the Leonov-like model. The lowest limit was shown by the UCM model. For the P2 and P3 flow geometries, on the contrary, the W-M and the UCM models gave the same limits and the lowest was given by Leonov. In terms of the flow rates, the highest limits were given by the W-M, followed by the the P-T T, the Leonov-like and the UCM models. The reasons for this reversing between the W-M and the P-T T models with regard to the limits of the flow rate are probably the same as for the entry flow discussed above. In terms of the De , the results are similar to the limits of the previous flow.

Comparing the limits for flow geometries P2 and P3, one can see that the "rounded" corners of P3 have some effect on the convergence. In general, the P3 configuration resulted in higher limits of convergence than the configuration P2. One should note here that "rounding" the corners does not eliminate them, because of the linear elements that are used. This "rounding" merely means that the 90° angle of the corner is replaced by a polygon, which describes the curve of the corner of the experimental die of P3. Therefore, the singularity is not avoided. It is rather surprising, that this change affects the limits of convergence to any degree. The difference may just reflect the added region of slow flow over the hole in place of the missing corners in the P3 geometry. For the Leonov-like model, however, this rounding of the corners decreases the limit of convergence. It is not known at this time why this model shows such contrasting behaviour from the others.

The comparison of the limits between the different flow geometries can only be done qualitatively. MESH2 for the flow over the hole and MESH1 for the flow into the contraction both have around 300 nodes each. They also show comparable limits for convergence. It can be seen in Table 6, however, that the limits increase much faster for the coarser mesh in the entry flow than in the flow over the hole. The major rheological difference between the two flows is the existence of a stronger extensional flow field around the reentrant corner at the contraction than the elongational flow around the corners of the hole. The more pronounced elongational nature of the entry flow may, therefore, be responsible for the higher sensitivity of the convergence of this flow to the mesh refinement. For each mesh and for both flows, the highest overall limits will be given by the P-T T and the J-S models. The W-M model will also give high limits of convergence at least in terms of the stress level and flow rate, even though the elasticity that it predicts is lower than the other models. Since the shear rates for which the limits of convergence occur are well within the shear thinning region, it seems that the models, which predict shear thinning viscosity and normal force coefficients, show higher limits for convergence. A possible explanation for this may be that

the gradients of the stresses near the corner are lower for these models because of the shear thinning and so the order of the singularity may be reduced. On the other hand, the UCM model seems to be limited, by the constant viscosity and the constant primary normal stress difference coefficient (Ψ_1) it predicts, to lower convergence limits than the previous models. The Leonov-like model also gives, in general, low limits for the flows and the meshes that were tried in this work in spite of the shear thinning viscosity and Ψ_1 . The lower limit for this model might be due to the existence of a quadratic in the stress term in the constitutive equation, which may take very high values near singularities such as the corners. The numerical method that was used for this work may not be adequate for this model. Another numerical approach to utilize the Leonov model with excellent results was followed by Uphadhyay and Isayev [88]. The authors used a finite element method which included an upwinding technique similar to the techniques that are used for the integral constitutive equations (integration of the strain tensor (ζ) along the fluid particle paths). No limit of convergence was found in that report, at least inside the useful range of the model. This fact is very encouraging and it may indicate that integral rheological equations that show realistic predictions of the viscometric flows also show less severe limits for the convergence of the numerical methods.

It was shown in this section how the limits of convergence of the numerical solution depend both on the mesh and on the rheological method. In the following section, the accuracy of the numerical results for the flow over a transverse slot will be examined, by comparing the FEM solutions with experimental values of the stresses and the streamlines for the same flow conditions. The same comparison for entry flow will be presented in ch. 5.3.

5.2 Comparison of the Results of the Hole Flow with the Experimental Data

It was mentioned in ch. 2.1.1 that one of the advantages of the FEM is that a general computer code utilizing this method can be written once and then the same program can be used for many different flow geometries and conditions with simple changes in the input data. Therefore, as soon as the code was developed, it was quite easy to generate a large number of numerical results for all the flows and all the different models and meshes. The only limitations were the running cost and the storage capacity of the computer, both of which also concern the success of the developed

method and the meshes that may be used. It was shown earlier that coarse meshes may produce solutions with high oscillations and low accuracy. They are, however, inexpensive to run. On the other hand, more refined meshes may give better results as long as they are not near their limits of convergence but these limits are more severe and usually lower than the ones of the coarse meshes. The cost of the runs for the fine meshes is also much higher. One has then to choose a mesh that represents the best compromise, which in most cases and in view of the problem of the convergence may be closer to the coarse side. Also the rheological model that is used for the simulation may affect the results. In this chapter, the effect of several meshes on the convergence and on the accuracy of the results for flow over a hole will be considered, as well as the differences that may be found in using different models with each mesh.

5.2.1 The Stresses in the Flow Over a Hole

A rigorous mathematical way to examine the effect of mesh refinement on the results of the numerical simulation has not yet been adequately defined. All that is known is that mesh refinement affects the the limit of convergence as it has been demonstrated by Keunings [75]. Since for most viscoelastic models there is no analytical solution, with which to compare the numerical one, the only available method to examine the accuracy of the numerical solution and its improvement (or worsening) with the refinement of the mesh is to compare it with experimental results. In the present work, experimental results were taken from [11] and [86], where values of stresses were found by means of flow birefringence measurements at several points in the domain of the flow over a slot placed transverse to the flow. These stress values could then be directly compared with the results of the numerical computations for the same flow conditions.

In a flow birefringence experiment, one obtains the isochromatic fringes of the stress field using circularly polarized light. These fringes are dark and light streaks corresponding to points in the fluid with the same value of birefringence. The order of these fringes is related to the values of the stresses and for a two dimensional flow it is given by equation 3.65 (from ref. [11]):

$$\bar{N} = \frac{WC}{\lambda'} \sqrt{(\tau_{11} - \tau_{22})^2 + 4\tau_{12}^2}$$

where the Cartesian coordinates are defined so that 1 is the direction of the flow, 2 is the direction normal to 1 that lies on the flow plane and 3 is the third coordinate along which the laser beam is directed. The value of the wavelength of the laser beam (λ') that was used in ref. [11] was 632.8 nm. For polystyrene at 190° C the stress optical coefficient (C) was found to be $4.51 \times 10^{-9} \text{ m}^2/\text{N}$ [11], and the width of the die is listed in Table 4. The above equation with these values was used in the present work to determine the values of \bar{N} . More details on the theory and the technique of flow birefringence may be found in [87] and [11].

A first test of the results of the numerical simulation, therefore, may be the direct comparison between the photograph of the fringes taken from the experimental apparatus and the contours of constant \bar{N} at several points in the flow domain as calculated by eq. 3.65 with the values of τ_{12} and N_1 calculated by the present numerical method. This comparison is shown in Fig. 21, where the direction of the flow is from left to right for both experimental and numerical plots (as it is the case for all such plots in this work). In this figure one may observe that the Phan-Thien Tanner model at 15.35 kPa wall shear stress will give results close to the experimental ones for at least two of the three meshes that were tried. It can be seen there that indeed the stress field as predicted by this model is asymmetric and the stresses (or equivalently the isochromatics) concentrate towards the corner at the upstream plane of the hole, in a manner similar to the experimental data.

Comparing the results of the three different meshes, it can be seen that MESH1 will only give a rough idea of the stress field of the flow. MESH2 will give a much better result than the previous mesh and there is no obvious improvement of the solution by using the finer MESH3. There are also many wiggles in the plots. These wiggles may indicate oscillations of the predicted stress field. Some of the wiggles, however, may be attributed solely to the plotting routine. This routine has to generate a regular grid from the irregular mesh on which the data are input. For the generation of this grid, high order interpolation polynomials are used that may lead to artificial wiggles not present in the original output of the FEM. It is obvious that a better routine to plot the contours is needed.

A comparison of the other models under consideration in this work is given in Fig. 22 for which MESH2 was used. The agreement of the numerical predictions with the experimental data is not so good for the UCM and the Leonov-like models. A possible explanation of this may be that a wall shear stress of 15.35 kPa is very close to the limit of convergence for these two models (see Table 7), while the P-T T and the W M models can converge for this mesh far beyond that

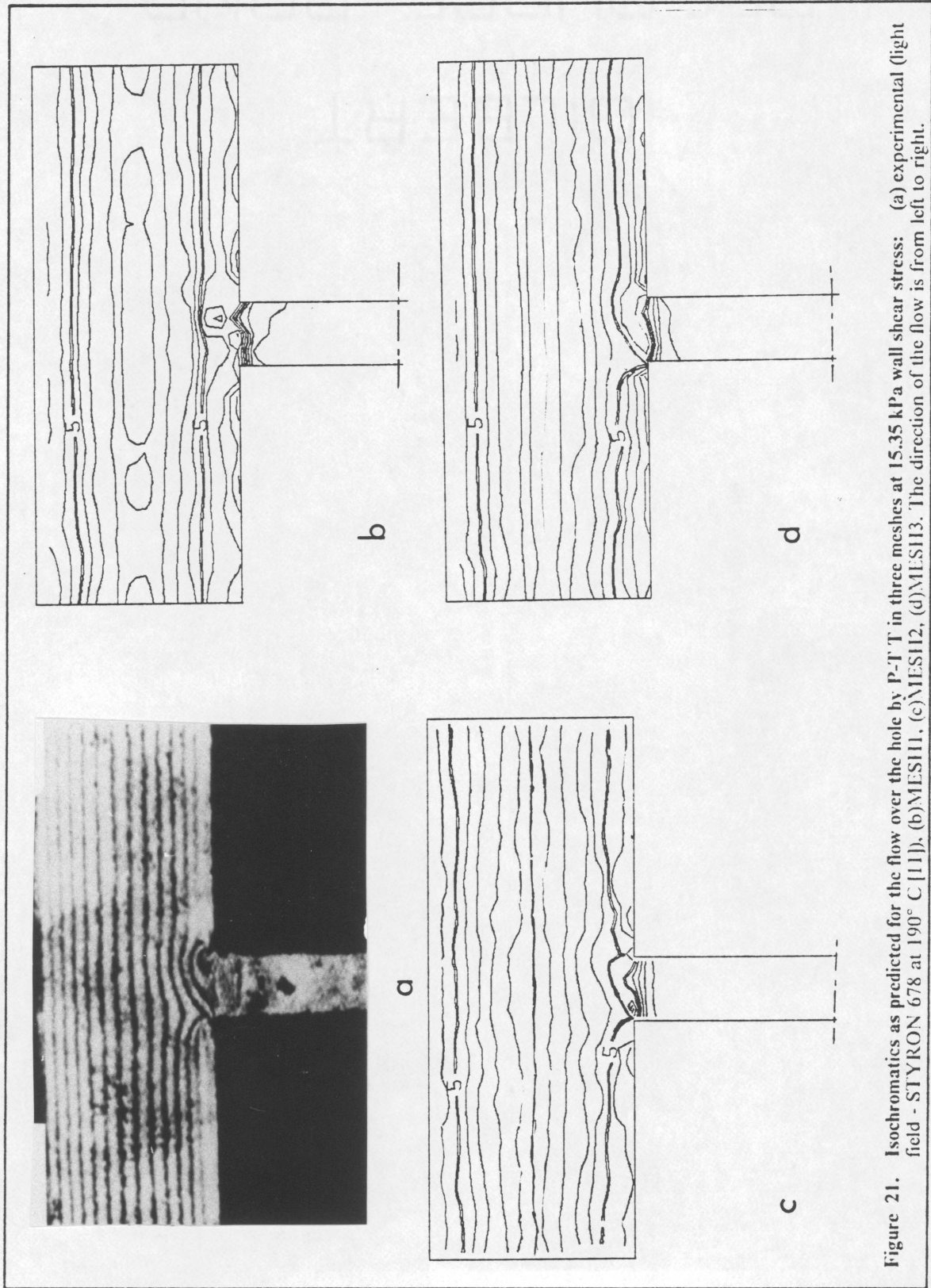


Figure 21. Isochromatics as predicted for the flow over the hole by P-T in three meshes at 15.35 kPa wall shear stress: (a) experimental (light field - STYRON 678 at 190°C [11]), (b)MESH1, (c)MESH11, (d)MESH113. The direction of the flow is from left to right.

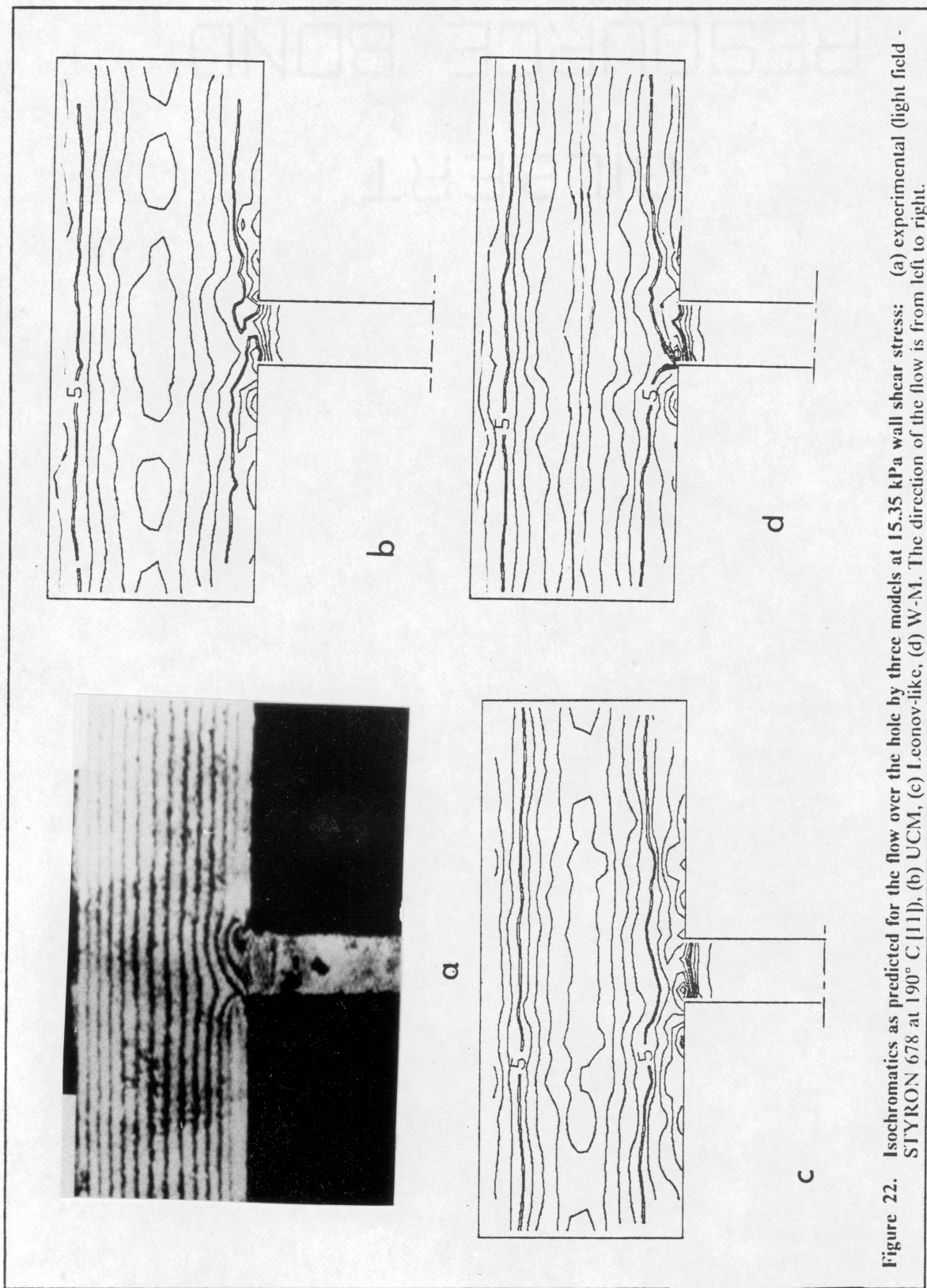


Figure 22. Isochromatics as predicted for the flow over the hole by three models at 15.35 kPa wall shear stress: (a) experimental (light field - STYRON 678 at 190° C [11]), (b) UCM, (c) Leonov-like, (d) W-M. The direction of the flow is from left to right.

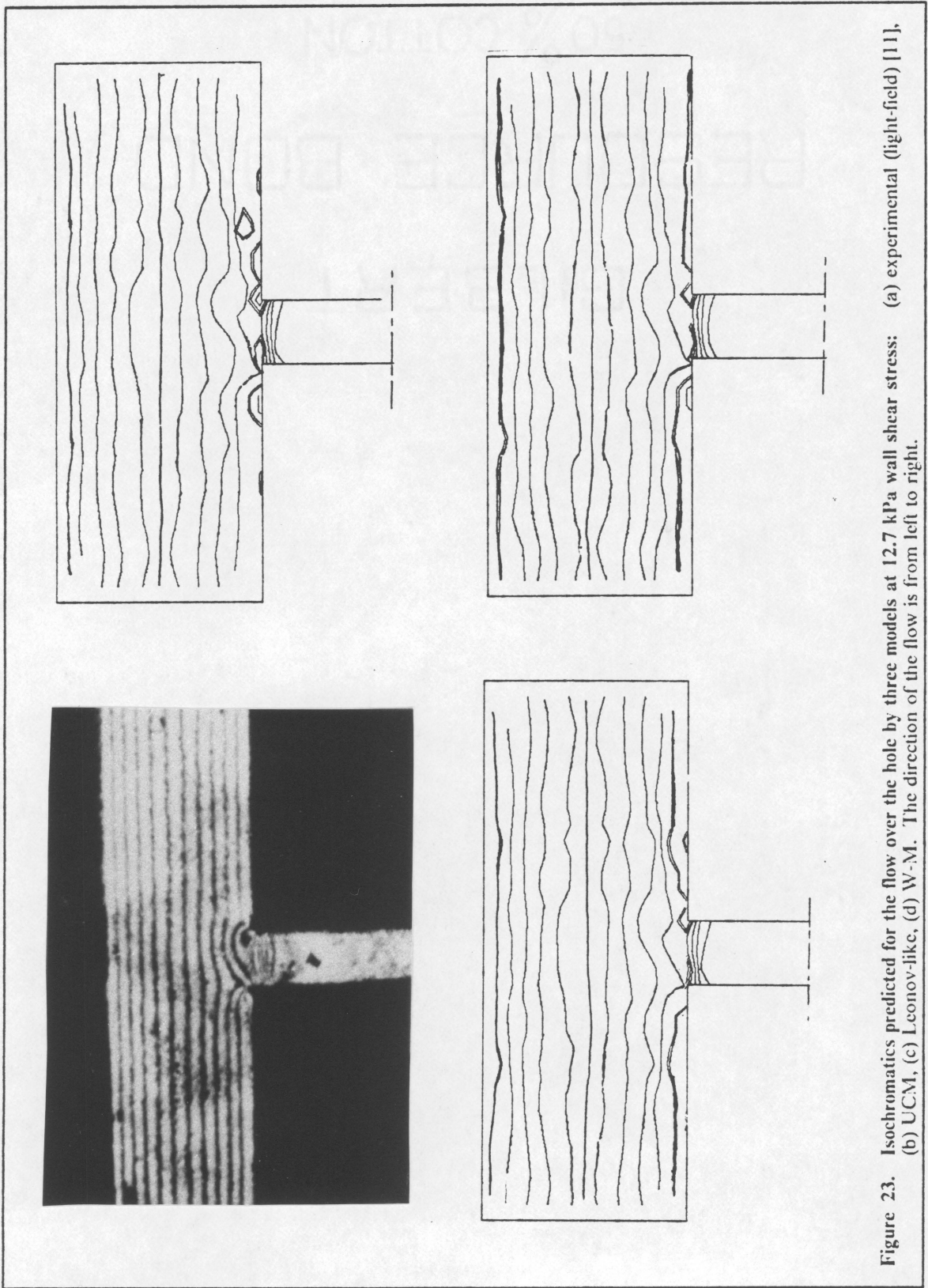


Figure 23. Isochromatics predicted for the flow over the hole by three models at 12.7 kPa wall shear stress: (a) experimental (light-field) [11], (b) UCM, (c) Leonov-like, (d) W-M. The direction of the flow is from left to right.

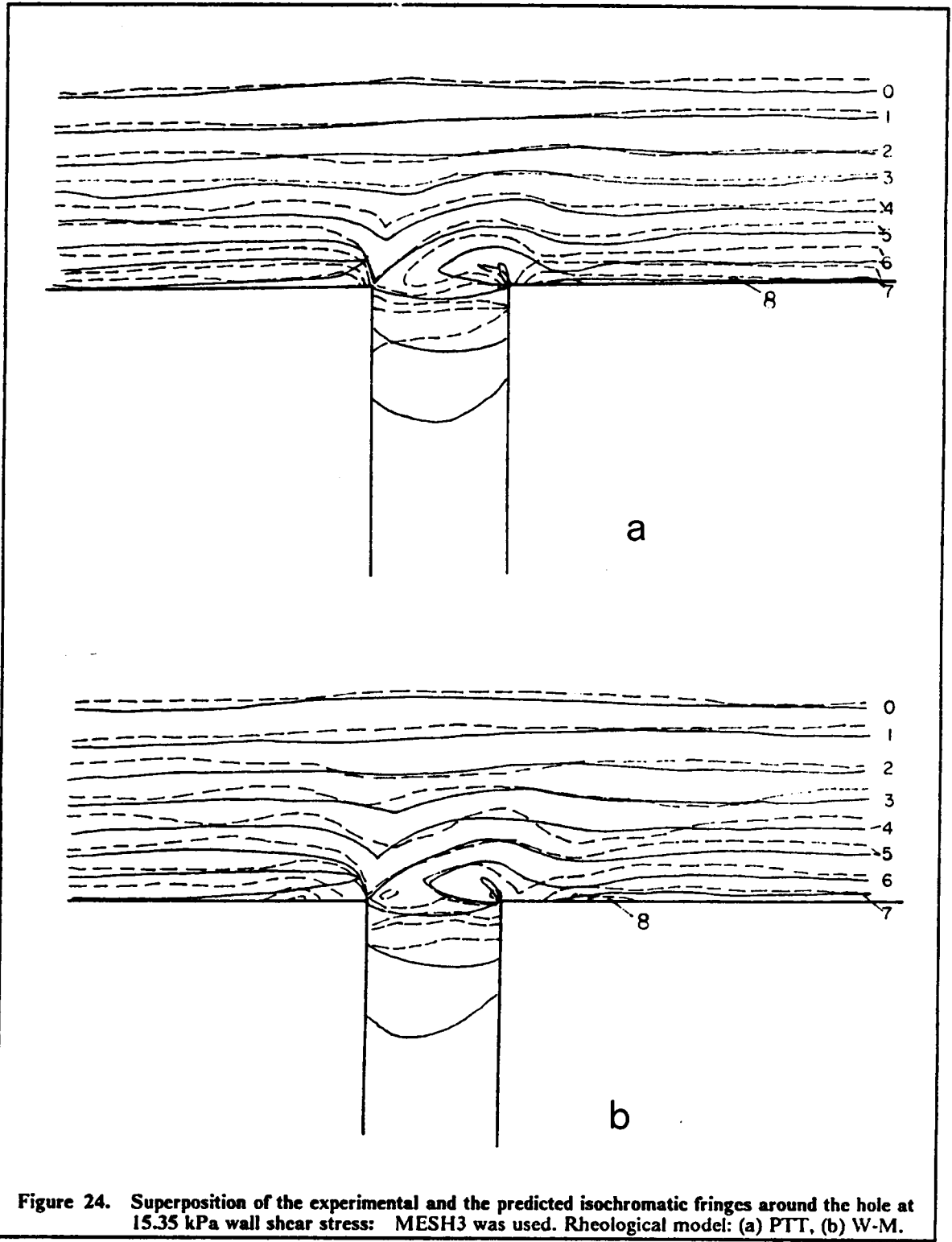


Figure 24. Superposition of the experimental and the predicted isochromatic fringes around the hole at 15.35 kPa wall shear stress: MESH3 was used. Rheological model: (a) PTT, (b) W-M.

stress level. Indeed a better behaviour can be observed for all models in Fig. 23, which shows the isochromatic fringes for a wall shear stress of 12.7 kPa, a stress level that is further away from the limit of convergence for all the models. The P-T T and the W-M models give a rather good agreement with the experimental data as it can be better seen in Fig. 24, where the predicted fringes are superimposed on the experimental ones. This agreement, however, deteriorates near the corners. Also the P-T T model gives a slightly higher fringe order near the wall. Quantitative comparisons can not be made from these plots, however, but the White-Metzner model seems to give the best picture.

A more comprehensive picture may be gained from another set of graphs. Since the corners may be singular points [76], it is expected that a more severe test of the results of the numerical simulation will be the behaviour of the solution around these points. It was chosen here to examine the values of σ_{12} and $\sigma_{11} - \sigma_{22}$ around the two corners at the mouth of the hole. Figure 25 shows the lines along which the values of the stresses were plotted for the comparisons with the experimental data. The plot of the dimensionless σ_{12} (σ_{12}/σ_{12w}) vs a dimensionless x (x/d) at the mouth of the hole (that is along AB in Fig. 25) is shown in Fig. 26a. In this figure are shown experimental data, as well as numerical results from the three different meshes and the P-T T model for a wall shear stress of 8.23 kPa. The same is shown for a wall shear stress of 11.35 kPa in Fig. 26b. The first thing that can be seen in these figures is that there are severe oscillations for all meshes and for the whole width of the hole. The oscillations follow the pattern of the mesh and their wavelengths are the distances between successive nodes. Yet the numerical solutions oscillate around or close to the experimental data. The magnitude of the oscillations decreases in general away from the corners with the refinement of the mesh. The agreement of the numerical and the experimental results also becomes better for the finest mesh, even though one might note that the agreement of the results of the other meshes is also reasonable. The basic asymmetry of the flow across the hole is also apparent here, with the shear stress decreasing sharply near the entrance plane of the hole and then rising towards the exit. High peaks are predicted by the models at the corners (higher than the data) especially in the results of the finer meshes and the agreement is much worse upstream and downstream the region over the hole than inside that region. Upstream and downstream of the hole the experimental results show that the disturbance extends further along the die than in the numerical results. A possible explanation of this may be that the length of the upstream and downstream part of the meshes between the hole and their ends was not enough for the dissipation of

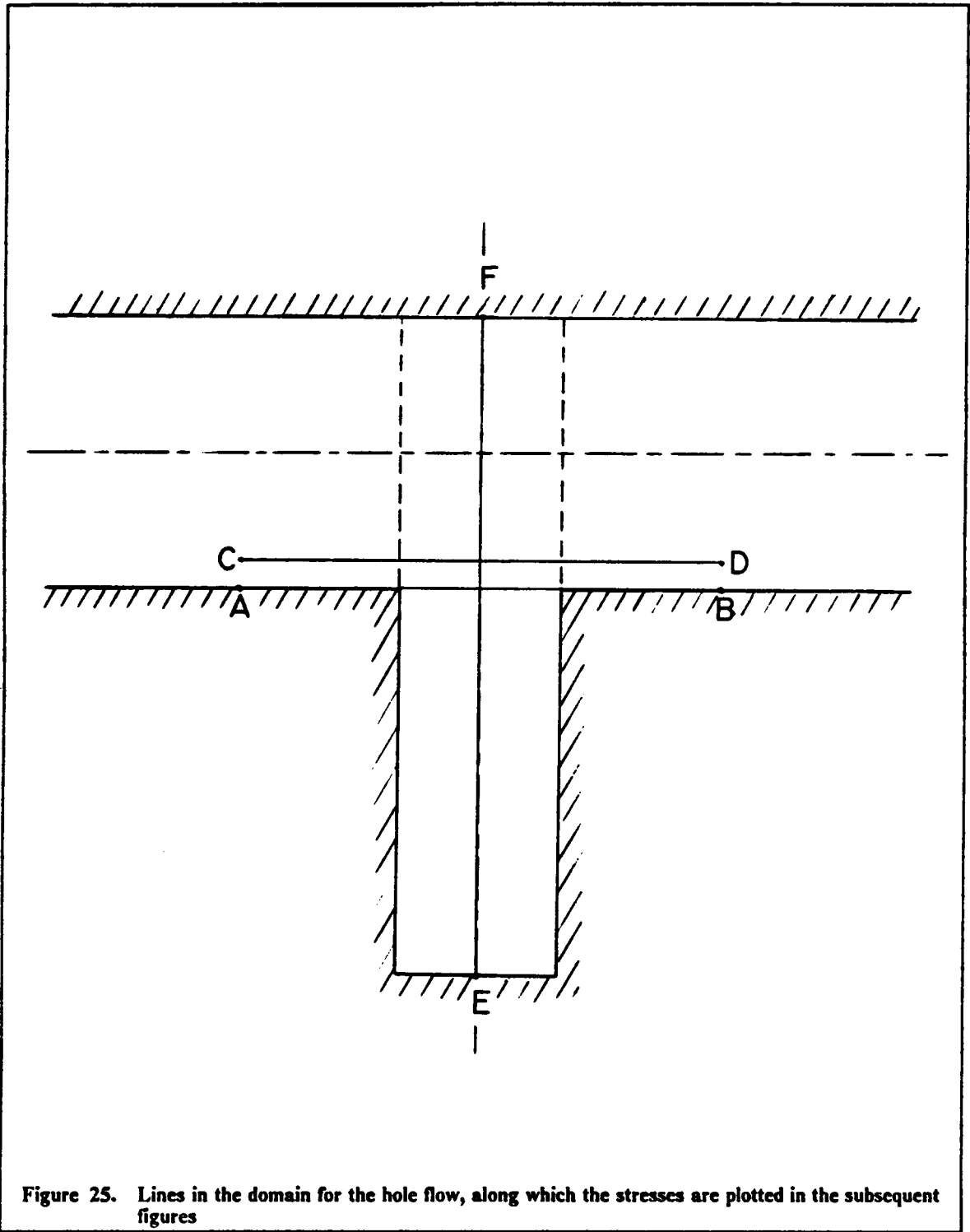


Figure 25. Lines in the domain for the hole flow, along which the stresses are plotted in the subsequent figures

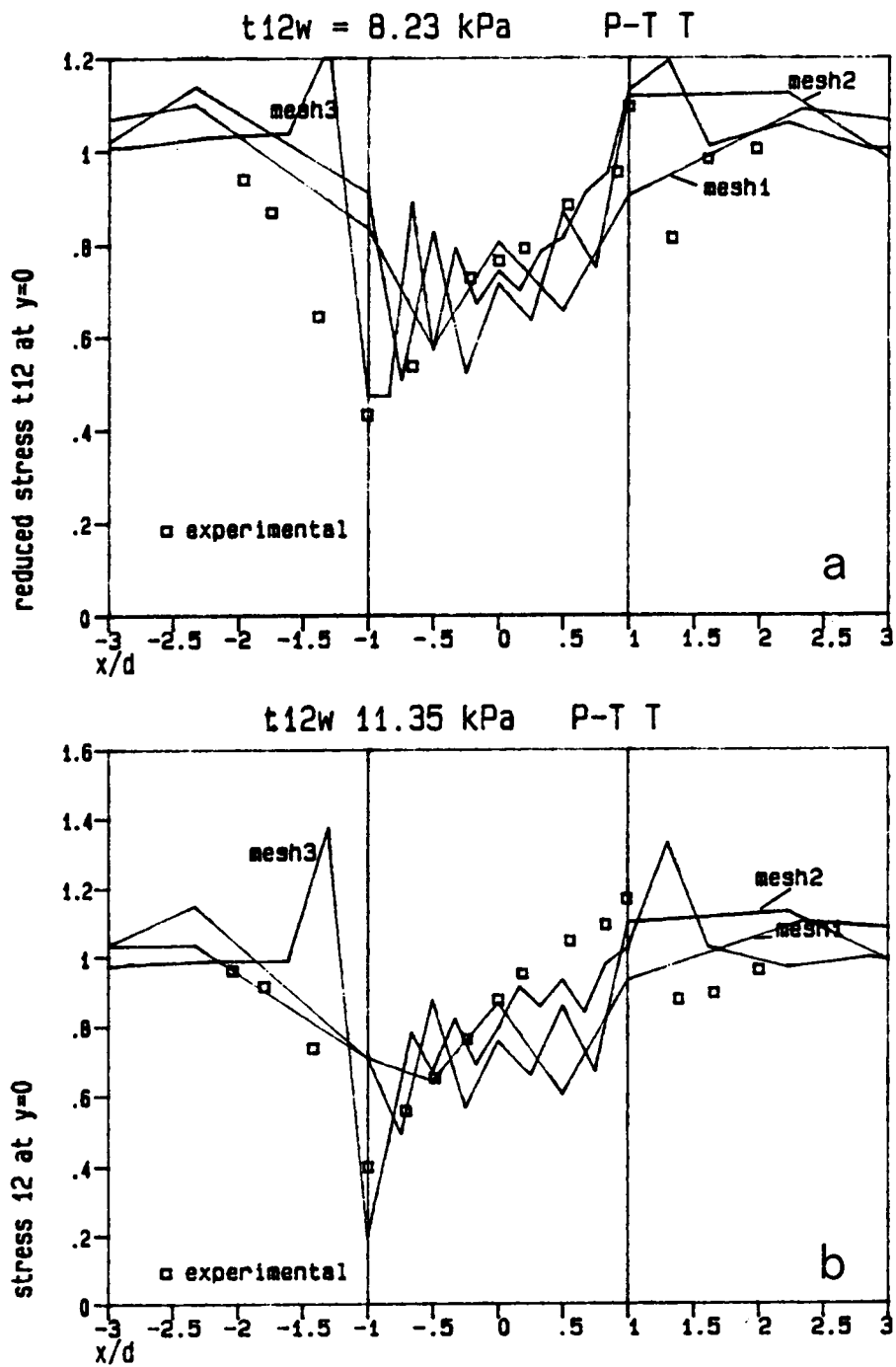
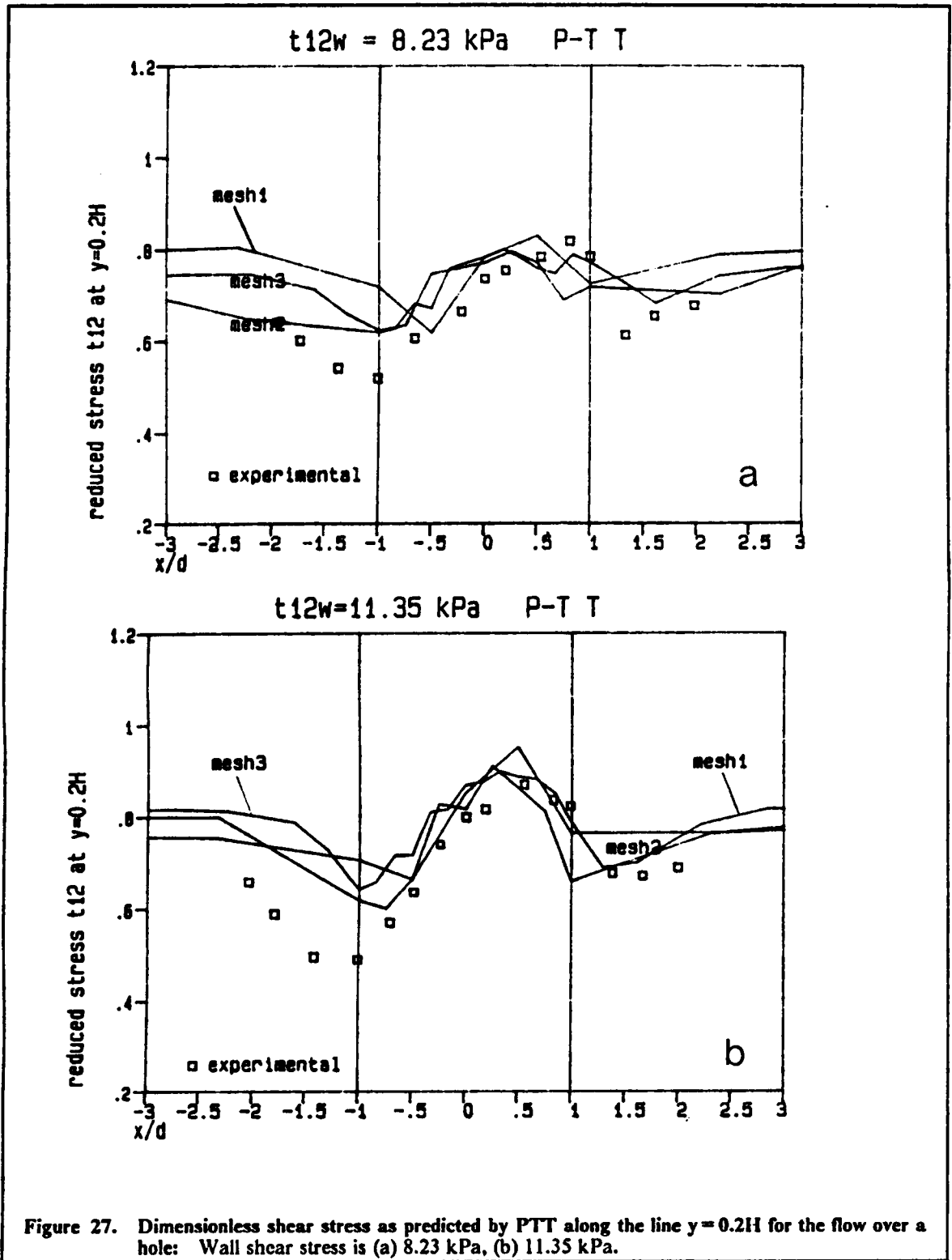


Figure 26. Dimensionless shear stress as predicted by PTT along the mouth of the hole: Wall shear stress is (a) 8.23 kPa, (b) 11.35 kPa.



the disturbance in the flow caused by the hole. So, the imposed fully developed velocity profile at both ends of the mesh forces the deviations from the slit flow to be confounded in an area between the planes that flank the hole or very close to this area. The effect of the limited length of the meshes on the velocity and the stress fields when the assumption of fully developed velocity profiles at the ends is used, as it is the case of the flow over a hole is a subject that needs more study. Examining the photographs in Fig. 21, it can be seen that the disturbance of the isochromatics and, therefore, of the stress field above the hole is eliminated at a rather short distance away from the hole. Further away the isochromatics coincide with those for the flow in a slit die. This distance is at most within $\pm 4d$, which is much shorter than the chosen length of the meshes upstream and downstream of the hole. Physically, then, the meshes used here were long enough to avoid end problems. Whether this length is insufficient for the numerical method, that is, whether it imposes numerical instabilities in the discretized form of the flow equations is a subject that extends beyond the scope of this thesis. This problem was studied by Vrentas et al [72] and by Debaut and Crochet [78] for entry flow and the interested reader should look there for a more detailed investigation.

A little higher up into the slit, at a position $y = 0.2H$ (along the line CD in Fig. 25) the oscillations decrease considerably (Fig. 27). This smoothing of the oscillations a little away from the corner supports the theory that the singularity at the corners may produce the instability of the solution. At $y = 0.2H$ the predicted curves for all three meshes follow qualitatively the shape of the experimental data but the actual agreement does not improve for upstream and downstream of the hole where again the data deviate from the predictions. Again the results of MESH2 and MESH3 are better than MESH1.

The values of $\sigma_{11} - \sigma_{22}$ along the same lines for the same conditions and for the same model (P-T T) are shown in Figures 28 and 29 for values of the wall shear stress of 8.23 and 11.35 kPa. For the plot of $\sigma_{11} - \sigma_{22}$ along the mouth of the hole (Figures 28a and b) one can see that the peaks at the corners and the big undershoot at a point around $x = +0.75d$ are more pronounced in the numerical results, even though their positions are correct. These high peaks reveal instabilities of the numerical method rather than the actual behaviour of the flow as it can be seen by the smoothness of the experimental results. The overall agreement with the experimental data is worse for $\sigma_{11} - \sigma_{22}$ than for the shear stress. The problem of the reduced accuracy of the results upstream and downstream of the hole that was mentioned for the plots of the shear stress is again present here especially at the downstream side of the hole. The limited downstream and upstream length

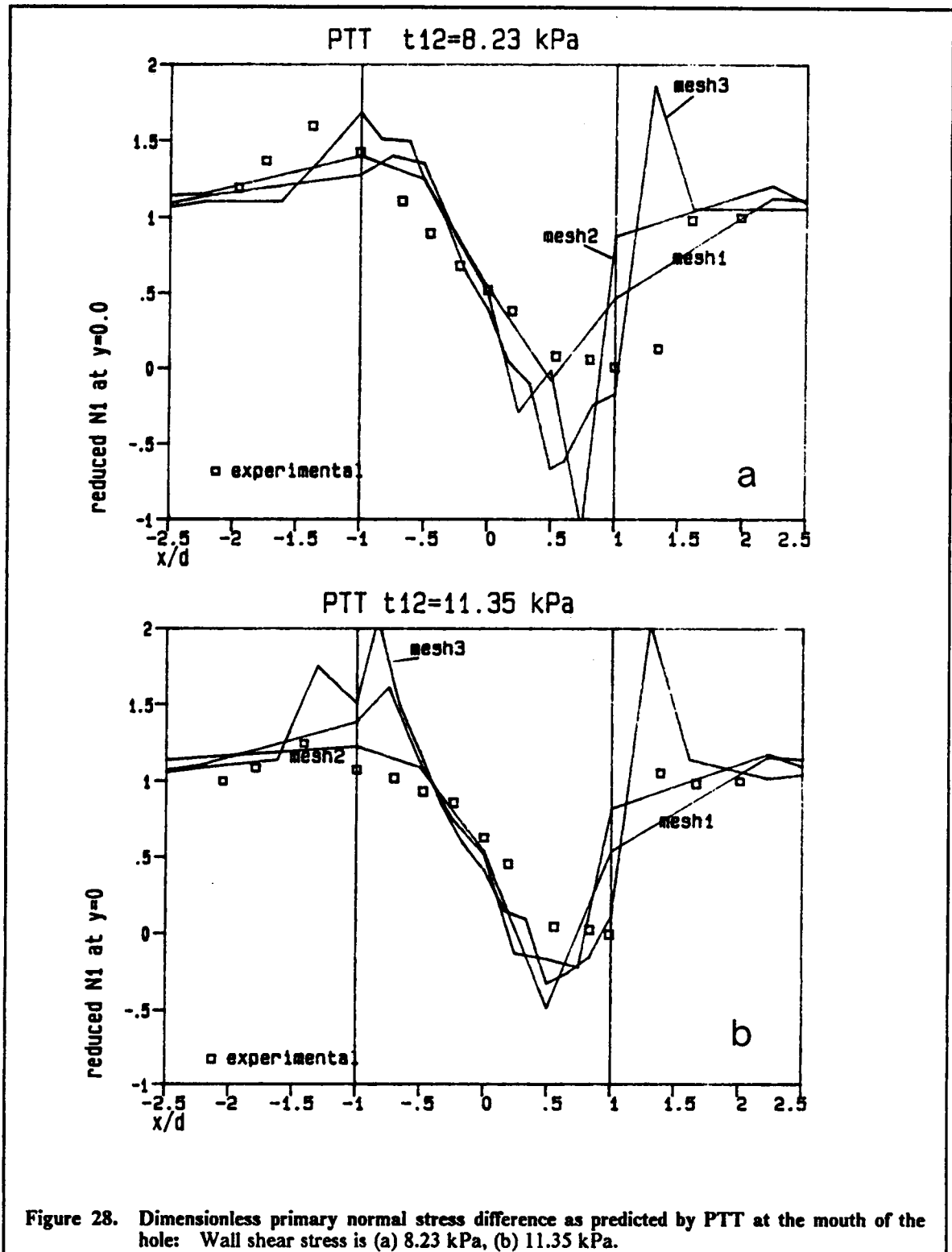


Figure 28. Dimensionless primary normal stress difference as predicted by PTT at the mouth of the hole: Wall shear stress is (a) 8.23 kPa, (b) 11.35 kPa.

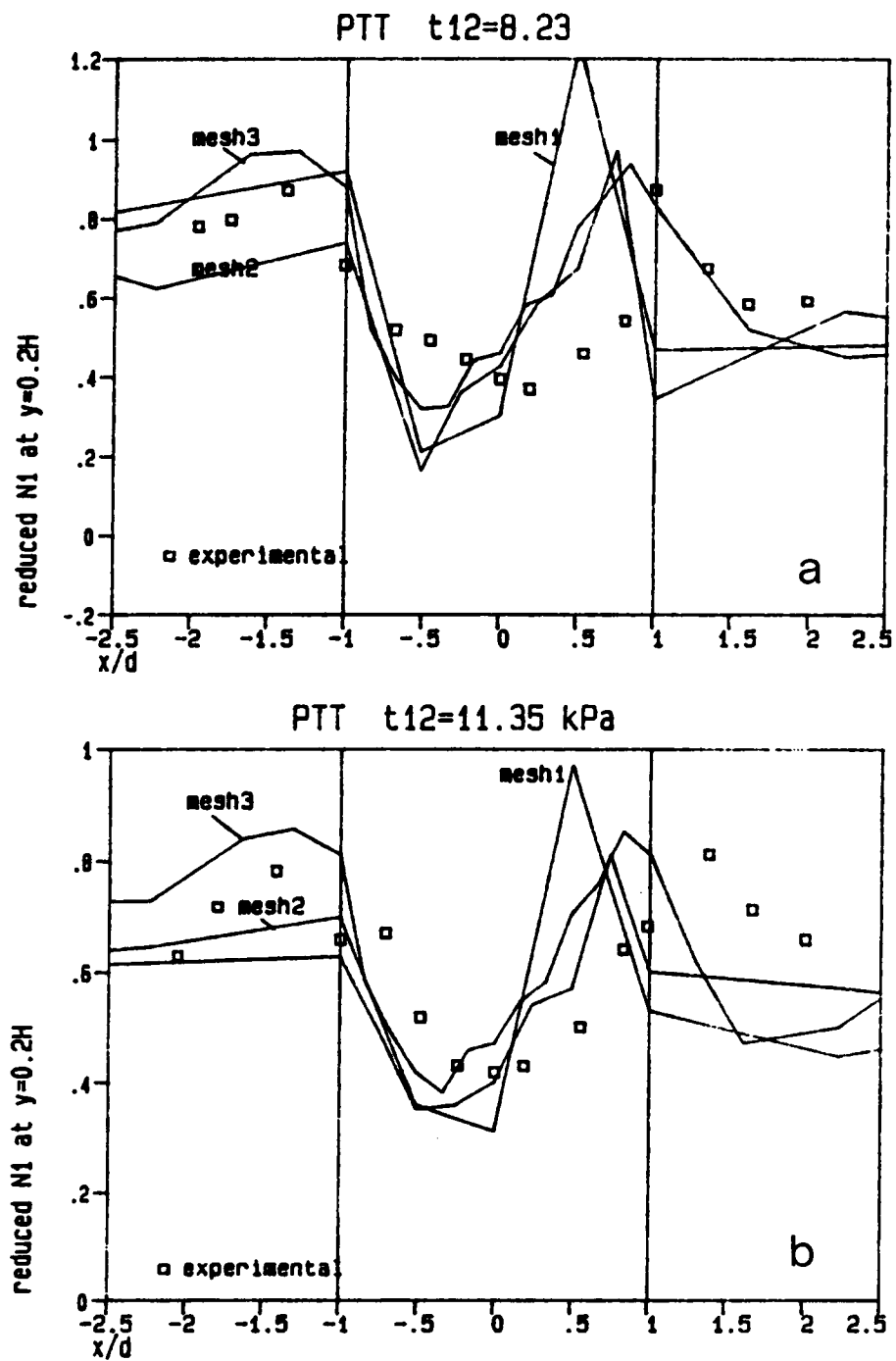


Figure 29. Dimensionless primary normal stress difference as predicted by PTT along a line $h = 0.2H$ for the flow over a hole: Wall shear stress is (a) 8.23 kPa, (b) 11.35 kPa.

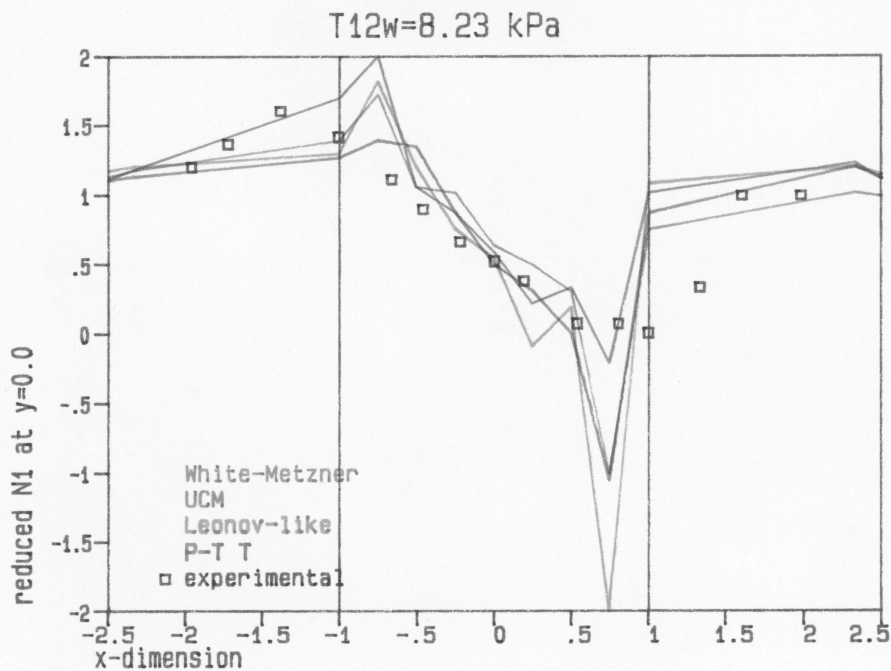
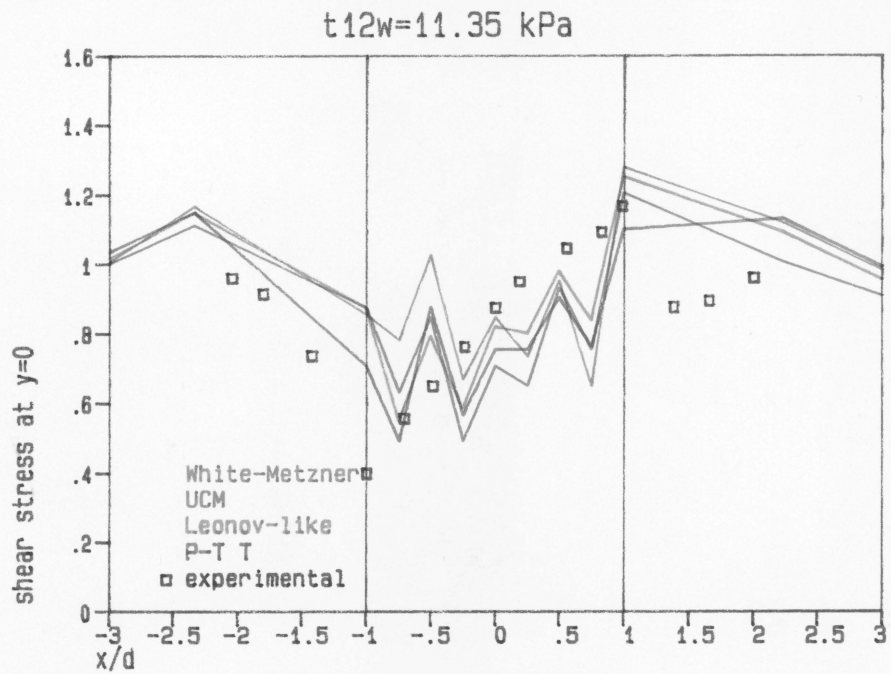


Figure 30. Comparison of the predictions of four models for the stresses at the mouth of the hole: 11.35 kPa wall shear stress. (a) Shear stress, (b) Primary normal stress difference (dimensionless)

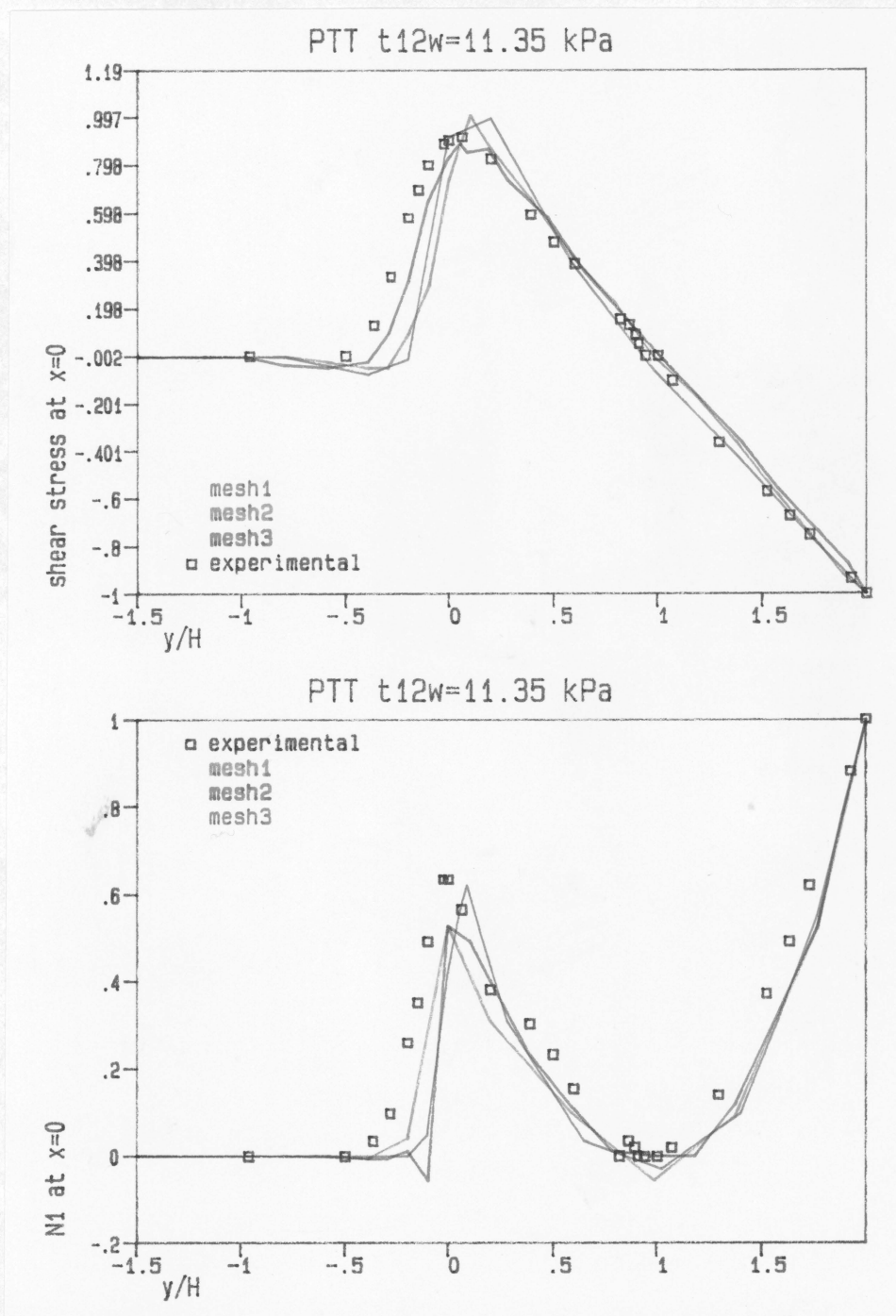


Figure 31. Comparison of the stresses along the centerline of the hole as predicted by the PTT model: 11.35 kPa wall shear stress. (a) Shear stress, (b) Primary normal stress difference (dimensionless).

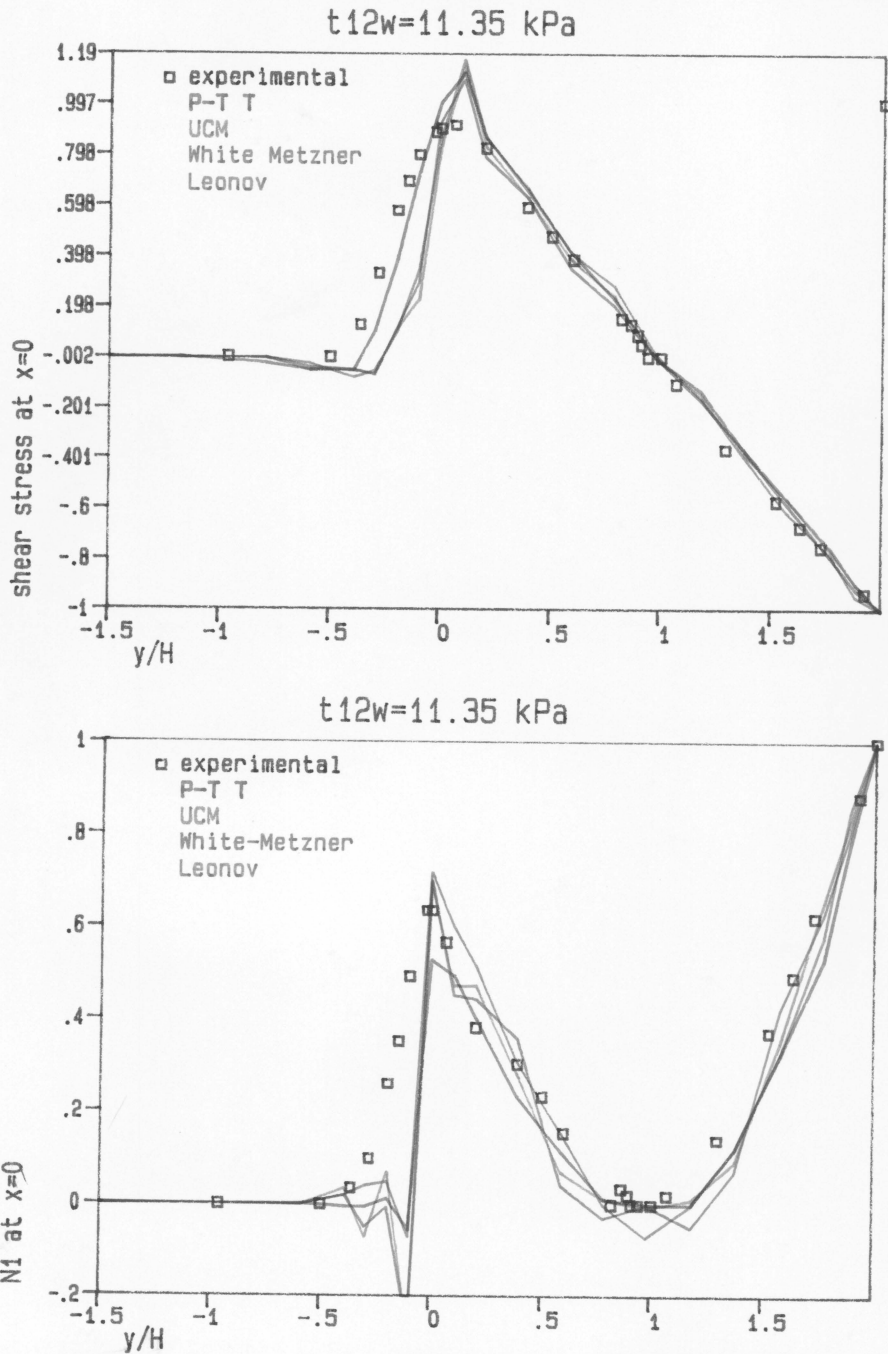


Figure 32. Comparison of the stresses along the centerline of the hole as predicted by three models: MESH2 was used at 11.35 kPa wall shear stress. (a) Shear stress, (b) Primary normal stress difference.

of the mesh may be the cause of this also. The effect of the mesh is also obvious in these figures. It can be seen that the coarser mesh shows the smallest undershoot at $x = +0.75d$ in Fig. 28 but it also shows a slightly lower overall agreement with the data than the finer meshes. The finest mesh shows a rather large undershoot there and also high peaks at the corners. MESH2 also shows high oscillations at $x = +0.75d$ but lower peaks at the corners. At $y = 0.2H$ the shape of the curves of the predicted $\sigma_{11} - \sigma_{22}$ are close to the data (Fig. 29) and the values fall in the same region as the experimental data but the agreement is only qualitative.

The relative behaviour of the several models for the same mesh (MESH2) is shown in Fig. 30. It can be seen in this figure that all the models show reasonable agreement with each other and with the data. It should be noted here that the levels of the stress are low enough in this figure so that all the models are well within their convergence limits. However, all models show the same oscillations between the nodes and the magnitude of the oscillations does not differ significantly between the models. From these graphs it is not possible to make conclusions about the relative quality of the solutions produced by one model versus another at this stress level.

Another set of graphs can be produced by plotting the values of σ_{12} and $\sigma_{11} - \sigma_{22}$ along the centerline of the hole. One expects the instability associated with the two corners to be minimized at the centerline because this line represents the points furthest away from the corners. And this is indeed the case as it can be seen in Fig. 31 and 32. The first of these figures shows the values of reduced σ_{12} along y as predicted by the P-T T model and using the three meshes of the P1 geometry (the narrow hole). It can be seen there that the agreement with the data is very good for all the three meshes. The same is true for the predicted values of $\sigma_{11} - \sigma_{22}$ (Fig. 31b). The comparison of the different models again can not reveal an advantage of using one model over the other as the results of all the models fall very close to each other in the plot of σ_{12} vs y (Fig. 32a). The corresponding plot for $\sigma_{11} - \sigma_{22}$ (Fig. 32b) might suggest that the P-T T model gives slightly better results than the others, especially inside the hole ($y < 0$) but the differences might be too small to be significant at these flow conditions.

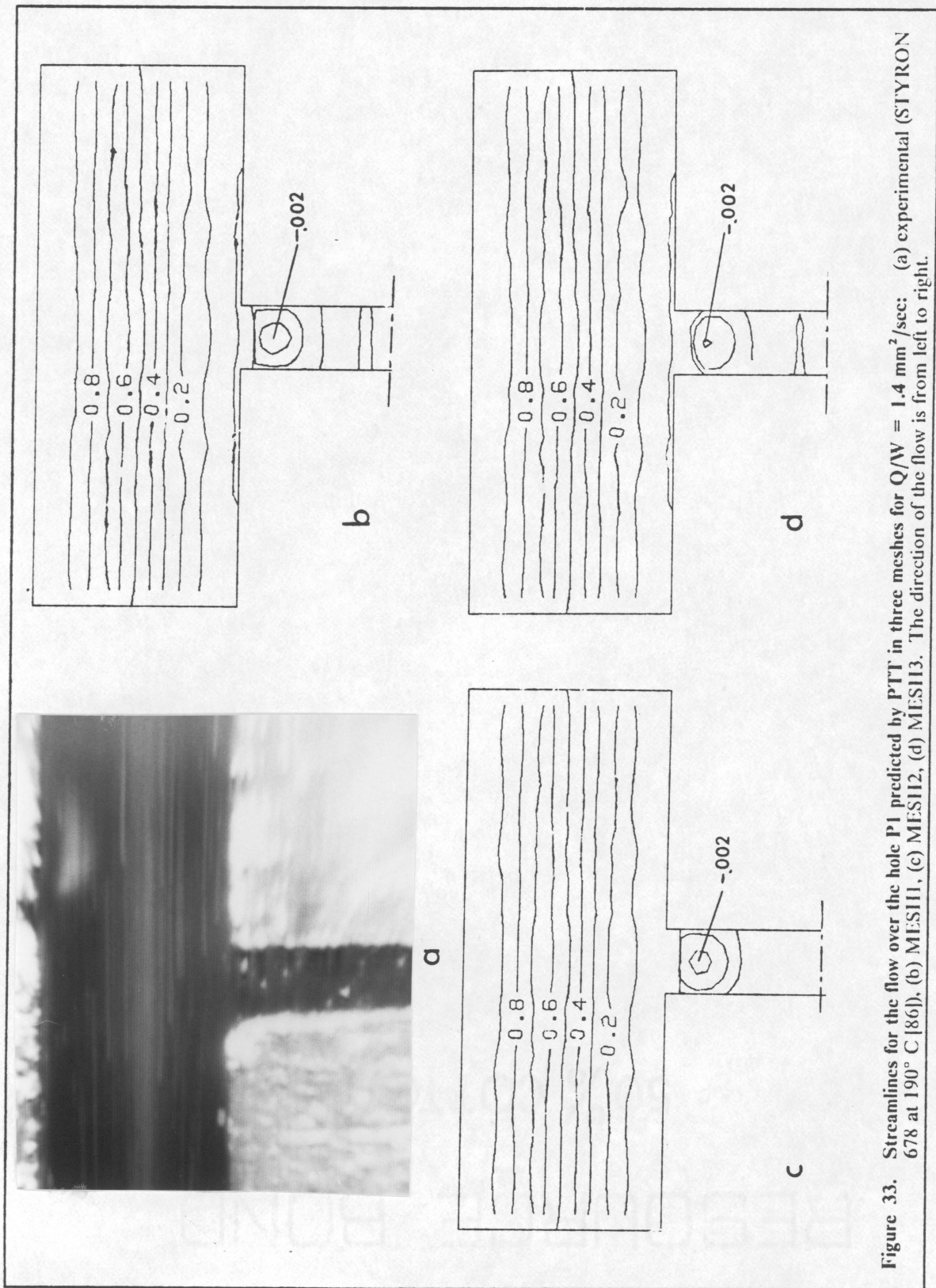
In summary, it seems that in the flow over the hole and for flow conditions that are well within the range of convergence of the method, the stress field that is generated is little affected by the choice of the rheological model (as long as it is among the five models that were studied in this work). For an overall agreement with the experimental data, the P-T T and the W-M models give perhaps the best picture, when the same mesh is used. The other models also give comparable re-

sults, often equivalent to the former two but their low limits of convergence restrict their usefulness at relatively low stress and flow rate levels (or elasticity). In terms of the mesh refinement it seems that MESH1 is not fine enough to adequately describe the stresses in this flow. MESH2 and MESH3 both give acceptable results, with the latter mesh being slightly better. MESH3 is, however, almost 7 times more expensive in CPU time than MESH2. On the quality of the solutions that are obtained by the numerical method it should be mentioned that both the shear and the normal stresses will show oscillations around the corners for all the three meshes. The peaks of the normal stresses that are found near the corners seem to be more unrealistic than the peaks shown by the shear stress. Away from the corners, however, the solutions are smooth and rather accurate, something that supports the assumption that the corners may be a major cause of the oscillations and the instability of the solutions. Ways to reduce this instability like the assumption of limited slip at the neighborhood of the corners [76,95] will probably improve both the quality of the solution around these points and the convergence. Finally, the numerical method will predict a strong asymmetry in the stress field of the flow over the hole, in agreement with the experimental data.

5.2.2 Streamlines for Flow over a Slot

The streamlines are another way to study the flow field, because at steady state conditions these lines are tangent to the velocity vector at every point and represent the paths that the fluid elements follow. The streamlines are lines of constant value of the stream function. In the numerical method that was developed in this work, the stream function was calculated after the velocity field was found. The streamlines could, therefore, be plotted as contour lines of the stream function in the flow domain.

In a flow visualization experiment tracer particles are inserted into the fluid and the streamlines will be shown by the streaks that the images of the tracer particles will make on a long time exposure photograph of the flow. Such a photograph taken from Chang [86] in the P1 flow geometry for the flow of polystyrene at 190° C and a flow rate of 1.4 mm³/sec mm-width is shown in Fig 34. In the same figure the streamlines predicted by the P-T T model for three meshes are also shown. The streamlines are parallel to the wall in the slit die and there is a very slight deflection towards the hole in the area above the hole. The predicted streamlines also show the same behaviour but the deflection over the hole is even smaller than that observed experimentally. The same wiggles are found here as in the plots of the birefringence (Figures 21-23) also partly due to the plotting



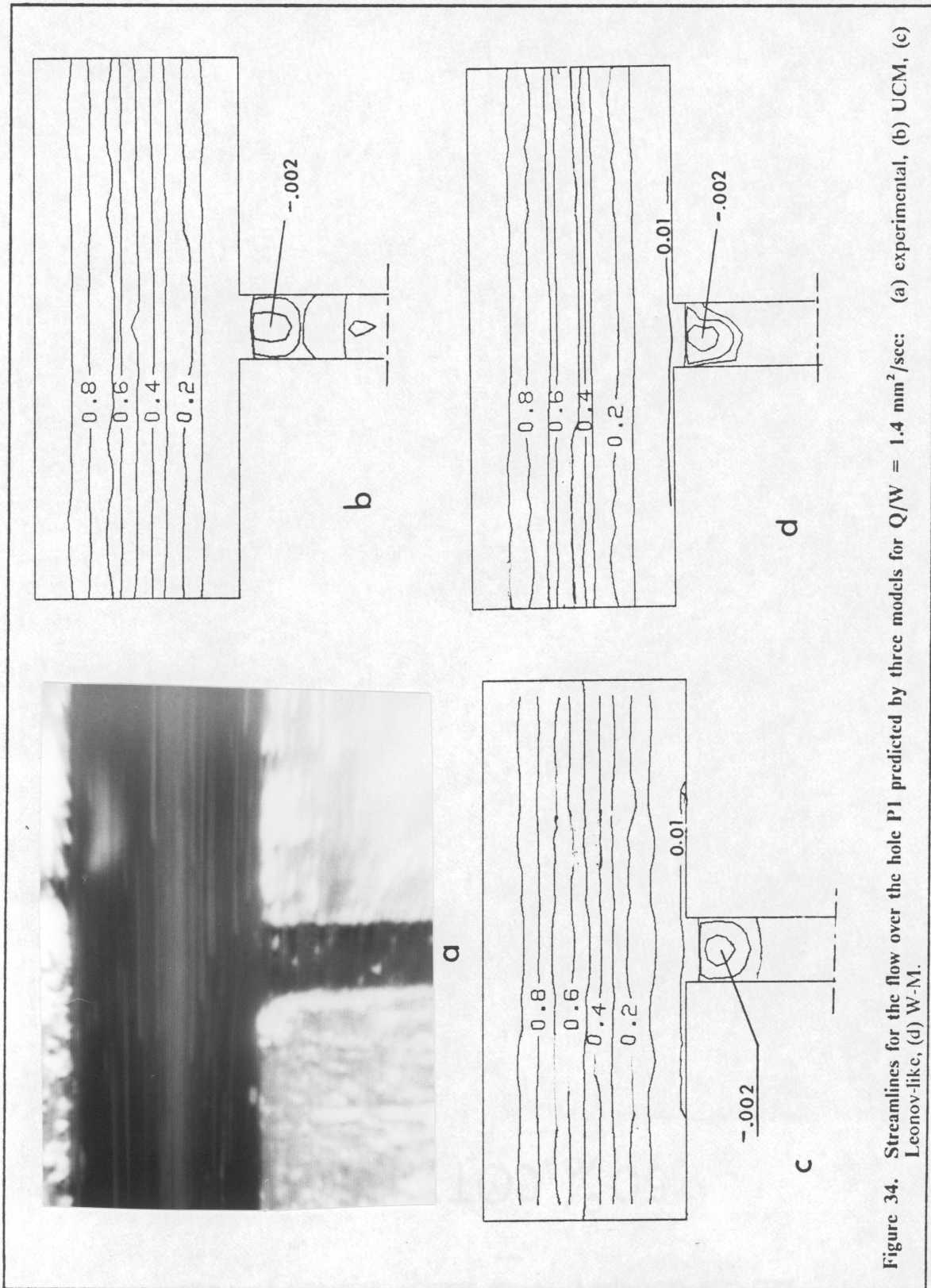


Figure 34. Streamlines for the flow over the hole P1 predicted by three models for $Q/W = 1.4 \text{ mm}^2/\text{sec}$: (a) experimental, (b) UCM, (c) Leonov-like, (d) W-M.

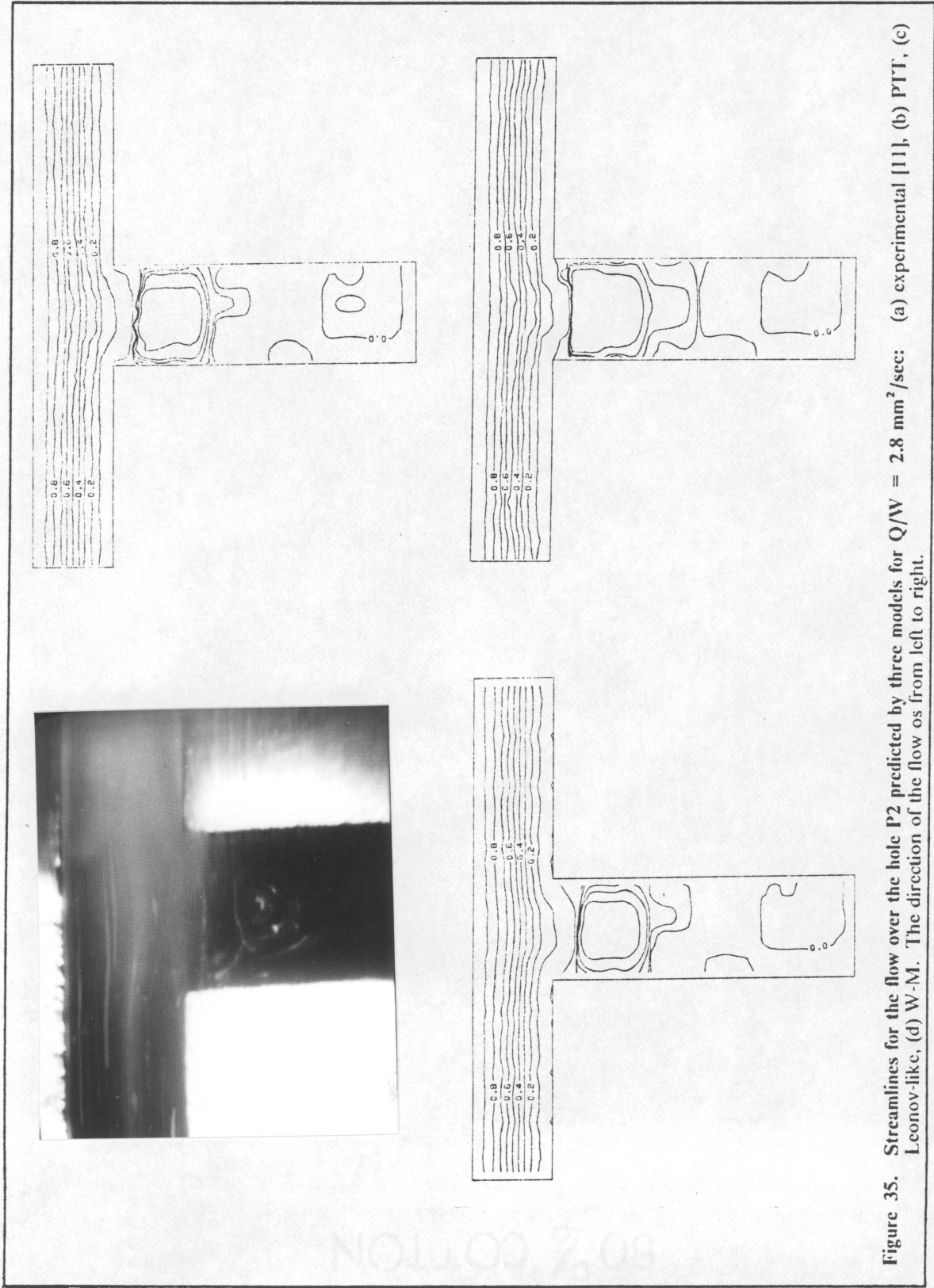


Figure 35. Streamlines for the flow over the hole P2 predicted by three models for $Q/W = 2.8 \text{ mm}^2/\text{sec}$: (a) experimental [11], (b) PTT, (c) Leonov-Ikic, (d) W-M. The direction of the flow is from left to right.

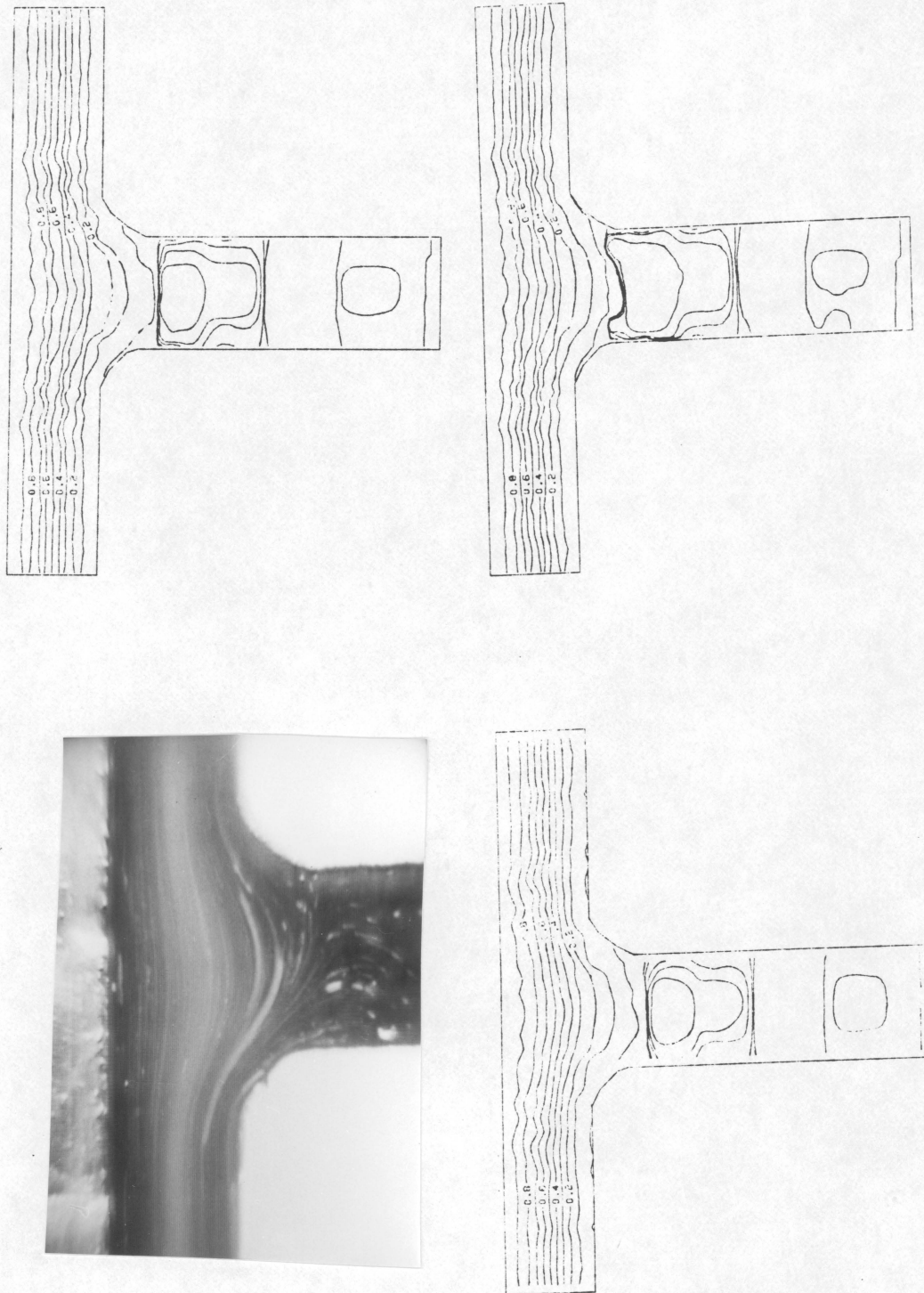


Figure 36. Streamlines for the flow over the hole P3 predicted by three models for $Q/W = 2.8 \text{ mm}^2/\text{sec}$: (a) experimental [11], (b) PTT, (c) Leonov-like, (d) W-M. The direction of the flow is from left to right.

routine. There is also a weak vortex just under the mouth of the hole in the results produced by the numerical simulation that can not be found in the streak photograph. The intensity of this vortex is of the order of 10^{-3} (the streamlines were normalized to a value of 0 at the lower wall and to 1 at the higher). It is difficult, therefore, to conclude whether the vortex is real and not a result of approximation error. On the other hand it is possible that there exists a vortex there but it is too slow to be recorded in the photograph.

The comparison of the results of the several meshes is quite difficult for the streamlines in the P1 flow geometry. All meshes give the same intensity for the vortex that is found inside the hole and the same position for it just under the mouth of the hole. It seems that there is no advantage in using a fine mesh if the desired result is the streamline pattern in this flow geometry. The differences in the results of the several models are also minimum (Fig. 33). Apparently the effect of the narrow hole, P1, on the streamlines is not large enough for differences between the several viscoelastic models to be distinguished. The small effect of this hole is, however, found only in the streamlines. As it was shown in the previous section the stress field is strongly affected by the presence of the hole.

In the flow geometry P1 the width of the hole is much smaller than the height of the die. In P2 and P3 flow geometries the slot is wider than the die height. As a consequence, the deflection of the streamlines over the holes P2 and P3 is greater than over the hole P1. Figures 35 and 36 show these streamlines for flow rates of 2.8 ($\text{mm}^3/\text{sec mm die width}$). Photographs of the particle paths are included in the figures, as well as the predictions of three models for the same conditions. It can be seen there that the numerical simulation will predict smaller penetration of the streamlines into the hole than what the photograph shows. The penetration becomes larger in the hole with the rounded corners. A vortex is also predicted inside the hole for these flow geometries. Here the intensity is of the order of 10^{-2} , an order of magnitude higher than the vortex of P1. The vortex seems to be real and it is verified by the photographs. Its position in the hole changes in the two hole geometries. In the hole with the sharp corners (P2) the vortex is located quite high near the mouth. In the hole with the rounded corners (P3) it lies further low in the hole. The experimental results show an asymmetry around the centerline of the slot. The streamlines dip into the hole more in the upstream half of the hole. The predicted streamlines, however, are more symmetric.

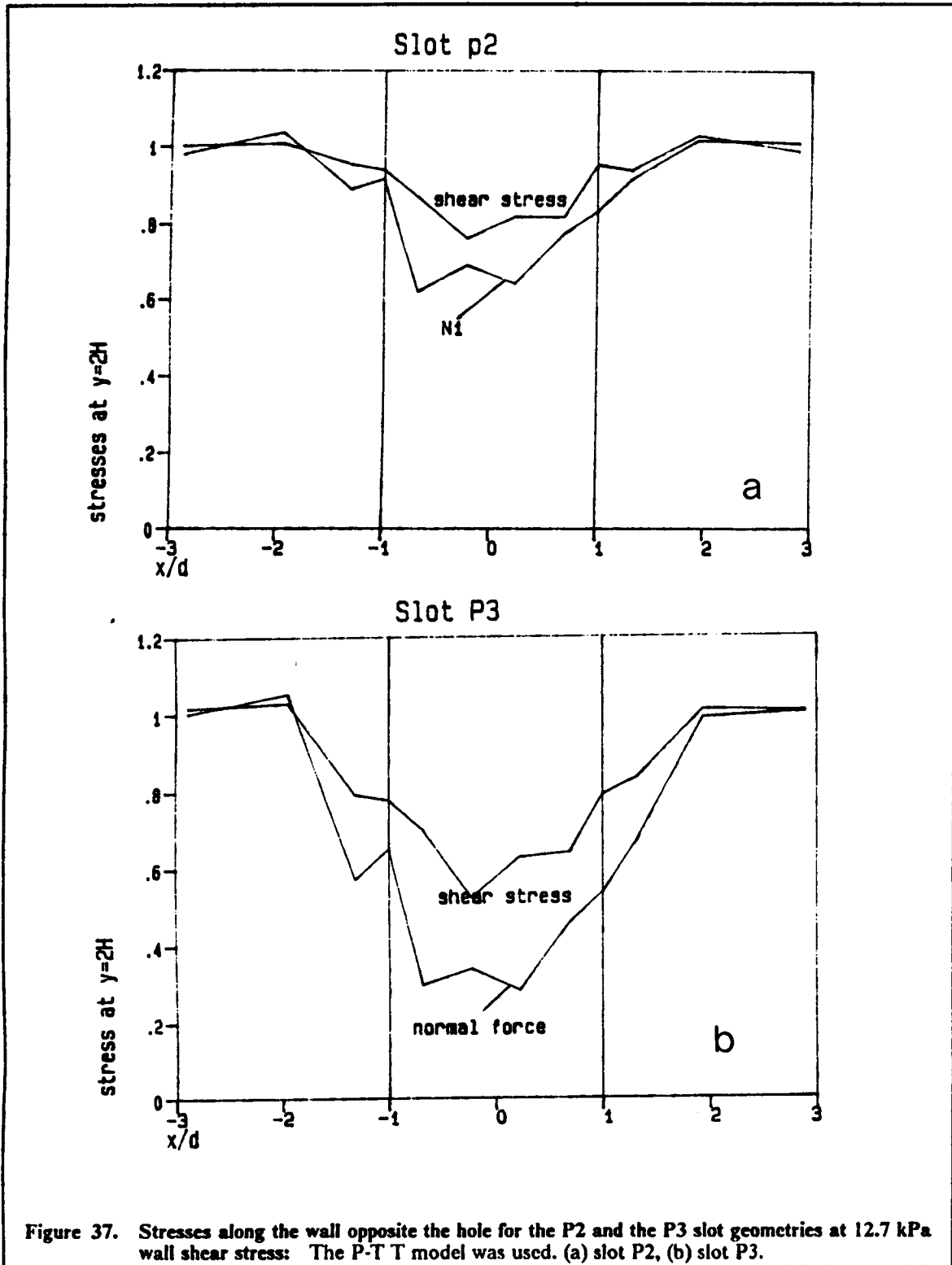
The same strong influence of the presence of the wide slot on the flow above can also be seen in the stress field of this flow. While for the P1 hole the effect of the slot on the shear and the

normal stresses was diminished a little above the mouth of the hole (well below the centerline of the slit die) as can be seen from the birefringence plots (Figures 21-23), the stresses over the wide slots P2 and P3 are affected even on the opposite wall. In Fig. 37 it can be seen that the oscillations of the shear and the normal stress due to the numerical discretization reach the upper wall for both these geometries. Apparently the meshes used for this flow geometry were not fine enough for the accurate presentation of the flow domain and only qualitative conclusions may be made. If these oscillations are overlooked, it may be seen that the values of the stresses go through a minimum at a point upstream near the centerline of the hole. The flow in this case, however, is strongly deformed in the area above the slot and can not be described as approximately viscometric, even in the upper half of the die.

The smaller effect of the hole on the streamlines that is predicted by the numerical method than the effect shown by the experimental results is quite surprising in view of the great effect on the stress field that was described in the previous chapter. Another surprising observation is the low asymmetry of the predicted streamlines around the centerline of the hole. This is again contrary to the results of the flow visualization experiment [86] and in spite of the strong asymmetry of the calculated stress field. It seems that the numerical method (penalty formulation) that was used may not be accurate enough to calculate streamlines because of the poor satisfaction of the incompressibility requirement in the penalty terms.

5.2.3 Pressure Effects in Flow over a Slot

It was mentioned in ch. 2.5 that the main characteristic that distinguishes the flow over a hole of a viscoelastic fluid from the same flow of a Newtonian fluid is the existence of the hole pressure ΔP_H . In most of the experimental studies that have been reported the slot that was used was so narrow that only one transducer could be fitted at the bottom. Therefore, only one pressure measurement could be made there. From the numerical simulation, however, the values of the pressure can be calculated at several points across the bottom and the top of the hole. The values of the hole pressure ($\Delta P_H = (-P + \tau_{yy})_1 - (-P + \tau_{yy})_2$, with "1" representing the wall opposite to the hole and "2" representing the bottom of the hole) calculated using MESH2 are shown in Fig. 38 along the width of the slot for a value of the wall shear stress of 8.23 kPa. Values of the hole pressure calculated in ref. [11] from the experimentally measured stress field using the assumptions of the hole pressure theory are also shown in this figure. The hole pressure evaluated in this way shows



low values at both ends of the hole and a maximum at a point upstream of the centerline of the slot. It can be seen from Fig. 38 that the numerical calculations show a different change of ΔP_H with x . The hole pressure predicted by all models decreases linearly from the entry plane of the hole, where it is positive, to the exit plane, where it is negative. Except for the value of ΔP_H at $x = -d$, the predicted hole pressure is constantly lower than the experimental value. The differences between the models are again small. The slope of the curves is the same, but the curve for the Leonov-like model is shifted slightly to higher values than the other models, the curves of which fall close together. All the models predict a positive value of the hole pressure at $x = 0$. Since this is the point, where a well centered pressure transducer will make its measurement, the value of ΔP_H at $x = 0$ is used for the comparison with the direct experimental measurements. This comparison is shown in Fig. 39, where the hole pressure is plotted versus the wall shear stress in the slit die. Since no consistent improvement to the values of ΔP_H was found with the refinement of the mesh, values taken with MESH3 are plotted in this figure at low shear stress levels, while the values of ΔP_H at higher τ_{12w} were taken with MESH1. It may be seen there that the agreement between the experimental data and the predictions of the models is by no means good, the experimental data showing much higher values for the hole pressure than the numerical results. The predictions also fall lower than the line $\Delta P_H = 0.25N_1$, which is also shown in Fig. 39. No model shows any significantly better agreement with the data. As it was said in chapter 2.1, the penalty formulation may be responsible for the reduced accuracy of the results for the hole pressure.

It may be interesting to note here that the models do show differences in the values that they predict for the isotropic pressure P and the normal component of the extra stress τ_{yy} that come into eq. 2.90 for the calculation of the hole pressure. All models will predict a constant value of P and a zero value of τ_{yy} at the bottom of the hole because no flow occurs there. On the opposite wall, where the flow deviates very little from the slit flow (at least for the P1 slot geometry), the values of τ_{yy} predicted by the W-M and the UCM models are zero. The P-T T and the Leonov-like models, however, predict a non-zero value for τ_{yy} there. The isotropic pressure at the wall opposite the slot is predicted by all the models to decrease linearly with x . Despite these differences, though, the resulting values for the hole pressure are very close for all the models.

The hole pressure across the hole for the slots P2 and P3 can be seen in Fig. 40. Both these slots show a positive ΔP_H at the centerline of the hole and a linear decrease with x . The values of ΔP_H calculated for the two slots are of the same order as in the slot P1. This relative insensitivity

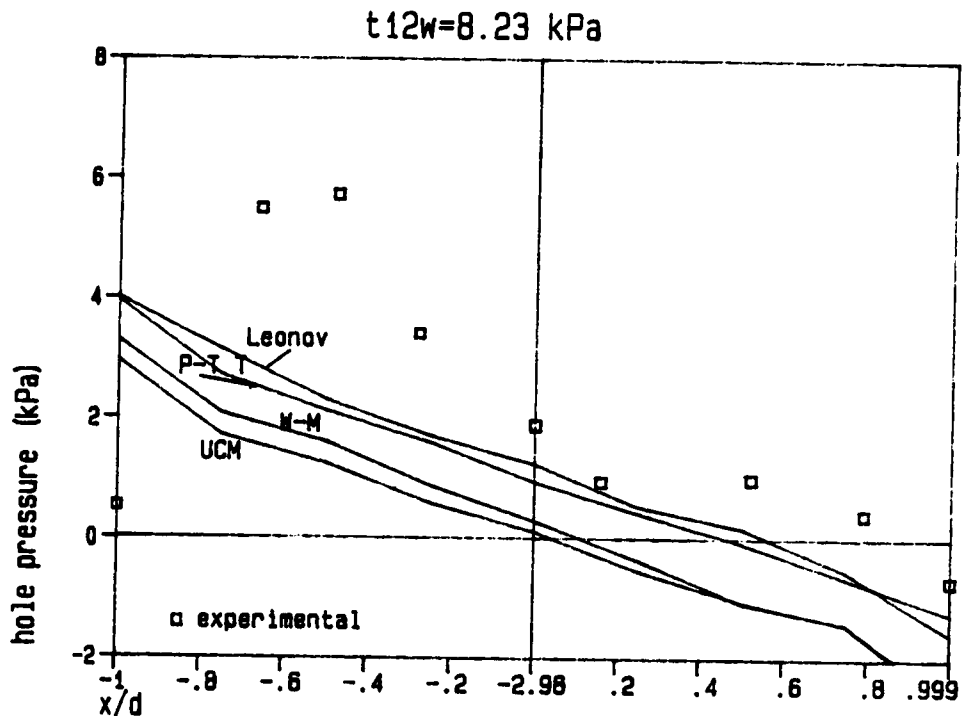


Figure 38. Hole pressure across the hole as predicted by the several rheological models at 8.23 kPa wall shear stress: MESH2 for slot P1 was used. Symbols represent values calculated by integrating the shear stress derivative ($d\sigma/dx$) from the bottom of the hole to the opposite wall (from ref. [11]).

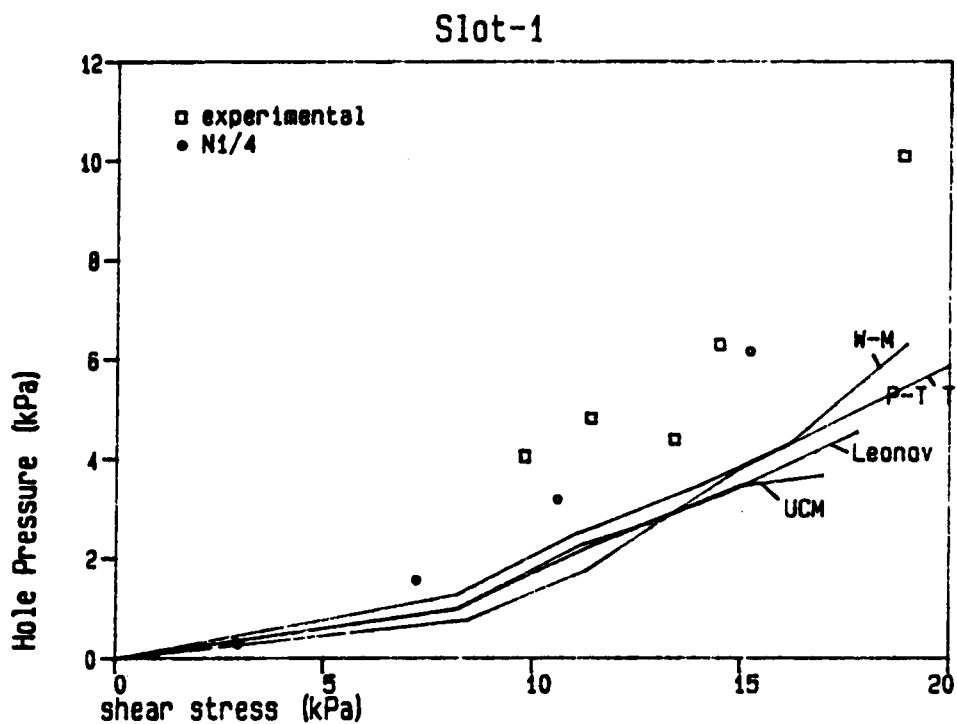


Figure 39. Hole pressure as a function of the wall shear stress for the P1 geometry: Symbols represent experimental values measured in slot P1 for polystyrene at 190° C (ref. [11]): (o) : N₁/4, (□) : ΔPH.

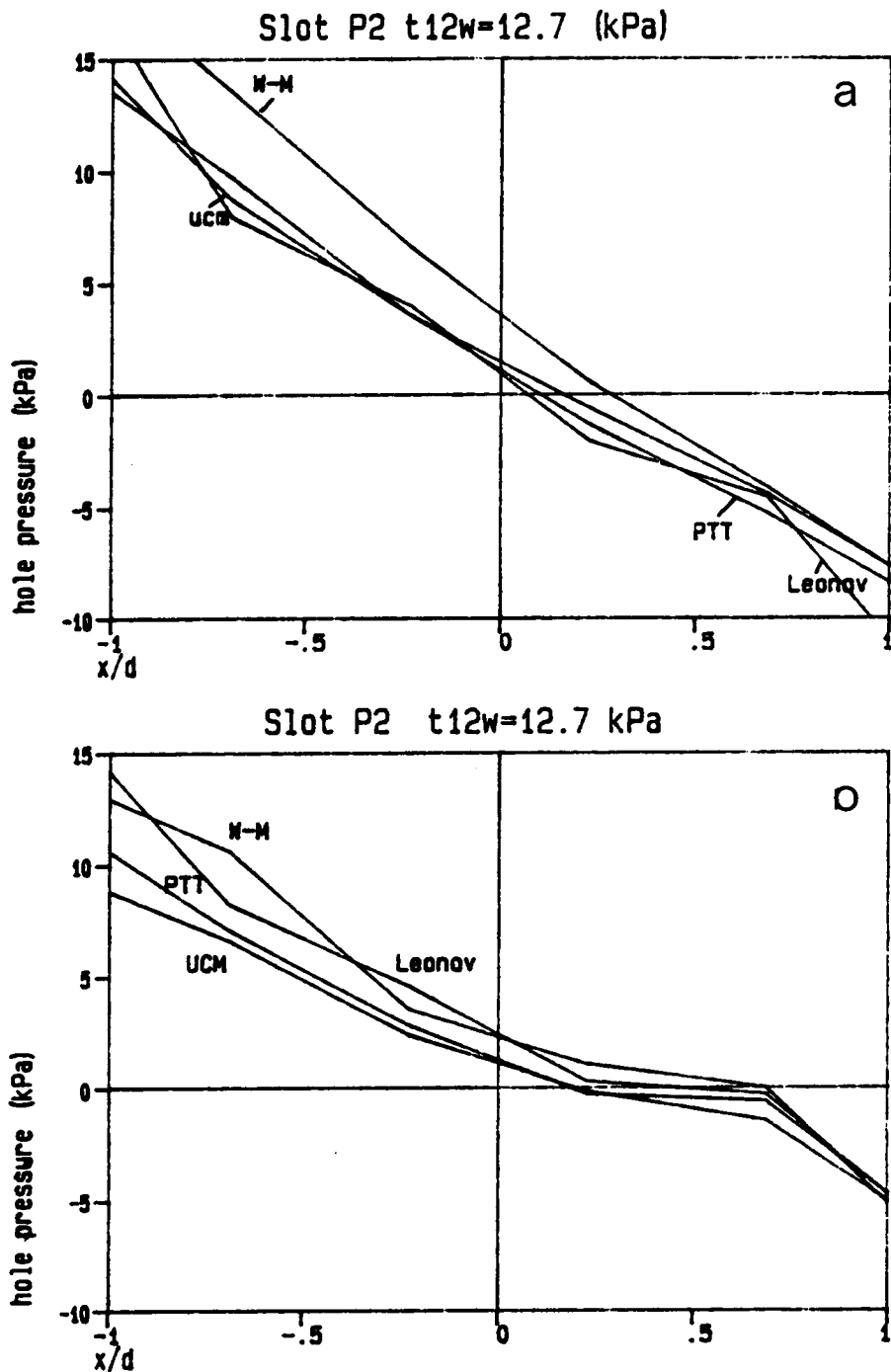


Figure 40. Hole pressure across the hole as predicted by the several rheological models for P2 and P3 slot geometries: Wall shear stress 12.7 kPa. (a) slot P2, (b) slot P3.

Table 8. Values of $\Delta P/L$ (kPa) for 12.7 kPa wall shear stress predicted by four models

Model	Without Slot	Slot P1 MESH2	Slot P2	Slot P3
P-T T	10.0	9.3	8.8	7.8
W-M	10.0	10.1	10.2	9.6
L-1	10.0	9.7	9.3	8.4
UCM	10.0	10.1	8.94	8.0

of the hole pressure to the width of the hole was also found in ref. [11] and it is found in spite of the strong disturbance of both the velocity and the stress fields in the region over the wide hole. The effect of the rounded corners on the value of ΔP_H is also minimal, except that for the W-M model, where the hole pressure decreases. The slopes, however, of the curves in Fig. 40 are different for each slot, the slot with the rounded corners showing the lower gradient.

Some influence of the hole can also be found on the total pressure drop ($\Delta P/L$) along the die. Table 8 shows this pressure drop calculated along the top wall of the die for the three slots, as well as for the case without a slot (slit die flow). It can be seen there that the presence of the small hole affects $\Delta P/L$ very little, usually decreasing its value slightly. As the hole becomes wider, the pressure drop along the die decreases. It decreases even more for the die with the slot with the rounded corners. It is obvious that as the hole width increases, the flow becomes more like an expansion/contraction flow with the hole acting as the region between the expansion and the contraction and thus lowering the total pressure drop.

5.3 Results of Flow into a Contraction

The flow of viscoelastic fluids in an abrupt contraction has been studied quite extensively in the literature as a test problem for evaluating numerical methods because, even though it represents a simple geometry, it shows the differences between viscoelastic and Newtonian fluids. Some of the reports on the results of the numerical simulation of this flow have been described in chapter 2.5. In the following, the results of the numerical method that was developed in this work will be described and compared with results of flow birefringence measurements and photographs of the streamlines. In this section the emphasis is given again on the effect of the mesh refinement and the differences between the results of the several rheological models. The existence of the corner vortex will be examined in section 5.3.2. The entrance pressure loss is another quantity of interest and it will be studied in section 5.3.3.

5.3.1 Stress Field for Flow into a Contraction

Flow birefringence experiments for this geometry were done by White [85] in a die with the same dimensions as the meshes used in the numerical simulation of this work. As in the case of the flow over a transverse slot, the picture of the isochromatic fringes that were photographed during

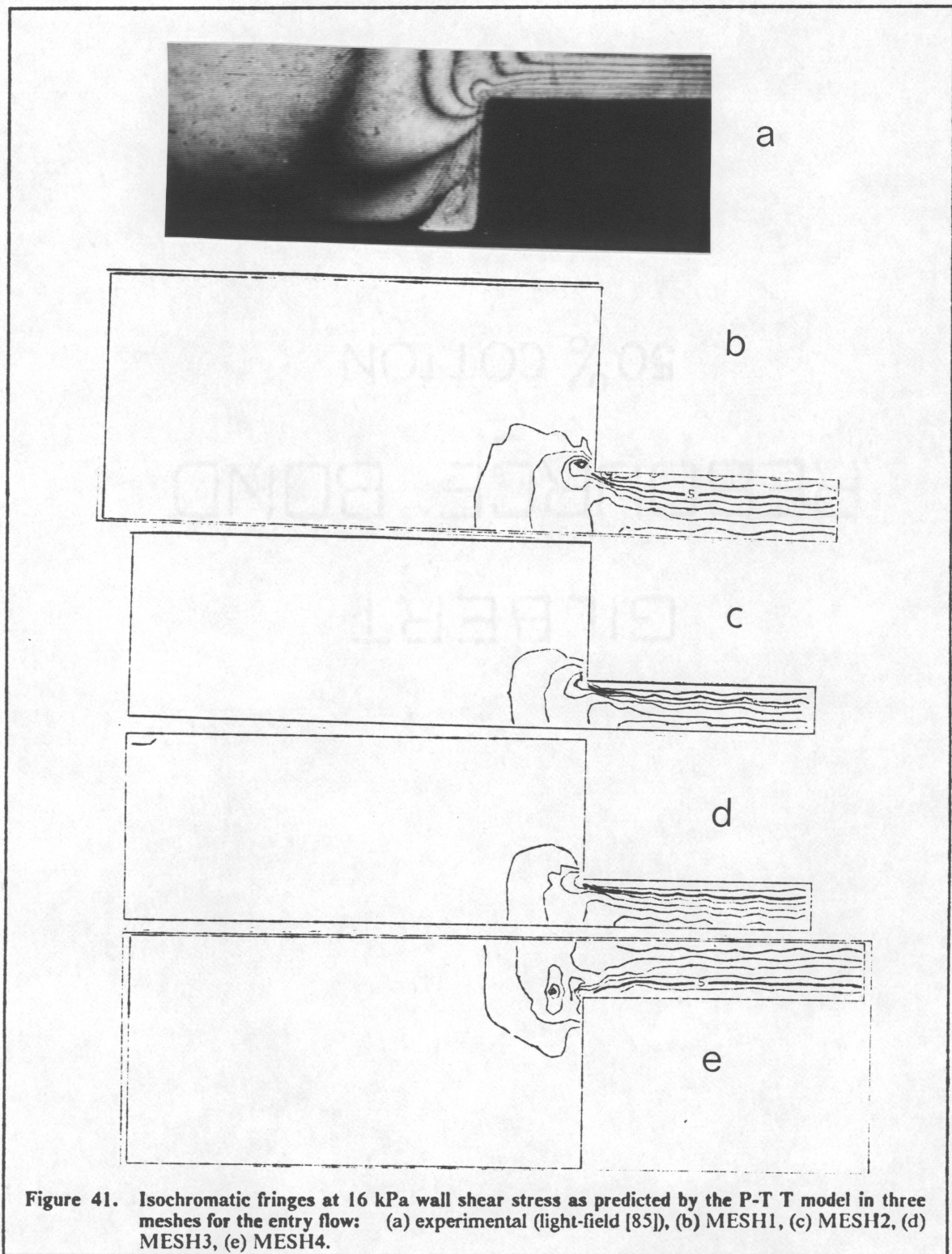


Figure 41. Isochromatic fringes at 16 kPa wall shear stress as predicted by the P-T T model in three meshes for the entry flow: (a) experimental (light-field [85]), (b) MESH1, (c) MESH2, (d) MESH3, (e) MESH4.

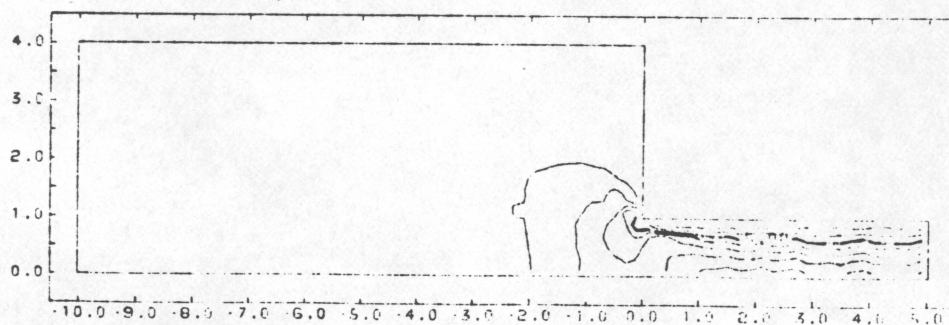
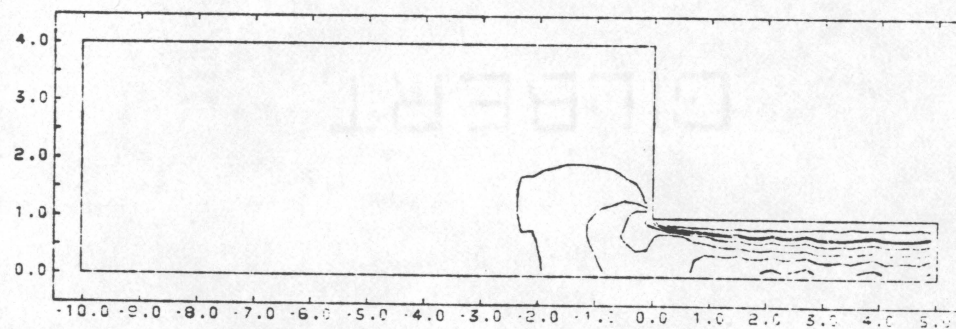
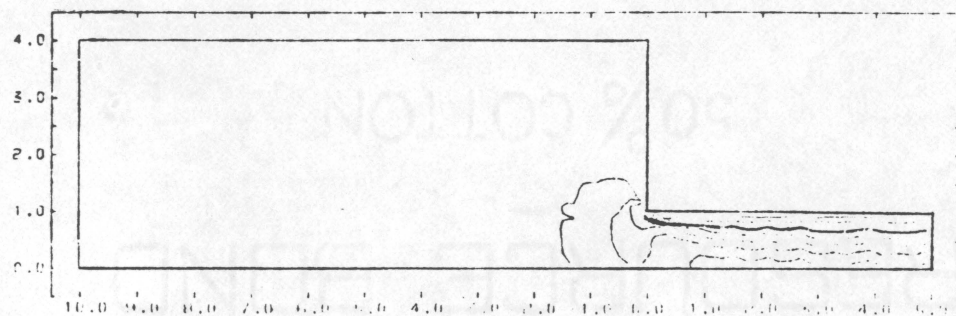


Figure 42. Isochromatic fringes at 16 kPa wall shear stress as predicted by three models in MESH2 for the entry flow: (a) experimental (light-field [85]), (b) UCM, (c) White Metzner (d) Leonov-like.

the flow experiments can be compared directly with the contours of \bar{N} as calculated from eq. 3.65. These contour plots are shown in Fig. 41 for a wall shear stress of 16 kPa. The birefringence was calculated using the P-T T model and four meshes. In Fig. 42 are shown the same contour plots calculated using MESH3 and three different rheological models under the same flow conditions. From these figures it can be seen that all three meshes give an acceptable overall picture for the isochromatic fringes at these stress levels. Also there is no distinguishable qualitative difference between the solutions obtained from the several models. Both the calculated plots and the experimental data do not show any isochromatic fringes extending far into the region upstream from the contraction because the stress levels are very low there and the order of the fringes is less than one. From the neighborhood of the reentrant corner, however, many fringes originate and extend into the downstream channel. In the photograph the maximum in \bar{N} lies on the corner itself. In the numerical results, an overshoot is predicted, which is missing from the data and the position of which depends on the mesh that was used. The coarsest mesh (MESH1) and the mesh with the quadratic elements (MESH4) show a maximum in \bar{N} at a point to some small distance upstream from the corner. The two finer meshes with linear elements show this local maximum at a point very close to the corner itself. The results of all meshes show another maximum on the wall at a distance 0.1h to 0.2h downstream, a peak which is absent from the experimental data. The presence of oscillations around the corner in the numerical results may be responsible for the existence of these false peaks, as it will be described below.

In order to quantify the comparisons between the results of the numerical simulation and the experimental data, graphs similar to Figures 26 to 32 in the previous section were made. In the case of the entry flow, because only the upper half of the die is considered and symmetry conditions are assumed for the lower half, there is only one corner, around which the values of the stresses should be plotted. For this flow then, values of the fringe order were measured at several points in the flow domain and were plotted along y and x on lines on and near the wall around the corner. The lines, along which \bar{N} was plotted are shown in Fig. 43, where the origin of the coordinates (0,0) coincides with the reentrant corner O. The values of \bar{N} along the lines AB and CD can be seen in Fig. 44 as calculated for the four meshes by the P-T T model and compared with the experimental data. It should be noted for the plots in Fig. 44 and 45 that \bar{N} takes a high value at $x > 0$ (downstream) because this section of the graph corresponds to points along the wall of the exit channel. In the section of $x < 0$ (upstream) the stress levels are lower not only because of the greater height of the

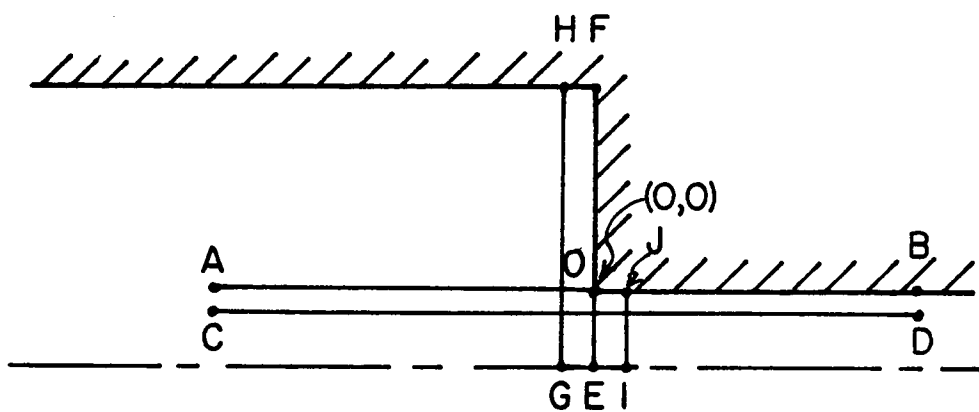


Figure 43. Lines in the domain of the flow into a contraction, along which the birefringence was plotted in the following graphs: The origin coincides with the corner O .

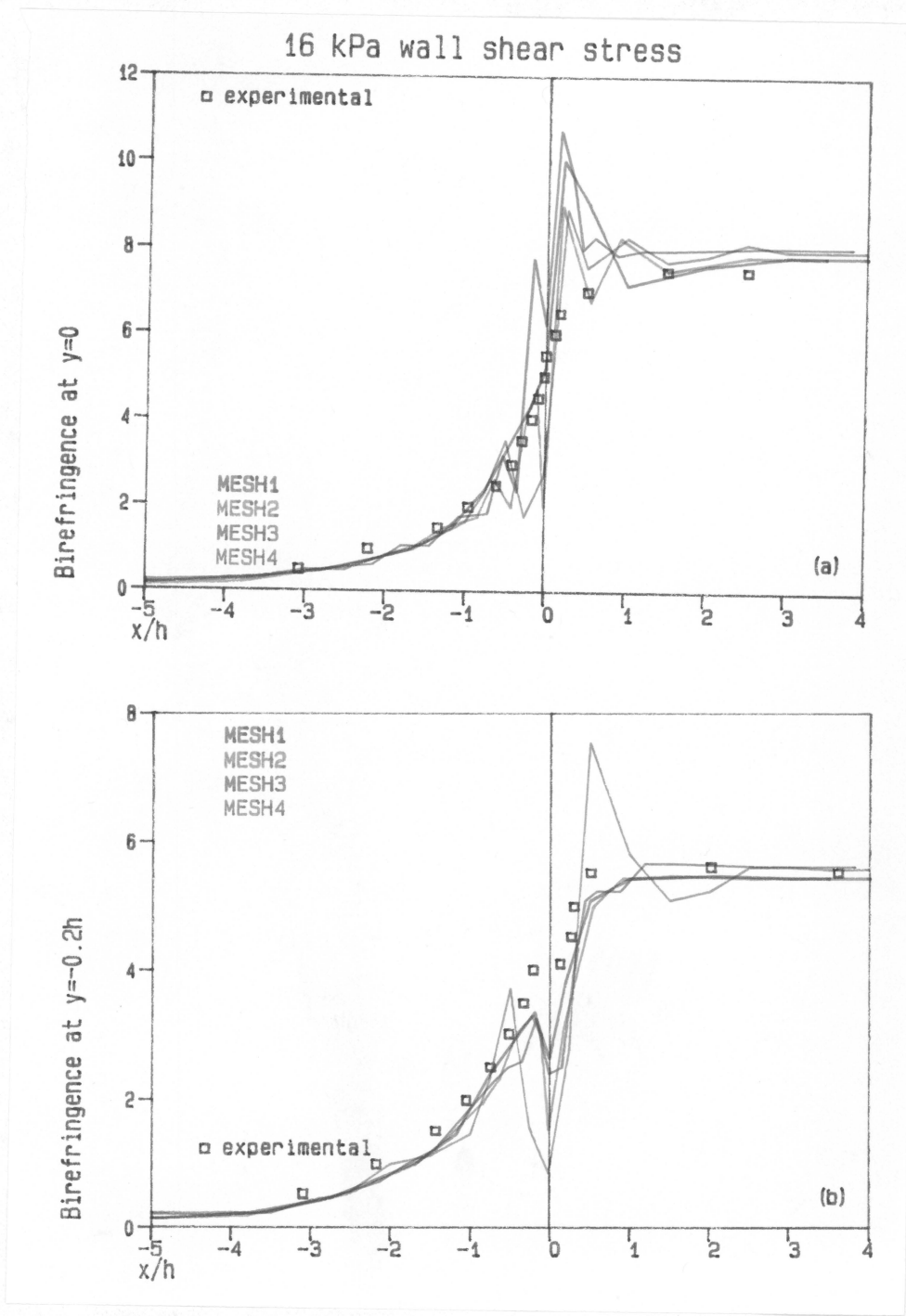


Figure 44. Fringe order along x as predicted by P-T T for three meshes in the flow into a contraction: Wall shear stress 16 kPa. (a) $y=0$, (b) $y=-0.2h$

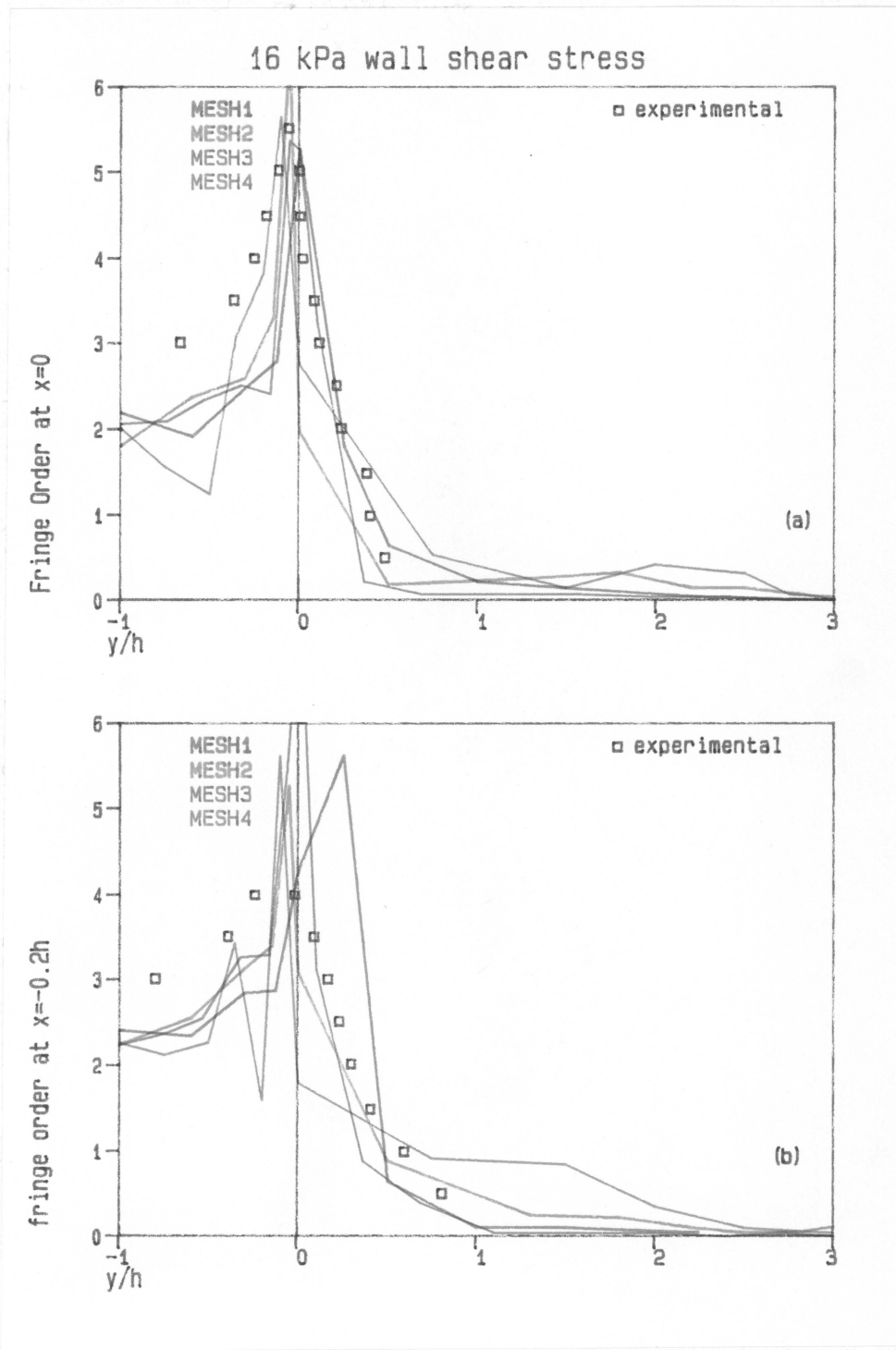


Figure 45. Fringe order along y as predicted by P-T T for three meshes in the flow into a contraction: Wall shear stress 16 kPa. (a) $x=0$, (b) $x=-0.2h$

die there, but also because the line, along which \bar{N} is plotted, lies relatively closer to the centerline. The values of \bar{N} , therefore, at $x < 0$ and far from the corner are very close to zero. In the experimental results the birefringence increases approaching the contraction and reaches the value of the downstream channel asymptotically without showing an overshoot. The numerical results for all the models and all the meshes show a high overshoot around $x = 0.2h$.

From Fig. 44a it can be seen that the oscillations that were found around the mouth of the hole in the flow over a transverse slot, are again present in the contraction flow. The lowest apparent oscillations in the upstream channel are found for the coarsest mesh. The oscillations in the results based on MESH3 are more pronounced near the entrance plane and extend up to $x = -3h$ upstream and $+1.5h$ downstream, a distance which is common for all the meshes. MESH2 gives oscillations, the magnitude of which is intermediate between the other two meshes with the linear elements. MESH4 also shows high oscillations. However, all calculated values oscillate about the experimental values.

Along the line $y = -0.2h$ (line CD in Fig. 43), a line that is parallel to the wall of the exit channel a little away from the wall, the oscillations have been smoothed to some degree (Fig. 44b). Here all the meshes will show a local maximum at a point around $0.2h$ upstream then a minimum at $x = 0$ and finally \bar{N} rises asymptotically to its unperturbed value in the exit die. This local maximum is probably an oscillation because the experimental data only show a small shoulder around $x = 0$ and then they continue to rise. No overshoot is shown by either the experimental or the numerical results in the downstream channel, except for the results of MESH4. The quadratic mesh shows a local maximum at a position further upstream, as well as a more pronounced minimum at $x = 0$ and another peak downstream.

Following y on the entrance plane from the top blind corner towards the centerline (Fig. 45a) it can be seen that the values of \bar{N} at $y > 0$ (above the reentrant corner) are very low because the deformation rates are small there, the region being a stagnation region or an area of slow recirculating flow [85]. Experimental points for \bar{N} are not available there. The small changes in \bar{N} that can be seen in that region in Fig. 45a, especially in the results of MESH4, may actually be due to error. However, when y approaches 0 (the reentrant corner), the stresses increase rapidly, showing a maximum either at $y = 0$ (MESH1) or slightly lower. The birefringence then decreases towards the centerline ($y = -h$). Some oscillations exist there, especially for MESH4. The birefringence does not become zero at the centerline because at that line and around the entrance plane there is a strong

elongational flow field. The fluid has to elongate and accelerate to enter the narrower channel. This extensional field causes the normal stress difference ($\sigma_{11} - \sigma_{22}$) to attain a high value, while the shear stress is zero because of the symmetry around the centerline. The values of \bar{N} predicted by all the meshes are approximately the same there. The experimental data also show the abrupt increase near the corner. The data show a maximum around $y = -0.1h$, in good agreement with the results of MESH2 and MESH3. The agreement at $y < 0$, however, is not so good, as the data show higher values than the numerical results of the P-T T model.

The values of the fringe order along y at a line $x = -0.2h$, somewhat upstream from the entrance plane can be seen in Fig. 45b. Strangely enough, the oscillations of the numerical solution seem to be higher here, even though one moves away from the singularity of the corner. This may be related to the fact that the maximum in the birefringence in that area is located (in the numerical results) near but not exactly on the corner. This is probably an erroneous result because the experimental data do not show such a maximum there. There is also a peak that is found at $y > 0$ for MESH1, at $y = 0$ for MESH3 and at $y < 0$ for MESH2 and 4. The highest oscillations are shown by MESH4. Towards the centerline \bar{N} again decreases to a finite value because of the extensional field there. The numerical results along this line compare poorly with the experimental data. Clearly MESH1 is unacceptable. Even though the increase of \bar{N} near the corner for $y > 0$ agrees well with the results of MESH2 and MESH3, the overshoot at $y = 0$ in the numerical results is higher than the experimental ones and at a different value of y .

Examining the differences between the results of the several meshes, it may be seen that for this flow the coarsest mesh will give the lowest oscillations. The agreement with the experimental data is, however, the poorest for this mesh. The fine meshes with linear elements show more severe oscillations and higher peaks, but their results agree better with the experimental data at points a little away from the corner. At the corner itself the overshoots in the numerical solution are much higher than the experimental ones. The quadratic mesh gives worse results than MESH2, with which it has the same number of nodes. It seems that the numerical method that was developed here works better with linear than quadratic elements. This is contrary to what was reported by Debaut and Crochet [78], where higher degree interpolation polynomials improved the solution. Again a possible explanation for this contradiction may be related to the penalty formulation that was used here instead of the mixed method that these authors used. The results obtained here should be compared

with results obtained under the same flow conditions and using the mixed formulation to clear these questions.

For the comparison of the results of the different rheological models, similar plots as in Fig. 44 and 45 were made. Figure 46 shows the results of the four models (using MESH3) for \bar{N} along the lines $y=0$ and $y=-0.2h$. It can be seen there that all the models show the same oscillations between the nodes of the mesh and the overshoots around the corner are approximately at the same position. The overall agreement between the numerical results and the experimental data is good, except at the area around the corner. In that area all the models show oscillations and high overshoots, which are absent from the data. The highest overshoot is shown by the UCM model on the wall at $x=0.2h$ downstream from the contraction. The best agreement in the exit channel is shown by the results of the White-Metzner model. Oscillations are also found in the results of \bar{N} along the line $y=-0.2h$, indicating that high stress gradients extend to some distance from the corner for all the models. Again the shoulder that is found in the experimental data around $x=0$ is exaggerated in the numerical results taking the form of an oscillation. The results of all the models fall very close to each other on this graph.

The predictions of the models along y on the lines FE and HG are shown in Fig. 47. The peak that is shown by the data around $x=0$ is duplicated well by the numerical predictions for all the models along the line $y=0$. The same maximum for the line $y=-0.2h$ is much higher in the numerical results than in the experimental data. All the models behave reasonably well at $y>0$ in both graphs. The best agreement with the data at $y<0$ is found in the results of the W-M and the Leonov-like models, the other two showing lower values for \bar{N} there.

Downstream from the contraction, the change of \bar{N} with y and x can be seen in Fig. 48. At $x=0.15h$ (Fig. 48a) the birefringence changes very little with y , remaining at a value of around 2-2.5 for 80% of the die height and then it rises rapidly near the wall. In this figure the value of \bar{N} at $y=-h$ reflects the high elongational stresses along the centerline in the neighborhood of the entrance plane. Also at that distance downstream the value of \bar{N} in the numerical results at the wall is much higher than that at the corner ($x=0$) because of the presence of the overshoot at $x=0.1-0.2h$ that can be seen in Fig. 44. In the experimental data such overshoot is not found and the value of \bar{N} at the wall ($y=0$) at that x is lower than the wall value for the birefringence further downstream. The agreement between the numerical and the experimental results in Fig. 48a is not so good. Moving further along the exit part of the die (Fig. 48b to f), it may be seen that the change of the

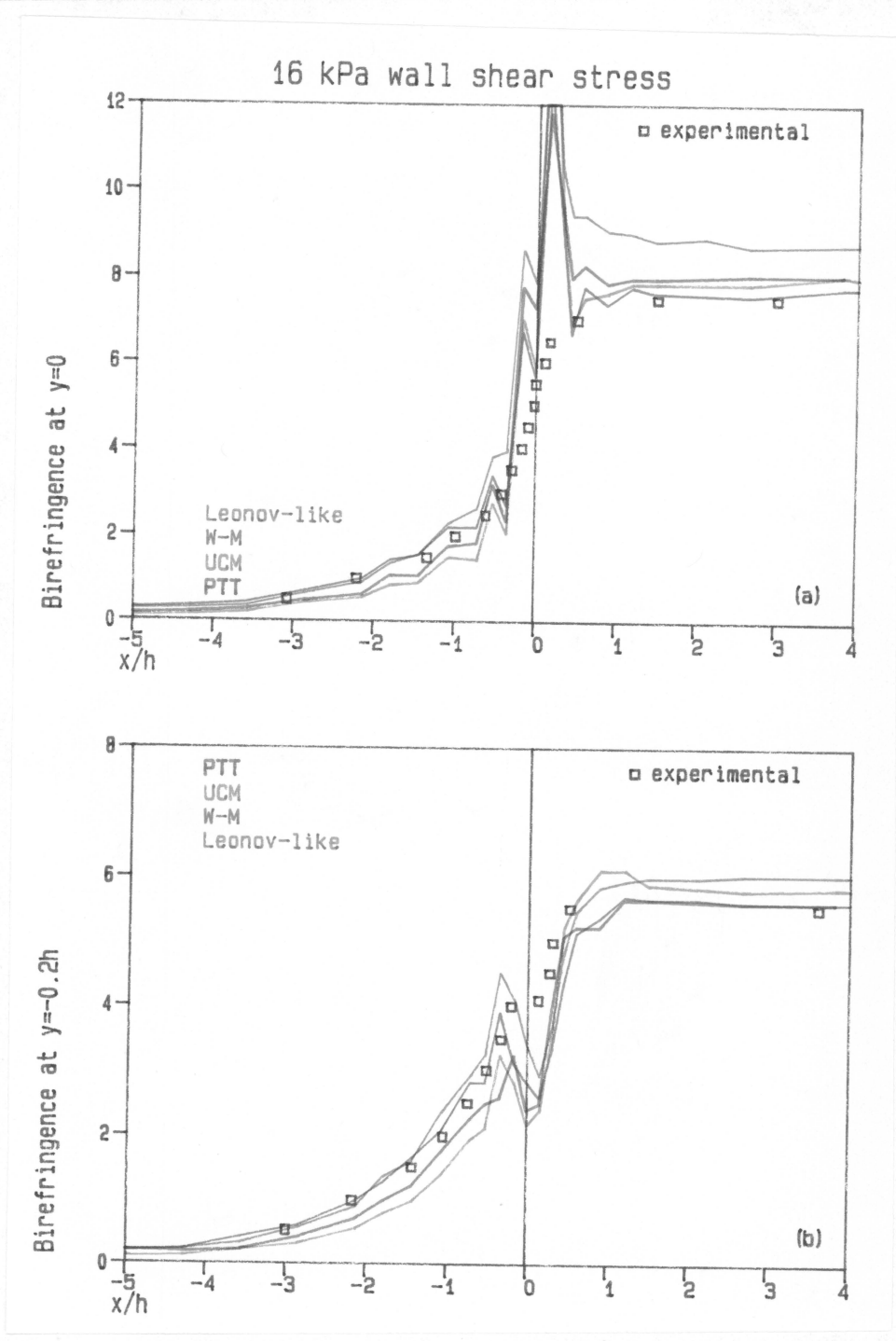


Figure 46. Fringe order along x as predicted by four models in the flow into a contraction at 16 kPa wall shear stress using MESH3: (a) $y=0$, (b) $y=-0.2h$

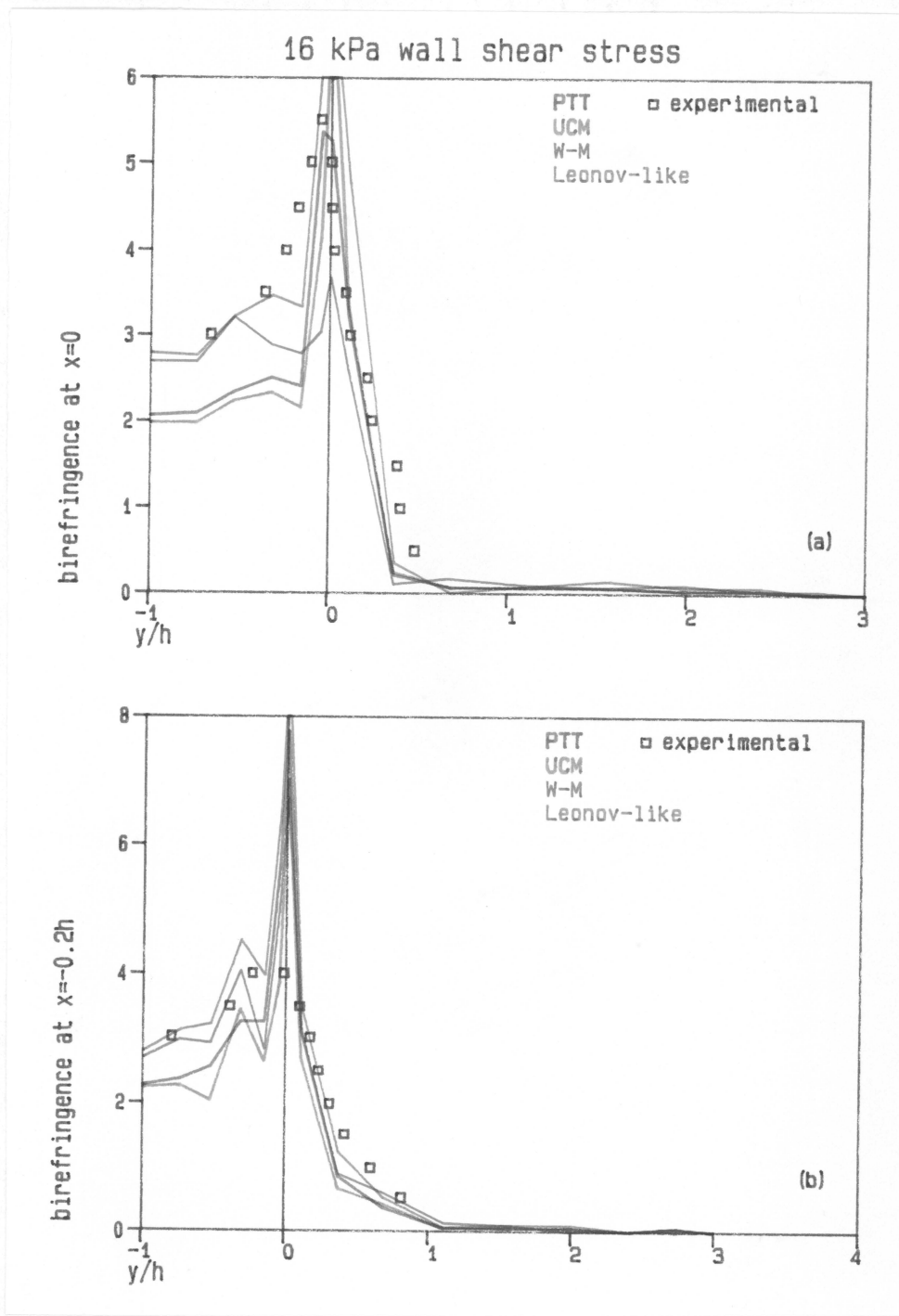


Figure 47. Fringe order along y as predicted by four models in the flow into a contraction at 16 kPa wall shear stress using MESH3: (a) $x=0$, (b) $x=-0.2h$

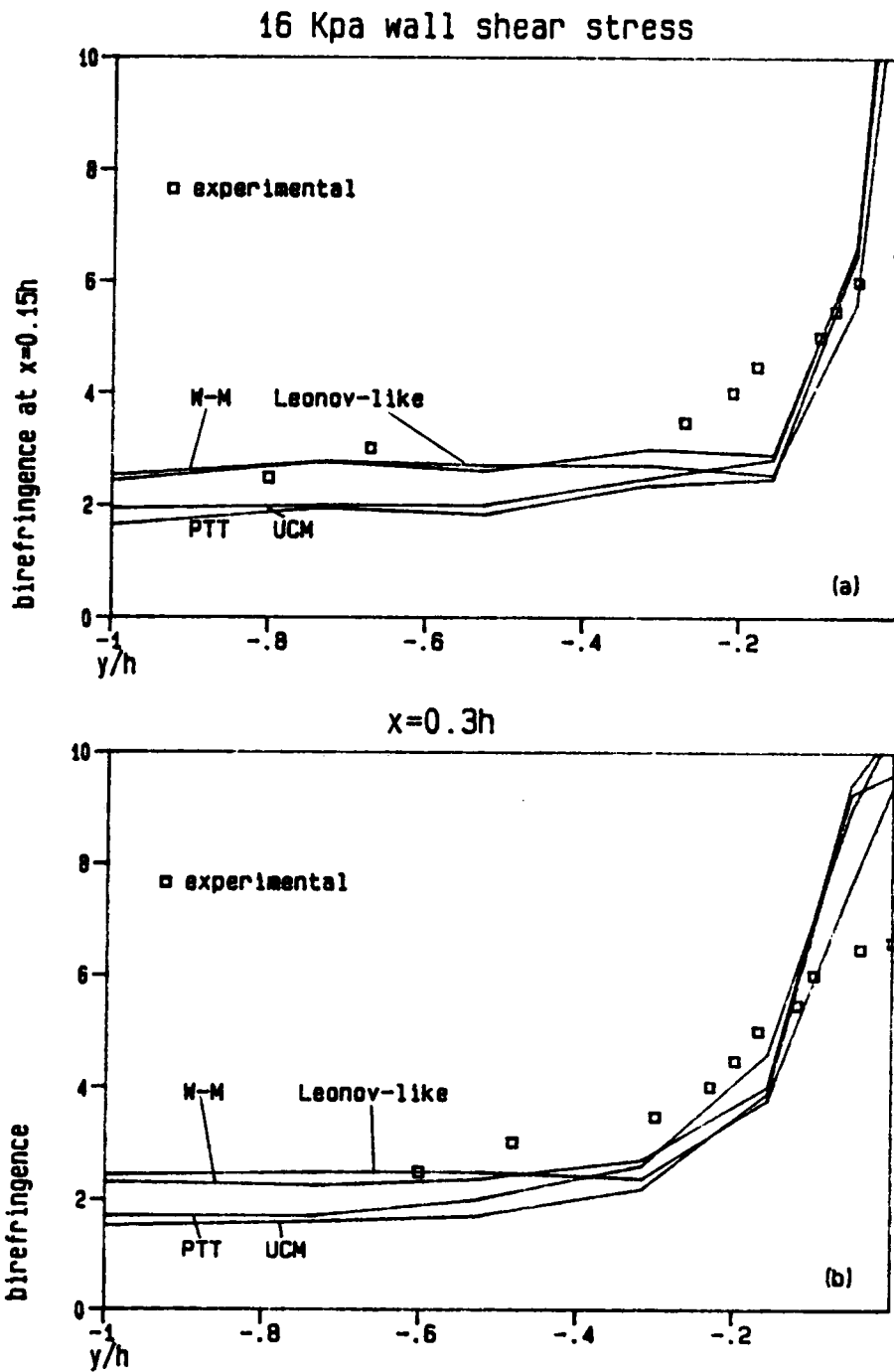


Figure 48. Fringe order downstream from the contraction for 16 kPa wall shear stress using MESH3.

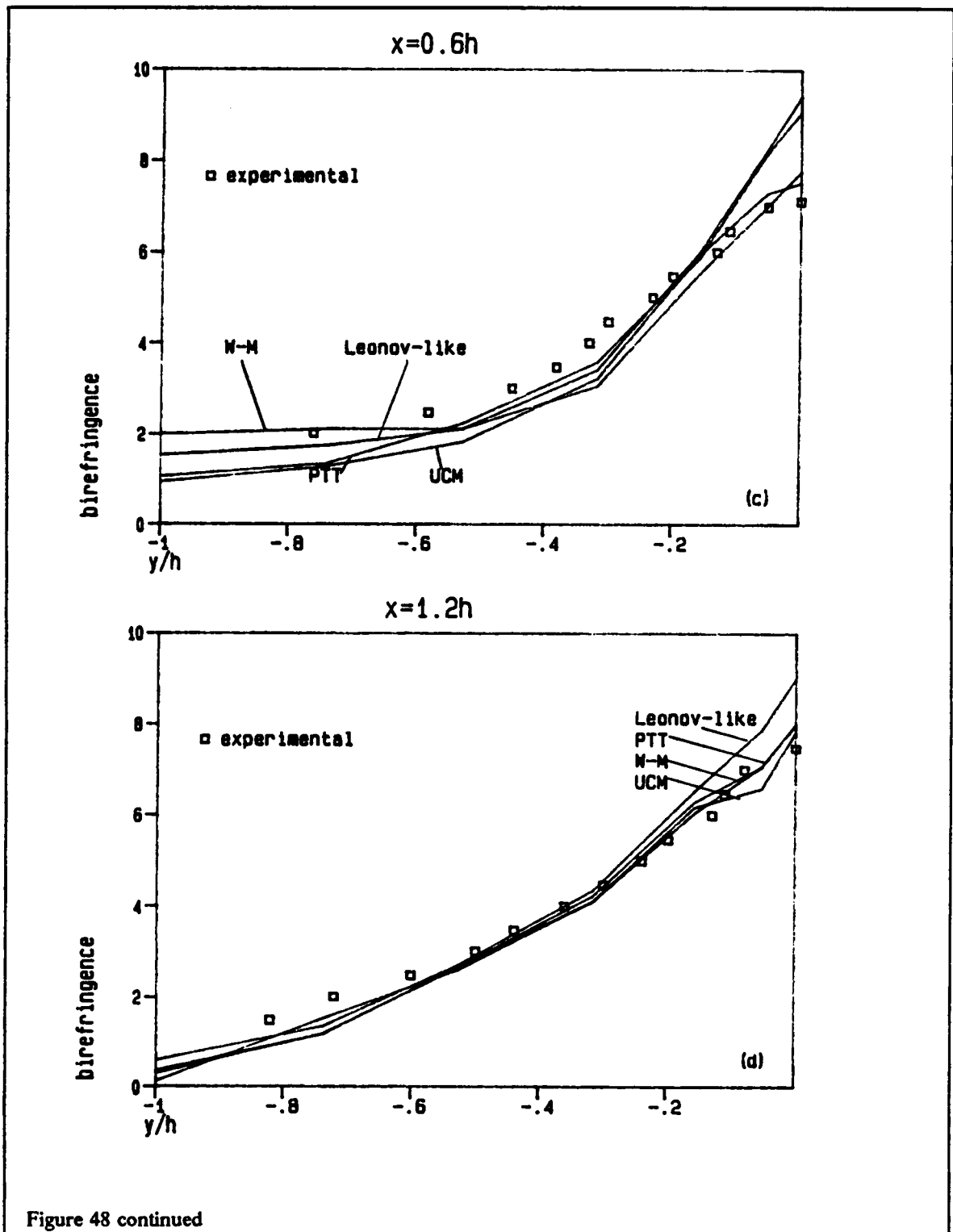


Figure 48 continued

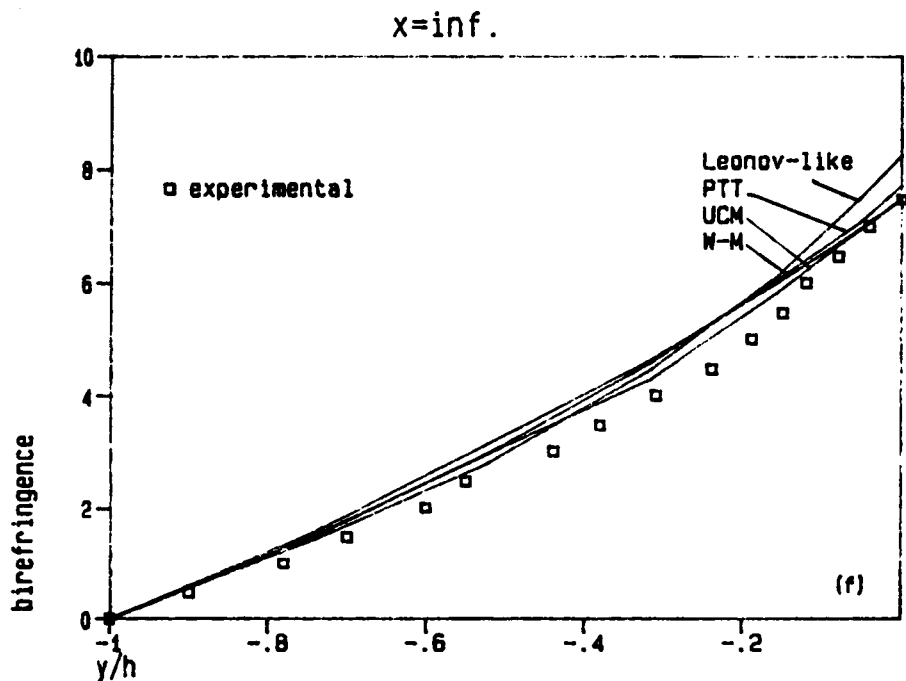
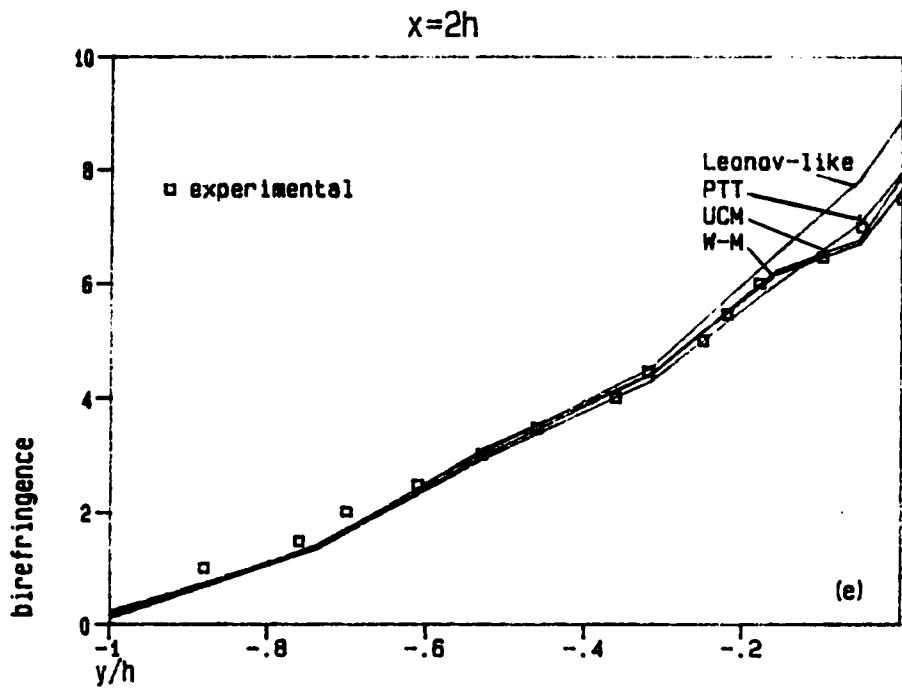


Figure 48 continued

birefringence with y spreads over a larger part of the die height and the agreement with the experimental data improves. At a distance $x = 2h$ from the entrance plane, the extension of the fluid elements at the centerline has finished. At that distance, \bar{N} is zero at the centerline and its change with y very little differs from the one in a slit die (Fig. 48f). The agreement with the data is also excellent at $x = 2h$. The effect of the contraction on the stress field seems, therefore, to be eliminated at a distance $2h$ to $4h$ downstream and $2H$ upstream. This is also verified by the flow birefringence plots (Fig. 41 and 42) and has been reported by Han [86]. In view of the above, the length of the meshes upstream and downstream from the entrance plane that were used in this simulation were thought to be sufficient for this flow. However, because of the influence of this length on the results of the numerical simulation that was found in [78] and studied in [72], different mesh lengths should be tried as it was mentioned in ch. 5.2.1. But this extends beyond the scope of this work.

The picture of the stresses in the extensional flow at the centerline around the entrance plane can be seen better from a plot of the normal stress difference along this line. Since σ_{12} is zero there, $\sigma_{11} - \sigma_{22}$ can be directly calculated from the birefringence data (eq. 3.65). These results together with the results of the computations are shown in Fig. 49. The normal stress difference is zero on the centerline far from the entrance plane. It starts rising at a distance around $-5h$ downstream. It shows a maximum at $x \cong -0.4h$ and then it approaches zero again at $x \cong +3h$. Even though the behaviour of the models is qualitatively correct as compared with the experimental data, only the W-M and the Leonov-like models show a quantitative agreement with the data. The P-T T shows lower values for $\sigma_{11} - \sigma_{22}$ than these two models (and the data) and the UCM shows the lowest values. It should be noted here that the extension rates that occur along the centerline at these flow conditions are low enough, so that $\bar{\eta} \cong 3\eta_0$ for all the models. The differences in the extensional viscosity predictions of the models that were described in ch. 4.1.2 can not be responsible for the disagreement between the several curves in Fig. 49. This disagreement is caused by the differences in the shear thinning behaviour predicted by the models for the shear viscosity rather than by the predictions for the extensional viscosity. The different forms of $\eta(\dot{\gamma})$ result to different flow rates predicted by each model for the same wall shear stress. Since the W-M and the Leonov-like models show the lowest viscosity for these stress levels, the flow rates that they predict are higher than the other models. As a consequence, the extension rates along the centerline will be higher for these two models. Since $\bar{\eta} \cong \eta_0$ as it was said above, the elongational stress (that is, $\sigma_{11} - \sigma_{22}$, which is plotted

in Fig. 49) will be proportional to the extension rate and higher for the W-M and the Leonov-like models than those predicted by the P-T T and the UCM models.

In summary, the comparison between the experimental data and the numerical results shows that a reasonable stress field in the flow into a contraction can be calculated by the numerical method that was developed in this work for all five rheological models. Oscillations, however, are found around the reentrant corner, indicating that there may exist a possible numerical singularity in the stresses at this point. A coarse mesh (like MESH1) will smooth these oscillations to some degree. The agreement of the results of MESH1 with the experimental data, however, is poor, making its use unacceptable (too coarse mesh). MESH2 and MESH3 give results in good agreement with the experimental data except in the very vicinity of the reentrant corner. In this flow high values of the stresses are also found a little upstream from the corner, a reason for the extension of the oscillations at a longer distance upstream than downstream. The comparison of the rheological models shows that for the stress field, the W-M and the Leonov-like models will give the best predictions. These two models will also show the best results in the extensional field along the centerline. The P-T T and the UCM models show lower values for the stresses there but their results elsewhere are very close to the results of the other models.

5.3.2 Velocity Field for Flow into a Contraction

It was seen in the previous section that the stress field for the flow into a contraction is little affected by the choice of the rheological model for the conditions that were studied. It was also shown that even a coarse mesh may give a reasonable solution. This is not so, however, for the velocity field of the same flow. The streamline patterns show a rather drastic change from the coarse mesh to the finer and from one model to the other.

A test for the streamlines of the entry flow that has been used to distinguish between the Newtonian and the viscoelastic solutions is the existence of the recirculating vortex in the blind corner upstream from the contraction. It was shown in ch. 2.5 that under the same flow conditions, some polymeric fluids will show vortices there and others will not. The material (polystyrene at 190° C), under which the parameters of the models were fitted in the present work, was found not to show such vortices [86] under the flow conditions that were simulated here. Instead a triangular stagnation region was found around that corner. In the following it will be examined how the nu-

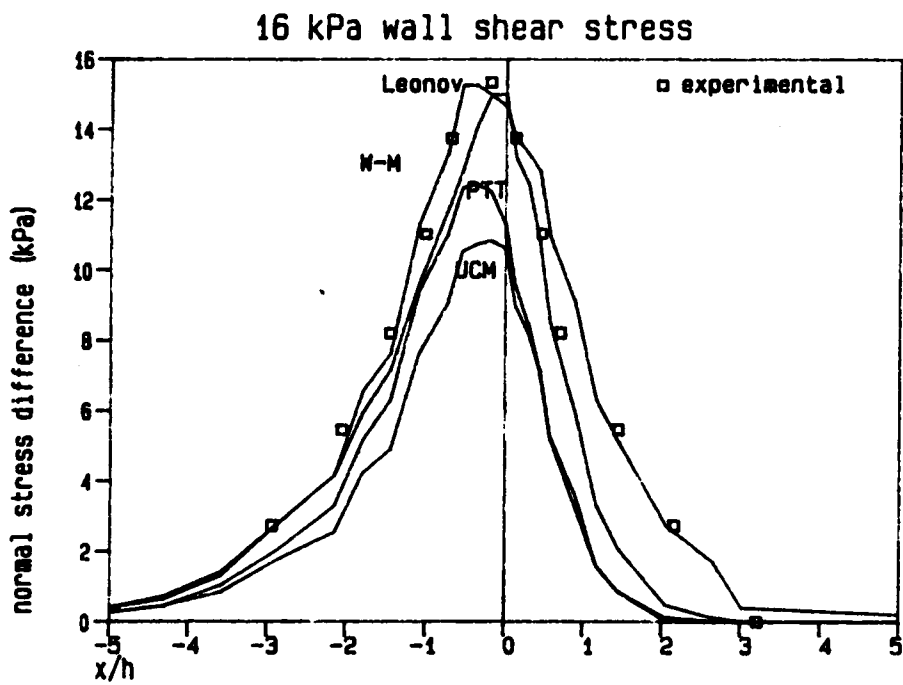


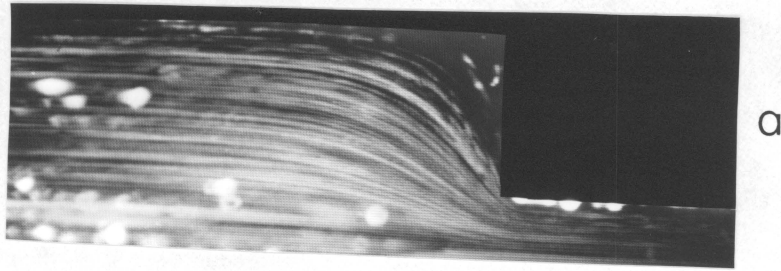
Figure 49. Normal stress difference along the centerline at 16 kPa wall shear stress for the flow into a contraction: MESH3 was used.

merical results compare with the experimental streamlines made from long time exposure streak photographs.

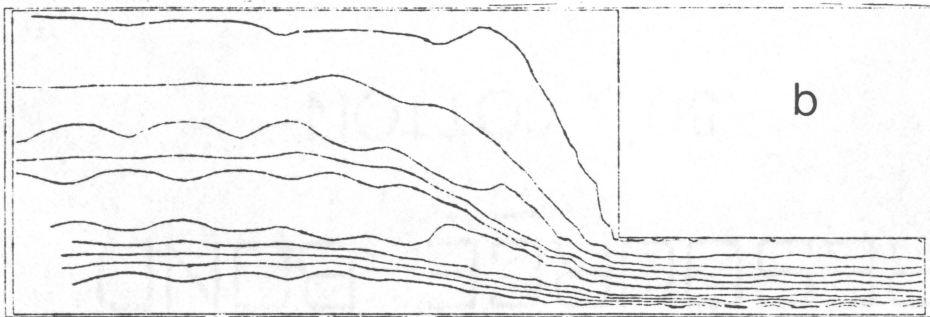
In Fig. 50 are shown the streamlines calculated by PTT using the four meshes, as well as the experimental results for a shear rate of 16 kPa at the wall of the downstream channel. The streamlines are normalized. They have a value of zero at the wall and a value of one at the centerline. The streamline that was plotted nearest to the wall has the value of 0.01. All the meshes show that this streamline starts moving away from the wall of the upstream channel at a distance of around $x = -H$ from the entrance plane leaving a triangular region around the blind corner. For MESH1 this region is slightly smaller than the other meshes and the angle with which the streamline approaches the reentrant corner is steeper. The value of the streamlines at the corner region are too low to be plotted for meshes 1 and 2. In MESH3, however, a weak recirculating vortex appears in that region. Its intensity is -0.001, which is quite low and may be within the approximation error. The validity of the vortex, however, is supported by the fact that it is lacking from the results of the more coarse meshes, appearing as the mesh is refined, its position and intensity is consistent among runs under different flow conditions and the velocity vector in that area also shows a very slow circulating motion. The absence of such a vortex from the experimental results may be due to very slow circulation as it is indicated by its calculated intensity and the values of the velocities. On the other hand, because of the very small intensity of this vortex, its existence may be of small rheological importance. It seems then that the PTT model will predict such a weak recirculating vortex for polystyrene at these conditions if the mesh is fine enough. Support to this result also comes from reports by Crochet [78] and Keunings [32,75], who predict such a vortex in this flow for the P-T model under the same elasticity levels. Its intensity that was reported in these articles was higher than in Fig. 10, perhaps because the parameters of the model that were used did not correspond to any real material.

The mesh with the quadratic elements shows a different vortex. Its center lies much closer to the reentrant corner and further upstream from the contraction wall. Its intensity is 5 times higher than MESH3. When the oscillations that are found in this mesh are considered, it is doubtful whether this vortex is a real result of the model or a numerical artifact generated by the specific mesh. No indication for such a vortex is present in the experimental results.

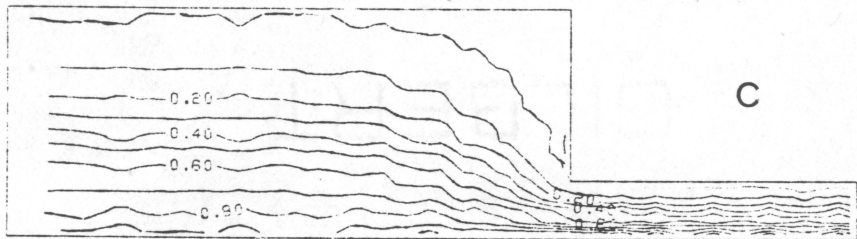
The comparison of the streamlines that result from the other rheological models for the same wall shear stress and calculated using MESH3 are shown in figure 51. It should be noted here that



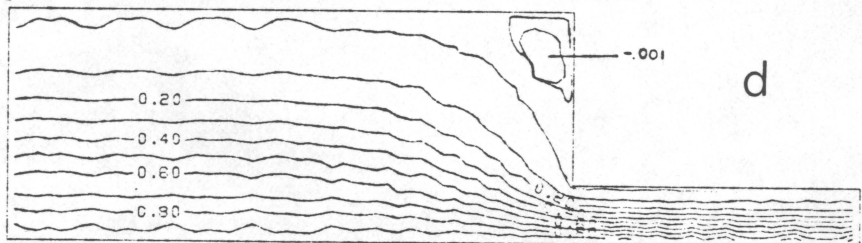
a



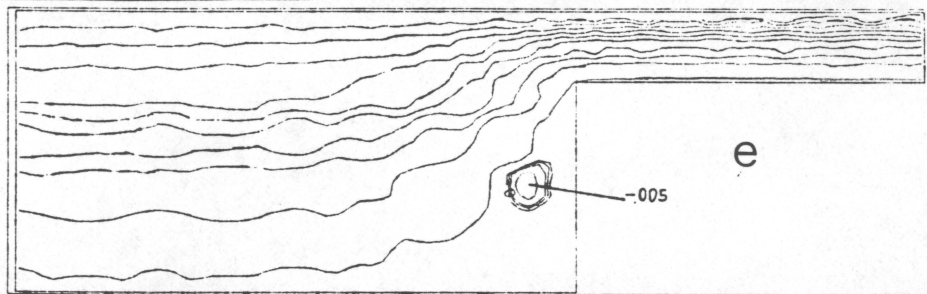
b



c

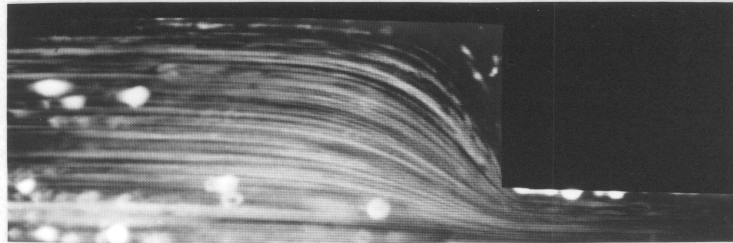


d

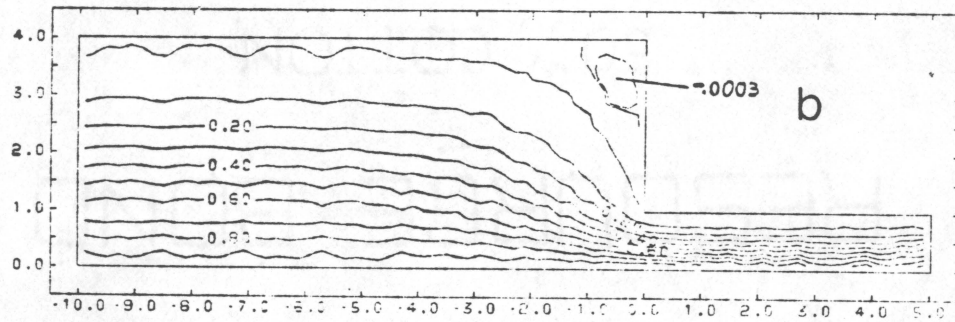


e

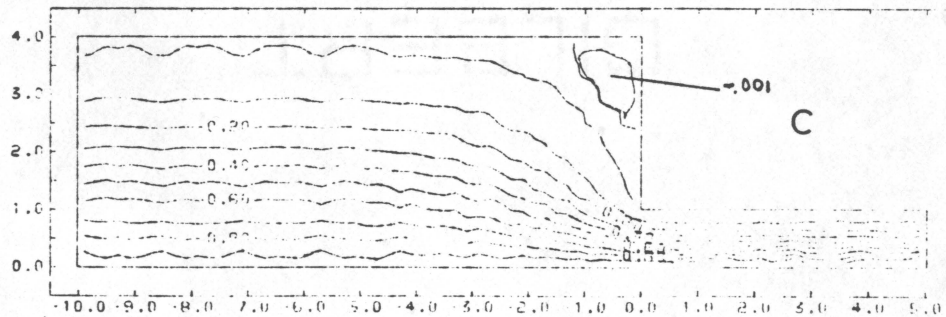
Figure 50. Streamlines in the entry flow as predicted by P-T T in three meshes at 16 kPa wall shear stress.: (a) experimental, (b) MESH1 , (c) MESH2 , (d) MESH3 , (e) MESH4.



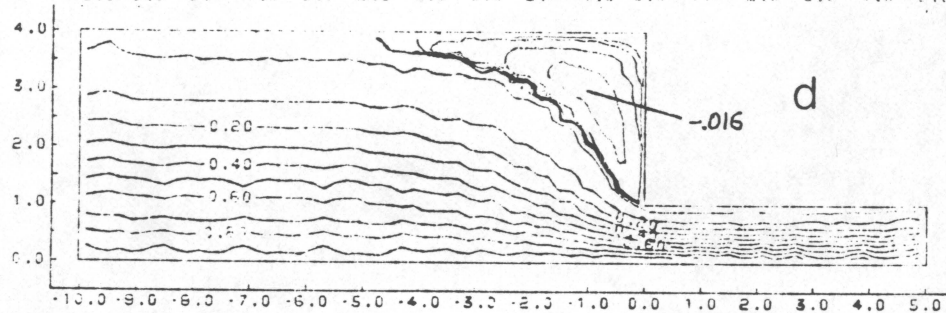
a



b



c



d

Figure 51. Streamlines in the entry flow as predicted by three models in MESH3 at 16 kPa wall shear stress.: (a) experimental [85], (b) UCM , (c) Leonov-like , (d) W-M.

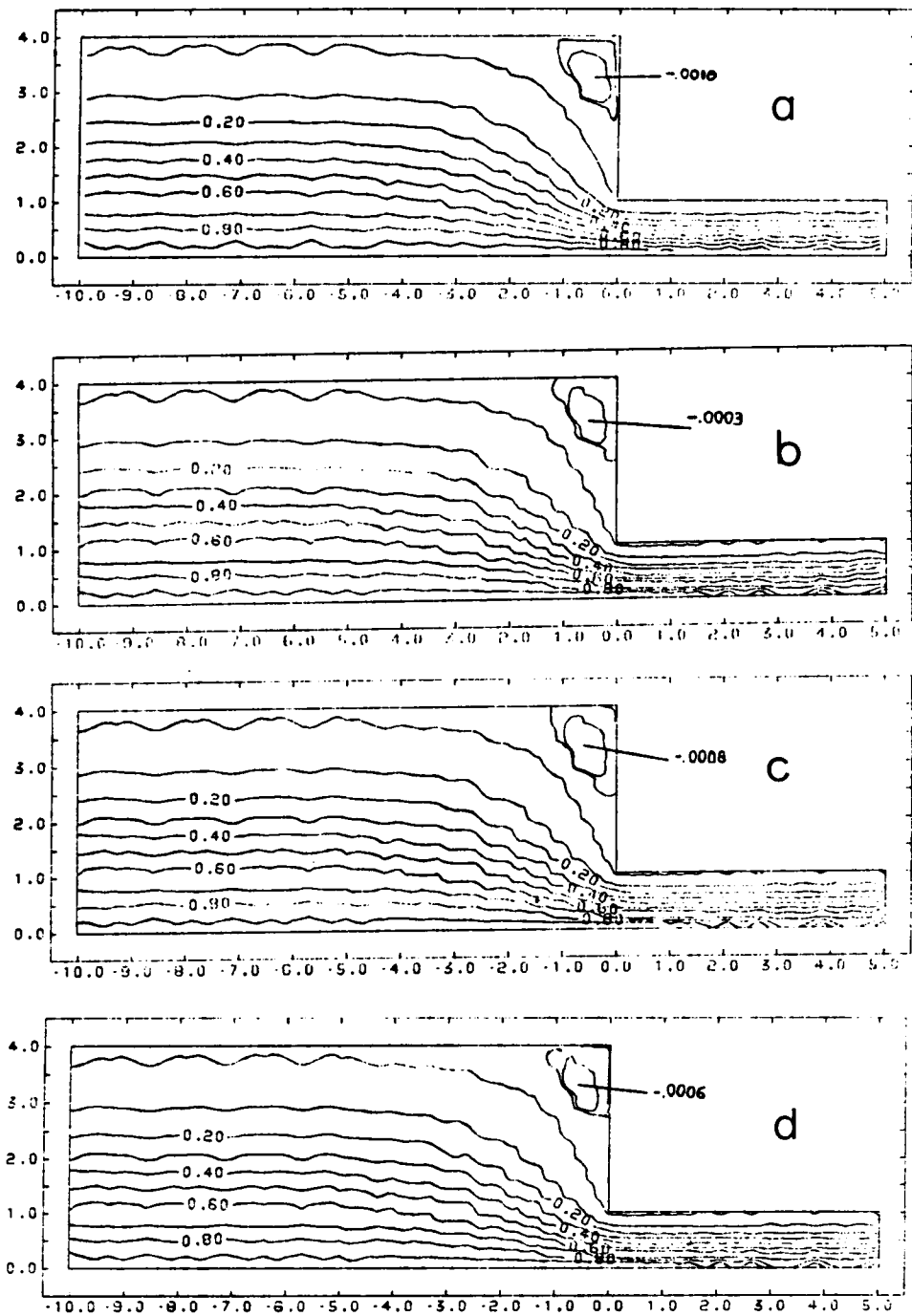


Figure 52. Streamlines in the entry flow as predicted by four models in MESH3 at $Q/W = 1.90$ mm^2/sec : (a) P-T T, (b) UCM, (c), Leonov-like, (d) W-M.

the flow rates for the same shear stress are different for each model in Fig. 51 because of their different shear thinning predictions. At 16 kPa wall shear stress the flow rate per unit width for the PTT model is 1.79, for the UCM model it is 1.55, for the W-M model it is 3.15 and for the Leonov-like model it is 2.69 mm³/sec mm-die-width. The fact that the vortex predicted by the W-M model is much bigger and stronger than the other models is probably due to the higher flow rate that this model shows under the same wall shear stress levels. Another possible reason for this stronger vortex may also be the fact that the ratio of $\bar{\eta}/\eta$ as predicted by this model is higher than the ones predicted by the other models under these conditions, again because of the shear thinning η . Vortices may be found to be formed more easily in experiments with fluids that show higher values for this ratio than for fluids with lower values of $\bar{\eta}/\eta$ [85]. The comparison of the streamlines for the same flow rate ($Q/W = 1.9$ mm³/sec mm) indicated that the vortex predicted by the White-Metzner model is around the same in intensity as the one predicted by the P-T T model (Fig. 52). For the same flow rate the weakest vortex is predicted by the UCM model, a fact which gives ground to doubts about its validity. The reports of Tanner [40] and Crochet [31] also suggest that such vortices may be just numerical artifacts for this model and they may disappear for very fine meshes.

To get a picture of the flow, except the streamlines, one can also examine how the velocity vector itself is affected by the mesh and the rheological model. At the centerline the y-component of the velocity (v) is zero. The x-component (u) of \vec{u} , on the other hand, goes through an acceleration field in the neighborhood of $x = 0$, extending into the downstream channel. Fig. 53 shows the values of the reduced u along the centerline as calculated by the P-T T model for the four meshes and by the other models in MESH3. The picture at that line is somewhat changed in terms of the oscillations predicted in the different meshes. Here the highest oscillations are shown for the coarsest mesh and the smoothest curve is predicted for the quadratic mesh. The magnitude of the oscillations in MESH1 is, however, much smaller than the ones found for the stresses around the corner in Fig. 44 and 46. Since the centerline lies far away from the reentrant corner, which is believed to be a singular point, it seems that the oscillations that are found along that line are not directly related to the singularity, but they are rather a result of an insufficient mesh. The results for u for all the models look reasonable but experimental data are needed for comparison.

The acceleration field around the contraction was examined in the previous sections by observing the change of the stresses and the velocity along the centerline only. Even though the flow

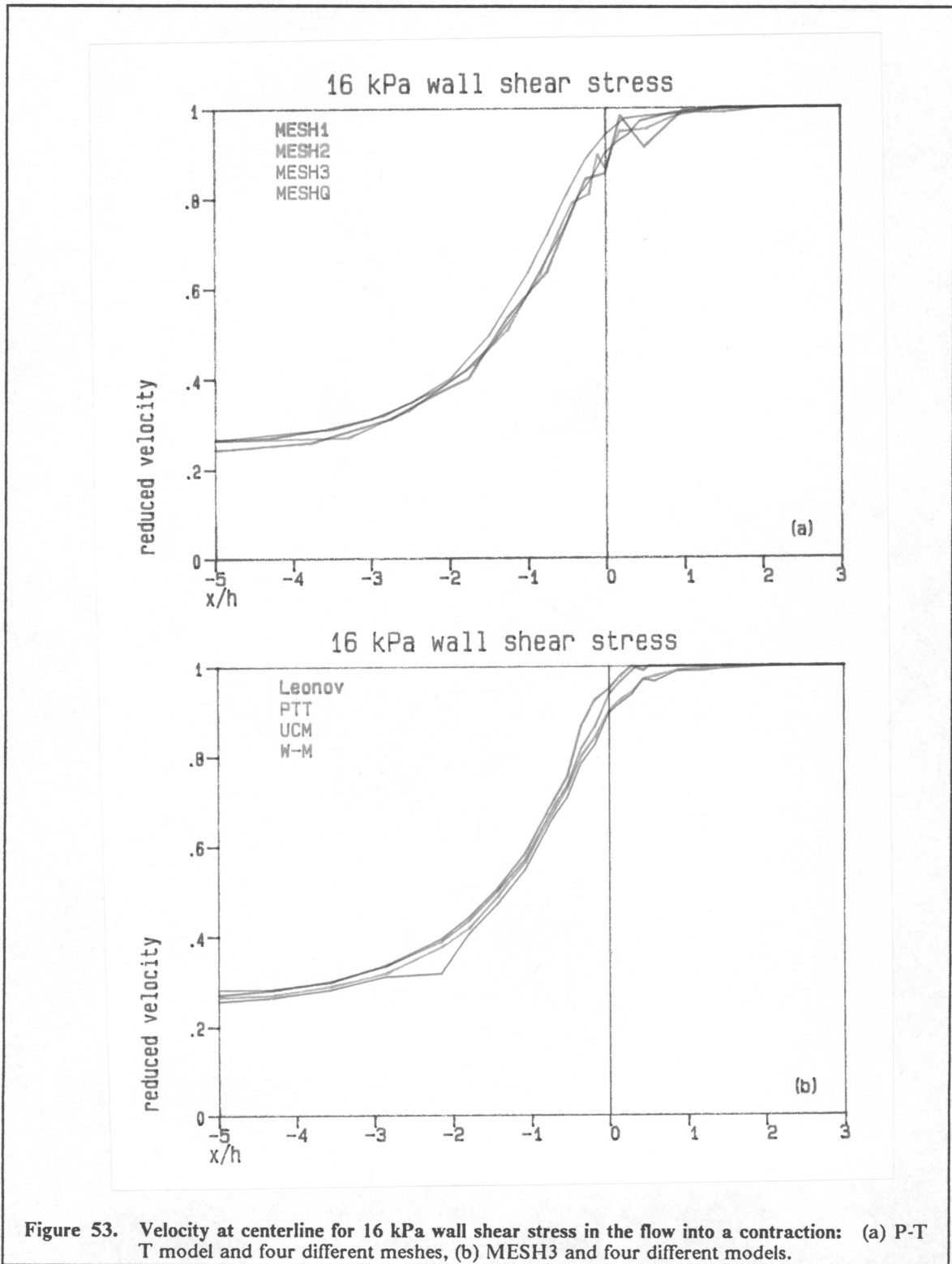


Figure 53. Velocity at centerline for 16 kPa wall shear stress in the flow into a contraction: (a) P-T model and four different meshes, (b) MESH3 and four different models.

field along this line is purely elongational, there is at least another area, where, in addition to shear flow, the fluid elements also undergo high extensional deformation. By extensional deformation, it is meant here the presence of non-zero diagonal terms of the rate of deformation tensor:

$$\frac{\partial u}{\partial x} \text{ and } \frac{\partial v}{\partial y}$$

If an extensional flow field exists, each of these two terms will have a finite value, even though their sum will be zero because of the incompressibility constraint. In order to define an extension rate in a flow which has both shear and extension and to be consistent with the quantity that is used in the uniaxial extension measurements ($\dot{\epsilon}$), the extension rate in this work was defined as follows:

$$\dot{\epsilon} = \sqrt{\frac{2}{3} \left[\left(\frac{\partial u}{\partial x} \right)^2 + \left(\frac{\partial v}{\partial y} \right)^2 \right]} \quad (5.2)$$

The quantity $\dot{\epsilon}$ will give a measure of the rate of extension in the complex flow domain. In a uniaxial extension flow $\dot{\epsilon}$ reduces to the same quantity as the one used for the extension rate in ch. 4.1.2. Clearly, in the entry flow far upstream and downstream from the contraction, $\dot{\epsilon}$ will be zero because the flow is pure shear there. The contour plot of $\dot{\epsilon}$ around the reentrant corner is shown in Fig. 54. It can be seen there that, except along the centerline, there is another area with high elongational flow, which lies along a line that starts from the corner and extends at a 45° angle towards the wall in the upstream channel. The point with the highest value of the extension rate (defined as in eq. 5.2) in the whole flow domain is located here, a little away from the corner, in the same area, where the maximum of the birefringence also occurs. It seems that the value of the birefringence at that area comes more from the contribution of the extensional stresses than the shear stress. Further, the angle, around which lies the area with the high extension rates, may be related to the *natural entry angle*. This is an angle, at which the viscoelastic fluid enters the downstream channel [86] and some researchers use it as a measure of the vortex that may exist in the blind corner in the upstream channel. If the vortex that was calculated from the streamlines in this work is compared to the above, it can be seen that the natural entry angle should be around 70° rather than 45°. It is possible, however, that the two angles above are related but they do not coincide.

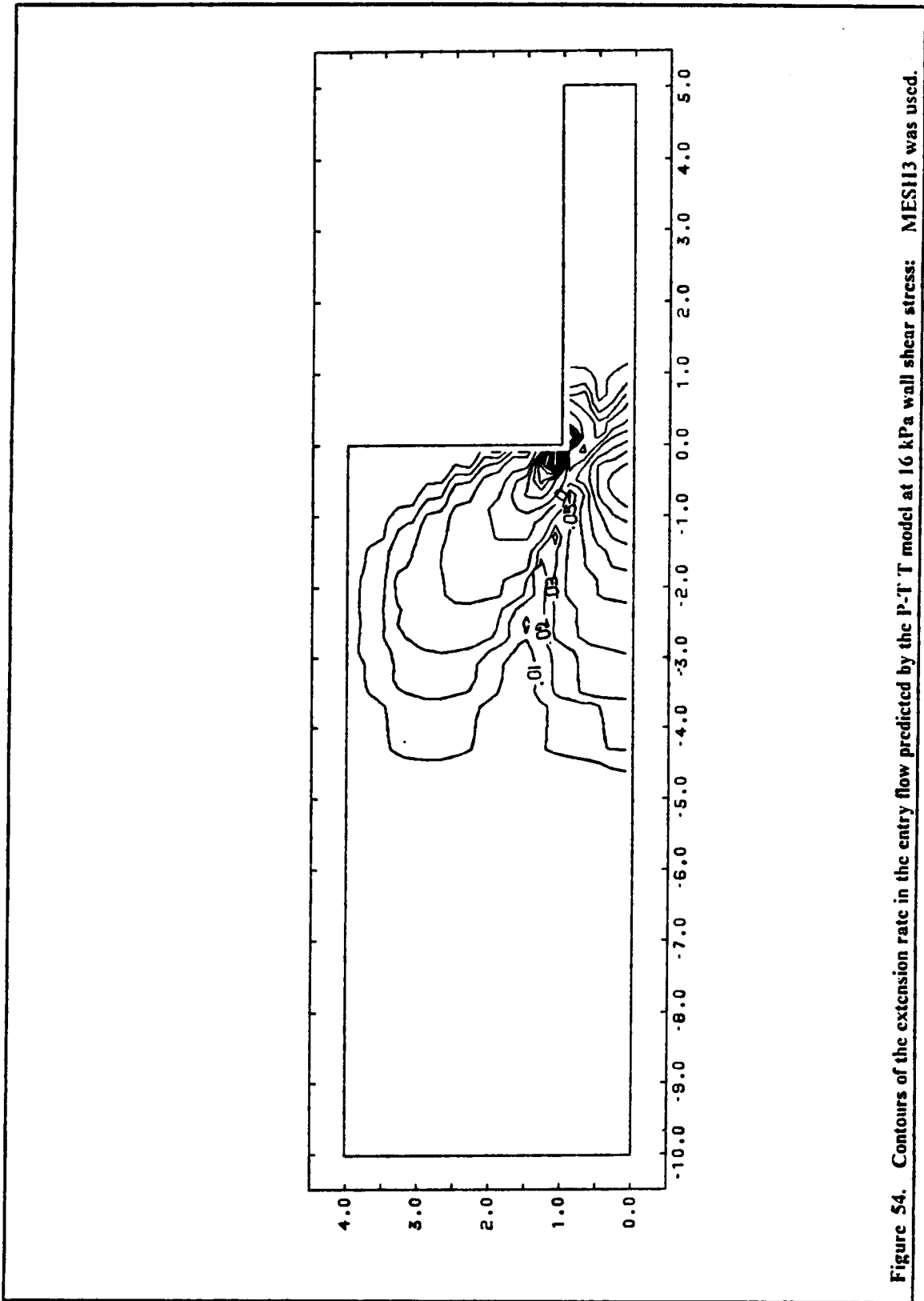


Figure 54. Contours of the extension rate in the entry flow predicted by the P-T model at 16 kPa wall shear stress: MESH3 was used.

5.3.3 Entrance Pressure Loss

In order to measure the entrance pressure loss, two points are chosen in the domain (A and B), one upstream (A) and another downstream (B) far from the contraction and usually on the wall. The entrance pressure loss, then, is the difference between the total pressure drop from A to B minus the sum of the pressure drops that would occur in isolated entry and exit channels extending between each point of the pressure measurements and the entrance plane. The extra pressure drop in the entry region is a characteristic of viscoelastic flow and accounts for the extra energy that is needed to accelerate and deform the elastic fluid elements as they flow into the contraction. The entrance pressure loss has been found experimentally to be positive and it has to be accounted for in the design of equipment that use such flows, as extra power requirement for the driving system. It should also be accounted for in the measurements of viscosity in slit or capillary rheometers as a correction of the measured total pressure drop.

The isotropic pressure is a secondary variable in the penalty formulation and it is calculated from the velocity field at the center of each element in the post processing step. For all the models the entrance pressure loss is shown in figure 55 plotted vs. the shear stress at the wall. It can be seen there that ΔP_{ent} increases monotonically with τ_w for the PTT and the Leonov-like models. The UCM and the W-M models, however, predict a maximum in ΔP_{ent} . Then the entrance pressure loss decreases and it becomes negative. Negative values for ΔP_{ent} were also found by Keunings and Crochet [32] for the Oldroyd-B and the UCM models. The results in that report compare qualitatively well with the present results. Because of these negative values, the PTT and the Leonov models are more useful than the UCM and the W-M for calculations of the entrance pressure loss.

5.4 *Behaviour of Solution at Limit of Convergence*

Much was said in ch. 2.5 about the problem of convergence in the numerical calculations of the viscoelastic flows. The presence of limit or bifurcation points, either due to the discretized or the original form of the flow equations was not studied directly in this thesis because the Jacobian of the global system, the sign of which will indicate such anomalous points, was not calculated in the iterative method that was used here. Several reports [78,79,82] concerned with such points,

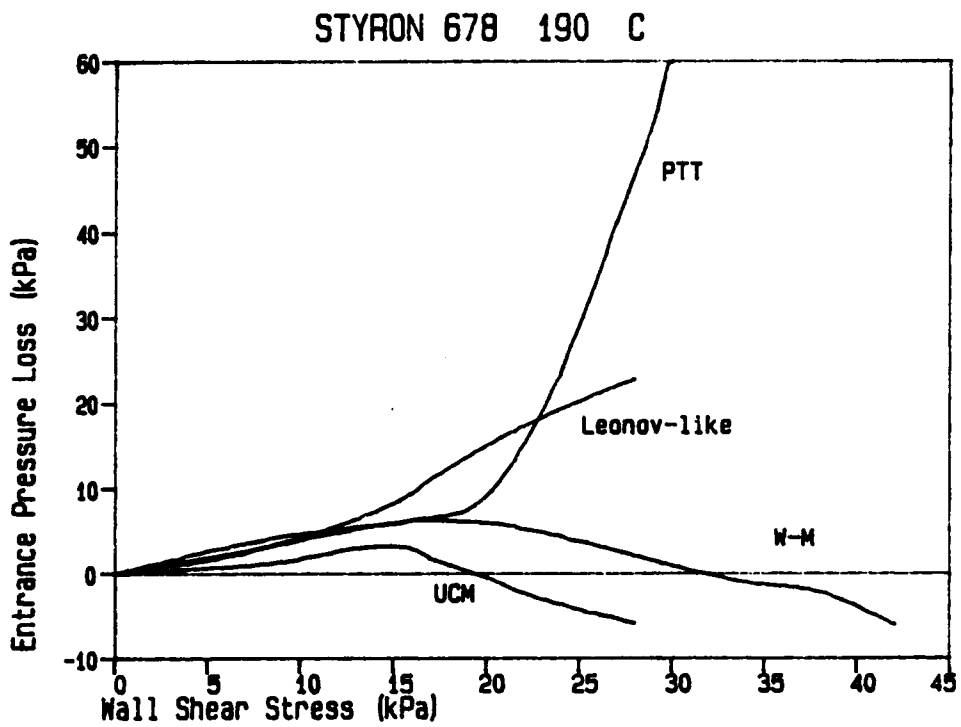


Figure 55. Entrance pressure loss in a 4/1 contraction as predicted by four models

however, show that they are probably numerical artifacts and dependent on the mesh. The oscillations around the corners and their increase with the mesh refinement give indications of a spatial singularity there. This has been studied by Lipscomb et al [76], as well as others [30,78], as it was mentioned earlier. Lipscomb gave evidence of a singularity at the corner for a second order fluid and a UCM model. Following the presence of the oscillations in the results of the calculations in the present work, as well as the reports by Keunings and Crochet [32,75], it is believed that this singularity may also exist for the PTT and the Leonov-like model, at least in their discretized weak form.

Indeed the oscillations of the stresses at the corner can be seen to increase as the limit of convergence is approached. Figure 56 shows the evolution of the oscillations in \bar{N} along the line $y=0$ for values of wall shear stress of 12, 16, 20, 24 and 26 kPa, given by the PTT model in MESH3. At a wall shear stress of 26 kPa the method did not converge and the results correspond to the iteration with the least error. The values of the birefringence in this figure are reduced for comparison, by division by the value of \bar{N} at the wall in the downstream channel for each shear stress. It can be seen there that at 12 kPa wall shear stress there is only one oscillation at $x=0$ of small amplitude. As the stress level increases, the oscillations also increase in magnitude but moderately up to 20 kPa wall shear stress. At 24 kPa, however, where the convergence is marginal, the oscillations extend $-4h$ and $+1.5h$ upstream and downstream, respectively. At 26 kPa τ_w , for which the solution can not converge to the specified tolerance, the oscillations are worse than the previous τ_w and extend even further in the upstream and downstream channels. There is not, however, a qualitative change in the solution from the previous solutions. It seems that the accumulation of the error at that point is just too large for the method to converge.

The same increase of the oscillations in faster flows can be seen even in the results of the velocity (u) at the centerline (Fig. 57). For this variable no oscillations exist at 12 kPa wall shear stress. Approaching the limit of convergence, however, oscillations start to appear even in the values of u along the centerline. Except for these oscillations, that are quite low in comparison to the ones of the stresses, the velocity behaves properly even at 26 kPa wall stress, that is beyond the convergence limit. Again there is no qualitative change in the curve of u as the limit itself is passed.

Because of the lack of reflection on the values of the stresses and the velocity of the transition from convergence to divergence of the solution, it is interesting to see whether the results obtained as described above at 26 kPa wall shear stress agree with the experimental data. This can be seen

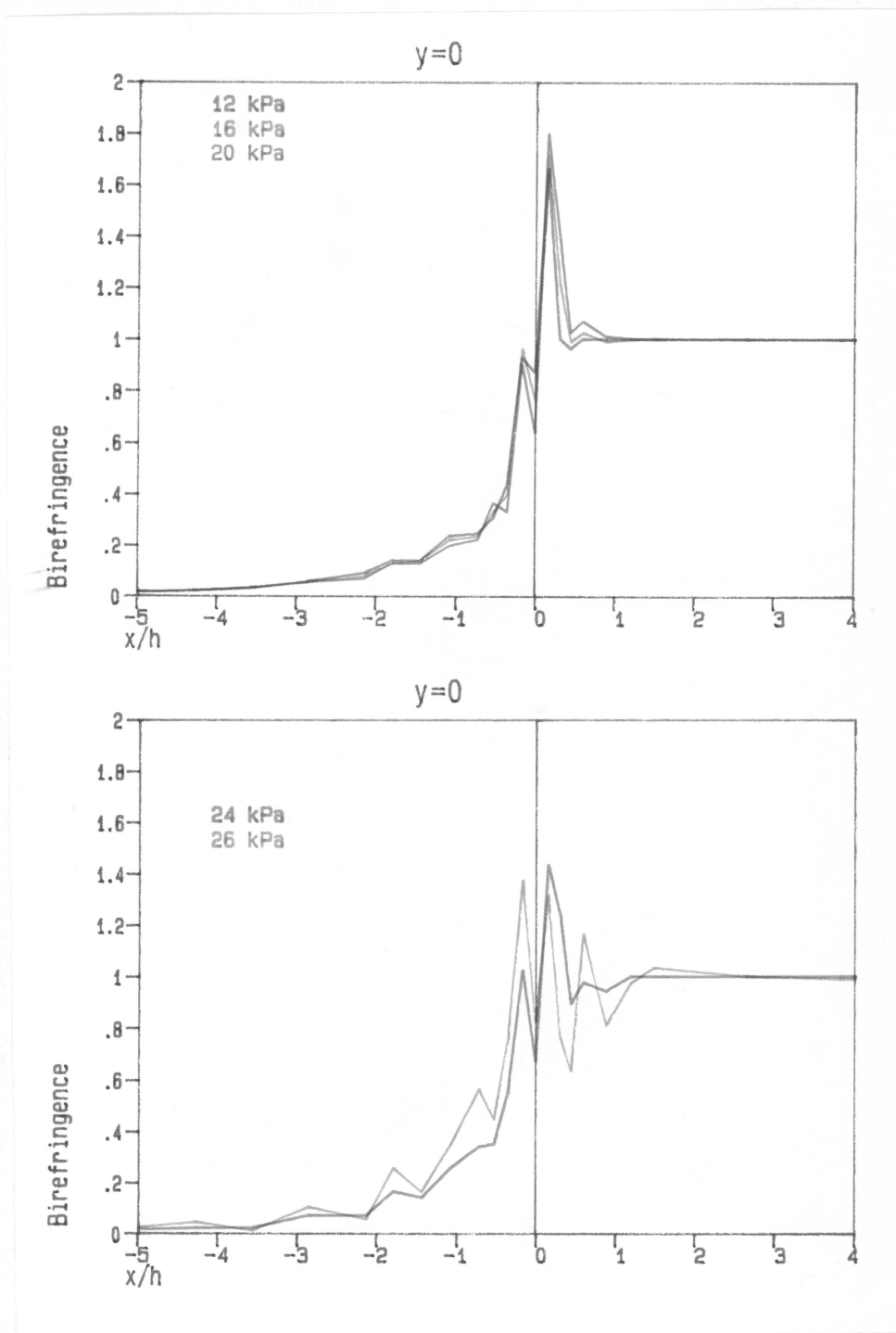


Figure 56. Fringe order along the line $y=0$ for several wall shear stress levels around the limit of convergence in the entry flow: P-T T and MESH3 were used. (a) τ_w of 12, 16, and 20 kPa, (b) τ_w of 24 and 26 kPa.

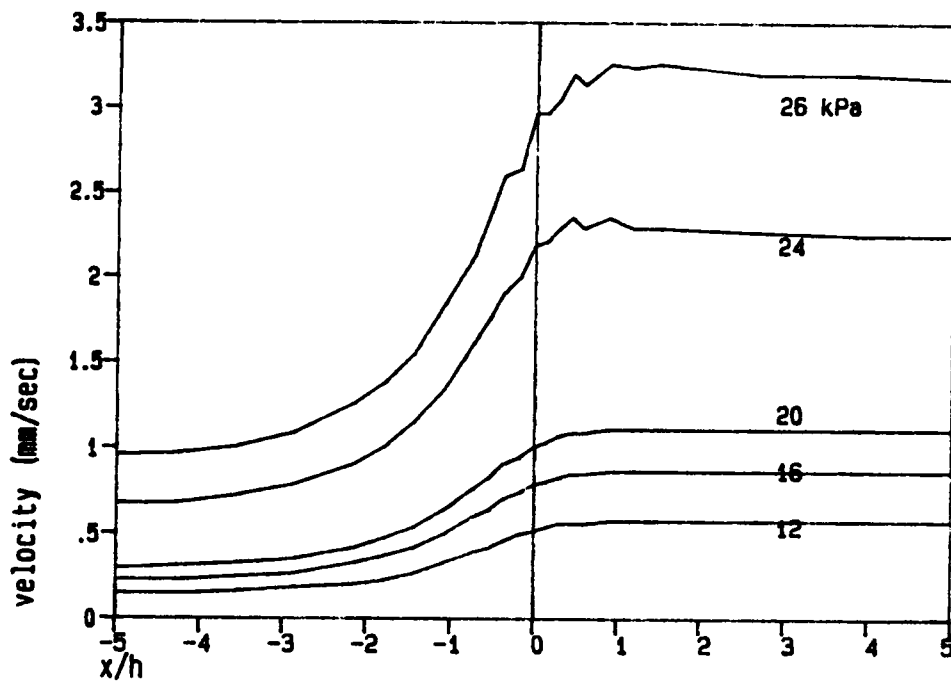


Figure 57. Velocity along the centerline at several wall shear stress values around the limit of convergence.: P-T T and MESH3 were used.

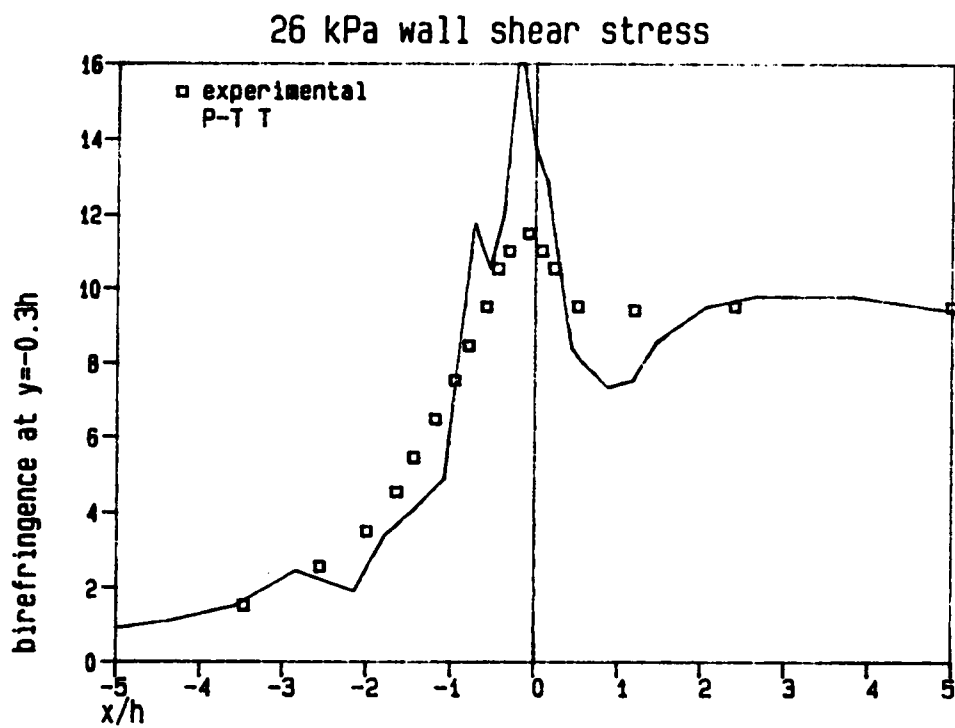


Figure 58. Birefringence along the line $y = -0.30h$ at a wall shear stress of 26 kPa beyond the limit of convergence

in Fig. 58. The comparison close to the entrance corner is impossible because of the high oscillations of the numerical results and also because the resolution of the experimental technique is greatly reduced at high stress levels, where there are too many fringes in the same area. The results, however, a little away from the corner fall in the same area as the experimental data. Following this and considering the parametric family of solutions with the stress level at the wall (or the elasticity De) as the parameter, it seems that the limit of convergence does not occur at some singular value of the parameter, such as a limit or a bifurcation point. That is, such points that have been found elsewhere, may just be numerical artifacts as it has already been suggested in [78]. Rather, the divergence occurs because of accumulation of error above the level that the method can handle. This error may be connected with the possible existence of a spatial singularity of the stresses at the corner. This problem, therefore, will not be avoided in finer meshes. The effect of such singularity will be enhanced if the size of the elements around the corner is reduced [76] and the convergence will deteriorate.

It was said in ch. 5.1 that the reason that the limits of convergence of the entry flow are more sensitive to mesh refinement than the ones for the flow over a transverse slot, may be connected to the stronger elongational nature of the former flow. It was also shown in ch. 4 that the models predict different extensional flow behaviour, including predictions of a critical extension rate, above which the extensional viscosity takes an infinite value for some rheological models. Therefore, the way that the models will handle the different extension rates that are present in the flow field is expected to be different. In the numerical solution of the flow into a contraction, the value of the extension rate was found to attain a maximum value at a point upstream near the reentrant corner (Fig.54). These values for $\dot{\epsilon}_{\max}$ for each model and for each mesh at the limits of convergence are shown in Table 9, together with the values of the critical extension rate for these models that predict one. As it was expected the maximum in $\dot{\epsilon}$ decreases with mesh refinement. The value of $\dot{\epsilon}_{\max}$ for the coarsest mesh is higher than the extensional rate, where the extensional viscosity will become unbounded in a uniaxial extension flow ($\dot{\epsilon}_{crit}$). As the mesh becomes finer, $\dot{\epsilon}_{\max}$ decreases below the critical extension rate. It is thought here that the coarse discretization of MESH1 actually smoothens out the infinite peak in the stresses that should be caused by an extension rate greater than the critical. This peak, however, is not the only cause of divergence, as it can be seen from the existence of limits even in models that do not show such unbounded values for the extensional viscosity. This was also reported by Keunings [75], who showed that the limit for convergence may

Table 9. Maximum extension rates that can be predicted by five models in the flow into a contraction

Model	Mesh	$\dot{\epsilon}_{max}$ sec ⁻¹	$\dot{\epsilon}_{crit}$ sec ⁻¹	Position of Maximum
PTT	1	2.87	-	-0.1, 0.01
	2	2.54		-0.16, 0.0
	3	2.07		-0.26, 0.05
J-S	1	2.78	1.25	-0.1, 0.01
	2	2.57		-0.16, 0.0
	3	2.09		-0.26, 0.05
Leonov like	1	2.43	-	-0.1, 0.01
	2	1.83		-0.16, 0.0
	3	1.14		-0.26, 0.05
W-M	1	3.18	2.4	-0.1, 0.01
	2	1.88		-0.16, 0.0
	3	1.20		-0.26, 0.05
UCM	1	1.44	0.83	-0.1, 0.01
	2	0.79		-0.16, 0.0
	3	0.59		-0.26, 0.05

go to zero for an infinitely fine mesh even for the Leonov-like model, which shows an extensional viscosity that increases gently with the extension rate to an asymptotic value of $6\eta_0$.

In view of the above and of the fact that reasonable results can be obtained for both flows in rather coarse meshes, it seems that very fine meshes are not the answer for the problem of the limitations in the numerical calculations of viscoelastic flows. It was shown that a medium mesh (as MESH2 for the hole flow or MESH3 for the entry flow) will give rather high limits of convergence and acceptable results; that is, numerical results comparable to the experimental data. Such meshes, therefore, are the best to use in engineering calculations of processes that involve flows of polymeric materials. The optimum mesh, however, is dependent on the specific flow geometry and no rigorous guidelines can be given here. On the other hand, the approach followed in this work does not solve the problem of the eventual failure of the method at high stress (or elasticity) levels in all meshes. There is strong evidence for the existence of singularities in the flow and it seems that they may be major causes of divergence. To solve the problem of the divergence, therefore, these singularities should be studied first. The implementation of boundary conditions that will allow slip at the wall near the corners is also recommended because slip in that area is expected to eliminate the effect of the singularity [76]. Finally, relaxing the viscoelastic nature of the fluid in the neighborhood of the corner may also extend the range of the stress levels where convergence is still possible for a specific mesh.

6.0 Conclusions and Recommendations

In the final chapter of this work is presented the summary of some conclusions that can be drawn from the results and the discussion in ch. 5. The paragraphs here are organized so that conclusions concerning the numerical method itself and the effects of the mesh and the rheological model on the numerical solutions are listed first. Then, some conclusions drawn from the numerical results in the flow over a transverse slot concerning the nature of that flow will be summarized. Finally, the conclusions from the numerical predictions of the flow into a contraction are given. Some recommendations for studies needed in order to further understand (and utilize) the numerical simulation of the viscoelastic flow and the problem of the failure of the methods at high elasticity levels are also given in this chapter.

6.1.1 The Numerical Method

1. Results with reasonable accuracy can be obtained by the finite element/penalty method (15% error or less except near corners) at least for the flow of a viscoelastic fluid into a contraction and the flow over a transverse slot, up to some limit of the elasticity or the stress levels. The quality of the solution that is obtained by the models depends little on the rheological model that is used, as long as the the specific flow conditions and the mesh used provide any solution at all.
2. Limits exist in the convergence of the iterations in the numerical simulation of viscoelastic flow and depend both on the rheological model that is used and on the mesh. These limits decrease monotonically with the mesh refinement. This decrease is more pronounced in the contraction

flow than in the flow over a slot. A possible reason for this difference may be the stronger elongational nature of the former flow than the latter.

3. Of the codeformational models that were used, the upper convected Maxwell model gives the lowest limits of convergence. The Leonov-like model also gives fairly low limits. The Phan-Thien Tanner model and the White-Metzner models show the highest limits in terms of the maximum stress levels and the flow rates that they can handle for a specific mesh.
4. Oscillations exist around corners in the numerical solutions of both flows. The magnitude of these oscillations increases as the limit of convergence is approached and is in general higher for finer meshes. It seems that this limit occurs when the error due to these oscillations cannot be reduced by the iterations.
5. The quality of the solution deteriorates when the limit of convergence is approached. However, even a little beyond the divergence of the iterations, the solution remains reasonable at least somewhat away from the corners.
6. Parametric singularities such as bifurcation and limit points were not found in the method that was used in this work. One of the main causes of the divergence in the flows that were studied seems to be the presence of spatial singularities in the stresses near the corners of the walls that contain the flow domain.
7. A possible reason for the higher limit of convergence predicted by the P-T T and the W-M models than the one predicted by the UCM model may be due to the shear thinning viscosity and primary normal stress difference functions predicted by the two models in shear flow. This shear thinning reduces the values of the stresses near the possible singularities at the corners. The low limits predicted by the Leonov-like model on the other hand, may be due to the quadratic stress term that this model includes, which may increase the order of these singularities.
8. Very fine meshes are not the answer to the problems found in the numerical simulations of viscoelastic flows because they trigger high oscillations around singular points and decrease the

convergence limit below any useful range of conditions. Very coarse meshes are not recommended either, because their results are not sufficiently accurate. Medium fine meshes are the best to be used in engineering calculations of viscoelastic flow (in this work meshes with 300 nodes were found to give the best picture for both flows). No rigorous guideline can be given as to how fine that mesh should be, however, because the optimum mesh depends on the specific flow geometry.

9. The unbounded values of the extensional viscosity that some rheological models predict above a certain extension rate are not the main cause of the divergence of the numerical method. Such values, if they exist, can be smoothed out by the discretization.
10. The use of the elasticity parameters (De and Wei) as the only criterion for the comparisons between results and limits obtained by several methods for viscoelastic flows is not justified because the values of these parameters for specific flow conditions depend on the rheological model that is used.

6.1.2 Flow Over a Transverse Hole

1. The stress field that is found experimentally and is predicted numerically by all the models is strongly asymmetric around the centerline of the hole and shows a strong concentration of high values of the stresses at the upstream corner.
2. The streamlines are found to be asymmetric in the experimental data but not so in the numerical predictions. The penetration of the streamlines into the hole is small for narrow holes. The penetration increases for wider slots and when the corners at the mouth of hole are grounded.
3. A vortex is predicted near the mouth inside the hole. The intensity and the position of this vortex depends both on the width of the slot and on the condition of the corners (sharp or grounded). This vortex can not always be seen from the experimental streamlines because of its very slow rate of circulation.

4. The hole pressure that is predicted by all the rheological models is lower than the experimental results by a factor of 0.5. Both experimental and numerical results are independent of the hole width and increase with the shear stress level.

6.1.3 Flow into a Contraction

1. A weak vortex is predicted by some rheological models at the blind corners upstream of the contraction. Its intensity is very low for most flow conditions for which convergence could be achieved. Such vortex is not found in the experimental results of polystyrene at these conditions, possibly because of its very slow circulation rate as indicated by its very low (calculated) intensity.
2. The entrance pressure loss as predicted by the Phan-Thien Tanner and the Leonov-like models increases monotonically with the shear stress. The predictions of the upper convected Maxwell and the White-Metzner models for the same quantity show a maximum and then they decrease, becoming eventually negative. In view of the behaviour of the entrance pressure loss that has been found experimentally, the predictions of the two latter models seem to be unacceptable.
3. There are two regions with strong elongational fields in the flow domain near the contraction. One lies along the centerline (purely elongational flow) and another lies along a line starting from the reentrant corner and extending upstream towards the wall at an angle that depends on the flow rate. It is possible that this angle is related to the *natural entrance* angle observed in streamline photographs of such flows.

6.2 Recommendations

It was mentioned in ch. 2 and in the discussion section that extensive work has been done already on the subject of the simulation of the viscoelastic flow. There are several questions, however, that still remain unanswered about the behaviour of the numerical solution and especially about the divergence of the methods. In this section, a few recommendations are listed suggesting some future work that is needed to answer such questions that arise from this study.

1. It was found in the previous chapters that a coarse mesh will decrease the oscillations but also decrease the accuracy of the solution. A finer mesh, on the other hand, improves the accuracy of the solution away from the corner but it decreases the limit of the convergence. It is suggested, therefore, to study the use of relatively larger elements around the corners and finer away from these points. Thus the overall results will be accurate except in the neighborhood of the corner. In this way, however, the convergence limits may also be higher and the oscillations may decrease.
2. Another way to avoid a possible singularity at the corners may be the implementation of boundary conditions that would allow slip at that point. Such boundary conditions may actually exist physically when the stresses become higher than the affinity between the fluid elements and the wall or they may only be a correction of the unrealistic high stresses predicted by a rheological model. A few unsuccessful attempts for such boundary conditions have already been made [5]. The search for successful slip conditions may, therefore, be one of the ways to solve the problem of the singularities at the corners and is strongly recommended.
3. It has been shown that the presence of severe singularities even in slow flows is a characteristic of viscoelastic nature. It is recommended, therefore, to study the effect of the relaxation of this viscoelastic nature of the fluid near the corners or other "difficult" points. That is, to set the relaxation time equal to zero near these points and keep its original value away from them. This is also an attempt to correct the erroneous predictions of the models near the corners.
4. It was found that several models show better predictions for specific types of flows than others. In geometries that include several different types of flow (as e.g. extensional and shear) it is recommended that different rheological models be used in different areas so that their better predictions for the specific flow types be utilized. To do so the existing program should be extended to allow changes from one model to the other.
5. All the recommendations above do not attempt to solve the problem of the singularities. Instead, they try to bypass them. The final answer for the problem of the divergence of the numerical methods will only be obtained when the origin and the order of the singularity is found.

The study of the (mathematical) singularity is, therefore, strongly recommended. When its order is found, the application of singular elements may possibly cure its effects.

6. Whether the stress concentration at the corners is a result of the rheological model or it is a "true" effect, can also be studied by flow birefringence methods. Good resolution is, however, essential because of the large number of fringes that may exist near the corner and may be beyond the resolution of the system that was used here.
7. Even though the length of the meshes upstream and downstream of the hole or the contraction were found to be physically sufficient for the absorbance of the disturbance, they may not be sufficient for the numerical method. It is recommended, therefore, that different lengths of the mesh be tried and the results compared.
8. Only the penalty formulation was used in this work. This method is more efficient in saving computer storage because of the less variables that it requires. Since the results that were thus obtained were acceptable, it is recommended that they be compared to results taken by the mixed FEM formulation so that the usefulness of the penalty method may be (or not) established.
9. All the rheological models that were used in this thesis were differential models. Integral models have been shown to give better predictions in simple flows but they are more complicated to use and often much more expensive. It was shown, however, in the case of the Leonov-like model that a method based on calculations along the paths of the fluid particles gave excellent results, while in the present work the limits of convergence for this model were found to be low. The development of codes using path tracking techniques and integral constitutive equations may, therefore, be necessary for better results in solving viscoelastic flows.
10. It was mentioned in ch. 2 that most rheological models show better predictions when multiple relaxation modes are used. The addition of more relaxation modes will add up to the storage and time requirements of the computer code. The comparison with the present results will show whether such multiple relaxation modes are needed.

11. The behaviour of the numerical solution in the present work was tested only for one material. There is, however, a great variety in the behaviour of the several polymeric materials under the same conditions, as e.g. the appearance or not of vortices in the entry flow described in ch. 2. It would be interesting to study whether this different behaviour can be predicted by the several models when the appropriate changes in their coefficients are made to fit the simple flows of these materials.
12. The flow into a contraction and the flow over a hole are two flows that have been extensively studied as test problems for numerical methods. The conclusions made until now based on these two flows should also be tested on other flow geometries. Some other simple geometries that are recommended are the journal bearing flow because it offers a domain without corners (see also [40,47]), the flow around a corner because it is found in all polymer processes, the exit flow because the point at the lip may show a more severe singularity (see [96]) and because it employs a free surface, and other flow geometries.
13. Since it has been reported that axisymmetric contraction flows may show stronger vortices at the blind corners, it is recommended that the present numerical code be extended to handle axisymmetric flows. Then comparisons can be made between the vortices predicted for planar and axisymmetric contraction flows under similar conditions.
14. It was mentioned in ch. 5.3 that there is an extensional field in the entry flow extending upstream near the reentrant corner that may be related to the natural entry angle. It is suggested here to study this relation, which may also give some insight in the problem of the vortex formation in the blind corner upstream of the contraction.
15. Finally the velocity field that was calculated in this thesis could not be directly compared to any experimental data. This comparison is essential in order to fully investigate the two flows. Experimental data for the velocities at several points in the domain are, therefore, needed.

References

1. Bird R.B., R.C. Armstrong, O. Hassager, "Dynamics of Polymeric Liquids" vol. 1, Wiley Publ. 1977.
2. Bird R.B., R.C. Armstrong, O. Hassager, "Dynamics of Polymeric Liquids" vol. 2, Wiley Publ. 1977.
3. Johnson M.W., D. Segalman, *J.Non-Newt.Fl.Mech.* 2, 255 (1977).
4. Viriyayuthakorn M., B. Caswell, *J.Non-Newt.Fl.Mech.* 16, 245 (1980).
5. Mendelson M.A., R.A. Brown, R.C. Armstrong, *J.Non-Newt.Fl.Mech.* 10, 31 (1982).
6. Leonov A.I., *Rheol.Acta* 15, 85 (1976).
7. Leonov A.I., M.N. Prokunin, *Rheol.Acta* 19, 393 (1980)
8. Phan-Thien N., R.I. Tanner, *J.Non-Newt.Fl.Mech.* 2, 313 (1977).
9. Phan-Thien N., R.I. Tanner, *J.Rheol.* 22(3), 259 (1978).
10. Leonov A.I., E.H. Lipkina, E.D. Pashkin, A.N. Prokunin, *Rheo.Acta* 15, 411 (1976).
11. Pike D., Phd. Dissertation, VPI & SU Blacksburg 1985.
12. Baird D.G., M.D. Read, J.N. Reddy, 'Comparison of Flow Birefringence Data with a Numerical Simulation of the Hole Pressure Problem', subm. to *J.Non-Newt.Fl.Mech.*, 1985.
13. Turner M.J., R.W. Clough, H.C. Martin, L.J. Topp, *J.Aeron.Sci.* 23, 805 (1956).
14. Argyris J.H., S. Kelsey, "Energy Theorems and Structural Analysis", Butterworth Sci. Publ. London 1960.
15. Clough R.W., *J.Struct.Div. ASCE, Proc.2nd.Conf. Electr.Comp.* p.345 (1960).
16. Rao S.S., "The Finite Element Method in Engineering", Pergamon Press 1982.
17. Redy J.N., "Introduction to Finite Element Method", McGraw Hill Publ. 1984.
18. Hasbani Y., M. Engelman, *Comp. and Fluids* 7, 13 (1979).
19. Crochet M.J., A.R. Davies, K. Walters, "Numerical Simulation of Non-Newtonian Flows", *Rheology Series*, 1, Elsevier Publ. 1984.
20. Reddy J.N. *Int.J.Num.Meth.Fl.* 2, 151 (1982).
21. Malkus D.S., *Nucl.Eng.Des.* 57, 441 (1980).

22. Kawahara M., N. Takeuchi, *Comp. and Fluids* 5, 33 (1977).
23. Crochet M.J., K. Walters, *Ann.Rev.Fl.Mech.* 15, 241 (1983).
24. Chang P. T.W. Patten, B.A. Finlayson, *Comp. and Fluids* 7, 267 (1979).
25. Malone M.F., S. Middleman, annual meeting of AIChE, Nov. 1979.
26. Crochet M.J., M. Bezy, *J.Non-Newt.Fl.Mech.* 5, 201 (1979).
27. Mitsoulis E., J. Vlachopoulos, F.A. Mirza, "Finite Element Analysis of Isothermal and Anisothermal Polymer Melt Flow", paper presented at IMRI/NRCC mini symposium "Mathematical Modelling of Plastics Processing and Control", Montreal Feb. 1983.
28. Mitsoulis E., J. Vlachopoulos, F.A. Mirza, "A Numerical Study of the Effect of Normal Stresses and the Elongational Viscosity on Entry Vortex Growth and on Extrudate Swell", paper presented at IMRI/NRCC 3d. symposium on "Mathematical Modelling of Plastics Processing", Montreal Jan. 1984.
29. Mitsoulis E., J.Vlachopoulos, F.A. Mirza, *Polym.Eng.Sci.* 24(9), 707 (1984).
30. Davies A.R., S.J. Lee, M.F. Webster, *J.Non-Newt.Fl.Mech.* 16, 117 (1984).
31. Crochet M.J., S. Dupont, M.J. Marshal, "The Numerical Simulation of the Flow of Viscoelastic Fluids of the Differential and Integral Types: A Comparison", Proc. IX Intl. Congress on Rheology, Mexico 1984.
32. Keunings R., M.J. Crochet, *J.Non-Newt.Fl.Mech.* 14, 279 (1984).
33. Upadhyay R.K., PhD. Dissertation, Cornell University 1982.
34. Kim-E. M.E., R.A. Brown, R.C. Armstrong, *J.Non-Newt.Fl.Mech.* 13, 341 (1983).
35. Yeh P.W., M.E. Kim, R.C. Armstrong, R.A. Brown, *J.Non-Newt.Fl.Mech.* 16, 173 (1984).
36. Josse S.L., B.A. Finlayson, *J.Non-Newt.Fl.Mech.* 16, 13 (1984).
37. Bernstein B., M.K. Kadivar, D.S. Malkus, *Comp.Meth.Appl.Mech.Engr.* 27, 279 (1981).
38. Chang P-W., T.W. Patten, B.A. Finlayson, *Comp.& Fluids* 7, 285 (1979).
39. Crochet M.J., R. Keunings, *J.Non-Newt.Fl.Mech.* 10, 339 (1982).
40. Tanner R.I., "On the Stability of Computations in Processing Rheology", in Proc. IX Intl. Congress on Rheology, Mexico 1984.
41. Coleman C.J., *J.Non-Newt.Fl.Mech.* 7, 289 (1984).
42. Crochet M.J., G. Pilate, *J.Non-Newt.Fl.Mech.* 1, 247 (1976).
43. Bernstein B. D.S. Malkus, ACS Preprints, Kansas meeting, Sept 1982.
44. Jackson N.R., B.A. Finlayson, *J.Non-Newt.Fl.Mech.* 10, 71 (1982).
45. Richards G.D., P. Townsend, *Rheo.Acta* 20, 261 (1981).
46. Beris A.N., R.C. Armstrong, R.A. Brown, *J.Non-Newt.Fl.Mech.* 13, 109 (1983).
47. Beris A.N., R.C. Armstrong, R.A. Brown, *J.Non-Newt.Fl.Mech.* 16, 141 (1984).
48. Davies A.R., *J.Non-Newt.Fl.Mech.* 16, 195 (1984).

49. Tanner R.I., *J.Non-Newt.Fl.Mech.* 10, 169 (1982).
50. Lee K-C., B.A. Finlayson, "Stability of Polymer Flow", paper presented in AICHE meeting, San Francisco Nov. 1984.
51. Hughes T.J.R., T.E. Tezduyar, A.N. Brooks, pp 97-104 in 'Finite Element Flow Analysis', T. Kawai ed., Univ. of Tokyo Press 1982.
52. Treloar L.R.G., "The Physics of Rubber Elasticity", Clarendon Press, Oxford 1958.
53. Larson R.G., *Rheo.Acta* 22, 435 (1983).
54. Upadhyay R.K., A.I. Isayev, S.F. Shen, *Rheo.Acta* 20, 443 (1981).
55. Upadhyay R.K., A.I. Isayev, S.F. Shen, *J.Rheol.* 27(2), 155 (1983).
56. Oldroyd J.G., in "Rheology of Disperse Systems", Pergamon Pr. London 1959, pp.1-15.
57. Tadmor Z., C.G. Gogos, "Principles of Polymer Processing", Wiley Interscience Publ. 1979.
58. Crochet M.J. "Numerical Simulation of Die Entry and Die Exit Flow of a Viscoelastic Fluid", in "Numerical Methods in Industrial Forming Processes", p.85, Pineridge Press 1982.
59. Boger D.V. "Circular Entry Flow of Inelastic and Viscoelastic Fluids" in "Advances in Transport Process", 2, 1982.
60. Ballenger T.F., J.L. White, *Chem.Eng.Sci.* 25, 1191 (1970).
61. Ballenger T.F., J.L. White, *J.Appl.Polym.Sci.* 25, 1949 (1971).
62. White J.L., A. Kondo, *J.Non-Newt.Fl.Mech.* 3, 41 (1977).
63. Han C.D., L.H. Drexler, *J.Appl.Polym.Sci.* 17, 2329 (1973).
64. White S.A., D.G. Baird, *J.Non-Newt.Fl.Mech.* 20, (1986) 93.
65. Higashitani K., W.G. Pritchard, *Trans.Soc.Rheol.* 16, 687 (1972).
66. Baird D.G. PhD. Dissertation, University of Wisconsin-Madison 1974.
67. Baird D.G. *J.Appl.Polym.Sci.* 20, 3155 (1976).
68. Cochrane T., K. Walters, M.F. Webster, *Phil.Trans.Roy.Soc.London* 301, 163 (1981).
69. H. Giesekus, *Rheol.Acta* 5, (1966) 29.
70. H. Giesekus, *J.Non-Newt.Fl.Mech.* 11, (1982) 69.
71. R. Keunings, *J.Comp.Physics* 62, (1986) ???.
72. J.S. Vrentas, M.C. Vrentas, *J.Non-Newt.Fl.Mech.* 19, (1985) 1.
73. K. Walters, 'Experimental and Theoretical Aspects of Non-Newtonian Flows' in Non-Newtonian Flows' J.F. Wendt ed., Lecture series 1981-6, Von Karman Inst. for Fluid Dynamics, St. Genese Belgium (1981).
74. J.C. Maxwell, *Phil.Trans.Roy.Soc.* A157, (1867) 49.
75. R. Keunings, *J.Non-Newt.Fl.Mech.* 20, (1986) 209.
76. G.G. Lipscomb, R. Keunings, M.M. Denn, 'Implications of Boundary Singularities in Complex Geometries', *J.Non-Newt.Fl.Mech.* in press (1986).

77. A.I. Isayev, R.K. Upadhyay, *J.Non-Newt.Fl.Mech.* 19, (1985) 135.
78. B. Debaut, M.J. Crochet, *J.Non-Newt.Fl.Mech.* 20, (1986) 173.
79. S.L. Josse, K.-C. Lee, B.A. Finlayson, *J.Non-Newt.Fl.Mech.* 20, (1986) 257.
80. J.V. Lawler, S.J. Muller, R.A. Brown, R.C. Armstrong, *J.Non-Newt.Fl.Mech.* 20, (1986) 51.
81. D.D. Joseph, J.C. Saut *J.Non-Newt.Fl.Mech.* 20, (1986) 117.
82. J.M. Marchal, M.J. Crochet, *J.Non-Newt.Fl.Mech.* 20, (1986) 187.
83. D.H. Han, *Trans.Soc.Rheol.* 18(1), (1974) 163.
84. M.J. Crochet, *J.Non-Newt.Fl.Mech.* 20, (1986) 1.
85. S.A. White, Ph.D. Dissertation, Virginia Polytechnic Institute and State University under preparation 1986.
86. S.-P. Chang, MS Thesis, Virginia Polytechnic Institute and State University under preparation 1986.
87. H. Janeschitz-Kriegl, *Polymer Melt Rheology and Flow Birefringence*, Springer-Verlag, New York (1983).
88. A.I. Isayev, R.K. Upadhyay, *Rheo.Acta* 25, (1986) 80.
89. S.A. White, A.D. Gotsis, D.G. Baird, 'Review of the entry flow problem: Experimental and numerical', accep. for publ. in *J.Non-Newt.Fl.Mech.* 1986.
90. D.S. Malkus, M. Yao, MRC Technical report #2943, July 1986.
91. VERSATEC/CALCOMP ploter manual, doc. GR01, publ. User Services , Va Tech Computing Center, 1985.
92. D.H. Pelletier, 'GEN2D', Va Tech 1984.
93. MINPACK, Doc. MT09, publ. User Services Dept., VA Tech Computing Center, 1983.
94. IMSL User's guide, Doc. MT01, publ. User Services Dept., VA Tech Computing Center, 1983.
95. T.C. Papanastasiou, 'Die swell computations: I. Effects of slip velocity, Newtonian viscosity and surface tension', in prep. 1986.
96. M.D. Read, Ph.D. Dissertation, Virginia Polytechnic Institute and State University, Blacksburg VA 1986.
97. D.S. Malkus, 'Finite element methods for viscoelastic flows', in 'Viscoelasticity and Rheology', A.S. Lodge, M. Renardy, J.A. Nohel eds., Academic Press 1985, 391-419.
98. P. Le Tallec, *J.Non-Newt.Fl.Mech.* 20, (1986) 241.

Appendix A. Listing of NONEWT.FEM

In this section of the appendix, the computer code NONEWT.FEM is listed. The listing includes some explanatory documentation of the structure, the sections and the logical flow of the program, as well as a list of the main variables in the several parts. A list of the required input cards is also included in the documentation in the front part of the program, as well as the format that should be used.

```

C          P R O G R A M   N O N E W T
C          ( AN IN-CORE FINITE ELEMENT ANALYSIS COMPUTER PROGRAM )
C
C          .....
C          .
C          . FINITE-ELEMENT ANALYSIS OF TWO-DIMENSIONAL FLUID FLOW PROBLEMS
C          .
C          .
C          . THE PROGRAM USES LINEAR ISOPARAMETRIC QUADRILATERAL ELEMENTS FOR
C          . THE SOLUTION OF VISCOUS INCOMPRESSIBLE FLUID FLOW PROBLEMS BY
C          . THE PENALTY METHOD FORMULATION. A CHOICE OF FIVE DIFFERENT
C          . CONSTITUTIVE EQUATIONS IS GIVEN TO MODEL THE RHEOLOGICAL
C          . BEHAVIOR OF THE FLUID; A GENERALIZED NEWTONIAN FLUID (GNF),
C          . AN UPPER-CONVECTED MAXWELL MODEL, A WHITE-METZNER CONSTITUTIVE
C          . MODEL, A PHAN-THIEN TANNER MODEL OR A LEONOV LIKE MODEL.
C          . THE VISCOSITY FUNCTION MAY BE A CONSTANT (NEWTONIAN)
C          . A POWER-LAM, OR A CARREAU MODEL. THE NON-LINEAR FORMULATION
C          . IS SOLVED BY PICARD ITERATION WITH BOTH THE VELOCITIES AND THE
C          . STRESSES AS THE PRIMARY DEGREES OF FREEDOM. THE PRESSURE AND
C          . THE STREAM FUNCTION AND THE BIREFRINGENCE MAY BE CALCULATED
C          . IN THE POST PROCESSOR. THE RESULTS OF THE CALCULATIONS ARE
C          . STORED IN OUTPUT UNITS 11, 12, 14 AND 16 FOR PLOTTING USING
C          . AN EXTERNAL ROUTINE.
C
C          .....

```

D E S C R I P T I O N O F T H E V A R I A B L E S

```

C  AMU.....VISCOSITY FUNCTION
C  AMU2.....INFINITE SHEAR RATE VISCOSITY
C  AMBDA.....VALUE OF THE FLUID TIME CONSTANT IN SUBROUTINE STIFFQ
C  BETA.....ACCELERATION PARAMETER FOR THE PICARD ITERATION TECHNIQUE
C  C1,C2.....MATERIAL CONSTANTS FOR FLUID FLOW PROBLEM (INPUT)
C             C1= ZERO SHEAR VISCOSITY
C             C2= VALUE OF PENALTY PARAMETER
C  C3.....TOLERANCE PARAMETER
C  C4,C5.....MATERIAL CONSTANTS FOR NON-NEWTONIAN VISCOSITY FUNCTIONS
C             (INPUT)
C             C4= M-CONSTANT FOR POWERLAM MODEL OR LAMBDA FOR THE CARREAU
C                 THE PTT, THE MAXWELL OR THE LEONOV MODEL
C             C5= EXPONENT N USED IN BOTH THE POWERLAM AND CARREAU MODEL
C  C6.....PARAMETER XI IN PTT OR RATIO OF ETA-INF/ETA-0 FOR THE
C             CARREAU OR THE LEONOV MODELS. IT SHOULD BE ZERO FOR ALL
C             OTHERS UNLESS NON-ZERO INFINITE SHEAR RATE VISCOSITY IS
C             REQUIRED (INPUT)
C  DKSI.....PARAMETER XI FOR THE PTT AND THE J-S MODELS
C  DX(I).....ELEMENT DIMENSIONS AT THE X-DIRECTION FOR MESH (INPUT)
C  DY(I).....ELEMENT DIMENSIONS AT THE Y-DIRECTION FOR MESH (INPUT)
C             DX AND DY ARE NEEDED ONLY IF SUBROUTINE MESH IS USED
C  ELSTIF....ELEMENT COEFFICIENT (OR 'STIFFNESS') MATRIX
C  ELXY.....GLOBAL COORDINATES OF ELEMENT NODES:
C             ELXY(I,1)=XE(I); ELXY(I,2)=YE(I), I=1,NPE.
C  EPS.....PARAMETER EPSILON IN PTT MODEL (INPUT)
C  ERR.....GLOBAL ERROR FOR THE CURRENT SOLUTION
C  F(I).....ELEMENT FORCE VECTOR
C  GF(I).....ARRAY OF PREVIOUS SOLUTION FOR PICARD ITERATION
C  GPI(I).....ARRAY OF I-2 SOLUTION FOR PICARD ITERATION
C  GSTIF.....GLOBAL COEFFICIENT MATRIX. ASSEMBLED AND STORED IN
C             BANDED FORM.
C  IBDP(I)...ARRAY OF SPECIFIED BOUNDARY DEGREES OF FREEDOM (INPUT)
C  IBF(I)....ARRAY OF SPECIFIED NONZERO FORCES FOR THE STREAMLINES
C             CALCULATION (INPUT)
C  IBS(I)....ARRAY OF SPECIFIED VALUES OF THE STREAM FUNCTION (INPUT)
C  IBSF(I)...ARRAY OF SPECIFIED NONZERO FORCES (INPUT)
C  IEL.....INDICATOR FOR TYPE OF ELEMENT (INPUT)
C             IEL=1, FOUR-NODE QUADRILATERAL ELEMENT
C             IEL=2, QUADRATIC QUADRILATERAL

```

```

C  IGNF .....INDICATOR FOR THE POWER LAW OR THE CARREAU VISCOSITY
C      FUNCTION (INPUT)
C      IGNF=1  POWER LAW MODEL
C      IGNF=2  CARREAU MODEL
C      IGNF=0  CONSTANT VISCOSITY COEFFICIENT (DEFAULT)
C  IMESH.....INDICATOR FOR MESH GENERATION (INPUT)
C      IMESH=0, MESH INFORMATION IS TO BE READ INTO PROGRAM
C      IMESH=1, MESH IS GENERATED IN PROGRAM
C  IOUT(I)...ARRAY WITH THE NODES ON THE OUTLINE (INPUT)
C  ISTR.....STREAM FUNCTION CALCULATION FLAG (INTERNAL)
C      ISTR = 0, VELOCITY AND STRESS CALCULATIONS
C      ISTR = 1, CALCULATE STREAM FUNCTIONS FOR STREAM LINE PLOT
C  ITER.....VALUE OF THE ITERATION NUMBER FOR NON-LINEAR ITERATION
C  ITIME(I)..TIME CONSUMPTION X 100 IN SECONDS
C  ITHMAX....MAXIMUM NUMBER OF ITERATIONS FOR THE NONLINEAR ANALYSIS
C  ITYPE.....RHEOLOGICAL MODEL TO BE USED (INPUT):
C      ITYPE=0, NEWTONIAN MODEL
C      ITYPE=1, GENERALIZED NEWTONIAN FLUID
C              (POWER LAW OR CARREAU)
C      ITYPE=2, WHITE METZNER MODEL (CARREAU VISCOSITY FUNCTION)
C      ITYPE=3, UPPER CONVEXED MAXWELL MODEL
C      ITYPE=4, PHAN-THIEN TANNER MODEL
C      ITYPE=5, LEONOV-LIKE MODEL
C  IMEI.....NODE NUMBER WHERE THE CALCULATION OF WEISSENBERG NUMBER
C      TAKES PLACE (INPUT)
C  NBW.....BAND WIDTH OF THE COEFFICIENT MATRIX, GSTIF
C  NDF.....NUMBER OF DEGREES OF FREEDOM PER NODE (INTERNAL)
C      =5 STRESS/VELOCITY CALC., =1 STREAM FUNCTION CALC.
C  NEQ.....TOTAL NUMBER OF EQUATIONS IN THE PROBLEM (=NNM*NDF)
C  NEM.....NUMBER OF ELEMENTS IN THE MESH
C  NHBW.....HALF BAND WIDTH OF THE COEFFICIENT MATRIX, GSTIF
C  NN.....TOTAL NUMBER OF DEGREES OF FREEDOM PER ELEMENT (=NPE*NDF)
C  NNM.....NUMBER OF NODES IN THE FINITE ELEMENT MESH (INPUT)
C  NOD(I,J)..GLOBAL NODE NUMBER CORRESPONDING TO THE J-TH NODE OF
C      ELEMENT I (CONNECTIVITY MATRIX) (INPUT)
C  NOUT.....NUMBER OF THE NODES ON THE OUTLINE + 1 (INPUT)
C  NPE.....NUMBER OF NODES PER ELEMENT (IEL*4)
C  NPRNT.....INDICATOR FOR PRINTING ELEMENT MATRICES AND VECTORS
C      NPRNT=1, PRINT ELEMENT MATRICES (INPUT)
C      NPRNT=0, NO PRINT
C  NSF.....NUMBER OF SPEC. NONZERO FORCES FOR STREAM FUNCTION (INPUT)
C  NSBF.....NUMBER OF SPECIFIED NONZERO BOUNDARY 'FORCES' (INPUT)
C  NSDF.....NUMBER OF SPECIFIED PRIMARY DEGREES OF FREEDOM (INPUT)
C  NSSF.....NUMBER OF SPECIFIED VALUES OF THE STREAM FUNCTION (INPUT)
C  NX,NY....NUMBER OF ELEMENTS IN THE X AND Y DIRECTION, RESPECTIVELY
C  RHO.....DENSITY OF THE FLUID FOR FLUID INERTIA TERMS (IN G/MM3)
C  T11(I)...VALUE OF THE STRESS-11 AT NODE I (POST-PROCESSOR)
C  T12(I)...VALUE OF THE STRESS-12 AT NODE I (POST-PROCESSOR)
C  T22(I)...VALUE OF THE STRESS-22 AT NODE I (POST-PROCESSOR)
C  TIME1....TIME CONSUMPTION FOR THE READ-IN OF THE DATA
C  TIME2....TIME CONSUMPTION FOR THE CALCULATION OF THE ELEMENT
C      STIFFNESS MATRIX
C  TIME3....TIME CONSUMPTION FOR THE INVERSION OF THE GLOBAL
C      STIFFNESS MATRIX
C  TITLE....TITLE IDENTIFYING THE RUN
C  TOL.....MAXIMUM ALLOWABLE GLOBAL ERROR (INPUT)
C  VBDF(I)...ARRAY OF THE VALUES CORRESPONDING TO THE SPECIFIED DEGREES
C      OF FREEDOM IN ARRAY IBDF(I) FOR THE NEWTONIAN SOL. (INPUT)
C  VBDF2(I)..ARRAY OF THE VALUES CORRESPONDING TO THE SPECIFIED DEGREES
C      OF FREEDOM IN ARRAY IBDF(I) FOR NON-NEWTONIAN SOL. (INPUT)
C  VBF(I)...ARRAY OF THE VALUES OF THE SPECIFIED NONZERO FORCES FOR
C      THE STREAM FUNCTION CALCULATION (INPUT)
C  VBS(I)...ARRAY OF THE VALUES CORRESPONDING TO THE NODES WHERE THE
C      STREAM FUNCTION IS SPECIFIED (INPUT)
C  VBSF(I)...ARRAY OF THE VALUES CORRESPONDING TO THE SPECIFIED NONZERO
C      FORCES IN ARRAY IBSF(I) (INPUT)
C  VEL(I)...VALUES OF THE VARIABLES AT THE PREVIOUS ITERATION

```


C 6-10 NY NUMBER OF SUBDIVISIONS IN THE Y-DIRECTION
C
C *DATA CARD 7 AND 8 (8F10.4) IEL*NX+1 ENTRIES FOR NX AND IEL*NY+1
C ENTRIES FOR NY
C
C 1-80 DX(I) DISTANCE BETWEEN NODES ALONG X-DIRECTION
C 1-80 DY(I) DISTANCE BETWEEN NODES ALONG Y-DIRECTION
C
C *DATA CARD 9 (1I5) INPUT FOR THE DRAWING OF THE OUTLINE OF THE
C DOMAIN
C
C 1-5 NOUT NUMBER OF THE NODES ON THE OUTLINE + 1
C
C *DATA CARD 10 (16I5) NODES ON THE OUTLINE OF THE FLOW DOMAIN
C
C 1-80 IOUT(I) NODE NUMBER ON THE OUTLINE. THE FIRST AND THE
C LAST VALUE FOR IOUT(I) SHOULD BE THE SAME AND
C THE OUTLINE SHOULD BE CLOSED.
C
C *DATA CARD 11 (5F10.4) CONSTANTS DEPENDING ON PROBLEM TYPE
C
C 1-10 C1 ZERO SHEAR VISCOSITY
C 11-20 C4 M-CONSTANT FOR POWERLAW OR LAMBDA FOR
C THE CARREAU MODEL.
C 21-30 C5 EXPONENT N USED IN BOTH THE POWERLAW AND
C THE CARREAU MODEL.
C 31-40 C6 XI PARAMETER FOR THE PTT AND JS MODELS OR
C RATIO OF ETA-0/ETA-INF.
C 41-50 EPS EPSILON PARAMETER FOR THE PTT MODEL
C 51-60 RHO DENSITY OF THE FLUID (G/MM3)
C
C *DATA CARD 12 (4F10.5) CONSTANTS OF THE METHOD
C
C 1-10 C2 PENALTY PARAMETER
C 11-20 BETA ACCELERATION PARAMETER BETA
C 21-30 C3 TOLERANCE FOR THE ITERATIONS
C
C *DATA CARD 13 (16I5) IF NDSF=0, ENTER ZERO IN COLUMN 5 AND
C SKIP CARDS 11 AND 12
C
C 1-5 NSDF NUMBER OF SPECIFIED PRIMARY DEGREES OF
C FREEDOM.
C
C *DATA CARD 14 (16I5) READ NSDF ENTRIES
C
C 1-80 IBDF(I) SPECIFIES DEGREES OF FREEDOM
C
C *DATA CARD 15 (8F10.4) READ NSDF ENTRIES
C
C 1-80 VBDF(I) VALUES OF THE SPECIFIED DEGREES OF FREEDOM
C IN ARRAY IBDF(I) FOR THE NEWTONIAN CASE
C
C *DATA CARD 16 (8F10.4) READ NSDF ENTRIES
C
C 1-80 VBDF2(I) VALUES OF THE SPECIFIED DEGREES OF FREEDOM
C FOR THE SUBSEQUENT ITERATIONS.
C
C *DATA CARD 17 (16I5) IF NSBF=0, ENTER ZERO IN COLUMN 5 AND
C SKIP CARDS 14 AND 15.

```

C
C 1-5      NSBF      NUMBER OF SPECIFIES NONZERO SECONDARY
C          DEGREES OF FREEDOM.
C
C *DATA CARD 18  (16I5)      READ NSBF ENTRIES
C
C 1-80     IBSF(I)      SPECIFIED NONZERO SECONDARY DEGREES OF
C          FREEDOM.
C
C *DATA CARD 19  (8F10.4)    READ NSBF ENTRIES
C
C 1-80     VBSF(I)      VALUES OF SECONDARY DEGREES OF FREEDOM
C
C *DATA CARD 20  (I5)        IF NSSF=0 SKIP CARDS 19 AND 20
C
C 1-5      NSSF        NUMBER OF SPECIFIED VALUES OF STREAM
C          FUNCTION
C
C *DATA CARD 21  (16I5)      READ NSSF ENTRIES
C
C 1-80     IBS        SPECIFIED DEGREES OF FREEDOM FOR STREAM
C          FUNCTION CALCULATIONS
C
C *DATA CARD 22  (8F10.5)    READ NSSF ENTRIES
C
C 1-80     VBS        VALUES OF SPECIFIED DOF'S FOR STREAM
C          FUNCTION CALCULATIONS
C
C *DATA CARD 23  (I5)        IF NSF = 0 SKIP CARD 22
C
C 1-5      NSF        SPECIFIED FORCES FOR STREAM FUNCTION
C          CALCULATIONS
C
C *DATA CARD 24  (8F10.5)    READ NSF ENTRIES
C
C 1-80     VALUES OF THE SPECIFIED FORCES FOR THE
C          STREAM LINE CALCULATION
C
C *DATA CARD 25  (I5)
C
C 1-5      INEI        NODE # (AT THE WALL), WHERE THE VALUE OF THE
C          HEISSENBERG NUMBER WILL BE CALCULATED
C
C 6-10     IPSI        NODE #, WHERE THE VALUE OF THE STREAM FUNCTION
C          WILL BE EQUAL TO 1. (FOR NORMALIZATION OF THE
C          STREAM FUNCTION)

```

```

C-----
C

```

```

C      IMPLICIT REAL*8(A-H,O-Z)
C      DIMENSION GF(1665),GP(1665),Z1(1002),
C 1      VEL(45),IBDF(200),VBDF(200),IBSF(45),VBSF(45),TITLE(20)
C 2      ,VBDF2(200),T11(350),T12(350),T22(350),ITIME(6)
C 3      ,IBS(200),VBS(200),VISC(320),DLA(320),SR(320),EXTR(320)
C 4      ,XN(320),YN(320),PRE(320),VORT(320),IBF(200),VBF(200)
C 5      ,XS(1002),YS(1002),Z(1002),XO(40),YO(40),IOUT(40)
C
C      COMMON/MSH/DX(21),DY(21),X(350),Y(350),NOD(320,9)
C      COMMON/STF/ELSTIF(45,45),ELXY(9,2),F(45)
C      COMMON/PTT/DKSI,EPSIL
C      COMMON/VIS/ETAM,ETAN,AMBDA,RHO,ITER,IGNF

```

```

COMMON/INTE/NDF,NPE,NEM,NNM
COMMON/GSTFM/GSTIF(1450,320)

C
C .....
C .
C .           P R E P R O C E S S O R   U N I T           .
C .
C .....
C
C R E A D - I N   T H E   I N P U T   D A T A   H E R E
C
CALL TIMEON
READ(5,1000) TITLE
READ(5,1010) IEL,ITYPE,IMESH,NPRNT,ITMAX,IGNF

C
C CHECK THE DATA
C IF THERE IS A SERIOUS ERROR IN THE INPUT WRITE MESSAGES AND STOP
C
IF(IEL.GE.3.OR.ITYPE.GE.6) GO TO 900
IF(NPRINT.NE.1) NPRINT=0
NPE = 4*IEL
IF(ITYPE.LT.1.OR.ITYPE.GT.2) IGNF = 0
IF(IGNF.LT.0.OR.IGNF.GT.2) GO TO 950

C
IF(IMESH.EQ.1)GOTO 30

C
C READ NODAL DATA
C
READ(5,1010) NEM,NNM
WRITE (11,1010)NEM,NNM
DO 20 N=1,NEM
20 READ(5,1010) (NOD(N,I),I=1,NPE)
READ(5,1020) (X(I),Y(I),I=1,NNM)

C
C READ THE OULTINE FOR THE FLOW DOMAIN
C
READ(5,1010) NOUT
READ(5,1010) (IOUT(I),I=1,NOUT)
GOTO 40

C
C CALL THE MESH GENERATOR IF DESIRED
C
30 READ(5,1010) NX,NY
NOX1=IEL*NX+1
NOY1=IEL*NY+1
READ(5,1020) (DX(I),I=1,NOX1)
READ(5,1020) (DY(I),I=1,NOY1)
CALL MESH(IEL,NX,NY)
40 CONTINUE

C
C READ THE CONSTANTS OF THE MODEL AND OF THE FEM FORMULATION
C
READ(5,1030) C1,C4,C5,C6,EPSIL,RHO
READ(5,1030) C2,BETA,C3
IF (C3.GT.1.D-8) GOTO 45
C3 = 0.01
WRITE (6,2800)
45 IF (BETA.GT.1.D-6) GO TO 47
WRITE (6,2810)
BETA = 1.

C
C READ THE BOUNDARY CONDITIONS
C
C READ THE SPECIFIED DEGREES OF FREEDOM
C
47 READ(5,1010) NSDF
IF (NSDF.EQ.0) GO TO 50

```

```

      READ(5,1010) (IBDF(I),I=1,NSDF)
      READ(5,1020) (VBDF(I),I=1,NSDF)
      READ(5,1020) (VBDF2(I),I=1,NSDF)
C
C   READ THE SPECIFIED FORCES
C
50  READ(5,1010) NSBF
      IF(NSBF.EQ.0)GOTO 60
      READ(5,1010) (IBSF(I),I=1,NSBF)
      READ(5,1020) (VBSF(I),I=1,NSBF)
C
C   READ THE SPECIFIED VALUES OF THE STREAM FUNCTION
C
60  READ(5,1010) NSSF
      IF (NSSF.EQ.0) GO TO 65
      READ(5,1010) (IBS(I),I=1,NSSF)
      READ(5,1020) (VBS(I),I=1,NSSF)
C
C   READ THE NATURAL BOUNDARY CONDITIONS FOR THE STREAM FUNCTION
C
65  READ(5,1010) NSF
      WRITE (11,1010) NSF
      IF (NSF.EQ.0) GO TO 70
      READ(5,1010) (IBF(I),I=1,NSF)
      READ(5,1020) (VBF(I),I=1,NSF)
C
C   READ THE NODE, FOR THE CALCULATION OF THE ELASTICITY PARAMETER
C   AND THE NODE FOR WHICH THE STREAM FUNCTION WILL BE 1.00
C
70  READ(5,1010) IMEI,IPSI
C
C   END OF THE DATA INPUT
C
C   SET INTERNAL VARIABLES NEEDED FOR COMPUTATIONS ACCORDING TO
C   THE MODEL
C
      NDF = 5
      TOL = C3
      AMU2 = 0.
      DKSI = 0.
      ETAM = C4
      ETAN = 1.
      ERR1 = 0.
      ERR2 = 0.
C
      GO TO (75,80,80,95,90,80),(ITYPE+1)
75  ETAM = 0.
      EPSIL = 0.
      GO TO 95
80  AMU2 = C1*C6
      ETAN = C5
      GO TO 95
90  AMU2 = C1/7.5
      DKSI = C6
95  C2=C2*1.0D6
      NEQ=NNM*NDF
      NN=NPE*NDF
C
C   COMPUTE THE HALF BAND WIDTH
C
      NHBW=0
      DO 100 N=1,NEM
      DO 100 I=1,NPE
      DO 100 J=1,NPE
      NM=(IABS(NOD(N,I)-NOD(N,J))+1)*NDF
100 IF (NHBW.LT.NM) NHBW=NM

```

```

      NBM = 2*NHBM
C
C   D A T A   E C H O
C
C   PRINT IDENTIFICATION OF THE RUN
C
      WRITE (6,2910)
      WRITE (6,2000) TITLE
      GO TO (111,112,113,114,115,116),(ITYPE+1)
111  WRITE (6,2005)
      GO TO 118
112  IF (IGNF.EQ.1) WRITE (6,2010)
      IF (IGNF.EQ.2) WRITE (6,2020)
      GOTO 118
113  WRITE (6,2030)
      GO TO 118
114  WRITE (6,2040)
      GO TO 118
115  IF (EPSIL.GE.1.D-12) WRITE (6,2050)
      IF (EPSIL.LT.1.D-12) WRITE (6,2060)
      GO TO 118
116  WRITE (6,2070)
C
C   PRINT FLUID PARAMETERS AND PARAMETERS OF THE METHOD
C
118  WRITE (6,2075)
      WRITE (6,2080)
      WRITE (6,2100) C1,RHO
      IF(ITYPE.EQ.1) WRITE (6,2110) C4,C5
      IF(ITYPE.EQ.2) WRITE (6,2120) C4,C5
      IF(ITYPE.GT.2) WRITE (6,2130) C4
      IF(ITYPE.EQ.4) WRITE (6,2140) DKSI,EPSIL
      IF(ITYPE.GE.4) WRITE (6,2150) AMU2
      WRITE (6,2160)
      WRITE (6,2170) IEL,IGNF,ITYPE,BETA
      WRITE (6,2180) C2,C3
      IF(C3.LT.1.D-8) WRITE(6,2980)
      WRITE (6,2190) NEM,NNM,NEQ
      WRITE (6,2200) NHBM
C
C   PRINT ELEMENT DATA (IF DESIRED)
C
      IF(NPRINT.NE.1) GO TO 130
      WRITE (6,2210)
      DO 120 I=1,NEM
120  WRITE (6,2215) I,(NOD(I,J),J=1,NPE)
      WRITE (6,2220)
      WRITE (6,1020) (X(I),Y(I),I=1,NNM)
130  CONTINUE
C
C   PRINT BOUNDARY CONDITIONS
C
      WRITE (6,2240)
      IF(NSDF.EQ.0) GO TO 135
      WRITE (6,2250) NSDF
      WRITE (6,1010)(IBDF(I),I=1,NSDF)
135  IF(NSBF.EQ.0) GOTO 140
      WRITE (6,2270) NSBF,(IBSF(I),I=1,NSBF)
      WRITE (6,2280)
      WRITE (6,2300) (VBSF(I),I=1,NSBF)
140  IF (NSSF.LE.0) GO TO 150
      WRITE (6,2310) NSSF
      WRITE (6,1010) (IBS(I),I=1,NSSF)
      WRITE (6,2320)
      WRITE (6,2300) (VBS(I),I=1,NSSF)
      WRITE (6,2330)
150  IF (NSF.EQ.0) GO TO 155

```

```

WRITE (6,2315) NSF
WRITE (6,2325)
WRITE (6,2300) (VBF(I),I=1,NSF)
C
C   IF NO VISCOSITY OR NO BOUNDARY CONDITION ARE GIVEN STOP !
C
155 IF(C1.LT.1.D-12) GOTO 960
    IF((NSDF+NSBF).EQ.0) GOTO 970
C
C   PLOT THE MESH IN STANDARD DIMENSIONS
C
    XMIN = 0.
    YMIN = 0.
    XMAX = 0.
    YMAX = 0.
    DO 166 I=1,NNM
    XMIN = DMIN1(XMIN,X(I))
    XMAX = DMAX1(XMAX,X(I))
    YMIN = DMIN1(YMIN,Y(I))
166 YMAX = DMAX1(YMAX,Y(I))
    XL = XMAX - XMIN
    YL = YMAX - YMIN
    XYL = DMAX1(XL,YL)
    DO 167 I=1,NNM
    XS(I) = X(I)*8./XYL
167 YS(I) = Y(I)*8./XYL
    XL = XL*8./XYL
    YL = YL*8./XYL
    CALL MPLOT(XL,YL,XS,YS,NOD,NEM,NNM,NPE,XMIN,YMIN)
    CALL PLOT(9.,-2.,999)
C
C   WRITE THE DATA FOR THE OUTLINE OF THE FLOW DOMAIN IN FILE 14 AND 16
C
    WRITE(14,1012) NOUT
    WRITE(16,1012) NOUT
    DO 168 I=1,NOUT
    XO(I) = XS(IOUT(I))*1.002
    YO(I) = YS(IOUT(I))*1.002
    WRITE(16,1022) XO(I),YO(I)
168 WRITE(14,1022) XO(I),YO(I)
C
C   .....
C   .
C   .           P R O C E S S O R   U N I T           .
C   .
C   .....
C
C   INITIALIZE THE GLOBAL STIFFNESS MATRIX AND FORCE VECTOR
C
    DO 169 I=1,NEQ
    GF(I)=0.0
    GP(I) = 0.0
169 GSTIF(I,NBM) = 0.0
C
C   EVALUATE THE TIME NEEDED FOR READ-IN OF INPUT
C
    ITER = 0
    CALL TIMECK(ITIME(1))
    TIME1 = DFLOAT(ITIME(1))/100.
    WRITE (6,2340) TIME1
C
C   B E G I N   I T E R A T I O N S   F O R   T H E   N O N   L I N E A R   P R O B L E M
C
    ISTR = 0
800 ITER = ITER + 1
    ERR2 = ERR1

```

```

ERR1 = ERR
ERR = 0.
IF (ITER.EQ.2) CALL TIMEON
C
C UPDATE THE SOLUTION VECTORS AND INITIALIZE THE GLOBAL STIFFNESS
C MATRIX
C
DO 170 I = 1,5*NNM
GP(I) = GF(I)
GF(I) = GSTIF(I,NBM)
DO 170 J = 1,NBM
170 GSTIF(I,J) = 0.0
C
C DO-LOOP ON THE NUMBER OF ELEMENTS TO CALCULATE THE ELEMENT
C MATRICES, AND ASSEMBLY OF THE ELEMENT MATRICES BEGINS HERE
C
DO 300 N=1,NEM
C
C UPDATE THE NONLINEAR VELOCITY TERMS
C
B = BETA
IF(ITER.EQ.1) B = 1.
CALL UPDATE(N,VEL,B,GF,GP,ELXY,NDF,NPE)
C
C CALCULATE THE ELEMENT STIFFNESS MATRIX
C
CALL STIFFQ(IEL,ITYPE,C1,C2,VEL,ISTR,AMU2)
C
C PRINT THE ELEMENT STIFFNESS MATRIX IF DESIRED
C
IF(N.NE.NPRNT.OR.ITER.GT.1)GOTO 250
WRITE (6,2350)
DO 220 I=1,NN
220 WRITE (6,2360) (ELSTIF(I,J),J=1,NN)
C
C ASSEMBLE ELEMENT MATRICES TO OBTAIN GLOBAL MATRIX
C
250 CALL ASMBLE(NHBM,N)
C
C LOOP OVER THE ELEMENTS FINISHES HERE
C
300 CONTINUE
C
C ASSEMBLED MATRIX EQUATIONS ARE NOW READY FOR IMPLEMENTATION OF
C THE BOUNDARY CONDITIONS ON PRIMARY AND SECONDARY VARIABLES
C
IF(ITER.EQ.1) CALL BOUND(NSBF,NSDF,IBSF,IBDF,VBSF,VBDF,NHBM)
IF(ITER.GT.1) CALL BOUND(NSBF,NSDF,IBSF,IBDF,VBSF,VBDF2,NHBM)
C
C CALL SUBROUTINE 'SOLVER' TO SOLVE THE SYSTEM OF EQUATIONS FOR
C THE PRIMARY DEGREES OF FREEDOM (THE SOLUTION IS RETURNED IN
C GSTIF(I,NBM)) AND CHECK FOR THE TIME NEEDED FOR THE INVERSION
C OF THE GLOBAL STIFFNESS MATRIX
C
IF (ITER.EQ.2) CALL TIMECK(ITIME(2))
CALL SOLVER (NEQ,NHBM)
IF (ITER.NE.2) GOTO 360
CALL TIMECK(ITIME(3))
C
C TIME CONSUMPTION CALCULATION
C
TIME2 = DFLOAT(ITIME(2))/100.
TIME3 = (DFLOAT(ITIME(3))-DFLOAT(ITIME(2)))/100.
WRITE (6,2400)TIME2,TIME3
WRITE (6,2410)
C
C .....
```

```

C      .
C      .           P O S T P R O C E S S O R   U N I T           .
C      .
C      .
C      .....
C
360 IF (ITMAX.EQ.1.OR.ITYPE.EQ.0) GOTO 440
370 IF (ITER.EQ.1) GOTO 800
C
C      ERROR CALCULATION AND CONVERGENCE CHECK
C
      ERR = 0.0
      DO 375 I = 1,NEQ
      IF (GSTIF(I,NBW).LT.1.D-4) GOTO 375
      ERR = ERR + (GF(I)-GSTIF(I,NBW))**2/GSTIF(I,NBW)**2
375 CONTINUE
      WRITE (6,2420) ITER,ERR
      IF(ERR.LT.TOL) GOTO 440
      IF (ERR2.LT.ERR1.AND.ERR1.LT.ERR) GOTO 410
      IF(ITER.LT.ITMAX) GO TO 800
400 WRITE (6,2450)ITER,ERR
      GOTO 440
410 WRITE (6,2500) ITER,ERR1,ERR
440 CONTINUE
C
C      CALCULATE THE RETARDATION TERMS AND THE ELASTICITY PARAMETERS
C
      CALL STRESS(NBW,T11,T12,T22,AMU2,IMEI,ITYPE,DEB)
      WEI = DABS((T11(IMEI)-T22(IMEI))/2./T12(IMEI))
C
      WRITE (6,2460) IMEI,WEI,DEB
C
      WRITE (6,2910)
      WRITE (6,2470)
      WRITE (6,2480)
      WRITE (6,2490) (I,X(I),Y(I),GSTIF(5*I-4,NBW),GSTIF(5*I-3,NBW),
*      T11(I),T12(I),T22(I),T11(I)-T22(I),I=1,NNM)
C      WRITE (11,1040) (GSTIF(5*I-4,NBW),GSTIF(5*I-3,NBW),I=1,NNM)
C
C      CALCULATE AND PRINT PRESSURE, SHEAR RATE ETC.
C
      CALL PRESS(NBW,AMU2,ITYPE,VISC,C1,SR,DLA,XN,YN,PRE,EXTR,VORT,C2)
C
      WRITE (6,2910)
      WRITE (6,2610)
      WRITE (6,2620)
      WRITE(6,2630) (N,XN(N),YN(N),PRE(N),SR(N),VISC(N),EXTR(N),DLA(N),
&      VORT(N),N=1,NEM)
      WRITE (6,2910)
C
C      CALCULATE THE BIREFRINGENCE
C
      DO 500 I=1,NNM
      Z(I) = 1.8223D-4*DSQRT(4.*T12(I)**2+(T11(I)-T22(I))**2)
      Z1(I) = Z(I)
500 WRITE (11,1045) XS(I),YS(I),Z(I)
      DO 510 I=NNM+1,1000
510 WRITE (11,1045) XS(1),YS(1),Z(1)
C
C.....
C
C      S T R E A M L I N E S   C A L C U L A T I O N           .
C.....
C
      IF((NSSF+NSF).EQ.0) GOTO 990
C
      ISTR = 1
      NNOF = NOF

```

```

      NDF = 1
      B = 1.0
      NH = NHBW/NDF
C
C   RERUN THE PROGRAM FOR THE STREAMLINES
C
      DO 845 I=1,NEQ
        GF(I) = GSTIF(I,NBW)
        DO 845 J=1,NBW
945   GSTIF(I,J) = 0.0
        DO 850 N=1,NEM
          CALL UPDATE(N,VEL,B,GF,GP,ELXY,NPDF,NPE)
          CALL STIFFQ(IEL,ITYPE,C1,C2,VEL,ISTR,AMU2)
          CALL ASMBLE(NH,N)
850   CONTINUE
        CALL BOUND(NSF,NSSF,IBF,IBS,VBF,VBS,NH)
        CALL SOLVER(NNM,NH)
C
C   PRINT RESULTS OF STREAM FUNCTION AND STOP THE RUN...  END !!!
C
      WRITE (6,2710)
      IF(IPSI.EQ.0) GOTO 854
      IF(DABS(GSTIF(IPSI,2*NH)).GT.1.D-12) GO TO 875
854   IIP = 0
      DO 855 I=1,NSSF
        IF(ABS(I).EQ.1.AND.DABS(VBS(I)).LT.1.D-12) GO TO 860
855   CONTINUE
      IPSI = 1
      GO TO 875
860   DO 865 I=1,NSSF
        IF (ABS(I).EQ.NNM.AND.DABS(VBS(I)).LT.1.D-12) GO TO 870
865   CONTINUE
      IPSI = NNM
      GOTO 875
870   WRITE (6,2930)
      IIP = 1
875   DO 891 I=1,NNM
        IF (IIP-1) 880,885,885
880   PSI = GSTIF(I,2*NH)/GSTIF(IPSI,2*NH)
        GO TO 890
885   PSI = GSTIF(I,2*NH)
890   Z(I) = PSI
        WRITE (12,1045) XS(I),YS(I),Z(I)
891   WRITE (6,2720) I,X(I),Y(I),PSI,Z(I)
C
      DO 895 I=NNM+1,1000
895   WRITE (12,1045) XS(1),YS(1),Z(1)
      STOP
C
C   WRITE ERROR MESSAGES AND INTERRUPT THE PROGRAM
C
900   WRITE(6,2900) IEL,ITYPE
      STOP
950   WRITE(6,2920) IGNF
      STOP
960   WRITE(6,2960)
      STOP
970   WRITE(6,2970)
      STOP
990   WRITE(6,2990)
      STOP
C
C   F O R M A T S
C
1000  FORMAT (20A4)
1010  FORMAT (16I5)
1012  FORMAT (I4,4H 1)

```

1020 FORMAT (8F10.4)
 1022 FORMAT (2E15.5)
 1030 FORMAT (7F10.4)
 1040 FORMAT (6E12.5)
 1045 FORMAT (4E15.5)

C

2000 FORMAT(1H1,10X,20A4/10X)
 2005 FORMAT (10X,'NEWTONIAN MODEL'/)
 2010 FORMAT (10X,'POWER LAW MODEL'/)
 2020 FORMAT (10X,'CARREAU MODEL'/)
 2030 FORMAT (10X,'WHITE METZNER MODEL WITH VARIABLE RELAXATION TIME',/)
 2040 FORMAT (10X,'UPPER CONVEXED MAXWELL MODEL',/)
 2050 FORMAT (10X,'PHAN-THIEN TANNER MODEL',/)
 2060 FORMAT (10X,'JOHNSON SEGALMAN MODEL',/)
 2070 FORMAT (10X,'LEONOV MODEL',/)
 2075 FORMAT (//1X,90(1H*),//,10X,'DATA ECHO',/)
 2080 FORMAT (10X/10X,'FLUID PARAMETERS'/)
 2100 FORMAT(10X,'ZERO SHEAR VISCOSITY.....=' ,E10.3,/,
 * 10X,'FLUID DENSITY.....=' ,E10.3)
 2110 FORMAT(10X,'ETA M.....=' ,E10.3,
 & /,10X,'EXPONENT N.....=' ,E10.3,/)
 2120 FORMAT(10X,'LAMBDA (CARREAU).....=' ,E10.3
 & /,10X,'EXPONENT N.....=' ,E10.3,/)
 2130 FORMAT(10X,'LAMBDA.....=' ,E10.3)
 2140 FORMAT(10X,'PARAMETER KSI.....=' ,E10.3
 & /10X,'PARAMETER EPSILON.....=' ,E10.3)
 2150 FORMAT(10X,'SOLVENT (BASE) VISCOSITY.....=' ,E10.3)
 2160 FORMAT(5X/10X,'METHOD PARAMETERS'/)
 2170 FORMAT(10X,'ELEMENT TYPE.....=' ,I2,/,
 *14X,'1 = LINEAR',/,14X,'2 = QUADRATIC',/,
 *10X,'VISCOSITY MODEL.....=' ,I2,/,
 *14X,'0 = IRRELEVANT',/,
 *14X,'1 = POWER LAW',/,14X,'2 = CARREAU',/,
 *10X,'PROBLEM TYPE.....=' ,I2,/,10X,
 *'ACCELERATION PARAMETER BETA.....=' ,E10.3)
 2180 FORMAT(2X/10X,'PENALTY PARAMETER.....=' ,E10.3/
 *10X,'TOLERANCE.....=' ,F10.3)
 2190 FORMAT (//10X,'ACTUAL NUMBER OF ELEMENTS IN THE MESH.....=' ,I5,/,
 *10X,'NUMBER OF NODES IN THE MESH.....=' ,I5,/,10X,
 * 'TOTAL NUMBER OF EQUATIONS IN THE MODEL.....=' ,I5)
 2200 FORMAT (10X,'HALF BAND WIDTH OF GLOBAL STIFFNESS MATRIX =' ,I5)
 2210 FORMAT (/,5X,'BOOLEAN (CONNECTIVITY) MATRIX NOD(I,J) ',/)
 2215 FORMAT (10X,20I5)
 2220 FORMAT (/,15X,'X- AND Y- COORDINATES'/)
 2240 FORMAT (1X,//10X,'BOUNDARY CONDITIONS'/)
 2250 FORMAT (/,10X,'NO. OF SPECIFIED DEGREES OF FREEDOM.....=' ,I3,/,
 *10X,'ARRAY OF THE SPECIFIED DEGREES OF FREEDOM=' ,/)
 2270 FORMAT(/,5X,'NO. OF SPECIFIED FORCES =' ,I5,/,5X,'SPECIFIED FORCE
 IDEGREES OF FREEDOM :',15I5,/)
 2280 FORMAT(/,5X,'VALUES OF THE SPECIFIED FORCES:',/)
 2300 FORMAT (6(2X,E12.5))
 2310 FORMAT (/,10X,'NO. OF SPECIFIED VALUES OF THE STREAM FUNCTION =' ,
 *I3,/,10X,'ARRAY OF THE SPECIFIED VALUES OF THE STREAM FUNCTION:/')
 2315 FORMAT (/,10X,'NO. OF SPECIFIED NATURAL CONDITIONS OF THE ',
 &'STREAM FUNCTION =' ,I3/)
 2320 FORMAT (1X/10X,'VALUES OF THE STREAM FUNCTION AT THE BOUNDARY'/1X)
 2325 FORMAT (1X/10X,'VALUES OF THE SPECIFIED FORCES FOR THE STREAM ',
 &'FUNCTION')
 2330 FORMAT (//,10X,'END OF DATA ECHO',//1X,90(1H*),//
 * 10X,'** TIME CONSUMPTION FOR COMPUTATIONS **')
 2340 FORMAT(1X/10X,'TIME FOR READ-IN THE DATA AND INITIALIZATION',
 &14(1H.),' =' ,F8.2,' SEC')
 2350 FORMAT(3X,'ELEMENT MATRICES:',/)
 2360 FORMAT(5E15.5)
 2400 FORMAT(10X,'TIME FOR THE CALCULATION OF THE ELEMENT STIFFNESS',
 & ' MATRICES =' ,F8.2,' SEC PER ITERATION',
 & /10X,'TIME FOR THE SOLUTION OF THE ',

```

&      'EQUATIONS',20(1H.),' =',F8.2,' SEC PER ITERATION'///)
2410 FORMAT(//,10X,'** GLOBAL ERROR DURING ITERATIONS **'//)
2420 FORMAT(10X,'ITERATION NUMBER =',I3,8X,'ERROR = ',E12.5)
2450 FORMAT(///12X,'**CONVERGENCE NOT MET FOR ITMAX = ',I3,2X,'ERROR = '
1,E13.5,'**'//)
2460 FORMAT(5X//10X,'THE VALUE OF THE WEISSENBERG NUMBER AT THE WALL'
&,' (NODE',I5,') IS',F8.3//10X,'THE VALUE OF THE DEBORAH NUMBER',
&' AT THE SAME NODE IS',F8.3/)
2470 FORMAT (1H1,///,53X,'S O L U T I O N   V E C T O R :',/)
2480 FORMAT(//,5X,'NODE',6X,'X COORDINATE',3X,'Y COORDINATE',3X,
*'X VELOCITY',5X,'Y VELOCITY',5X,'STRESS T11',5X,'STRESS T12',
* 5X,'STRESS T22',9X,'N1',//)
2490 FORMAT (5X,I4,2X,8E15.5)
2500 FORMAT (10X//10X,'ERROR. THE METHOD DIVERGES. THE ERROR',
&' INCREASES AFTER THE ',I2,'TH ITERATION'//10X,'PREVIOUS ERROR WAS
&',E10.5,' CURRENT ERROR IS',E10.5)

2610 FORMAT (1X//10X,'R E S U L T S   O F   P R E S S U R E   E T C .')//)
2620 FORMAT (/,6X,'ELE.NO.',3X,'X-DIMEN.',6X,'Y-DIMEN.',
&7X,'PRESSURE ',3X,'SHEAR RATE ',4X,
*'VISCOSITY',4X,'EXTENSION RATE',3X,'RELAXATION TIME',3X,
&'VORTICITY'//)
2630 FORMAT (5X,I5,8E15.5)
2710 FORMAT(2X///6X,'OUTPUT OF THE VALUES OF THE STREAM FUNCTION'
&,' AND THE BIREFRINGENCE'//
&8X,'NODE X COORDINATE',4X,'Y COORDINATE',2X,'STREAM FUNCTION',
&2X,'BIREFRINGENCE'//)
2720 FORMAT (6X,I4,3X,4E15.5)
2800 FORMAT (1X/6X,10(1H*),'WARNING! TOLERANCE TOO SMALL. ADJUSTED '
&,'TO 0.01 ',10(1H*))
2810 FORMAT(1X/10X,10(1H*),'WARNING ! ACCELERATOR PARAMETER BETA WAS ',
&'TOO SMALL. ADJUSTED TO 1.00 ',10(1H*))
2900 FORMAT(10X/10X,'ERROR ! THE PARAMETER IEL (' ,I2,')',
*' OR ITYPE (' ,I2,') HAS AN INVALID VALUE')
2910 FORMAT(1X,/90(1H*))//)
2920 FORMAT (10X/10X,'ERROR ! THE PARAMETER IGNF HAS AN INVALID ',
&'VALUE (' ,I3,')')
2930 FORMAT (1X//5X,'WARNING !! THE NORMALIZATION OF THE ',
&'STREAMLINES WAS NOT POSSIBLE DUE TO LACK OF REFERENCE'/7X,
&'POINT. THE FOLLOWING RESULTS OF THE STREAM FUNCTION ARE NOT',
&' NORMALIZED')
2960 FORMAT(1X//10X,'ERROR !! ZERO SHEAR VISCOSITY HAS A ZERO VALUE !')
2970 FORMAT(1X//10X,'ERROR !! NO BOUNDARY CONDITIONS ARE SPECIFIED !')
2980 FORMAT(1X//10X,'WARNING !! NO TOLERANCE SPECIFIED. THE VALUE OF '
%, '0.01 (OR 1 %) IS USED !')
2990 FORMAT(1X//10X,'ERROR !! NO BOUNDARY CONDITIONS FOR THE ',
&' STREAMLINES SPECIFIED !',/15X,'THE PROGRAM TERMINATED ',
&' WITHOUT THE STREAMLINES CALCULATION')

```

C

END

C

C*****

SUBROUTINE ASMBLE(NBWM,N)

C

C

C

SUBROUTINE TO ASEMBLE THE ELEMENTS IN A GLOBAL MATRIX OF
NBW X NEQ DIMENSIONS (ADJUSTED FROM REDDY [17])

C

```

IMPLICIT REAL*8(A-H,O-Z)
COMMON/MSH/DX(21),DY(21),X(350),Y(350),NOD(320,9)
COMMON/STF/ELSTIF(45,45),ELXY(9,2),F(45)
COMMON/INTE/NDF,NPE,NEM,NNM
COMMON/GSTFM/GSTIF(1450,320)

```

C

```

NBW = 2.*NBWM
DO 280 I=1,NPE
NR=(NOD(N,I)-1)*NDF

```

```

DO 280 II=1,NDF
NR=NR+1
L=(I-1)*NDF+II
GSTIF(NR,NBM) = GSTIF(NR,NBM) + F(L)
DO 260 J=1,NPE
NCL=(NOD(N,J)-1)*NDF
DO 260 JJ=1,NDF
M=(J-1)*NDF+JJ
NC=NCL+JJ-NR+NHBW
IF (NC) 260,260,250
250 GSTIF(NR,NC)=GSTIF(NR,NC)+ELSTIF(L,M)
260 CONTINUE
280 CONTINUE
RETURN
END
C*****
SUBROUTINE BOUND(NSBF,NSDF,IBSF,IBDF,VBSF,VBDF,NHBW)
C .....
C
C SUBROUTINE TO INCORPORATE THE BOUNDARY CONDITIONS
C (ADJUSTED FROM REDDY [17])
C .....
C
C IMPLICIT REAL*8(A-H,O-Z)
C DIMENSION IBDF(200),VBDF(200),IBSF(45),VBSF(45)
C COMMON/GSTFM/GSTIF(1450,320)
C NBM = NHBW*2.
C IF (NSBF.EQ.0) GO TO 320
C
C IMPOSE SPECIFIED FORCES
C
C DO 310 I=1,NSBF
C II=IBSF(I)
310 GSTIF(II,NBM) = GSTIF(II,NBM) + VBSF(I)
C
C IMPOSE SPECIFIED PRIMARY DEGREES OF FREEDOM
C
320 DO 342 I = 1,NSDF
IB = IBDF(I)
VB = VBDF(I)
DO 344 J = 1,NBM
344 GSTIF(IB,J) = 0.0
GSTIF(IB,NHBW) = 1.0
342 GSTIF(IB,NBM) = VB
RETURN
END
C*****
SUBROUTINE LAMDA(DL,G)
C .....
C
C SUBROUTINE TO CALCULATE THE VARIABLE RELAXATION TIME FOR THE
C WHITE METZNER MODEL. DEPENDS ON THE MATERIAL AND SHOULD BE
C GIVEN BY THE USER. THIS VERSION GIVES LAMBDA AS A POLYNOMIAL
C OF LOG10(G), WITH G THE SHEAR RATE AND THE COEFFICIENTS FOUND
C FROM FITTING THE "STYRON 678" AT 190 C.
C
C DL .... RELAXATION TIME
C G ..... SHEAR RATE
C .....
C
C IMPLICIT REAL*8(A-H,O-Z)
C IF (G.LT.1D-2) DL = 2.0
C IF (G.GE.1D-2) DL = 0.43504 - 0.45297*DLOG10(G)
C * + 0.1388*(DLOG10(G))*2
C IF (G.GT.42.7D0) DL = 0.065
C RETURN

```

```

END
C*****
SUBROUTINE MESH( IEL,NX,NY)
C
C .....
C THE SUBROUTINE GENERATES ARRAY NOD(I,J), COORDINATES X(I),Y(I),
C AND MESH INFORMATION (NNM,NEM,NPE) FOR RECTANGULAR DOMAINS. THE
C DOMAIN IS DIVIDED INTO BILINEAR OR BIQUADRATIC QUADRILA-
C TERAL ELEMENTS (NX BY NY NONUNIFORM MESH IN GENERAL).
C (ADJUSTED FROM REDDY [17])
C .....
C
C IMPLICIT REAL*8 (A-H,O-Z)
C COMMON/MSH/DX(21),DY(21),X(350),Y(350),NOD(320,9)
C COMMON/INTE/NDF,NPE,NEM,NNM
C
C MESH OF QUADRILATERAL ELEMENTS WITH FOUR,EIGHT, OR NINE NODES
C
100 NEX1=NX+1
    NEY1=NY+1
    NOX = IEL*NX
    NYY = IEL*NY
    NOX1 = NOX + 1
    NYY1 = NYY + 1
    NEM=NOX*NY
    NNM = NOX1*NYY1 - (IEL-1)*NOX*NY
    IF (NPE .EQ. 9)NNM=NOX1*NYY1
    K0 = 0
    IF (NPE .EQ. 9) K0=1
C
C GENERATE THE ARRAY NOD(I,J)
C
    NOD(1,1) = 1
    NOD(1,2) = IEL+1
    NOD(1,3) = NOX1+(IEL-1)*NEX1+IEL+1
    IF (NPE .EQ. 9)NOD(1,3)=4*NX+5
    NOD(1,4) = NOD(1,3) - IEL
    IF(NPE .EQ. 4)GO TO 200
    NOD(1,5) = 2
    NOD(1,6) = NOX1 + (NPE-6)
    NOD(1,7) = NOD(1,3) - 1
    NOD(1,8) = NOX1+1
    IF (NPE .EQ. 9)NOD(1,9)=NOX1+2
200 IF(NY .EQ. 1)GOTO 230
    M = 1
    DO 220 N = 2,NY
    L = (N-1)*NX + 1
    DO 210 I = 1,NPE
210 NOD(L,I) = NOD(M,I)+NOX1+(IEL-1)*NEX1+K0*NX
220 M=L
230 IF(NX .EQ. 1)GO TO 270
    DO 260 NI = 2,NX
    DO 240 I = 1,NPE
    KI = IEL
    IF(I .EQ. 6 .OR. I .EQ. 8)K1=1+K0
240 NOD(NI,I) = NOD(NI-1,I)+K1
    M = NI
    DO 260 NJ = 2,NY
    L = (NJ-1)*NX+NI
    DO 250 J = 1,NPE
250 NOD(L,J) = NOD(M,J)+NOX1+(IEL-1)*NEX1+K0*NX
260 M = L
C
C GENERATE THE COORDINATES X(I) AND Y(I)
C
270 YC=0.0
    IF (NPE .EQ. 9) GOTO 310

```

```

DO 300 NI = 1, NEY1
I = (NOX1+(IEL-1)*NEX1)*(NI-1)+1
J = (NI-1)*IEL+1
X(I) = 0.0
Y(I) = YC
DO 280 NJ = 1,NOX
I=I+1
X(I) = X(I-1)+DX(NJ)
280 Y(I) = YC
IF(NI.GT.NY .OR. IEL.EQ.1)GO TO 300
J = J+1
YC = YC+DY(J-1)
I = I+1
X(I) = 0.0
Y(I) = YC
DO 290 II = 1, NX
K = 2*II-1
I = I+1
X(I) = X(I-1)+DX(K)+DX(K+1)
290 Y(I) = YC
300 YC = YC+DY(J)
RETURN

```

```

C
310 DO 330 NI=1,NYY1
I=NOX1*(NI-1)
XC=0.0
DO 320 NJ=1,NOX1
I = I+1
X(I) = XC
Y(I) = YC
320 XC = XC + DX(NJ)
330 YC = YC + DY(NI)
RETURN
END

```

```

C
SUBROUTINE MPlot(XLL,YLL,XX,YY,NOD,NEM,NND,NPE,XMIN,YMIN)
C*****
C SUBROUTINE TO DRAW THE MESH
C
C SUBROUTINE ARGUMENTS ARE:
C XLL, YLL LENGTH OF X AND Y DIMENSIONS OF ACTUAL PLOT (INCHES)
C (REAL*8)
C NEM NUMBER OF ELEMENTS IN THE MESH
C NND NUMBER OF NODES
C NPE NUMBER OF NODES PER ELEMENT
C*****
IMPLICIT REAL*8(A-H,O-Z)
REAL X(1000),Y(1000),TX(12),TY(12),XL,YL,XD,YD,H,XND,FPN,YM,XM
DIMENSION XX(1000),YY(1000),NOD(320,9)
XM = 0.
YM = 1.
C
C INITIALIZE THE PLOTTER
C
CALL PLOTS(0,0,50)
XXX = 0.
YYY = 0.
DO 10 I=1,NND
X(I) = SNGL(XX(I))
10 Y(I) = SNGL(YY(I))
DO 15 I=1,NND
X(I) = X(I) - SNGL(XMIN)
15 Y(I) = Y(I) - SNGL(YMIN)
XL = SNGL(XLL)
YL = SNGL(YLL)
TX(6) = 0.

```

```

        TY(6) = 0.
        TX(7) = 1.
        TY(7) = 1.
        CALL PLOT(1.,1.,-3)
C
C   DO LOOP FOR THE PLOTTING OF THE ELEMENTS STARTS HERE
C
        DO 100 N=1,NEM
        DO 50 I=1,4
        NX = NOD(N,I)
        TX(I) = X(NX)
50     TY(I) = Y(NX)
        TX(5) = TX(1)
        TY(5) = TY(1)
        CALL LINE(TX,TY,5,1,0,2)
100    CONTINUE
C
C   PLOT THE NODE NUMBERS
C
        H = 0.05
        DO 200 I=1,NND
        XD = X(I) - 0.4*H
        YD = Y(I) - 0.6*H
        FPN = FLOAT(I)
        CALL NUMBER(XD,YD,H,FPN,0.,-1)
200    CONTINUE
        RETURN
        END
C*****
        SUBROUTINE PRESS(NBM,AMU2,ITYPE,AMU,AK1,GAMADT,AMBDA,XD,YD,
&          P,STRAIN,VORT,GP)
C
C   .....
C   SUBROUTINE TO CALCULATE THE PRESSURE, THE SHEAR RATE AND
C   THE VORTICITY AT THE CENTER OF THE ELEMENTS
C   .....
C
        IMPLICIT REAL*8(A-H,O-Z)
        COMMON/MSH/DX(21),DY(21),X(350),Y(350),NOD(320,9)
        COMMON/GSTFM/A(1450,320)
        COMMON/INTE/NDF,NPE,NEM,NNM
        COMMON/VIS/EM,EN,DL,RHO,IT,IG
        DIMENSION SF(9),GDSF(2,9),ELXY(9,2),STRAIN(320),P(320),VORT(320),
&          GAMADT(320),XD(320),YD(320),AMU(320),AMBDA(320)
C
        GRAD = 0
        XIJ = 0.
        YIJ = 0.
C
C   DO LOOP OVER THE ELEMENTS
C
        DO 100 N=1,NEM
C
C   INITIALIZE THE COORDINATES FOR EACH ELEMENT
C
        T = 0.
        XD(N) = 0.
        YD(N) = 0.
        DUX = 0.
        DUJ = 0.
        DVX = 0.
        DVY = 0.
C
C   CALCULATE THE COORDINATES OF THE CENTROID OF THE ELEMENT
C
        DO 10 K=1,NPE
        NK = NOD(N,K)

```

```

        ELXY(K,1) = X(NK)
        ELXY(K,2) = Y(NK)
        XD(N) = XD(N) + ELXY(K,1)/DFLOAT(NPE)
10    YD(N) = YD(N) + ELXY(K,2)/DFLOAT(NPE)
C
C    CALCULATE THE VALUES OF THE DERIVATIVES OF THE VELOCITIES AT THE
C    CENTER OF THE ELEMENT
    CALL SHAPE (NPE,XIJ,YIJ,SF,GDSF,DET,ELXY)
    DO 30 J=1,NPE
        NJ = MOD(N,J)*NDF
        DUX = DUX + GDSF(1,J)*A(NJ-4,NBW)
        DUY = DUY + GDSF(2,J)*A(NJ-4,NBW)
        DVX = DVX + GDSF(1,J)*A(NJ-3,NBW)
        DVY = DVY + GDSF(2,J)*A(NJ-3,NBW)
C
C    CALCULATION OF THE SHEAR STRESS AT THE CENTER OF THE ELEMENT
C
30    T = T + SF(J)*A(NJ-1,NBW)
C
C    CALCULATION OF THE GRADIENT OF THE SOLUTION AND
C    PRESSURE COMPUTATION FOR THE STOKES FLOW (PENALTY METHOD)
C
    T = T + AMU2*(DUY+DVX)
    GRAD = DUX+DVY
    P(N) = -GP*GRAD
    STRAIN(N) = 2.*DSQRT(DUX**2 + DVY**2)
    VORT(N) = DUY-DVX
    GAMADT(N) = DSQRT(2.0*DUX**2 + 2.0*DVY**2 + (DVX+DUY)**2)
    AMBDA(N) = EM
    AMU(N) = DABS(T)/GAMADT(N)
    IF(IT.EQ.1) AMU(N) = AK1
    IF(ITYPE.GT.2.OR.ITYPE.LT.1) GOTO 100
    CALL VISF(AMU(N),GAMADT(N),AK1,AMU2)
    CALL LAMDA(AMBDA(N),GAMADT(N))
100 CONTINUE
    RETURN
    END
C*****
SUBROUTINE SHAPE(NPE,XI,ETA,SF,GDSF,DET,ELXY)
C
C    .....
C    THE SUBROUTINE EVALUATES THE INTERPOLATION FUNCTIONS (SF(I)) AND
C    ITS DERIVATIVES WITH RESPECT TO NATURAL COORDINATES (DSF(I,J)),
C    AND THE DERIVATIVES OF SF(I) WITH RESPECT TO GLOBAL COORDINATES
C    FOR FOUR, EIGHT, AND NINE NODE RECTANGULAR ISOPARAMETRIC ELEMENTS.
C    (ADJUSTED FROM REDDY [17])
C
C    SF(I).....INTERPOLATION FUNCTION FOR NODE I OF THE ELEMENT
C    DSF(I,J)....DERIVATIVE OF SF(J) WITH RESPECT TO XI IF I=1 AND
C                WITH RESPECT TO ETA IF I=2.
C    GDSF(I,J)...DERIVATIVE OF SF(J) WITH RESPECT TO X IF I=1 AND
C                WITH RESPECT TO Y IF I=2.
C    XNODE(I,J)...J-TH (J=1,2) COORDINATE OF NODE I OF THE ELEMENT
C    NP(I).....ARRAY OF ELEMENT NODES (USED FOR DEFINING SF AND DSF)
C    GJ(I,J).....JACOBIAN MATRIX
C    GIINV(I,J)...INVERSE OF THE JACOBIAN MATRIX
C    DET.....DETERMINANT OF THE JACOBIAN MATRIX
C    .....
C
C    IMPLICIT REAL*8 (A-H,O-Z)
    DIMENSION ELXY(9,2),XNODE(9,2),NP(9),DSF(2,9),GJ(2,2),GIINV(2,2),
1    SF(9),GDSF(2,9)
    DATA XNODE/-1.000,2*1.000,-1.000,0.000,1.000,0.000,-1.000,0.000,
2    2*-1.000,2*1.000,-1.000,0.000,1.000,2*0.000/
    DATA NP/1,2,3,4,5,7,6,8,9/
C
C    FNC(A,B) = A*B

```

```

      IF (NPE-8) 60,10,80
C
C   QUADRATIC INTERPOLATION FUNCTIONS (FOR THE EIGHT-NODE ELEMENT)
C
10 DO 40 I = 1, NPE
   NI = NP(I)
   XP = XNODE(NI,1)
   YP = XNODE(NI,2)
   XIO = 1.0+XI*XP
   ETAO = 1.0+ETA*YP
   XI1 = 1.0-XI*XI
   ETA1 = 1.0-ETA*ETA
   IF(I.GT.4) GO TO 20
   SF(NI) = 0.25*FNC(XIO,ETAO)*(XI*XP+ETA*YP-1.0)
   DSF(1,NI) = 0.25*FNC(ETAO,XP)*(2.0*XI*XP+ETA*YP)
   DSF(2,NI) = 0.25*FNC(XIO,YP)*(2.0*ETA*YP+XI*XP)
   GO TO 40
20 IF(I.GT.6) GO TO 30
   SF(NI) = 0.5*FNC(XI1,ETAO)
   DSF(1,NI) = -FNC(XI,ETAO)
   DSF(2,NI) = 0.5*FNC(YP,XI1)
   GO TO 40
30 SF(NI) = 0.5*FNC(ETA1,XIO)
   DSF(1,NI) = 0.5*FNC(XP,ETA1)
   DSF(2,NI) = -FNC(ETA,XIO)
40 CONTINUE
   GO TO 130
C
C   LINEAR INTERPOLATION FUNCTIONS (FOR FOUR-NODE ELEMENT)
C
60 DO 70 I = 1, NPE
   XP=XNODE(I,1)
   YP=XNODE(I,2)
   XIO=1.0+XI*XP
   ETAO=1.0+ETA*YP
   SF(I)=0.25*FNC(XIO,ETAO)
   DSF(1,I)=0.25*FNC(XP,ETAO)
70 DSF(2,I)=0.25*FNC(YP,XIO)
   GO TO 130
C
C   QUADRATIC INTERPOLATION FUNCTIONS (FOR THE NINE-NODE ELEMENT)
C
80 DO 120 I=1,NPE
   NI = NP(I)
   XP = XNODE(NI,1)
   YP = XNODE(NI,2)
   XIO = 1.0+XI*XP
   ETAO = 1.0+ETA*YP
   XI1 = 1.0-XI*XI
   ETA1 = 1.0-ETA*ETA
   XI2 = XP*XI
   ETA2 = YP*ETA
   IF(I .GT. 4)GOTO 90
   SF(NI) = 0.25*FNC(XIO,ETAO)*XI2*ETA2
   DSF(1,NI)=0.25*XP*FNC(ETA2,ETAO)*(1.0+2.0*XI2)
   DSF(2,NI)=0.25*YP*FNC(XI2,XIO)*(1.0+2.0*ETA2)
   GO TO 120
90 IF(I .GT. 6)GO TO 100
   SF(NI) = 0.5*FNC(XI1,ETAO)*ETA2
   DSF(1,NI) = -XI*FNC(ETA2,ETAO)
   DSF(2,NI) = 0.5*FNC(XI1,YP)*(1.0+2.0*ETA2)
   GO TO 120
100 IF(I .GT. 8)GO TO 110
   SF(NI) = 0.5*FNC(ETA1,XIO)*XI2
   DSF(2,NI) = -ETA*FNC(XI2,XIO)
   DSF(1,NI) = 0.5*FNC(ETA1,XP)*(1.0+2.0*XI2)
   GO TO 120

```

```

110 SF(NI) = FNC(XI1,ETA1)
    DSF(1,NI) = -2.0*XI*ETA1
    DSF(2,NI) = -2.0*ETA*XI1
120 CONTINUE
C
C   CALCULATE THE DETERMINANT AND THE INVERSE OF THE JACOBIAN
C
130 DO 140 I = 1,2
    DO 140 J = 1,2
    GJ(I,J) = 0.0
    DO 140 K = 1,NPE
140 GJ(I,J) = GJ(I,J) + DSF(I,K)*ELXY(K,J)
    DET = GJ(1,1)*GJ(2,2)-GJ(1,2)*GJ(2,1)
C
C   IF THE DETERMINANT IS NOT POSITIVE, THERE IS AN ERROR IN THE DATA
C
    IF(DET.LT.1.D-12) GO TO 160
C
    GJINV(1,1) = GJ(2,2)/DET
    GJINV(2,2) = GJ(1,1)/DET
    GJINV(1,2) = -GJ(1,2)/DET
    GJINV(2,1) = -GJ(2,1)/DET
    DO 150 I = 1,2
    DO 150 J = 1,NPE
    GDSF(I,J) = 0.0
    DO 150 K = 1, 2
150 GDSF(I,J) = GDSF(I,J) + GJINV(I,K)*DSF(K,J)
    RETURN
160 WRITE (6,170)
170 FORMAT(5X,'*** ERROR! THE DETERMINANT OF THE JACOBIAN IS LESS'
    &,' THAN OR EQUAL TO ZERO. CHECK INPUT DATA')
    STOP
    END
C*****
SUBROUTINE SOLVER (N,ITERM)
.....
C
C   SOLVER FOR NON-SYMMETRIC SYSTEM OF LINEAR BANDED EQUATIONS.
C   SOLUTION IS STORED IN A(N,2*ITERM).
C
C   A(I,J) .... GLOBAL STIFFNESS MATRIX
C   N ..... NUMBER OF EQUATIONS IN THE SYSTEM
C   ITERM..... HALF BAND-WIDTH
C   .....
C
    IMPLICIT REAL*8 (A-H,O-Z)
    COMMON/GSTFM/A(1450,320)
    PARE=1.D-12
    NBND=2*ITERM
    NBM=NBND-1
C
C   .... BEGIN ELIMINATION OF THE LOWER LEFT
C
    DO 80 I=1,N
C
C   CHECK IF THE DIAGONAL TERM IS ZERO
C
10 IF (DABS(A(I,ITERM)).LT.PARE) GO TO 110
C
20 JLAST=MIN0(I+ITERM-1,N)
    L=ITERM+1
    DO 40 J=I,JLAST
    L=L-1
    IF (DABS(A(J,L)).LT.PARE) GO TO 40
    B=A(J,L)
    DO 30 K=L,NBND
30 A(J,K)=A(J,K)/B

```

```

      IF (I.EQ.N) GO TO 90
40 CONTINUE
      L=0
      JFIRST=I+1
      IF (JLAST.LE.I) GO TO 80
      DO 70 J=JFIRST,JLAST
      L=L+1
      IF (DABS(A(J,ITERM-L)).LT.PARE) GO TO 70
      DO 50 K=ITERM,NBM
50 A(J,K-L)=A(J-L,K)-A(J,K-L)
      A(J,NBND)=A(J-L,NBND)-A(J,NBND)
      IF (I.GE.N-ITERM+1) GO TO 70
      DO 60 K=1,L
60 A(J,NBND-K)=-A(J,NBND-K)
70 CONTINUE
80 CONTINUE
C
90 L=ITERM-1
      DO 100 I=2,N
      DO 100 J=1,L
      IF (N+1-I+J.GT.N) GO TO 100
      A(N+1-I,NBND)=A(N+1-I,NBND)-A(N+1-I+J,NBND)*A(N+1-I,ITERM+J)
100 CONTINUE
      RETURN
C
C      IF ANY TERM ON THE DIAGONAL IS ZERO PRINT ERROR MESSAGE AND STOP
C
110 WRITE (6,140)
      STOP
C
140 FORMAT (' COMPUTATION STOPPED IN SOLVER BECAUSE ZERO APPEARED ON
      IMAIN DIAGONAL *** ERROR IN SOLVER ***' )
      END
C*****
      SUBROUTINE STIFFQ( IEL, ITYPE, AK1, AK2, VEL, ISTR, AMU2 )
C
C      .....
C      STIFFNESS MATRIX FOR ISOPARAMETRIC QUADRILATERAL ELEMENTS
C      .....
C
      IMPLICIT REAL*8(A-H,O-Z)
      COMMON/STF/ELSTIF(45,45),ELXY(9,2),F(45)
      COMMON/VIS/ETAM,ETAN,AMBDA,RHO,ITER,IGNF
      COMMON/PTT/DKSI,EPSIL
      COMMON/INTE/NDF,NPE,NEM,NNM
      DIMENSION SF(9),GDSF(2,9),GAUSS(4,4),MT(4,4),S(9,9),S01(9,9)
      *      ,S02(9,9),SV11(9,9),SV12(9,9),SV21(9,9),SV22(9,9),
      *      S01V1(9,9),S02V2(9,9),VEL(45),ST11(9,9),ST12(9,9)
      *      ,ST22(9,9),S11(9,9),S22(9,9),S12(9,9),FI(9)
      DATA GAUSS/4*0.000,-.5773502700,.5773502700,2*0.000,-.7745966700,
      20.000,.7745966700,0.000,-.8611363100,
      3-.3399810400,.3399810400,.8611363100/
      DATA MT/2.000,3*0.000,2*1.000,2*0.000,.5555555500,.8888888800,
      2.5555555500,0.000,.3478548500,2*.6521451500,.3478548500/
C
      NN = NPE*NDF
      NGP = IEL+1
      NGPS = NGP**2
      GIES = 0.5
      IF (ISTR.EQ.1) GO TO 10
C
C      CHOOSE THE CONSTITUTIVE MODEL
C
      CEPS = 0.
      CKSI = 0.
      DLEO = 0.0
      AMBDA = ETAM

```

```

    AMU = AK1
    IF (ITER.EQ.1) GO TO 10
    IF (ITYPE-4) 10,5,6
5  CEPS = EPSIL
    CKSI = DKSI
    GO TO 10
6  DLEO = ETAM*GIES/AK1
C
C  INITIALIZE THE ARRAYS
C
10 CONTINUE
    DO 20 I = 1, NPE
    DO 15 J = 1, NPE
    S(I,J)=0.0
    S01(I,J) = 0.0
    S02(I,J) = 0.0
    S11(I,J) = 0.
    S22(I,J) = 0.
    S01V1(I,J) = 0.0
    S02V2(I,J) = 0.0
    ST11(I,J) = 0.
    ST12(I,J) = 0.
    ST22(I,J) = 0.
    SV11(I,J) = 0.0
    SV12(I,J) = 0.0
    SV21(I,J) = 0.0
    SV22(I,J) = 0.0
15 CONTINUE
20 FI(I) = 0.
    DO 30 I = 1,NN
    F(I) = 0.0
    DO 30 J = 1,NN
30 ELSTIF(I,J) = 0.0
    DUDX = 0.0
    DUDY = 0.0
    DVDX = 0.0
    DVDY = 0.0
    GAMADT = 0.0
C
C  DO-LOOPS ON NUMERICAL (GAUSS) QUADRATURE BEGIN HERE
C
    DO 100 NI = 1,NGP
    DO 100 NJ = 1,NGP
C
C  INITIALIZE THE NON-LINEAR TERMS (PSEUDO-FORCES)
C
    T11 = 0.
    T12 = 0.
    T22 = 0.
    V1 = 0.0
    V2 = 0.0
    UX = 0.0
    UY = 0.0
    VX = 0.0
    VY = 0.0
C
C  EVALUATE THE SHAPE FUNCTIONS AT EACH GAUSS POINT
C
    XI = GAUSS(NI,NGP)
    ETA = GAUSS(NJ,NGP)
    CALL SHAPE(NPE,XI,ETA,SF,GDSF,DET,ELXY)
C
C  EVALUATE THE NON-LINEAR TERMS
C
    DO 50 I = 1,NPE
    L = 5*I - 4
    V1 = VEL(L)*SF(I) + V1

```

```

V2 = VEL(L+1)*SF(I) + V2
UX  = UX  + VEL(L)*GDSF(1,I)
UY  = UY  + VEL(L)*GDSF(2,I)
VX  = VX  + VEL(L+1)*GDSF(1,I)
VY  = VY  + VEL(L+1)*GDSF(2,I)
IF (ISTR.EQ.1) GOTO 50
T11 = T11 + VEL(L+2)*SF(I)
T12 = T12 + VEL(L+3)*SF(I)
T22 = T22 + VEL(L+4)*SF(I)
IF (ITYPE.GT.2) GO TO 50
50 CONTINUE
C
DUDX = UX/NGPS + DUDX
DUDY = UY/NGPS + DUDY
DVDX = VX/NGPS + DVDX
DV DY = VY/NGPS + DV DY
CONST = DET*MT(NI,NGP)*MT(NJ,NGP)
TRT = T11 + T22
CPTT = DEXP(ETAM*CEPS/AK1*TRT)
C
C
C CALCULATION OF THE GALERKIN INTEGRALS
C
DO 80 I=1,NPE
DO 70 J=1,NPE
S(I,J) = CPTT*CONST*SF(I)*SF(J) + S(I,J)
S01(I,J) = CONST*SF(I)*GDSF(1,J) + S01(I,J)
S02(I,J) = CONST*SF(I)*GDSF(2,J) + S02(I,J)
S11(I,J) = CONST*GDSF(1,I)*GDSF(1,J) + S11(I,J)
S22(I,J) = CONST*GDSF(2,I)*GDSF(2,J) + S22(I,J)
IF (ISTR.EQ.1) GO TO 70
S01V1(I,J) = CONST*V1*SF(I)*GDSF(1,J) + S01V1(I,J)
S02V2(I,J) = CONST*V2*SF(I)*GDSF(2,J) + S02V2(I,J)
SV11(I,J) = CONST*UX*SF(I)*SF(J) + SV11(I,J)
SV12(I,J) = CONST*UY*SF(I)*SF(J) + SV12(I,J)
SV21(I,J) = CONST*VX*SF(I)*SF(J) + SV21(I,J)
SV22(I,J) = CONST*VY*SF(I)*SF(J) + SV22(I,J)
ST11(I,J) = CONST*SF(I)*SF(J)*T11 + ST11(I,J)
ST12(I,J) = CONST*SF(I)*SF(J)*T12 + ST12(I,J)
ST22(I,J) = CONST*SF(I)*SF(J)*T22 + ST22(I,J)
70 CONTINUE
80 FI(I) = CONST*SF(I)*(UY-VX) + FI(I)
100 CONTINUE
C
IF (ISTR.EQ.1) GO TO 400
IF(ITYPE.GT.2.OR.ITER.EQ.1) GOTO 111
C
C
C EVALUATION OF THE VARIABLE VISCOSITY AND RELAXATION TIME
C
C
C GAMADT IS THE MAGNITUDE OF THE RATE OF DEFORMATION TENSOR
C
GAMADT = DSQRT(2.0*DUDX**2 + 2.0*DVDY**2 + (DV DX + DUDY)**2)
CALL VISF(AMU,GAMADT,AK1,AMU2)
IF (ITYPE.EQ.2) CALL LAMDA(AMBDA,GAMADT)
C
C
C EVALUATION OF THE ENTRIES IN THE ELEMENT STIFFNESS MATRIX
C
111 II = 1
DO 200 I=1,NPE
JJ = 1
DO 150 J=1,NPE
ELSTIF(II,JJ) = -RHO*S01V1(I,J) - RHO*S02V2(I,J) + AMU2*S22(I,J)
ELSTIF(II,JJ+2)= S01(J,I)
ELSTIF(II,JJ+3)= S02(J,I)
ELSTIF(II+1,JJ+1)= -RHO*S01V1(I,J)-RHO*S02V2(I,J)+AMU2*S11(I,J)
ELSTIF(II+1,JJ+3)= S01(J,I)
ELSTIF(II+1,JJ+4)= S02(J,I)
ELSTIF(II+2,JJ) = -2.0*AMU*S01(I,J)

```

```

      ELSTIF(II+2,JJ+2) = S(I,J) + AMBDA*S01V1(I,J)+AMBDA*S02V2(I,J)
*      - 2.0*SV11(I,J)*AMBDA + DLEO*ST11(I,J) + 2.*AMBDA*CKSI*
&      SV11(I,J)
      ELSTIF(II+2,JJ+3) = -2.0*AMBDA*SV12(I,J) + DLEO*ST12(I,J)
&      + AMBDA*CKSI*(SV12(I,J)+SV21(I,J))
      ELSTIF(II+3,JJ) = -AMU*S02(I,J)
      ELSTIF(II+3,JJ+1) = -AMU*S01(I,J)
      ELSTIF(II+3,JJ+2) = -AMBDA*SV21(I,J) + DLEO*ST12(I,J)
&      +.5*AMBDA*CKSI*(SV12(I,J)+SV21(I,J))
      ELSTIF(II+3,JJ+3) = S(I,J) + AMBDA*S01V1(I,J)+AMBDA*S02V2(I,J)
&      -AMBDA*(SV11(I,J) - SV22(I,J))
      ELSTIF(II+3,JJ+4) = -AMBDA*SV12(I,J) + DLEO*ST12(I,J)
&      + .5*AMBDA*CKSI*(SV12(I,J) + SV21(I,J))
      ELSTIF(II+4,JJ+1) = -2.0*AMU*S02(I,J)
      ELSTIF(II+4,JJ+3) = -2.0*AMBDA*SV21(I,J) + DLEO*ST12(I,J)
&      + AMBDA*CKSI*(SV12(I,J)+SV21(I,J))
      ELSTIF(II+4,JJ+4) = S(I,J) + AMBDA*S01V1(I,J)+AMBDA*S02V2(I,J)
*      - 2.0*AMBDA*SV22(I,J) + DLEO*ST22(I,J) + 2.*CKSI*AMBDA
&      *SV22(I,J)
150 JJ = NDF*J+1
200 II = NDF*I+1
C
C      PENALTY TERMS
C
      DO 300 NI = 1,IEL
      DO 300 NJ = 1,IEL
      XI = GAUSS(NI,IEL)
      ETA = GAUSS(NJ,IEL)
      CALL SHAPE(NPE,XI,ETA,SF,GDSF,DET,ELXY)
      CONST = DET*NT(NI,IEL)*NT(NJ,IEL)
      II = 1
      DO 280 I = 1,NPE
      JJ = 1
      DO 260 J = 1,NPE
      ELSTIF(II,JJ) = AK2*GDSF(1,I)*GDSF(1,J)*CONST+ELSTIF(II,JJ)
      ELSTIF(II+1,JJ) = AK2*GDSF(1,I)*GDSF(2,J)*CONST + ELSTIF(II+1,JJ)
      ELSTIF(II,JJ+1) = AK2*GDSF(2,I)*GDSF(1,J)*CONST + ELSTIF(II,JJ+1)
      ELSTIF(II+1,JJ+1)=AK2*GDSF(2,I)*GDSF(2,J)*CONST+ ELSTIF(II+1,JJ+1)
260 JJ = NDF*J + 1
280 II=NDF*I + 1
300 CONTINUE
      RETURN
C
C      STREAM FUNCTION CALCULATION
C
400 CONTINUE
      DO 500 I=1,NPE
      DO 450 J=1,NPE
450 ELSTIF(I,J) = S11(I,J) + S22(I,J)
500 F(I) = -FI(I)
      RETURN
      END
C*****
      SUBROUTINE STRESS(NBM,T11,T12,T22,AMU2,INEI,ITYPE,DEB)
      .....
C
C      SUBROUTINE THAT CALCULATES THE STRESSES WITH THE ADDITION
C      OF THE RETARDATION PARAMETER. THE STRESSES ARE COMPUTED AT
C      THE CENTER OF EACH ELEMENT AND FOR EVERY GLOBAL NODE THEY
C      ARE AVERAGED OVER THE ELEMENTS THEY BELONG
C      .....
C
      IMPLICIT REAL*8(A-H,O-Z)
      DIMENSION T1(350,9),T2(350,9),T3(350,9),T11(350),T12(350),
&      T22(350),SF(9),GDSF(2,9),ELXY(9,2),XI(9),YI(9),
&      INODE(350)
      COMMON/MSH/DX(21),DY(21),X(350),Y(350),NOD(320,9)

```

```

COMMON/GSTFM/A(1450,320)
COMMON/INTE/NDF,NPE,NEM,NNM
COMMON/VIS/EM,EN,DL,RHO,IT,IG
DATA XI/-1.,2*1.,-1.,0.,1.,0.,-1.,0./,YI/-1.,-1.,2*1.,-1.,
& 0.,1.,2*0./
C
C INITIALIZE THE RATES ETC.
C
G = 0.
DLA = EM
C
DO 100 N=1,NEM
C
DO 10 K=1,NPE
NK = NOD(N,K)
ELXY(K,1) = X(NK)
10 ELXY(K,2) = Y(NK)
C
DO 90 I=1,NPE
C
SR1 = 0.
SR2 = 0.
SR3 = 0.
DO 85 J=1,NPE
NNJ = NOD(N,J)*NDF
CALL SHAPE(NPE,XI(I),YI(I),SF,GDSF,DET,ELXY)
SR1 = SR1 + 2.*GDSF(1,J)*A(NNJ-4,NBW)
SR2 = SR2 + GDSF(2,J)*A(NNJ-4,NBW) + GDSF(1,J)*A(NNJ-3,NBW)
85 SR3 = SR3 + 2.*GDSF(2,J)*A(NNJ-3,NBW)
C
T1(N,I) = AMU2*SR1
T2(N,I) = AMU2*SR2
T3(N,I) = AMU2*SR3
IF (NOD(N,I).EQ.IWEI) G = G + DSQRT(SR1**2/2.+SR2**2+SR3**2/2.)
90 CONTINUE
100 CONTINUE
C
C FIND THE CONTRIBUTION OF EACH ELEMENT TO EACH GLOBAL NODE
C
DO 120 I=1,NNM
INODE(I) = 0
T11(I) = 0.
T12(I) = 0.
120 T22(I) = 0.
DO 200 I=1,NNM
DO 190 J=1,NEM
DO 180 K=1,NPE
IF(NOD(J,K).NE.I) GOTO 180
INODE(I) = INODE(I) + 1
T11(I) = T1(J,K)+T11(I)
T12(I) = T2(J,K)+T12(I)
T22(I) = T3(J,K)+T22(I)
180 CONTINUE
190 CONTINUE
C
C AVERAGE THE RETARDATION TERMS AT THE NODES OVER THE ELEMENTS
C THEY BELONG AND ADD THE VISCOELASTIC PART
C
IF (INODE(I).LT.1) GO TO 210
NI = I*NDF
T11(I) = T11(I)/DFLOAT(INODE(I)) + A(NI-2,NBW)
T12(I) = T12(I)/DFLOAT(INODE(I)) + A(NI-1,NBW)
T22(I) = T22(I)/DFLOAT(INODE(I)) + A(NI,NBW)
200 CONTINUE
C
C CALCULATE THE DEBORAH NUMBER AT NODE IWEI

```

```

      G = G/DFLOAT(INODE(IWEI))
      IF (ITYPE.EQ.1.OR.ITYPE.EQ.2) CALL LAMDA(DLA,G)
      DEB = DLA*G
C
      RETURN
C
      210 WRITE(6,1000)
          STOP
C
      1000 FORMAT(10X,'ERROR!! IN SUBROUTINE STRESS. CHECK PROCEDURE FOR'
&,' INODE' )
          END
C*****
      SUBROUTINE UPDATE(N,V,B,GF,GP,XY,M,K)
C
C .....
C
      SUBROUTINE THAT UPDATES THE SOLUTION VECTOR FOR EACH ELEMENT
C .....
C
      IMPLICIT REAL*8(A-H,O-Z)
      DIMENSION GF(1665),GP(1665),V(45),XY(9,2)
      COMMON/MSH/DX(21),DY(21),X(350),Y(350),NOD(320,9)
C
      DO 200 I=1,K
          NI = NOD(N,I)
          L = M*(I-1) + 1
          LI = M*(NI-1) + 1
          DO 100 J=0,M-1
      100 V(L+J) = B*GF(LI+J) + (1.-B)*GP(LI+J)
          XY(I,1) = X(NI)
      200 XY(I,2) = Y(NI)
          RETURN
          END
C*****
      SUBROUTINE VISF(A,G,A1,A2)
C
C SUBROUTINE TO CALCULATE THE VISCOSITY FUNCTION
C
C A.....VISCOSITY
C G.....SHEAR RATE
C A1.....ZERO SHEAR VISCOSITY
C A2.....INFINITE SHEAR RATE VISCOSITY
C
      IMPLICIT REAL*8(A-H,O-Z)
      COMMON/VIS/EM,EN,DL,R,I,IT
      IF (IT.EQ.2) GOTO 10
      A = EM*G**((EN-1.0)
      RETURN
      10 A = A1*(1.0+(EM*G)**2)**((EN-1.0)/2.0) + A2
      RETURN
      END

```

Appendix B. Guide to the Program NONEWT.FEM

The program NONEWT.FEM is a finite element code that solves 2-D flow problems of newtonian, generalized newtonian and non-linear viscoelastic fluids. The program gives the choice of five codeformational viscoelastic models and the generalized Newtonian case. It also gives the choice of two viscosity functions for the GNF case. The selection of the rheological model is made by the value of parameter ITYPE. The selection of the viscosity function is made by the parameter IGNF. The function of the relaxation time should be given by the user if it is desired as a separate subroutine. The code gives the choice of bi-linear or bi-quadratic elements for the mesh, by using the value of the parameter IEL. There is also a routine to construct a mesh, but its use is limited to rectangular meshes. The code calculates the values of the stresses, the velocities and the birefringence at each node of the mesh. It also calculates the value of the pressure, the shear rate, the extension rate, the relaxation time (if it is variable), the viscosity and the vorticity at the center of each element. The value of the elasticity parameters $We = N_1/2\tau_{12}$ and $De = \lambda\dot{\gamma}_0$ is also calculated at a specified (by the user) node. The stream function is calculated (and normalized) at each node and can be plotted as a contour plot by connecting to the commercial routine SURFACE2 by means of an EXEC file.

The steps that are recommended to be followed for the use of this code are listed in the following:

1. Calculate the boundary conditions at the inlet and outlet planes (if such planes exist). A program for viscoelastic flows in slit dies is the code INIT that is described in ch. 3.6.6. The values

of the velocities for the Newtonian iteration, as well as the subsequent iterations and the stream function are needed at both the inlet and outlet planes. The values of the stresses are needed at the inlet plane.

2. Run the program GEN2D (also described in ch 3.6.6) to construct the mesh and reformat its output to be consistent with the input of NONEWT.FEM (the format for the input to this code will be listed in Appendix A). This step is not necessary, as the mesh can also be constructed manually or by NONEWT itself (if it is rectangular).
3. Construct a file with the input data. The cards that should be input are described in the documentation of the code in Appendix A, together with their format. A few comments will be listed here on the recommended values of the several input variables.

If the mesh was generated by GEN2D and reformatted to fit the input data, it should occupy the first part of the input file. Then the user has to input cards 9 and further after the cards generated by the previous program. Care should be taken so that the parameters of the model, the viscosity function and the maximum number of the iterations be written at their appropriate positions in card 2.

If the mesh was not generated by the previous routine and MESH is not used, the user has to input all cards as they appear in Appendix A. NPRNT should usually have a value of zero to decrease consumption of output paper, except when tracking of errors is desired.

The defined outline of the flow domain should be closed. That is, the last point should coincide with the first one. The number of points (NOUT) should reflect this. When a mesh generating routine is used, it is easier to draw the mesh first and then input the outline and the boundary conditions, when the node numbers and exact positions in the mesh will be known.

If inertia terms are to be kept in the equation of motion, the value of RHO should not be zero. This value should be given in compatible units (e.g. if the velocities are given in mm/sec, the geometric dimensions in mm and the stresses in Pa, the density should be

given in g/mm^3). If inertia terms are to be neglected, the user should set RHO equal to zero.

The penalty parameter is multiplied by the code by a factor of 10^6 . The input value for C2 should, therefore, have a value of the order of the viscosity. The value of BETA and TOL should not be zero. If they are the code will adjust them. The default values are BETA = 1 and TOL = 0.01.

NSDF and IBDF(I) include all specified degrees of freedom (velocities and stresses) and not just the boundary nodes. Boundary conditions should be given both for the first (newtonian) iteration and the subsequent iterations. Care should be taken that the inlet and the outlet velocity profiles give the same overall flow rate. If this does not happen it may lead to divergence or erroneous results for the pressure because of the penalty formulation.

The appropriate boundary forces should be specified. If insufficient number of this type of boundary conditions is specified, the program will assume zero values for those that are missing and errors may result.

The boundary conditions for the stream function may be calculated at the same step as the values of the velocities etc. If such boundary conditions are not given, the program will terminate without the stream function calculation giving an error message.

If the node number for the normalization of the stream function is not given, the program will attempt to define and use one, usually a node at the centerline or the wall.

4. Replace the subroutine that will calculate lambda as a function of the shear rate. it should have the following format:

```
SUBROUTINE LAMDA(DL,G)
ETC.
```

where G is the shear rate (input) and DL is the calculated relaxation time (output) both in double precision.

5. Run an EXEC file to compile and run the program with the input data file, print the output and plot the mesh, the birefringence contours and the streamlines. The output will contain the echo of the input data, the calculated values of the primary and secondary variables and the plots of the mesh, the contours of the fringe order and the streamlines.

**The vita has been removed from
the scanned document**